RECOVERY ACT – DECISION AIDS FOR GEOTHERMAL SYSTEMS

PROJECT ID: DE-EE0002743

Final Report

Further Development and Application of GEOFRAC-FLOW to a Geothermal Reservoir

---

Alessandra Vecchiarelli

Herbert Einstein

Massachusetts Institute of Technology

May 2014

Further Development and Application of GEOFRAC-FLOW to Geothermal Reservoirs

Executive Summary

GEOFRAC is a three-dimensional, geology-based, geometric-mechanical, hierarchical, stochastic model of natural rock fracture systems. The main characteristics of GEOFRAC are its use of statistical input representing fracture patterns in the field in form of the fracture intensity P_{32} (fracture area per volume) and the best estimate fracture size E(A). This information can be obtained from boreholes or scanlines on the surface, on the one hand, and from window sampling of fracture traces on the other hand.

In the context of this project, "Recovery Act - Decision Aids for Geothermal Systems", GEOFRAC was further developed into GEOFRAC-FLOW as has been reported in the reports, "Decision Aids for Geothermal Systems - Fracture Pattern Modelling" and "Decision Aids for Geothermal Systems - Fracture Flow Modeling". GEOFRAC-FLOW allows one to determine preferred, interconnected fracture paths and the flow through them.

In this report other models that can be used to model geothermal reservoirs are briefly reviewed in Chapter 2 followed by a summary of the main features of GEOFRAC-FLOW (Chapter 3) and a parametric study. In that study (Chapter 4) the effect of varying fracture orientation and fracture apertures was investigated. This showed that as expected, flow rate increased with aperture. The orientation effect is more complicated but also logical: For parallel fractures, flow is greater with secondary rotation; for randomly oriented fractures, flow is greater with no secondary rotation.

Chapters 5 and 6 describe the new developments. GEOFRAC-FLOW as originally developed assumed a fractured rock mass with flow entering into and exiting from the rock mass through planar boundaries. This may not correspond to a reality where, in most cases, flow occurs between injection and production wells. Hence a new feature with wells as boundaries was included. – The other development is a Graphical User Interface (GUI), which allows one to conveniently enter all the input ranging from reservoir geometry to fracture characterization and flow. Output in form of information on flow rates and graphical representations of the fracture networks is then provided.

The other main contribution developed in this report is the application of GEOFRAC-FLOW to the Bjarnaflag hydrothermal plant in Northern Iceland. This is making use of the Nármafjall geothermal field. Note that this application also included the simple heat transfer model described in the parallel report "Numerical and Analytical Modeling of Heat Transfer between Fluid and Fractured Rocks". Input parameters were obtained from information made available by the Icelandic energy company Landsvirkjun with some interpretation by the authors of this report. The resulting flow rates compare well to the actual values while the energy (heat) extraction is higher than the capacity of the powerplant. This is to be expected given the energy conversion effects of the geothermal plant and by the fact that the thermal model does not consider thermal drawdown. One can, therefore, state that the modeling is satisfactory, particularly given the work on thermal drawdown reported separately.

FURTHER DEVELOPMENT AND APPLICATION OF GEOFRAC-FLOW TO A GEOTHERMAL RESERVOIR

TABLE OF CONTENTS

CHAPTER 1

INTRODUCTION

In deep geothermal energy projects naturally and artificially induced fractures in rock are used to circulate a fluid (usually water) to extract heat; this heat is then either used directly or converted to electric energy. MIT has developed a stochastic fracture pattern model GEOFRAC (Ivanova, 1995; Ivanova et al., 2012). This is based on statistical input on fracture patterns from the field. The statistical input is in form of the fracture intensity P_{32} (fracture area per volume) and the best estimate fracture size. P_{32} can be obtained from fracture spacing information in boreholes and scanlines outcrops using the approach by Dershowitz and Herda (1992). Best estimate fracture size can be obtained from fracture trace lengths measured on outcrops with suitable bias corrections as developed by Zhang et al. (2002). Distribution and estimates of fracture size can also be obtained subjectively. GEOFRAC has been applied and tested by estimating the fracture intensity and estimated fracture size from tunnel records and from borehole logs. In the research presented here, GEOFRAC predictions were satisfactorily applied for geothermal basin characterization. Since its original development, GEOFRAC has been made more effective by basing it on Matlab, and it has been expanded by including an intersection algorithm and, most recently, a flow model. GEOFRAC belongs to the category of Discrete-Fracture Network models. In this type of model the porous medium (matrix) is not represented and all flow is restricted to the fractures. Fractures are represented by polygons in three dimensions. Both the fracture - and flow model have been

tested and a parametric study was conducted in order to check the sensitivity of the output results to the inputs.

In Chapter 2 the existing theoretical models of geothermal reservoir simulation are briefly described with emphasis on hydro-mechanical models. The available commercial software tools and their application in large scale projects are also introduced. Chapter 3 describes the basic concepts of GEOFRAC, a three-dimensional discrete fracture pattern model. In Chapter 4 the parametric analysis is used to capture the sensitivity to the input parameters of GEOFRAC. Chapter 5 introduces a new algorithm in GEOFRAC that can be used to model intersections between fractures and injection and production wells. In Chapter 6 the use of the GUI to run GEOFRAC is introduced and explained. In Chapter 7 a case study is presented, specifically, data from the Námafjall geothermal project in Iceland are used as inputs, and results from the simulation are compared with the real data. The conclusions in Chapter 8 are intended to explain the overall results and to briefly discuss future research.

CHAPTER 2

A REVIEW OF PREVIOUS MODELING OF GEOTHERMAL RESERVOIR

The development of simulation model for enhanced geothermal reservoirs requires predicting the capacity of hydraulically induced reservoirs. Geothermal reservoir modeling in turn requires an adequate mathematical representation of the physical and chemical processes during the long-term heat extraction period. During the last 20 years the use of computer modeling of geothermal areas has become standard practice.

The intent of this chapter is to describe available models on the basis of the geological, geometric, mechanical (both solid and fluid) and thermal conditions.

2.1 FRACTURE SYSTEM MODELS

Modeling is an essential phase in studying the fundamental processes occurring in rocks and for rock engineering design. Modeling rock masses represents, however, a very complex challenge; the most important reason is that the rock is a natural geological material. A rock mass is a discontinuous, anisotropic, inhomogeneous and non-elastic medium; it is subjected to stresses often by tectonic movements, uplift, subsidence, glaciation and tidal cycles. A rock mass is also a

fractured and porous medium containing fluids in either liquid or gas phases, for example, water, oil, natural gas and air, under different in situ conditions of temperature and fluid pressures. The combination of all these factors makes rock masses a difficult material for mathematical representation via numerical modeling. The difficulty increases when coupled thermal, hydraulic and mechanical processes need to be considered simultaneously.

Uncertainties are one of the main characteristics of rock mechanics. It is important to understand the uncertainties and assess them—so that it is possible to run models managing risks without being conservative.

The aim of this section is to present numerical methods that are currently used to model rock fractures. It will introduce each model with a brief description followed by application cases. After this section, some of the models used to simulate particular characteristics of a rock mass such as the aperture of fractures and the intensity of the fractures are presented.

2.1.1 Numerical methods

The most commonly applied numerical methods in rock mechanics are:

Continuum methods

- Finite Difference Method (FDM)
- Finite Element Method (FEM)
- Boundary Element Method (BEM)

Discontinuum methods

- Discrete Element Method (DEM)
- Discrete Fracture Network (DFN) methods

Hybrid continuum/discontinuum models

- Hybrid FEM/BEM
- Hybrid DEM/DEM
- Hybrid FEM/DEM
- Other hybrid models

I will briefly describe these methods and their application in rock mechanisms.

The first category of numerical models consists of the continuum methods. Continuity is a macroscopic concept. The continuum assumption implies that, the material cannot be split or broken into pieces. All material points originally in the neighborhood of a certain point in the problem domain remain in the same neighborhood throughout the deformation or transport process. Of course, at the microscopic scale, all materials are discrete systems. However, representing the microscopic components individually is mathematically complicated and often unnecessary in practice (Jing, 2003).

Figure 2.1 shows how to model a fractured rock mass (Figure 2.1 a) using a continuum method such as FDM or FEM (Figure 2.1 b), the BEM (Figure 2.1 c) (Jing, 2003). The description of these methods will be given in the next sections.

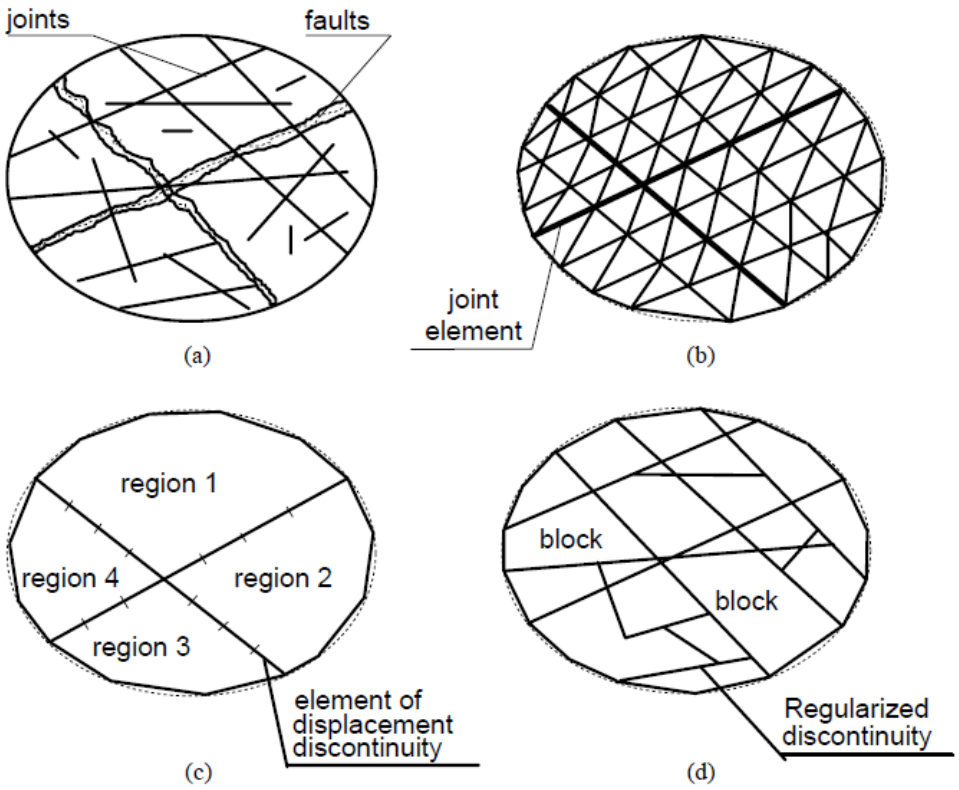

Figure 2.1 - Representation of a fractured rock mass shown in (a), by FDM or FEM shown in (b), BEM shown in (c), and DEM shown in (d). (Jing, 2003)

Discrete element methods are numerical procedures for simulating the complete behavior of systems of discrete, interacting bodies. Discrete Element Methods (DEM) and Discrete Fracture Networks (DFN) will be described after the continuum method.

The combination of the continuum and discrete models produces a very interesting group of so-called hybrid models. Hybrid models are frequently used in rock engineering, for flow and stress/deformation problems of fractured rocks. The main types of hybrid models are the hybrid BEM/FEM, DEM/BEM models.

Finite Difference Methods

The FDM approximates the governing PDEs by replacing partial derivatives with differences in regular (Figure 2.2 a) or irregular grids (Figure 2.2 b) imposed over the problem domain. The original PDEs are transformed into a system of algebraic equations in terms of unknowns at grid points. After imposing the necessary initial and boundary conditions the solution of the system equations is obtained.

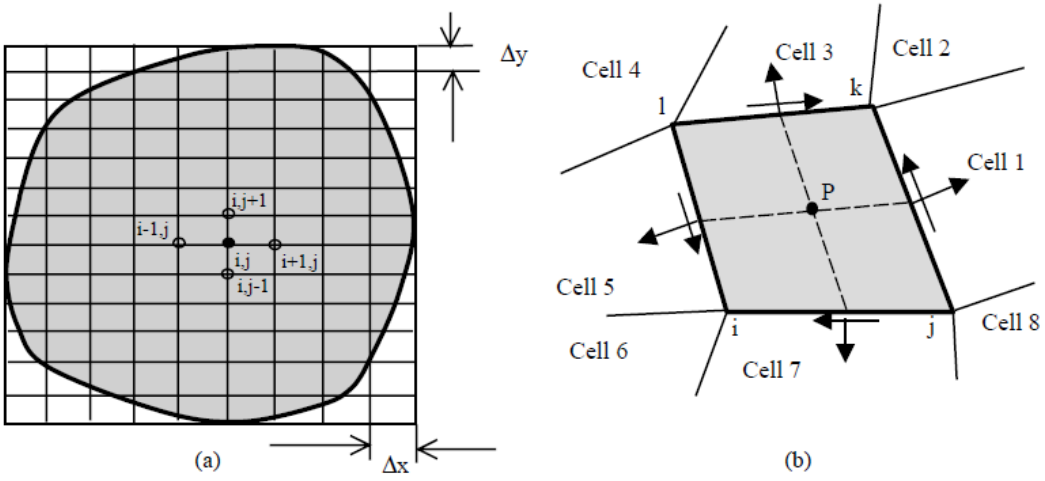

Figure 2.2 - (a) Regular quadrilateral grid for the FDM and (b) irregular quadrilateral grid for the FDM (Jing, 2003)

Coates and Schoenberg (1995) use the Finite Difference Method in order to model faults and fractures. What they try to do is to use the seismic propagation to detect slip surfaces. Figure 2.3 shows how they use the staggered grid and the locations at which the different components, for example, of the stress and velocity, are defined. The use of the FDM was successful and all equations used are well presented in their paper. The issue that they also reported in the conclusion is that it is not so easy to assess whether a slip surface is a realistic model of a fault.

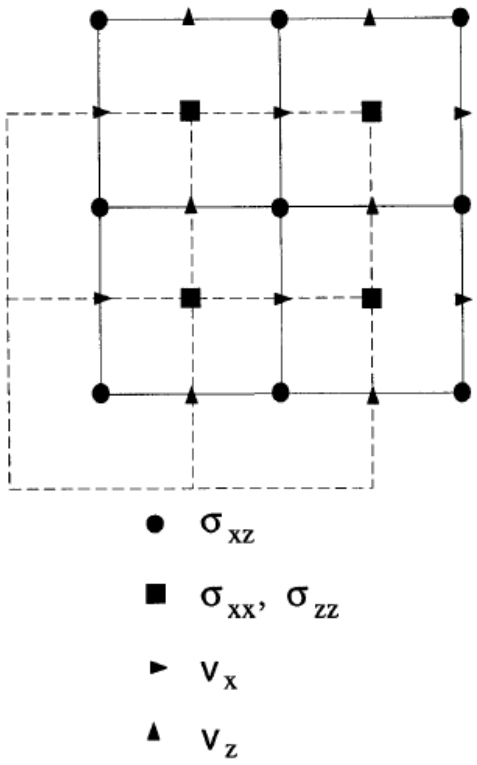

Figure 2.3 - Staggered grid used for the 2-D finite-difference scheme (Coates et al. 1995)

One of the best known commercially available FD codes is FLAC. FLAC is an advanced two-dimensional continuum model for geotechnical analysis of rock, soil, and structural support. Many researchers have used FLAC for studies such as stability of a slope and of a rock mass. (Shen et al., 2012; Apuani et al., 2005).

Finite Element Method

Finite element modeling is a well-established numerical technique that allows one to address the influence of the complexities that arise from non-linear behavior in geological deformations. Finite element models are used in addressing a broad variety of geological problems ranging from folding and fracturing of rocks (e.g., Zhang Y. et al., 2000) to tectonics (Kwon, 2004; Kwon et al., 2007).

The FEM requires the division of the problem domain into sub-domains; i.e. elements of smaller sizes and standard shapes such as triangles, quadrilaterals, tetrahedrals, etc. with a fixed number of nodes at the vertices and/or on the sides (Figure 2.1 b). Polynomials are used to approximate the behavior of the PDEs at the element level and generate the local algebraic equations representing the behavior of the elements.

Zhang Y. et al. (2000) compare the results of a numerical modeling of single-layer folding using the Finite Element FLAC and Finite- Element MARC (Zhang Y. et al., 1996; Mancktelow, 1999). Numerical models of single-layer folds obtained using FLAC are consistent with those using the MARC for the same material properties and boundary conditions. The differences in the results reported by Zhang et al. (1996) and Mancktelow (1999) were not due to the different computer codes used in the two studies. The explanation lies in the different strain rates employed.

Boundary Element Method

The BEM solves linear partial differential equations that have been formulated as integral equations (i.e., in boundary integral form) (Figure 2.1 c). The BEM requires discretization at the boundary of the solution domains, reducing the problem dimensions by one and greatly simplifying the input requirements. The information required in the solution domain is separately calculated from the information on the boundary, which is obtained by solution of a boundary integral equation, instead of direct solution of the PDEs, as in the FDM and FEM (Jing, 2003). The BEM, as FDM and FEM, can be used to solve both dynamic and static problems.

In order to use this method for fracture analysis, the fractures must be assumed to have two opposite surfaces. Denote Γ_c as the path of the fractures in the domain Ω with its two opposite surfaces represented by Γ_c^+ and Γ_c^- (Figure 2.4). Two techniques were proposed to model the

domain. The first is to divide the problem domain into multiple sub-domains with fractures along their interfaces, (Figure 2.4 a). The stiffness matrix contributed by opposite surfaces of the same fracture will belong to different sub-domain stiffness matrices, in this way the singularity of the global matrix is avoided (Jing, 2003). The second is to apply displacement boundary equations at one surface of a fracture element and traction boundary equations at its opposite surface, although the two opposing surfaces occupy practically the same space in the model (Figure 2.4 b).

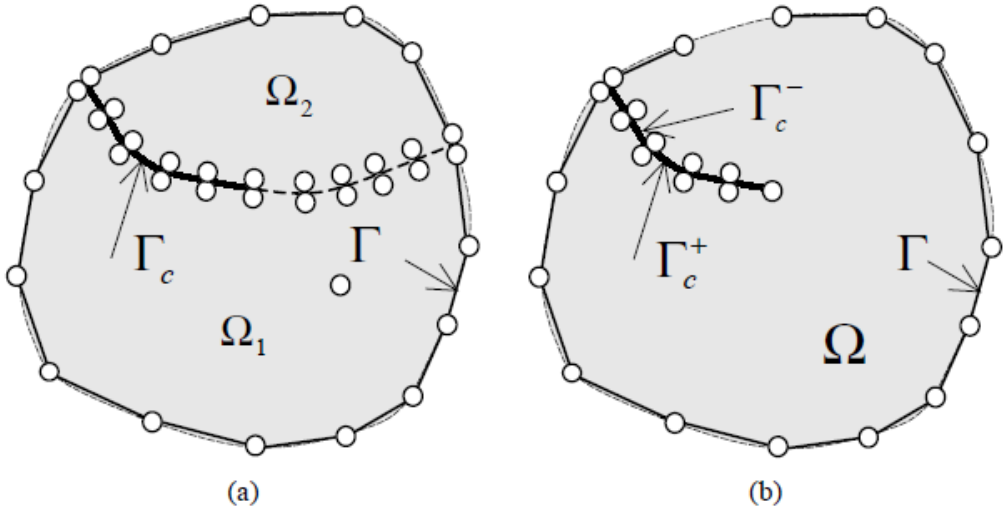

Figure 2.4 - Illustrative meshes for fracture analysis with BEM: (a) sub-domain, direct BEM; (b) single domain, dual BEM (Jing, 2003)

Discrete Element Method (DEM)

One of the original fields of DEM is rock mechanics. The first studies were conducted by Cundall (1971). The method has seen a wide variety of applications in rock mechanics, soil mechanics, granular materials, material processing, and fluid mechanics. This method can be used to represent block geometry and internal deformation of blocks (Figure 2.1 d).

Deng et al. (2011) state in their paper that DEMs can directly mimic rock and thus exhibit a rich set of emergent behaviors that correspond very well to real rock. Deng et al. (2011) implemented the DEM to handle rock deformation and fracturing processes. Rock is viewed, for instance, as a circular/spherical particle cluster with finite mass, and its mechanical performance is represented by the stiffness and strength of particles or bonds between particles (Figure 2.5). The solid rock is treated as a cemented granular material of complex-shaped grains.

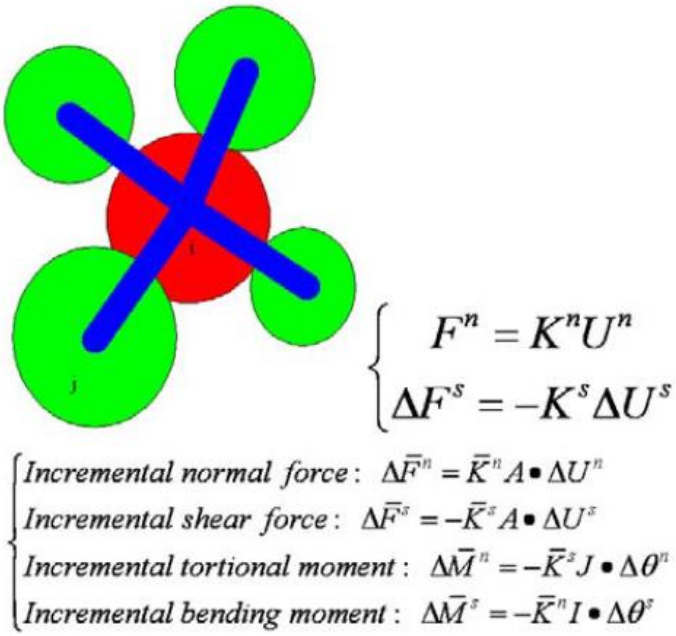

Figure 2.5 - Physical model of implemented DEM (Deng et al., 2011)

Discrete Fracture Network (DFN) methods

Among the methods for modeling fracture flow systems, the DFN approach is one of the most accurate, but also the most difficult to implement, as stated by many researchers. The DFN method is a special discrete model that can consider fluid flow and transport processes in fractured rock masses through a system of connected fractures (Jing, 2003). Like the DEM, this method was

created from a need to represent more realistic fracture system geometries in 2-D and 3-D. Up to now they are widely used in applications to problems of fractured rocks, and they are an irreplaceable tool for modeling fluid flow and transport phenomena. Table 2.1 shows a summary of the main fracture models based on DFN (Staub, 2002), and Figures 2.6 through 2.10 show some of the models presented in the table.

Due to its computational complexity these methods restrict fluid flow to the fractures and consider the surrounding rock as impermeable. With the progress in numerical techniques researchers are trying to model very complex systems of fractures and also take into account the fact that fractures can exchange fluid with the surrounding rock matrix (Reichenberg et al., 2006).

Table 2.1 - Main review of the DFN model, as regard to their applicability, advantages and limitations (Staub, 2002)

Model	Concept	Applicability	Advantages	Limitations
Orthogonal	Fracture network simulated from 3 sets of unbounded orthogonal joints	rock masses with completely defined rectangular rock blocks / mostly to hydrology	Simple geometry and treatment of data	Planar assumption, limitation in the variation of fracture orientation
Baecher disk	Generate fracture network from fracture centres that are distributed uniformly in space	Homogeneous rocks	Few field data available / Accurate in rock mechanics and hydraulics when a little is known	Do not simulate terminations of fractures, fractures must be planar / Do not account for complex features of fracture populations
Enhanced Baecher	Generate fractures from fracture centres located at random points in space. Intersections are calculated with pre-existing fractures	Fractured rock masses in which joint terminations are observed	Suited for simulation of connectivity of natural fracture population / Multiple intersections per fracture are possible	Fracture size distribution is not preserved; joints must be planar
BART	Same principle as for the Enhanced Baecher model, except that the centre of fracture terminating at intersections is generated from point on fracture intersection	Fractured rock masses in which fracture terminations are observed	Quick simulation / Fracture size distribution is preserved; spatial correlation in the simulated fracture population	fractures must be planar
Veneziano	Fracture network generated in 3 stochastic processes based on Poisson plane and Poisson lines	Suited for 100% persistent and unbounded fractures	Polygonal shapes are often observed in nature. More appropriate than orthogonal model for most cases, specially in case of coplanarity	Often fail to construct blocks / Intersections of fractures do not often match joint edges / Complex 3-D model
Dershowitz	Fracture network generated from 2 stochastic processes based on Poisson plane	Accurate for systems which exhibit distinct rock blocks, bounded polygonal fractures, and orientation dispersion	Model distinct rock blocks of various shape, flexibility in the distribution of fracture orientations / Joint intersection at joint edges	Can generate a large number of smaller polygons / Not so well fitted for coplanar fractures
Mosaic Tessellation	Deterministic and/or stochastic generation of the blocks, then definition of the fracture planes	Fracture systems resulting from a process of block formation (jointing in columnar basalts)	Manage non co-planarity, creation of the blocks first	Not so accurate in cases that do not display polyhedral blocks and polygonal fractures; blocks created first; indirect modelling of location, orientation and shape of fractures
Poisson Rectangle	Same concept as Enhanced Baecher except that fractures are rectangular	Same as Enhanced Baecher	Same as Enhanced Baecher	Specific conceptual model / Require a good knowledge of the rock mass geometry
Geostatistical	Generate fractures according to a specified variogram	Describe the spatial behaviour of regionalised variables of the fracture network	Account for a good spatial correlation	The size of the sampling area must be consequent compared to the study area
War Zone	Simulate higher densities of fractures between two major subparallel fractures	Simulation of fracture network in shear zones and in the surrounding rock mass	Binary model / identify "fracture zone" and "non-fracture zone"	Specific conceptual model / Require a good knowledge of the rock mass geometry
Non-Planar Zone	Generate fractures along a non-planar user defined surface	Simulation of fracture network along specific features (deformation zones,...)	Enhance rock zones with specific geometrical properties / binary model	Require a good knowledge of the rock mass geometry
Levy-Lee Fractal	Generate clusters of smaller fractures around wider fractures	In combination with geostatistical analysis: Hierarchical Fracture Trace Model	Accounts for the chronology of fracture formation / Ability to generate a non-stationary fracture system with a set of parameters that remain constant throughout the generation system	Do not consider the size and shape of the blocks delimited by the simulated fractures / Definition of the most appropriate fractal dimension
Nearest-neighbour	Fractures are organised into primary, secondary and tertiary groups, and are generated in this sequence	Can account for the generation of fracture network according to the theory of fracture genesis	Generate clusters of fractures around the primary group / More explicit than Levy-Lee model if fractures can be classified	Must have enough data to assess the different groups and chronology

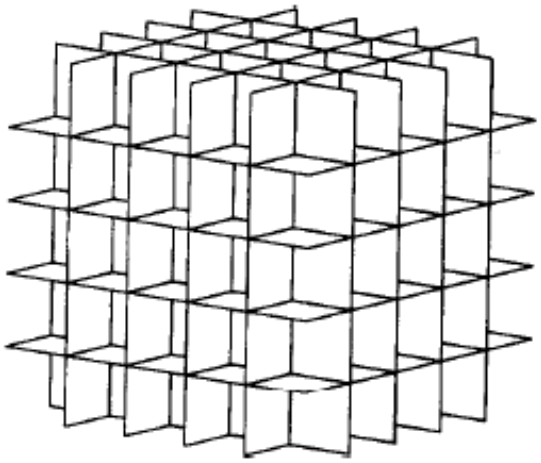

Figure 2.6 - Three-dimensional orthogonal model (Dershowitz and Einstein, 1988)

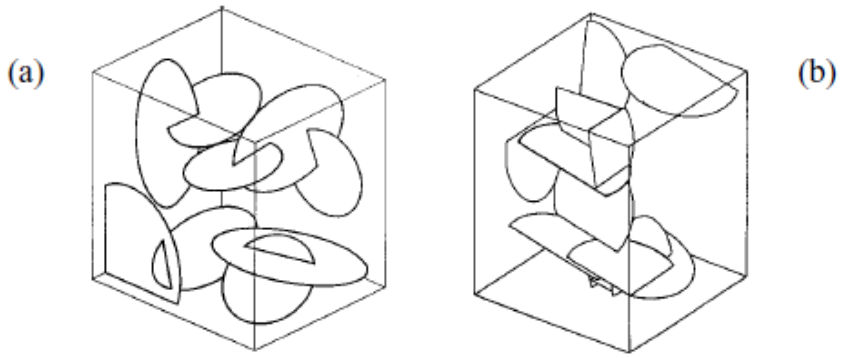

Figure 2.7 - Comparison of (a) the general Baecher model with (b) the Enhanced Baecher (Staub, 2002)

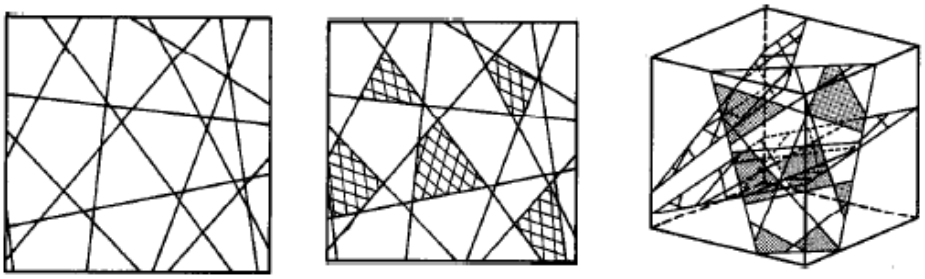

Figure 2.8 - "Generation of Veneziano joint system model" (Einstein, 1993)

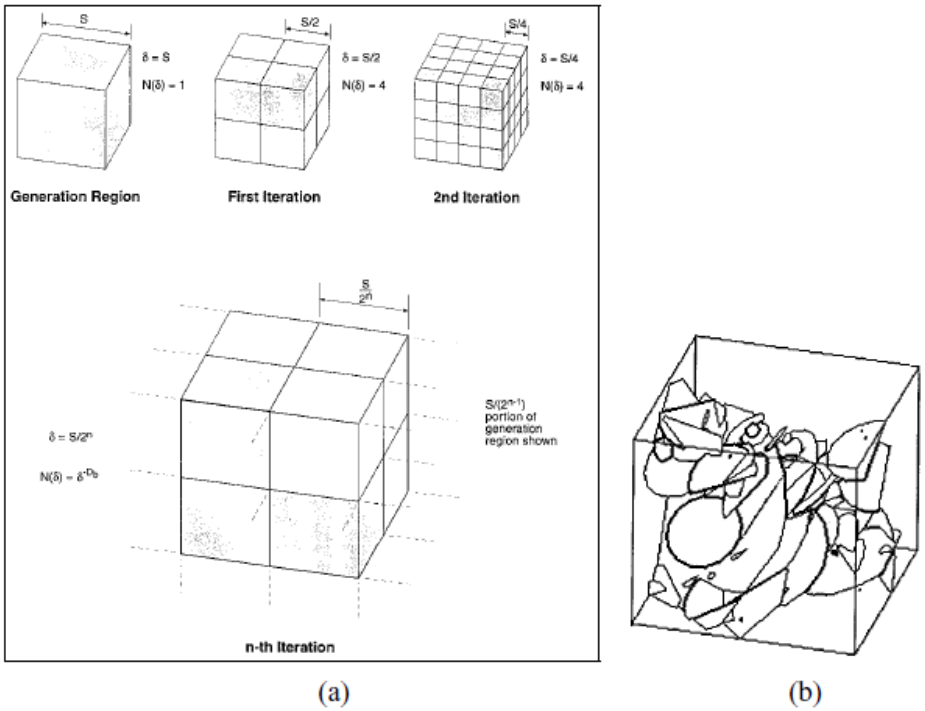

Figure 2.9 - (a) 3-D fractal Box algorithm, and (b) 3-D geometric model (Dershowitz et al, 1998)

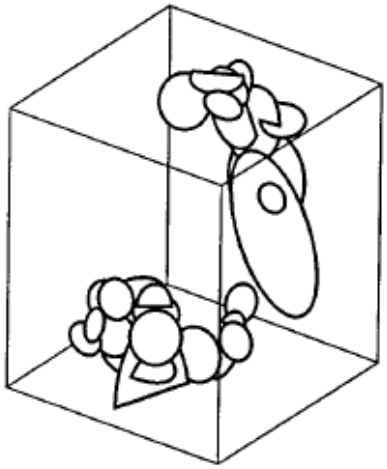

Figure 2.10 - 3D geometric Levy-Lee fractal model (Dershowitz et al, 1998)

Hybrid methods

Dershowitz (2006) describes the development of a hybrid model using DFN and EPM. The EPM (Equivalent Porous Media) volume elements are integrated with the DFN triangular elements. In the case presented in the paper the hybrid model was used to model shaft sinking at an underground laboratory. The schematic representation is shown in Figure 2.11.

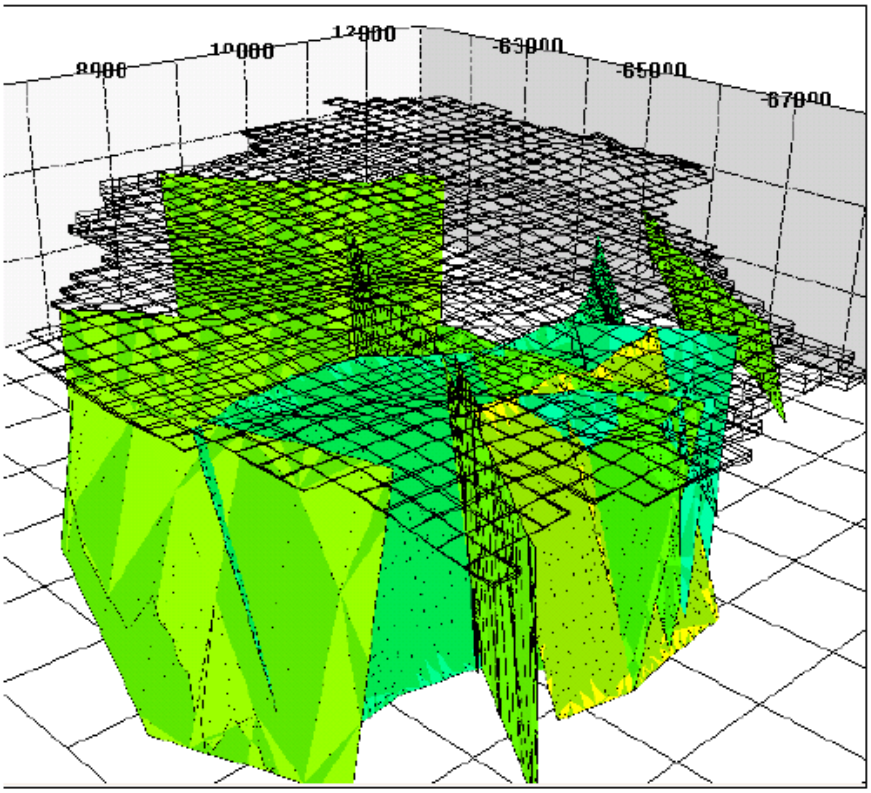

Figure 2.11 - Hybrid DFN/EPM Model Framework (Dershowitz, 2006)

The hybrid DFN/EPM model first implements the sedimentary strata using EPM volumetric elements (wire frame in Figure 2.11), with properties derived from well testing. Then the EPM volumetric elements are linked to DFN elements and the identified major faults are implemented using tessellated surfaces (green in Figure 2.11). Finally water conducting fractures are stochastically generated are implemented as DFN elements, with geometry and properties, based on interpretation of hydro-physical flow logs, packer tests, and borehole image logs (Figure 2.12) (Dershowitz,2006).

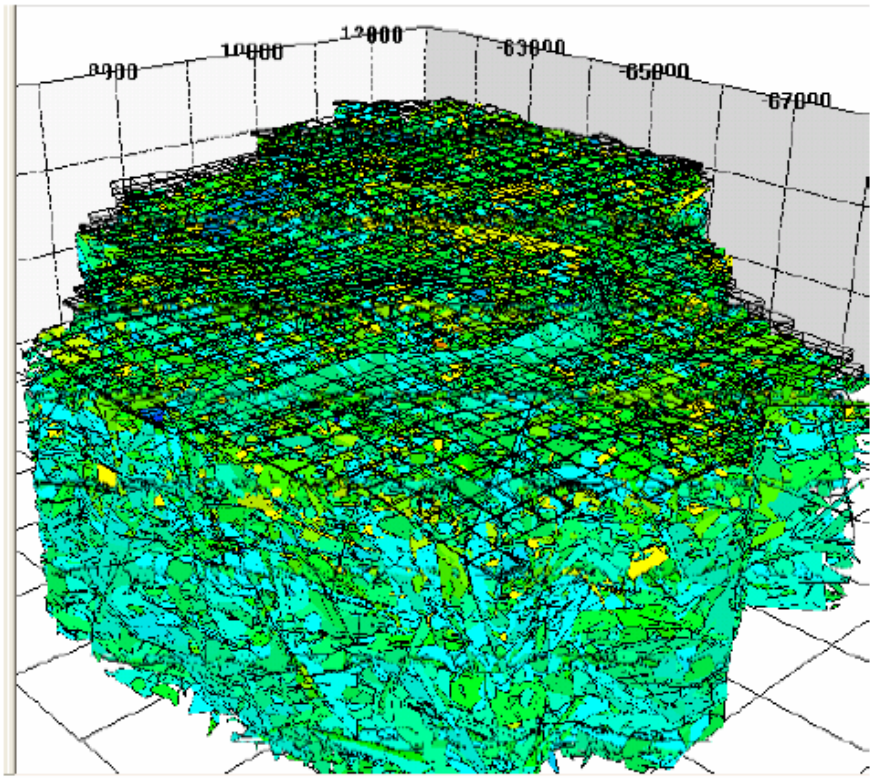

Figure 2.12 - Stochastically Generated Water Conducting Fracture Population (WCF) Throughout Model Region (Dershowitz, 2006)

2.1.2 Interpretation of fracture intensity

Dershowitz and Herda (1992) introduce in their paper a class of fracture intensity measures in 1-D, 2-D and 3-D. In three dimensions fracture intensity can be defined in terms of P31, the number of fractures in a volume; P32, the surface area of discontinuities per unit volume or P33; the volume of fractures in a volume (Figure 2.13).

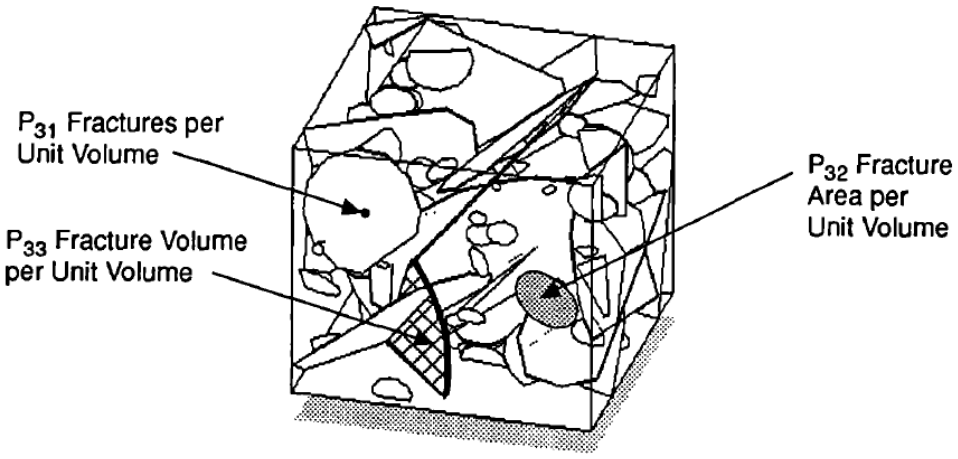

Figure 2.13 - Three dimensional fracture intensity measures (Dershowitz and Herda, 1992)

The most useful measure of intensity for three-dimensional fracture modeling is P_{32}, since it does not reflect any orientation effect. The size distribution and the number of discontinuities are needed for calculating intensity. Zhang and Einstein (2000) present in their paper methods for estimating the size distribution and the number of discontinuities. The discontinuity size distribution can be inferred from the trace data sampled in circular windows by using the stereological relationship between the true trace length distribution and the discontinuity diameter distribution for area (or window) sampling (Warburton, 1980). Zhang and Einstein (2000) present a method for estimating the true trace length distribution which is affected by bias when measured. Several types of bias occur during sampling: e.g., orientation bias, size bias, truncation bias, censoring bias. They analyze the biases using statistical tools for lognormal, negative exponential and gamma distributions of discontinuity diameters. In order to estimate the total number of discontinuities the approach of Mauldon and Mauldon (1997) is used. This approach estimates the probability that a discontinuity with its centroid in the objective volume will intersect the wall of a borehole (Figure 2.14).

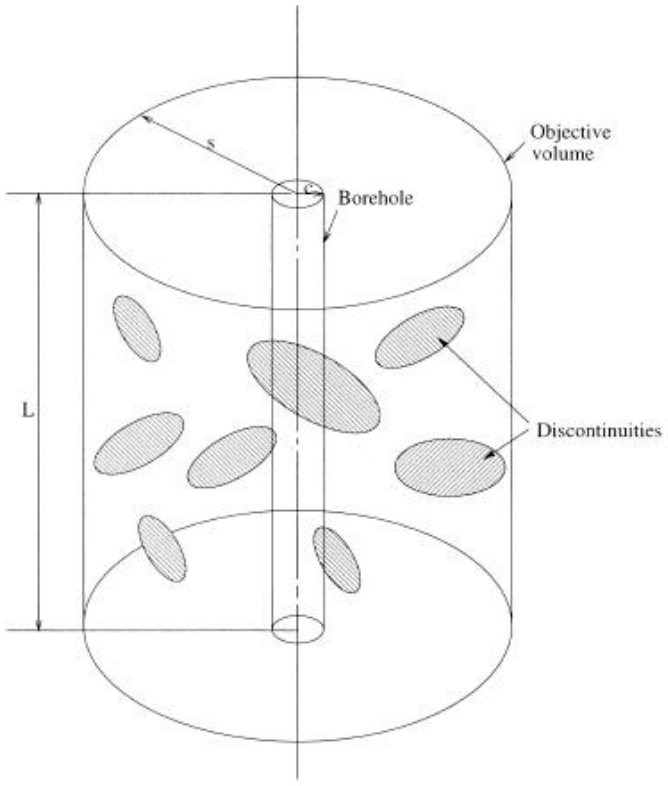

Figure 2.14 - Vertical borehole in an objective volume (Zhang, Einstein, 2000)

In order to describe both the intensity and the orientation distribution several tensor methods have been described. Those described by Oda (1982) and Kawamoto (1988) seems to take advantage of the concept of P_{32} and has a clear physical meaning.

P_{32} is one of the principal inputs in GEOFRAC, so its correct estimation is very important. P32 is used as intensity of Poisson planes in the Controlled Volume in the primary stochastic process in GEOFRAC. More information about the generation of planes in GEOFRAC is presented in the next chapter.

2.1.3 Models for the aperture of the fractures

Fluid flow in fractures is strongly dependent on the fracture aperture. For this reason it is very important, especially for geothermal applications, to have a model that well represents the geometric characteristics of the fractures. The relation between aperture and flow is commonly expressed in terms of the parallel plate laminar flow solution (Poisseuille equation) through a cubic law *(Equation 2.1)*:

$$q = \frac{h^3 \Delta P}{12 \mu \Delta L} \qquad \textit{Equation 2.1}$$

where

h: aperture of the fractures (m)

ΔP: pressure drop (Pa)

μ: fluid dynamic viscosity (Pa s)

ΔL: length of flow (m)

using a hydraulic aperture related to the mean mechanical fracture aperture. The hydraulic aperture is a non-linear function of effective normal stress, the fracture morphology, material properties and its history.

It is important to emphasize that the terminology used by different authors can be confusing. In fact, some authors refer to the aperture as the "width" or "opening". In this thesis I will always use "aperture" for the distance between two separate fractures surfaces.

Many researchers such as Stone (1984), Vermilye et al. (1995) and Johnston and Mccaffrey (1996), through observation of fracture properties from field mapping, have proposed a power-law correlation between aperture *h* and fracture length *l (Equation 2.2)*.

$l = ah^b$ *Equation 2.2*

where *b* varies between 0.6 and 1 and *a* varies between 20 and 2000. Length and aperture are in mm.

Tezuka and Watanabe (2000) used the Vermilye and Scholz (1995) equation to model the fracture network of the Hijiori hot dry rock reservoir. The aperture (in meters) is defined as shown in Equation 2.3:

$a = \alpha * \sqrt{r}$ *Equation 2.3*

where *a* is the fracture aperture, *r* is the fracture radius, and α is the factor that controls the relationship between the aperture and the radius. They conducted a sensitivity analysis for both the parameter α and r_{max} in order to find the most appropriate values. After comparison between a simulated flow and field observations, the values that they chose for the two parameters were:

$\alpha = 4.0*10^{-3}$

r_{max} = 200 m

Ivanova et al. (2012) assume that fracture aperture (in meters) can be related with fracture length by a power-law function *(Equation 2.4)*:

$h = \alpha(2R_e)^{\beta}$ *Equation 2.4*

where R_e (in meters) is the equivalent radius of the sphere that circumscribes the fracture (polygon), h is the aperture, and a and b are coefficients that depend on the site geology and that can be found in the literature (Vermilye and Scholz, 1995; Stone, 1984; Vermilye et al.,1995; Johnston and Mccaffrey, 1996).

Other researchers, such as Dverstop and Andersson, 1989; Cacas, et al., 1990 assume that the hydraulic aperture of fractures, h (in meters), follows a lognormal distribution, which can be written as:

$$f(h) = \frac{1}{h\sigma\sqrt{2\pi}} e^{\frac{-(\ln h-\mu)^2}{2\sigma^2}}, 0 \le h \le \infty \qquad \textit{Equation 2.5}$$

where $f(h)$ is the lognormal distribution of the aperture, h, with parameters μ and σ.

Ivanova et al. (2012) referring to these studies, implemented in their model this probabilistic approach but assuming that it as a truncated lognormal distribution that follows these relation:

$$f_{TR}(h) = \frac{f(h)}{\int_{\min}^{h_{\max}} f(h)d(h)}, h_{\min} \le h \le h_{\max} \qquad \textit{Equation2.6}$$

Where h_{min} and h_{max} (in meters) are the minimum and the maximum aperture values. This relation is presented in Figure 2.15.

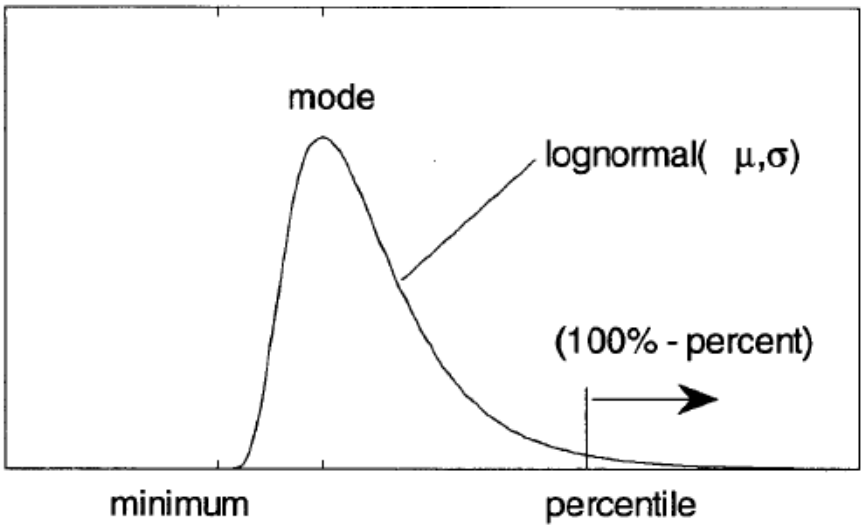

Figure 2.15 - Truncated lognormal distribution (Ivanova et al. 2012)

2. 2 FLOW SYSTEM MODELS

This section summarizes the numerical models describing fluid flow in fractured porous media. As reported by Diodato, 1994, four conceptual models have dominated the research:

1) Explicit discrete fractures
2) Dual continuum
3) Discrete fracture networks
4) Single equivalent continuum

The **Explicit Discrete Fracture model** allows one to explicitly represent fluid potential gradients and fluxes between fractures and porous media with minimal non-physical parameterization. As Diodato (1994) explains the data acquisition with this model can become onerous where large numbers of fractures need to be represented.

Travis (1984) represents fractures with orthogonal orientation. An implicit finite difference formulation is used and solved iteratively. The region of interest is represented by a computational mesh of rectangular cells as shown in Figure 2.16. The rows, columns, and layers of the cells are not equally spaced. Some variables such pressure, density, concentration, and saturation are evaluated at the cell centers; others (velocity components) are evaluated at cell interfaces.

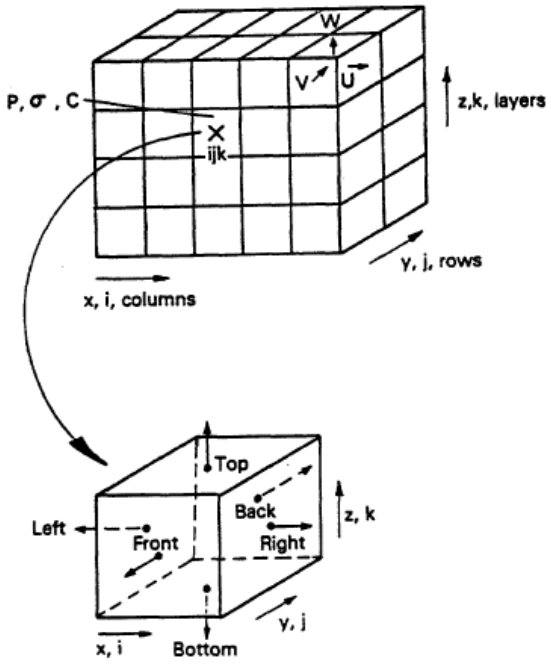

Figure 2.16 - Typical computational mesh (Travis, 1984)

Travis implemented an algorithm based on finite difference to create the TRACR3D code that was used to model time-dependent mass flow and chemical species transport in a three-dimensional, deformable, heterogeneous, reactive porous/fractured medium (Travis, 1984).

The **Dual-continuum** approaches are based on an idealized flow medium consisting of a primary porosity created by deposition and lithification and a secondary porosity created by fracturing,

jointing, or dissolution (Warren and Root 1963). The first studies were introduced by Barenblatt et al. (1960) and later extended by Warren and Root (1963). The porous medium and the fractures are envisioned as two separate but overlapping continua. Fluid mass transfer between porous media and fractures occurs at the fracture-porous medium interfaces (Diodato, 1994).

More recent studies such as that by IIlman et al. (2004) used a dual continuum two phase flow simulator called METRA to represent the matrix and the fractures as dual overlapping continua; liquid flux between continua are restricted by a uniform factor. Figure 2.17 shows an example of the steady state distribution of fracture saturation (Figure 2.17a), matrix saturation (Figure 2.17 b), fracture water flux (Figure 2.17 c), and matrix water flux (Figure 2.17 d) for a single realization of fracture permeability with q_a=42.5 mm/yr, where q_a is the water flux. In Figure 2.17 the materials, used in the test, are defined with the acronyms: Tiva Canyon Tuff (TCw), non-welded Paintbrush Tuff (PTn), and welded Topopah Spring Tuff (TSw). Illman et al., 2004 state: "*The distribution of saturation in the fracture continuum is highly variable in the nonwelded and welded units. The saturation is highest locally, where permeability in the fracture continuum is low and at the TCw/PTn boundary in the fracture continuum, where the contrast in permeability causes a permeability barrier. As water moves progressively from the fracture to the matrix continuum in the PTn unit, the variability in saturation decreases with depth in the PTn fracture continuum".*

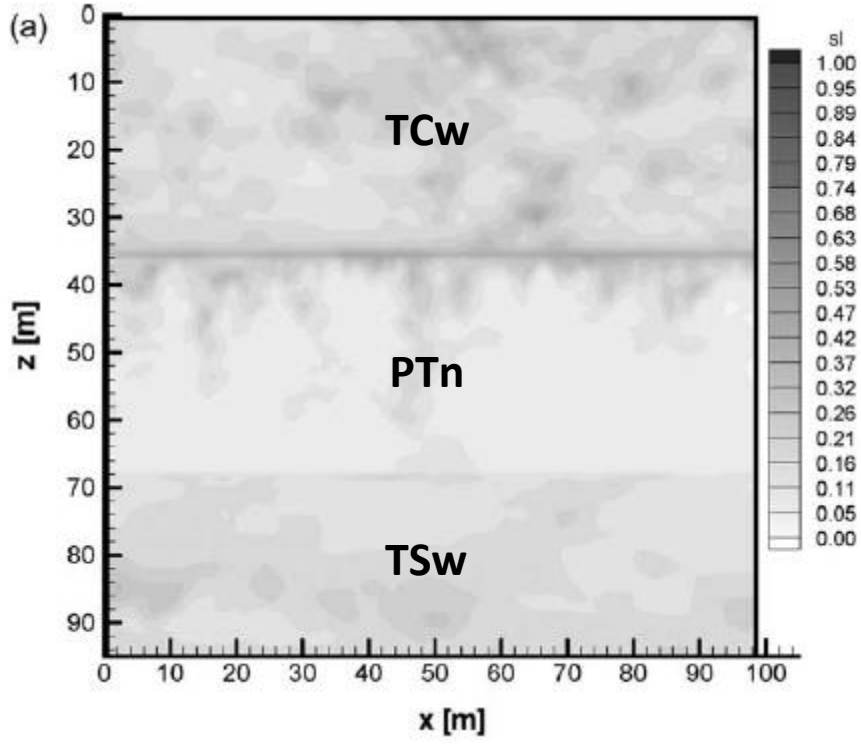
(a)
TCw
PTn
TSw
z [m]
x [m]
sl
1.00
0.95
0.89
0.84
0.79
0.74
0.68
0.63
0.58
0.53
0.47
0.42
0.37
0.32
0.26
0.21
0.16
0.11
0.05
0.00

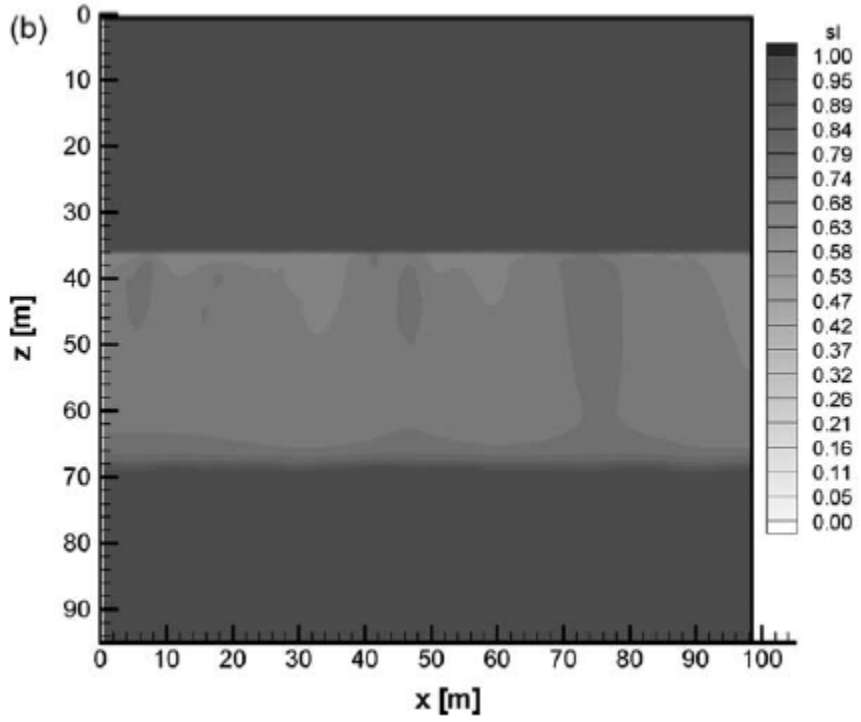
(b)
z [m]
x [m]
sl
1.00
0.95
0.89
0.84
0.79
0.74
0.68
0.63
0.58
0.53
0.47
0.42
0.37
0.32
0.26
0.21
0.16
0.11
0.05
0.00

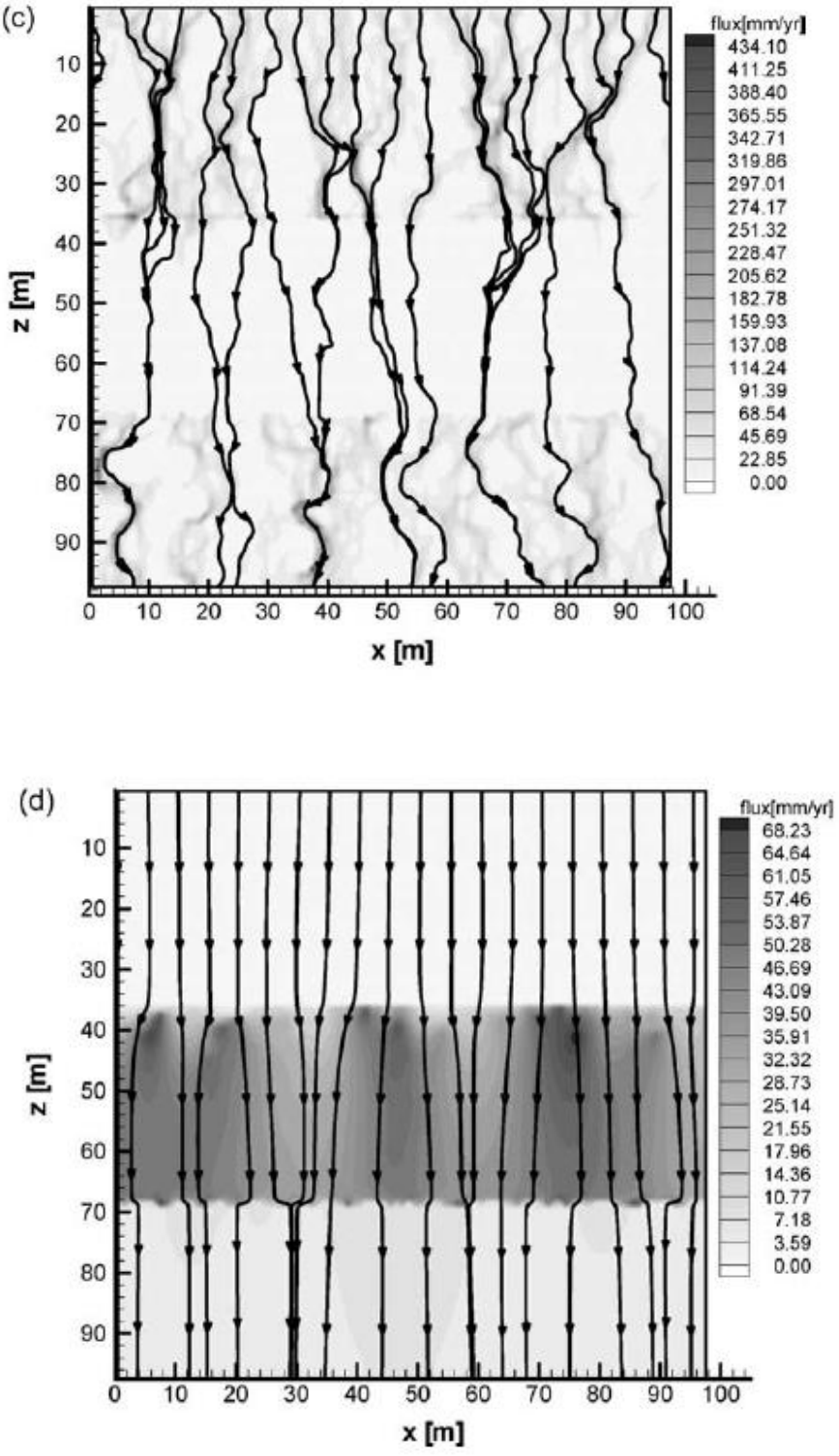

Figure 2.17 - Steady state distribution of: (a) fracture saturation; (b) matrix saturation; (c) fracture water flux; and (d) matrix water flux qa=42.5 mm/yr (Illman et al., 2005)

In **Discrete-fracture-networks** all flow is restricted to the fractures. This idealization reduces computational resource requirements. Fractures are often represented as lines or planes in two or three dimensions. For contaminant transport, some network models allow for diffusion between the fracture and porous medium (Diodato, 1994).

The model developed at MIT that will be introduced in Chapter 3 belongs to this category. Fractures are represented by polygons in three-dimensions, the porous medium is not represented and all flow is restricted to the fractures.

The **Single Equivalent Continuum Formulation** assumes that the volume of interest is considered to be large enough that, on average, permeability is a sum of fracture and porous media permeability. Pruess et al. (1990) demonstrated that where the scales of integration are sufficiently large, the single equivalent continuum approximation will model well the conserving fluid mass. It may, however, be a poor predictor of spatial and temporal distributions of contaminant fluxes (Diodato, 1994).

2.3 SOFTWARE TOOLS IN USE AND THEIR APPLICATION

Thermal-hydrological-mechanical processes are, conventionally, solved by coupling a fracture system model with a subsurface flow and heat transfer model. The term 'coupling' implies that one process affects the initiation and progress of another. It is possible to use coupling processes using the same software, as the Rock Mechanics Group at MIT is trying to create with GEOFRAC or using different software that model different part of the thermo-hydro-mechanical processes; for example, Rutquist et al. (2002) used FLAC, a rock mechanics simulator and TOUGH2, a widely used flow and heat transfer simulator, for their simulation. The two simulators run

sequentially with the output from one code serving as input to the other one (Podgorney et al., 2010).

2.3.1 TOUGH2

TOUGH ("Transport Of Unsaturated Groundwater and Heat") was developed at the Lawrence Berkeley National Laboratory (LBNL) in the early 1980s primarily for geothermal reservoir engineering. Now it is widely used for many other applications for instance nuclear waste disposal, environmental assessment and remediation.

TOUGH2 is the basic simulator for non-isothermal multiphase flow in fractured porous media. The TOUGH2 simulator was developed for problems involving strongly heat-driven flow. It takes into account the fluid flow in both liquid and gaseous phases occurring under pressure, as well as viscous, and gravity forces according to Darcy's law. Interference between the phases is represented by means of relative permeability functions. The code includes Klinkenberg effects and binary diffusion in the gas phase and capillary and phase adsorption effects for the liquid phase. Heat transport occurs by means of conduction (with thermal conductivity dependent on water saturation), convection, and binary diffusion, which includes both sensible and latent heat.

2.3.2 FALCON

FALCON (**F**racturing **A**nd **L**iquid **CON**vection) is a finite element based simulator solving fully coupled multiphase fluid flow, heat transport, rock deformation, and fracturing using a global

implicit approach (Podgorney et al. 2012). It was developed and now improved by the Idaho National Laboratory group.

Podgorney et al. (2010) describe the initial code. The approach is to develop a physics based rock deformation and fracture propagation simulator by coupling a discrete element model (DEM) for fracturing with a continuum multiphase flow and heat transport model. In this approach, the continuum flow and heat transport equations are solved in an underlying finite element mesh with evolving porosity and permeability for each element that depends on the local structure of the discrete element network. As a first step in the development of the code, governing equations for single-phase flow and transport of heat are being coupled with linear elastic equations. The basic architecture of the code allows one to conveniently couple different processes and incorporate new physics, such as stress dependent permeability-porosity, phase change, implicit fracturing. The code in FALCON is developed using a parallel computational framework called MOOSE (**M**ultiphysics **O**bject **O**riented **S**imulation **E**nvironment) developed at the Idaho National Laboratory (INL).

Podgorney et al. (2012) present some results. Figure 2.18 shows the simplest problem geometries, a small fracture network consisting of two horizontal and one vertical fracture.

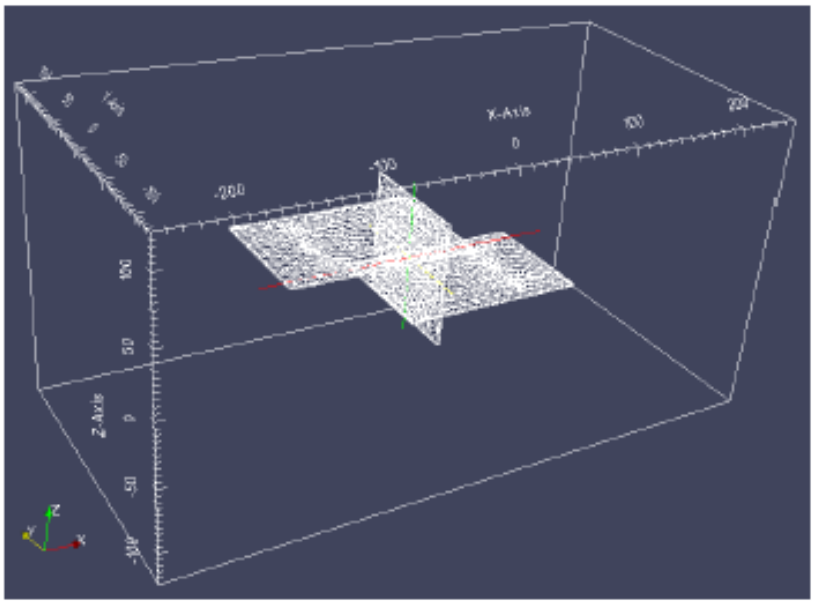

Figure 2.18 - Three-dimensional mesh for the simplest fracture flow problems under consideration (Podgorney et al., 2012)

Figure 2.19 shows the simulated temperature and pressure for two examples after several years of injection and production. Cold fluid is injected on the right side of the fracture domain, while production is on the left side. At early times, small changes are observed in the temperature field in the proximity of the production location.

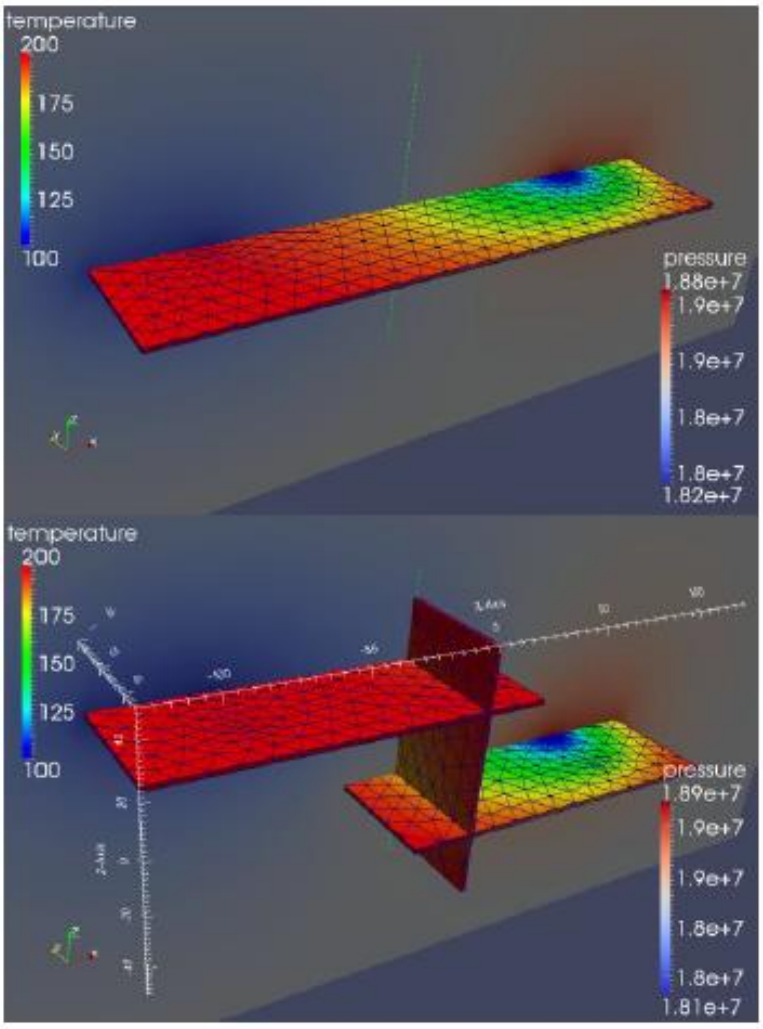

Figure 2.19 - Temperature (in fracture domain) and pressure along the center of the reservoir matrix domain for tow simulations. (Podgorney et al., 2012)

2.3.3 LEAPFROG

Leapfrog Geothermal is a 3D modeling tool that can be used in every stage of a project, from initial proof-of-concept to reservoir development and production. In 2010 ARANZ Geo together with the University of Auckland, Department of Engineering Science Geothermal Group and Contact Energy Ltd used the core technology to develop a geothermal "product".

Leapfrog Geothermal can be used for integration with Tough2 for flow modeling, regional geothermal resource evaluation, geothermal model review and maintenance, borehole planning for exploration, development and reservoir management, 3D fault.

2.3.4 FRACMAN

FracMan generates fractures in three dimensions within a given rock volume. Dershowitz et al, (1998) explain the definition of the input parameters and the theoretical background of Discrete Fracture Network introduced the DFN models into the FracMan. To take into account the variability of the input parameters, the DFN model is generated several times by means of Monte Carlo simulations, and the fracture population statistics analyzed for each simulation model (Staub I. et al., 2002). FracMan generates 3-D fracture network models to describe the pattern of faults, fractures, solution features and stratigraphic contacts in fractured rock.

2.3.5 CONCLUSIONS

The software tools presented above are very useful tools to be used in the field of geothermal energy. The disadvantage is that they need to be combined in order to obtain a complete fracture flow model simulation.

The program GEOFRAC, developed by the MIT Rock Mechanics Group and presented in Chapter 3, aims to model a geothermal reservoir as a complete and optimized tool. Particularly the well location optimization study that will be implemented as a next step, is quite innovative.

CHAPTER 3

GEOFRAC: 3-D HYDRO-MECHANICAL MODEL

3.1 INTRODUCTION

GEOFRAC is a three-dimensional, geology-based, geometric-mechanical, hierarchical, stochastic model of natural rock fracture systems (Ivanova, 1998). Fractures are represented as a network of interconnected polygons and are generated by the model through a sequence of stochastic processes (Ivanova et al., 2012). This is based on statistical input representing fracture patterns in the field in form of the fracture intensity P_{32} (fracture area per volume) and the best estimate fracture size E[A]. P_{32} can be obtained from spacing information in boreholes or from observations on outcrops using the approach by Dershowitz and Herda (1992). Best estimate fracture size E[A] can be obtained from fracture trace lengths on outcrops with suitable bias corrections as developed by Zhang et al. (2002). Distributions of fracture size can also be obtained subjectively. GEOFRAC has been applied and tested by estimating the fracture intensity and estimated fracture size from tunnel records and from borehole logs (Ivanova et al. 2004, Einstein and Locsin 2012). Since its original development, GEOFRAC has been made more effective by basing it on Matlab, and it has been expanded by including an intersection algorithm and, most recently, a flow model.

Focus of my research was to apply GEOFRAC in the EGS (Enhanced Geothermal System) modeling field. In this chapter I will present the basic concept of GEOFRAC and I will introduce the applicability in the geothermal field. The algorithms developed to apply GEOFRAC for the geothermal area are explained in more details in the next chapters.

A parametric study was conducted in order to test the efficiency of this model and to analyze the sensitivity of the output flow rate to the parameters used as input in the model. Chapter 4 will present the results of the parametric study.

3.2 BASIC CONCEPT

3.2.1 Fracture system model

The fracture system model in GEOFRAC was developed by Ivanova (1998). The concept is a three-dimensional geometric-mechanical model that represents rock fracture systems. The model has the characteristics to be hierarchical, so that fractures are grouped into hierarchically related fracture sets; and it is stochastic, using statistical methods to generate the fracture system from available geologic information. Fractures in GEOFRAC are represented as polygons (Figure 3.1). As shown in the figure each polygon is characterized by a pole and a radius Re that represent the radius of the equivalent circle that circumscribes the polygon.

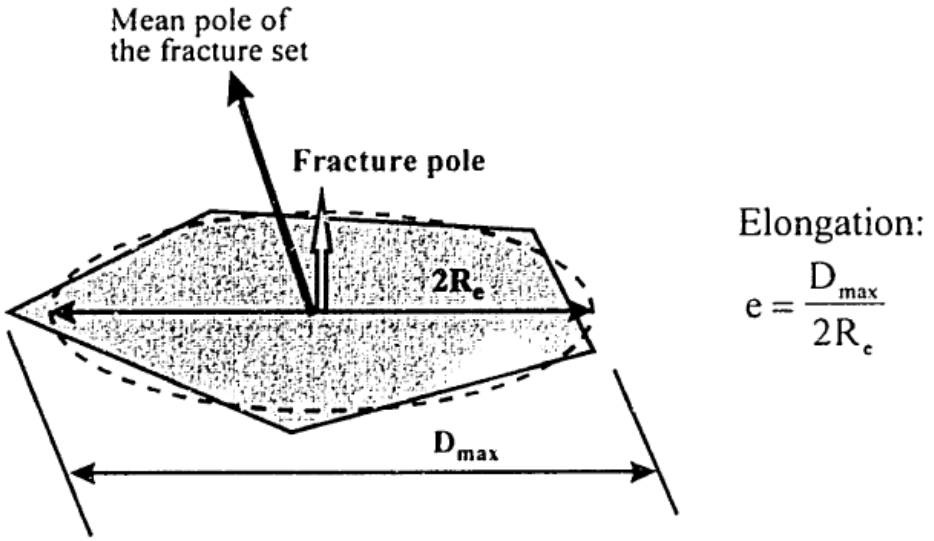

Figure 3.1- Fracture represented as a polygon with a pole and a radius (Ivanova, 1995)

The desired mean fracture size E[A] and fracture intensity P_{32} in a region V are given as input. GEOFRAC uses these inputs to generate the fracture system following a sequence of stochastic processes (for details on GEOFRAC and on the flow model see Ivanova et al. 2012, Sousa et al. 2012 and Sousa, 2013):

Primary Process: Fractures planes are generated in the volume V with a Poisson plane process of intensity μ where $\mu = P_{32}$. The orientation of the planes can be specified with the Fisher distribution. Recall that this is a single parameter distribution. Low values of the parameter κ simulate randomly generated planes; large κ will generate planes mostly parallel to each other.

Secondary Process: A Poisson point process with intensity λ is generated on the planes and the fractures are created with a Delaunay-Voronoi tessellation. It represents fracture intensity variation by size and location.

Tertiary Process: Random translation and rotation of the fractures (polygons) are conducted to represent the local variation of fracture position and orientation of individual fractures. In the tertiary process a new algorithm was recently added to the model to allow the user to model fractures with or without random rotation. The parametric study presented in the Chapter 4 will compare results with rotation and no rotation of the fractures.

The generation process of the fractures is visualized in Figure 3.2.

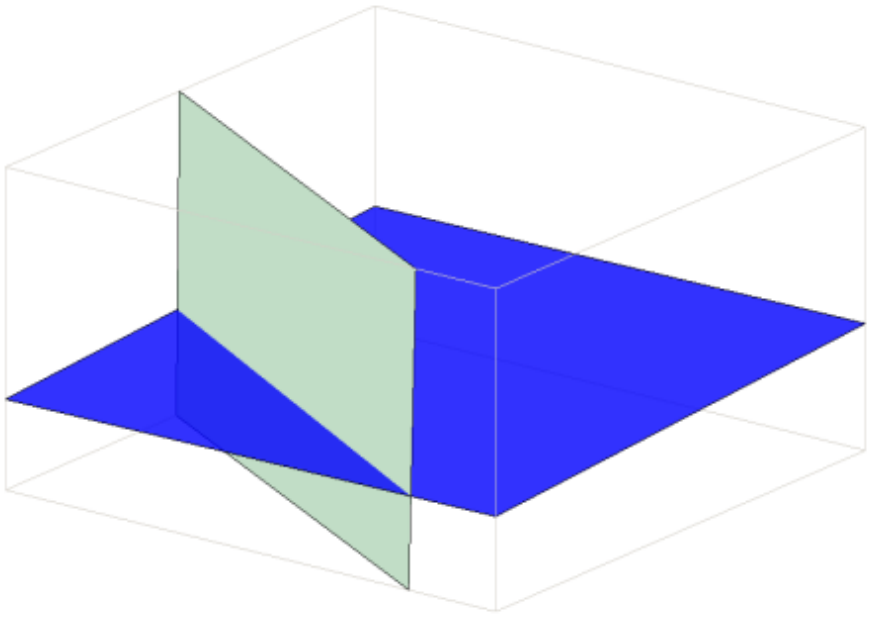

a) Primary Process: Generation of Planes

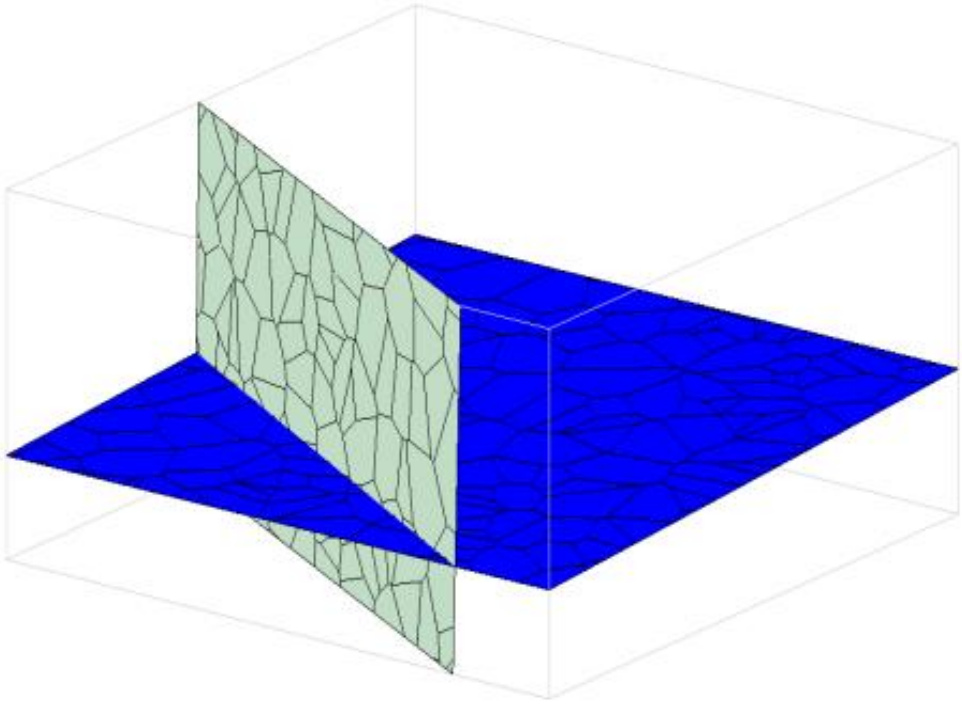

b) Secondary Process: Division of planes into polygons

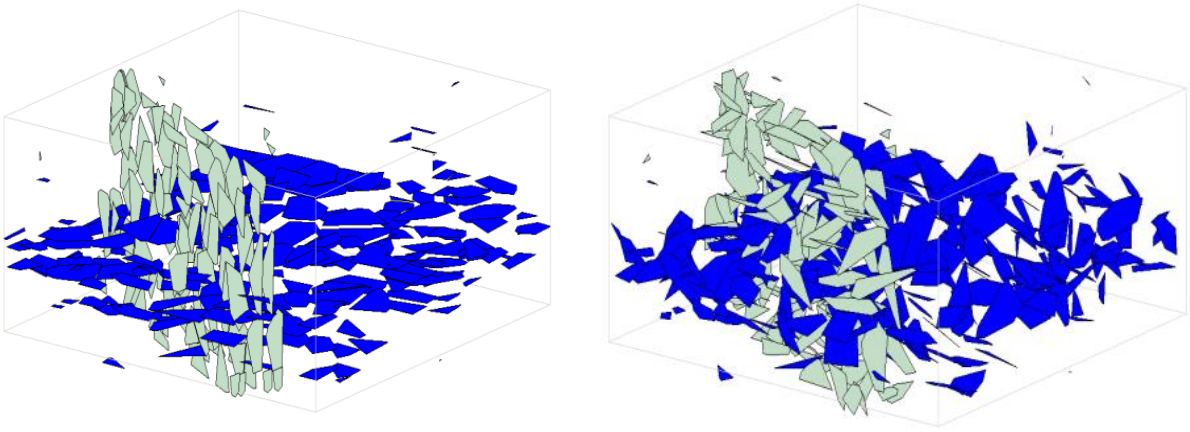

c) Tertiary Process: Random translation and rotation

Figure 3.2 - Generation of a fracture set with the GEOFRAC model. Primary process (a), secondary process (b), tertiary process (c) (Ivanova et al., 2012)

A parametric study was conducted in order to study the relationship between fractures intensity, size, and connectivity (Ivanova et al., 2012). Monte Carlo simulation was used in order to determine the mean fracture connectivity C, with the variation of P_{32} and E[A]. The results of the simulations are graphically presented in Figure 3.3. The plot shows the results for κ=0 (solid line) and for κ =10 (dotted line). The results suggest that the fracture connectivity C is a non-linear function of both the fracture size, measured by the expected mean area E[A], and the fracture intensity, measured as cumulative fracture area per unit rock volume, P_{32}.

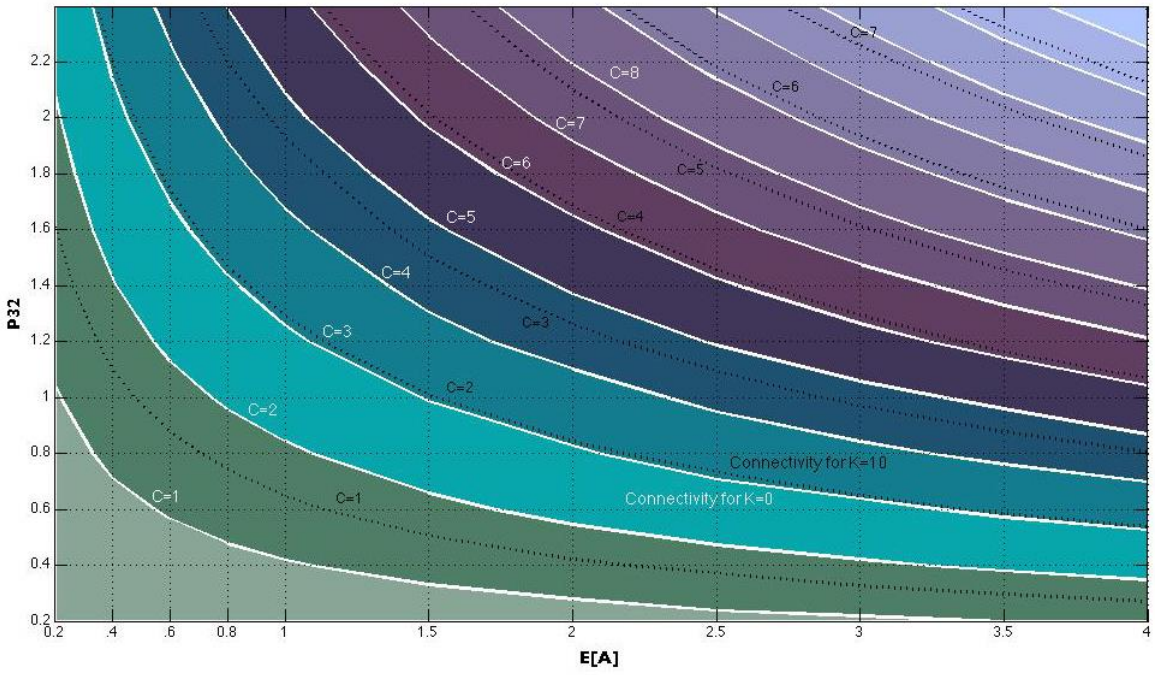

Figure 3.3 - Expected fracture connectivity, C, for given E[A] and P32 (Ivanova et al., 2012)

3.2.2 Flow system model

In section 2.1.2 I described the 4 methods that can be used to represents fracture flow. The circulation model in GEOFRAC belongs to the category of Discrete-Fracture Networks. In this type of model the porous medium is not represented and all flow is restricted to the fractures. Fractures are often represented as lines or planes in two or three dimensions. In this specific case the fractures are represented by polygons in three dimensions. The flow model in GEOFRAC was developed by Sousa (Sousa, 2012).

The flow equations used to model the flow through the fractures are those of linear flow between parallel plates. The water flows only in the x direction between two parallel plates with the no-slip condition for viscous fluids forming the velocity profile in the y direction (Figure 3.4).

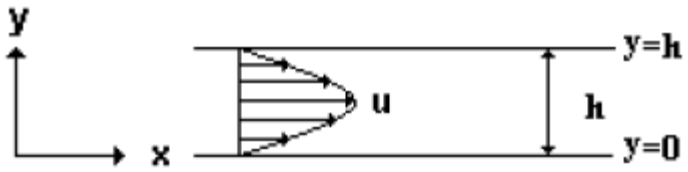

Figure 3.4- Schematic representation of linear flow between parallel plates

The water flow in fracture is assumed to be governed by the Poisseuille cubic law (Zimmerman and Bodvarsson, 1996) represented by the following equation:

$$q = \frac{h^3 \Delta P}{12 \mu \Delta L} \qquad \textit{Equation 3.1}$$

Where:

q is the volumetric flow rate (m^2/sec) per unit width;

h is the aperture of the fracture in m;

μ is the fluid dynamic viscosity in PA s;

ΔP is the pore pressure change in Pa after the flow travels through distance ΔL.

Considering the fracture width, w(s) (see Figure 3.5) (in m, variable with length) the equation for flow between parallel plates is:

$$q = \frac{w(s)h^3 \Delta P}{12\mu \Delta L} \qquad \textit{Equation 3. 2}$$

The schematic representation of the fracture width is shown in Figure 3.5.

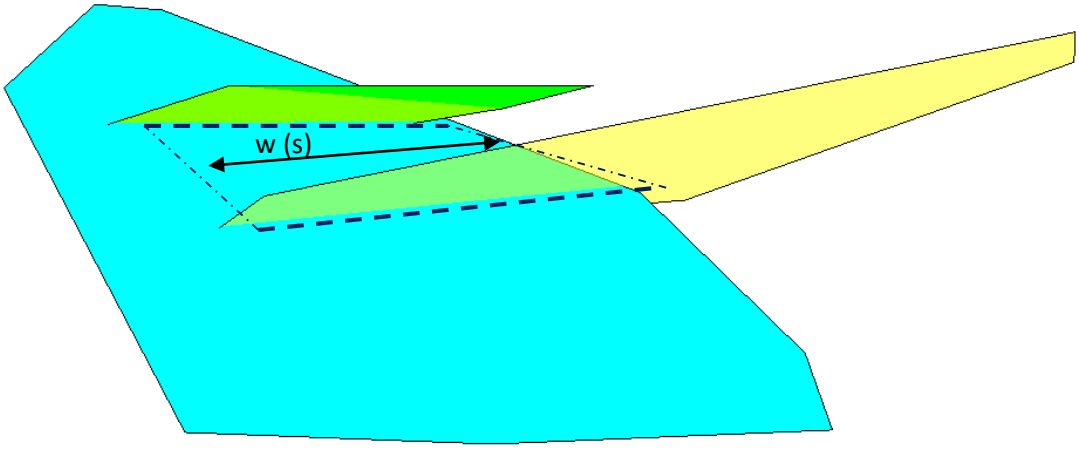

Figure 3.5 – Mean fracture width between fractures intersection

The fracture aperture in GEOFRAC can be modeled in three different ways:

- Deterministic approach using a power law relation between fracture length and aperture.
- A probabilistic approach based on the truncated lognormal distribution.
- A fixed value. This was used to perform the parametric study that will be presented in the Chapter 4.

These methods are explained in more detail in Chapter 6.

In order to calculate the geometric flow paths and the flow rate GEOFRAC follows seven steps:

1) Determination of the fractures that intersect the left boundary;
2) Determination of the fractures that intersect the right boundary;
3) Determination of the score of each fracture;
4) Determination of the highest score paths amongst all initial fractures (that intersect the left boundary) and all end fractures (that intersect the right boundary);
5) Determination of the intersections between the paths;
6) Determination of the flow thought each path;
7) Determination of the total flow through the reservoir;

I will briefly describe the above steps that are more thoroughly explained in Sousa (2012).

Step 1 & 2 – Select and store the fractures that intersect the injection and the production boundaries

A function called buildNodesList.m was created. This function creates an Nx2 matrix containing a list of edge connections.

Figure 3.6 shows an example of how the connections are considered and stored in the matrix E:

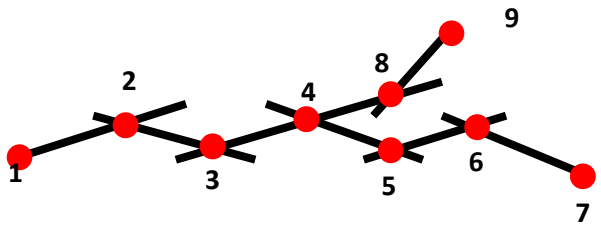

Figure 3.6 - Representation of the fracture intersections (Sousa, 2013)

The matrix containing the list of edge connections in this case would be as follows:

$$E = \begin{bmatrix} 1 & 2 \\ 2 & 3 \\ 3 & 4 \\ 3 & 8 \\ 4 & 8 \\ 4 & 5 \\ 8 & 9 \\ 5 & 6 \\ 6 & 7 \end{bmatrix}$$

Step 3 - Scoring system:

The model at this point assigns a score to each fracture. The scoring system is based on the concept that for the same drop of pressure the flow rate is proportional to $\frac{wh^3}{\Delta L}$.

The score for each fracture is calculated as:

$$SC = \frac{\bar{w}h^3}{\Delta L} \qquad \textit{Equation 3.3}$$

where:

$\bar{w}$ is the mean width of the fracture in m;

h is the aperture of the fracture in m;

ΔL is the distance between fractures (See Figure 3.7).

The fractures with greater aperture and greater mean width will have a greater volumetric flow for the same drop of pressure.

Figure 3.8 illustrates the different geometric components of the scoring formula. The length of a "fracture path" corresponds to the distance between the middle points of the intersections between fractures. For example in Figure 3.7 the length ΔL of fracture 1 is the distance between the middle point of the intersection of fracture 1 and 3 and the middle point of the intersection of fracture 1 and 2. Figure 3.8 shows the score components when a fracture intersects more than one fracture.

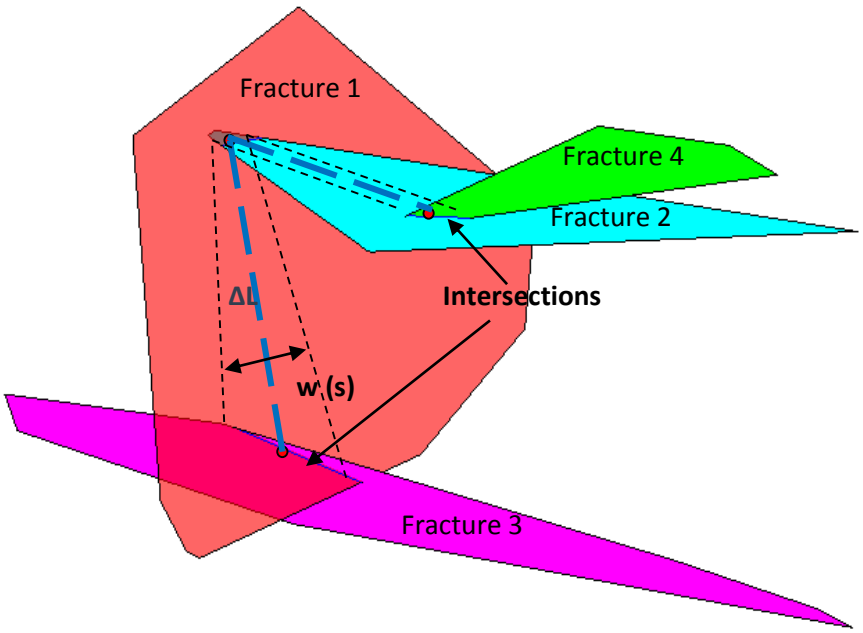

Figure 3.7 - Score components between two fracture intersections

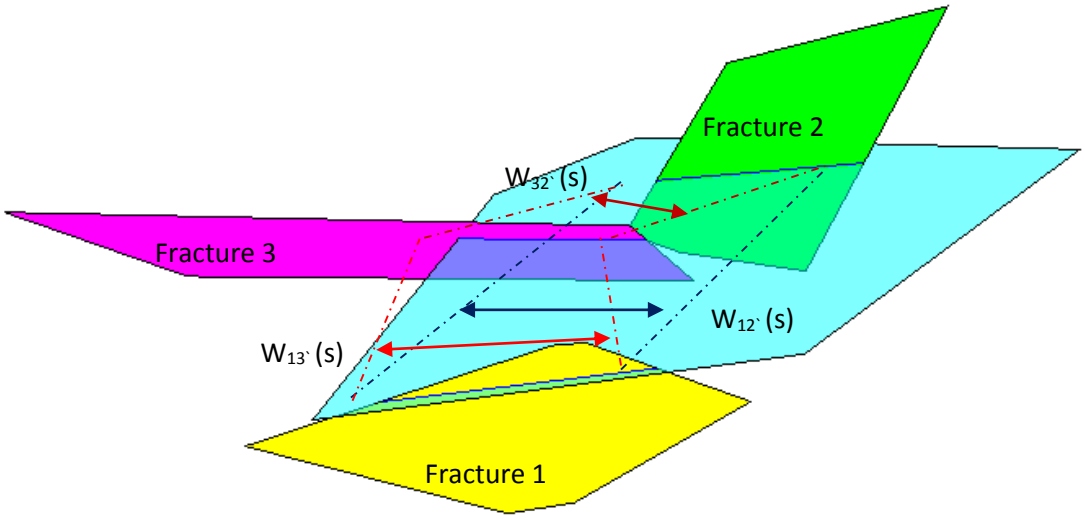

Figure 3.8 - Score components: fracture intersects more than one fracture

Step 4 - Highest score path

The model then finds the paths that have the highest score based of the score of the fractures. The highest score path(s) is calculated using the Dijkstra's algorithm (Dijkstra, 1959).

In GEOFRAC, the Dijkstra's algorithm is used to calculate the "highest score paths" (or most likely path) between all the fractures that intersect the injection boundary and all the fractures that intersect the production boundary. Figure 3.11 shows an example of a most likely overall path, i.e. the path with the highest score in a specific reservoir. Figure 3.12 shows three different highest score paths between initial fractures and different final fractures.

Step 5 – Intersection between paths

At this point the model generates a list of several branches, each one composed of numerous fractures and nodes that are the intersection between branches or the intersection between branches and one of the boundaries, as illustrated in Figure 3.9 . Branches are then joined to form paths. Each path is composed of several fractures that can be represented schematically as shown in Figure 3.10. The path can be represented by an equivalent fracture width and equivalent aperture and a length that is equal to the sum of the lengths of all fractures.

The equivalent aperture can be calculated with Equation 3.4.

$$h_{eq} = \frac{1}{\sqrt[3]{\sum_{i=1}^{n} \frac{l_i}{l}\left(\frac{1}{h_i^3}\right)}}$$ Equation 3.4

where, l_i and h_i are the length and aperture of the i^{th} fracture ;

l is the total length of the series of fractures, i.e. the sum of all the fractures in the series.

The equivalent length of a path is the sum of the lengths of all fractures that constitute the path (Equation 3.5)

$$l_{eq} = \sum_{i=1}^{n} l_i \qquad \text{Equation 3.5}$$

Where, l_i is the length of the i^{th} fracture

The equivalent width can be computed by a weighted average of all the fractures that are part of the path. This is represented by Equation 3.6.

$$w_{eq} = \frac{\sum w_i l_i}{\sum l_i} \qquad \text{Equation 3.6}$$

Where

w_i is the width of the i^{th} fracture

l_i is the length of the i^{th} fracture

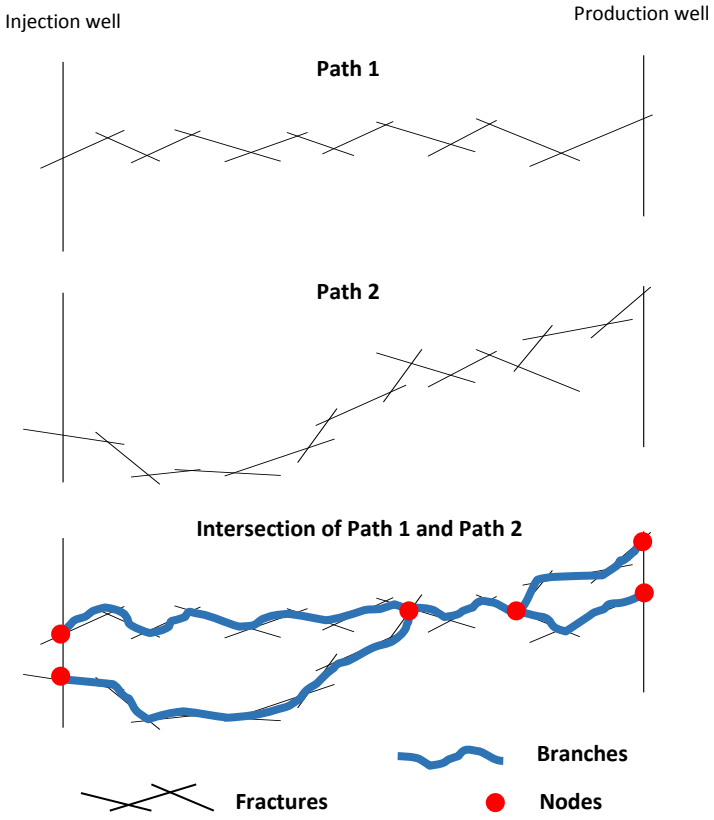

Figure 3.9 - Intersection of two paths; representation of branches and nodes.

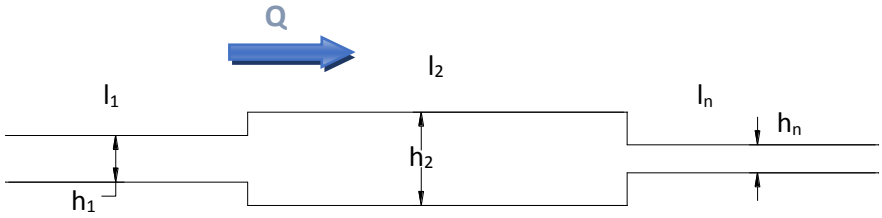

Figure 3.10 - Series of fractures modeled as parallel plates

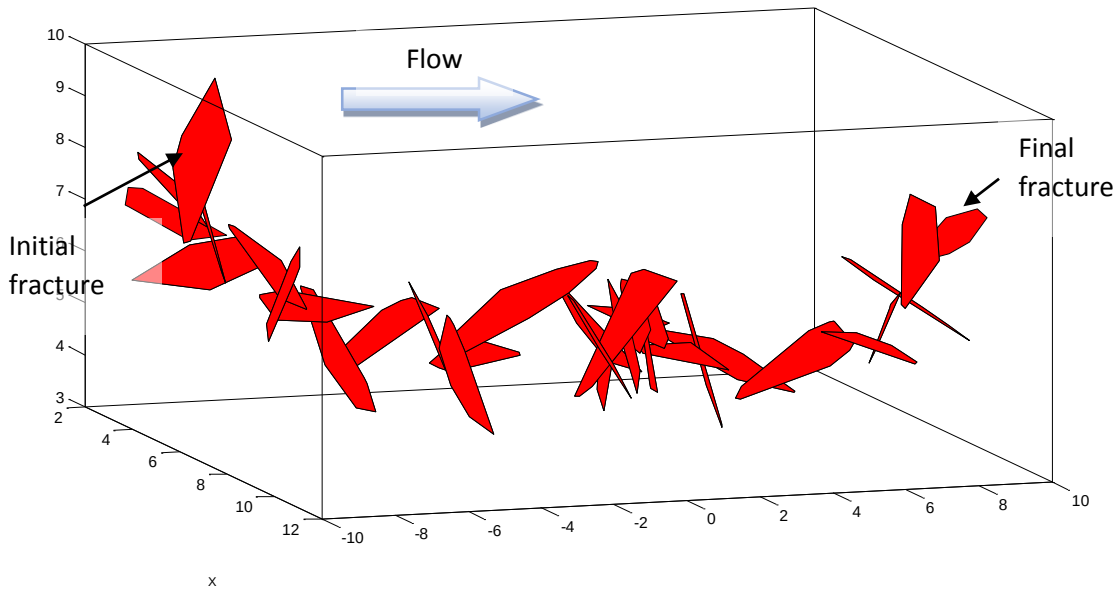

a) 3D view

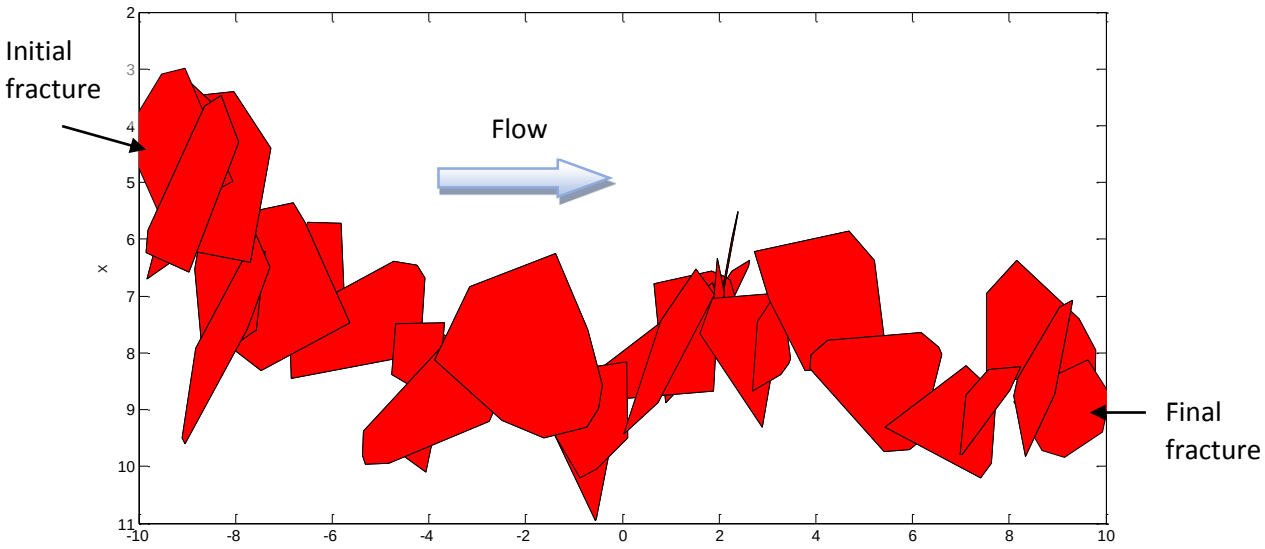

b) X-Y view

Figure 3.11 - Highest score path between two fractures that intersect the two boundaries

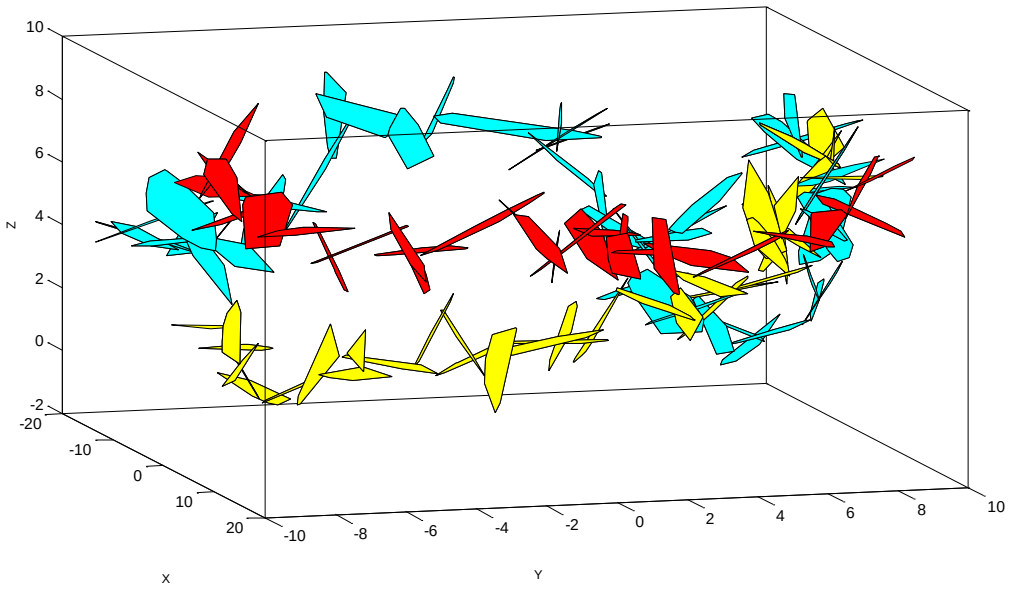

a) 3D view

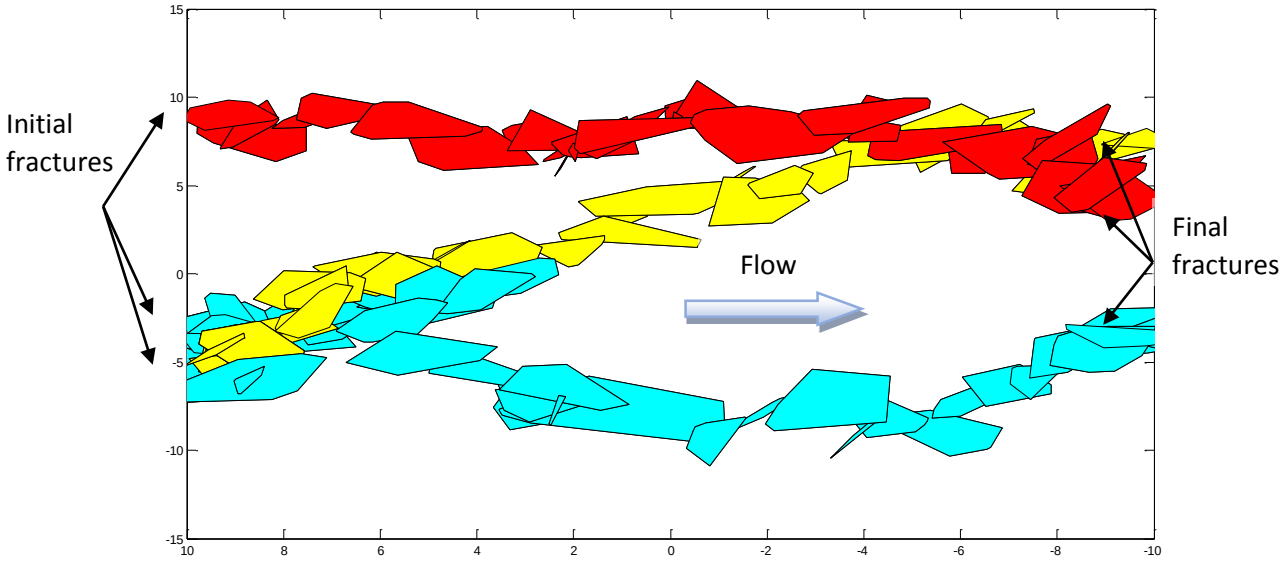

B) X-Y view

Figure 3.12 - Highest score path between different pairs of fractures

After finding the best geometric solution (fracture system) to create the system of the branches the model calculates the output flow (equation 3.2) as the sum of the output flow from each path.

CHAPTER 4

PARAMETRIC STUDY

4.1 Introduction

The parametric analysis was conducted in order to check the consistency of the model and determine which parameters have the greatest effects on the final results. The parametric analysis considers simplified conditions:

- A synthetic 20x20x10 m volume
- Injection and production wells are the left and right boundaries of the volume
- The water temperature is assumed to be 20°C, i.e. the dynamic viscosity is 1.002×10^{-3} Pa s.

These simplifications are both justified and necessary since the parametric study intends to verify the intrinsic correctness of GEOFRAC flow model.

The results of this analysis are presented in the next paragraphs and are sub-divided into the following sections:

- output analysis when varying the aperture parameter;
- output analysis when varying the Fisher parameter that affects the orientation of the planes during the primary process;

- output analysis when varying the rotation the fractures during the tertiary process.

Each section will conclude with a brief summary of the results obtained.

The following code will be used to identify the simulations done using the follow abbreviated indicators, in the charts as well as in some comments:

E[A] - P_{32} - κ - R – h

Where:

E[A] = Expected area of the fracture (m^2)

P_{32} = Fracture intensity (fracture area/volume)

κ = Fisher parameter

R= 0 ‘no rotation’ of the fractures in the tertiary process

R=1 ‘random rotation’ of the fractures in the tertiary process

h = Aperture of the fracture (m)

For example: the code 2-3-1-0-0.005 means:

E[A]=2 m^2, P_{32}=3, κ=1, R=0 (no rotation), aperture=0.005 m

4.2 Parametric study results

4.2.1 Output analysis when varying the aperture parameter

GEOFRAC allows the user to generate the aperture (h) of the fractures using three models: a deterministic approach, in which the aperture is a function of the radius of the sphere that circumscribes the fracture (polygon); a probabilistic approach, which follows a truncated lognormal distribution, and a fixed value approach in which the users can fix the value of the aperture. This last approach was used for this analysis, in order to establish the sensitivity of the results and to confirm the direct relation between the aperture of the fractures and Qout (m^3/s). Two cases are analyzed: h = 0.005 m and h = 0.01 m. Most of the other parameters are kept fixed in this particular sensitivity analysis:

E[A]= 2

P_{32} = 3

κ =1

R = 1 (rotation) or 0 (no rotation)

For both cases shown in Figure 4.1 (h = 0.005 m) and Figure 4.2 (h = 0.01 m), the results for no rotation and random rotation of the polygons are reported in the same chart. Just 40 simulations were run; a number considered representative since the aim of this analysis is to study the trend of the results and not to evaluate the exact value of Qout. A detailed study of sample analysis is presented in Vecchiarelli and Li (2013).

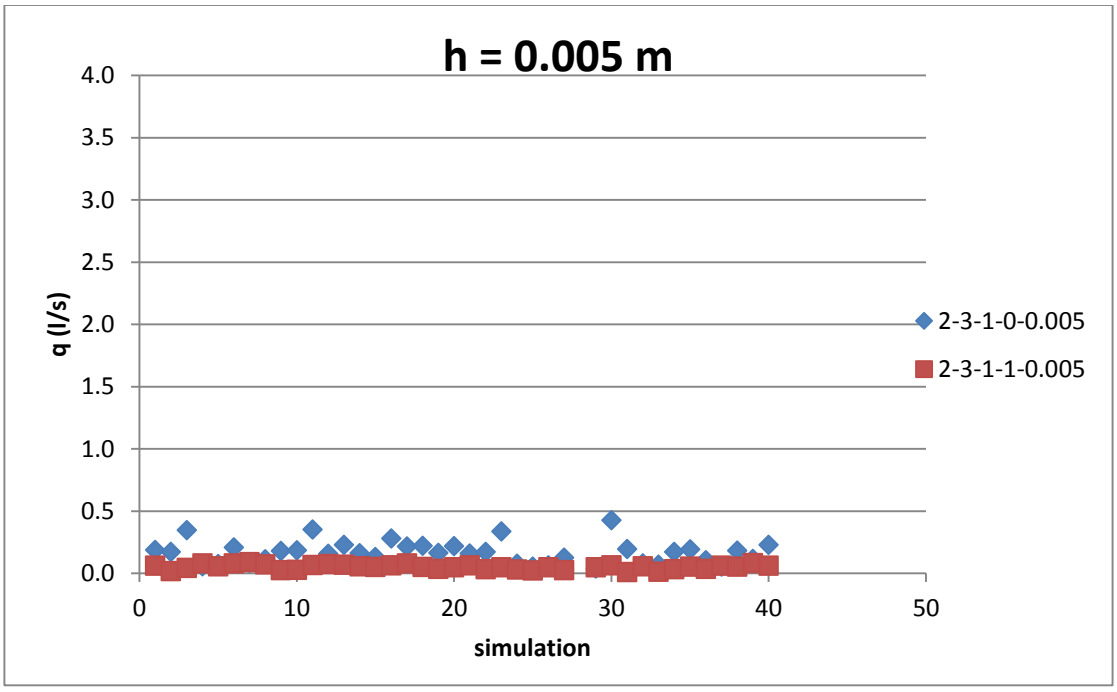

Figure 4.11 - Flow rate for h=0.005 m for no rotation and random rotation of the fractures

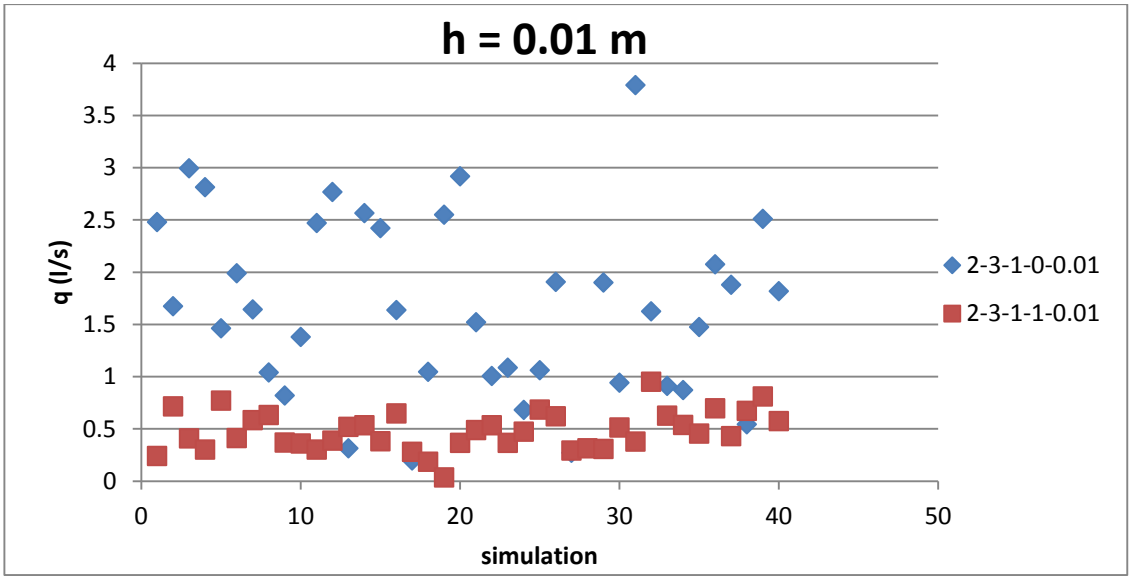

Figure 4.12 -Flow rate for h=0.01 m for no rotation and random rotation of the fractures

In Tables 4.1 and 4.2 the mean, the standard deviation and the coefficient of variation of the simulations are summarized.

Table 4.2- Values of Qout (m3/s) for h = 0.005 m

	Mean Qout (m^3/s)	Standard Deviation Qout (m^3/s)	Coefficient of variation Qout (m^3/s)
no rotation	0.16	0.09	0.54
rotation	0.05	0.02	0.40

Table 4.3 - Values of Qout (m3/s) for h = 0.01 m

	Mean Qout (m^3/s)	Standard Deviation Qout (m^3/s)	Coefficient of variation Qout (m^3/s)
no rotation	1.64	0.85	0.52
rotation	0.48	0.19	0.38

The results correspond well to the theory. The ratio of the cubic values of the aperture parameters chosen for this analysis is 0.01^3/0.005^3=8. Qout for the rotation case for example is Qout= 5.16 m^3/s for h=0.005 m and Qout=47.94 m^3/s for h=0.01 m and producing a ratio of about 9 which is very close to 8. A similar ratio is obtained for the no rotation case. (The differences in absolute values for rotation and no rotation will be discussed later). The

variability as expressed by the coefficient of variation is apparently not affected by the absolute value of h.

4.2.2 Output analysis when varying the Fisher parameter

In order to check the variability of the results of Qout, using different Fisher parameters, two values were selected for the analysis presented in this section: κ =1 and κ=40. These two values represent the extreme conditions with κ=1 representing randomly generated planes (Figure 4.3) and κ=40 mostly parallel planes (Figure 4.4). The resulting Qout are plotted in Figures 4.5 and 4.6.

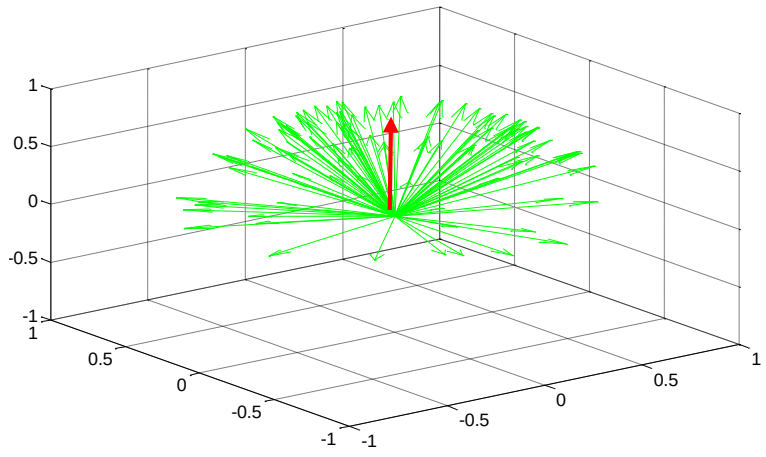

Figure 4.13 - Fracture set poles. Orientation distribution: Univariate Fisher κ =1

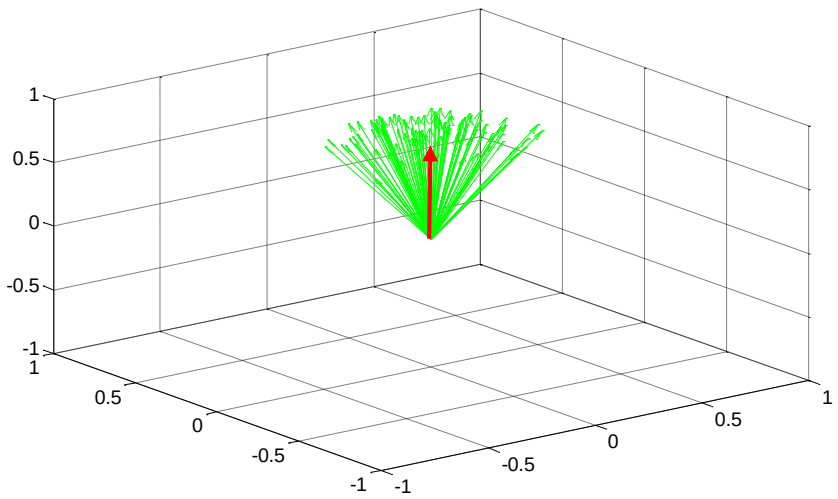

Figure 4.14 - Fracture set poles. Orientation distribution: Univariate Fisher κ =40

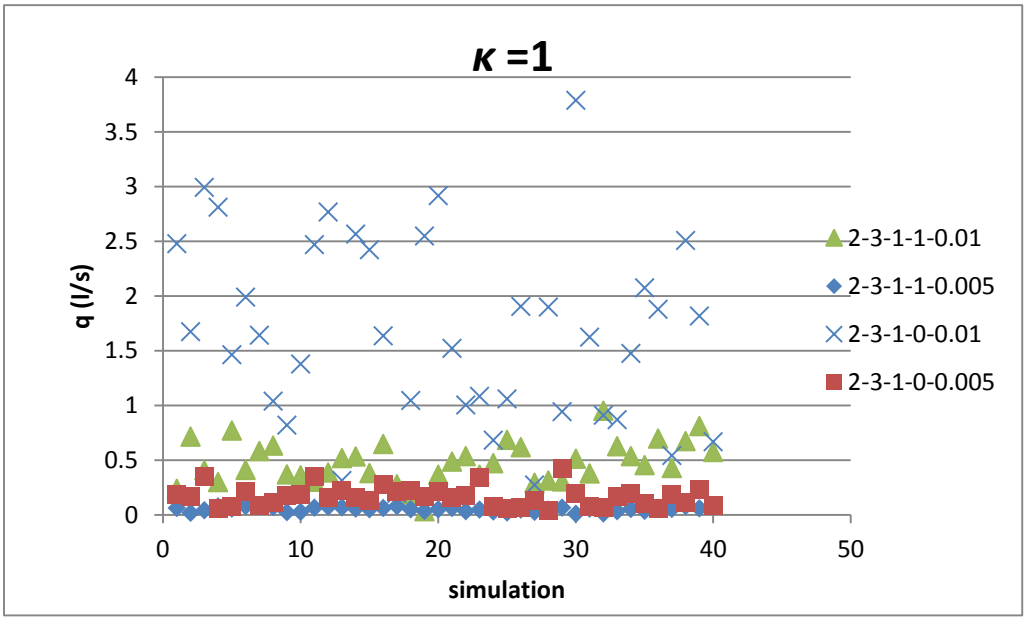

Figure 4.15 – Flow rate (Qout) values for κ =1

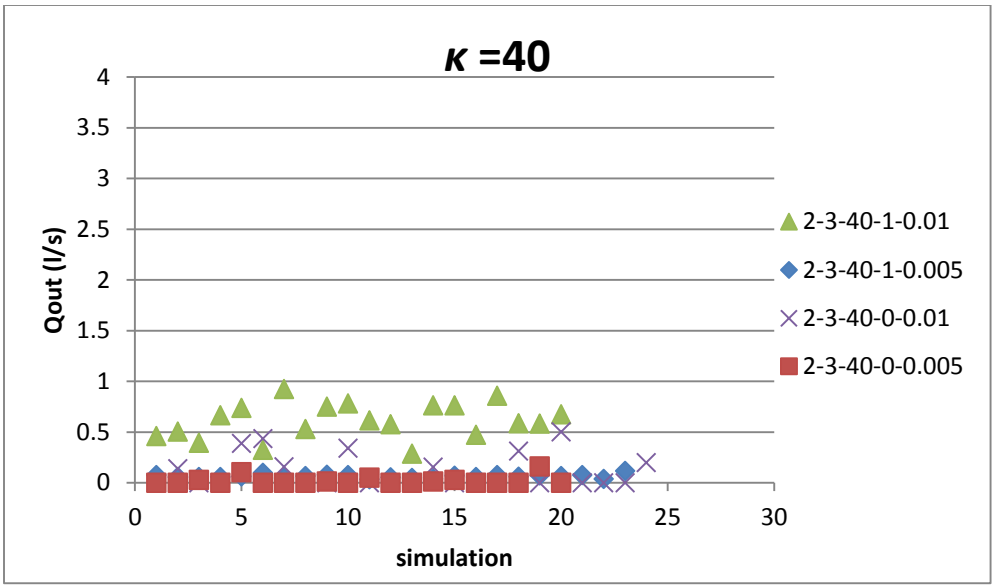

Figure 4.16 - Flow rate (Qout) for κ =40

For κ =1 (Figure 4.5) the largest values are obtained for h=0.01 m and no rotation. For κ =40 this is different (Figure 4.6). In fact, for κ =40 and h=0.01 the highest values of Qout occur for random rotation. A possible explanation is as follows: the rotation of the fractures starting from almost parallel planes (κ=40) adds some randomness that increases the intersections between fractures generating more flow. On the other hand starting from random orientation of the planes (κ=1) the fractures intersect because of the orientations of the planes with no rotation. The rotation appears to remove some of these intersections. In order to better understand this behavior the number of paths and their physical location in the control volume are shown in the following figures (Figures 4.7 to 4.14) in which the variation of all parameters is investigated (κ=1, κ =40; h=0.01 m, h=0.005 m; rotation, no rotation).

- *Plots of the paths for κ=1*

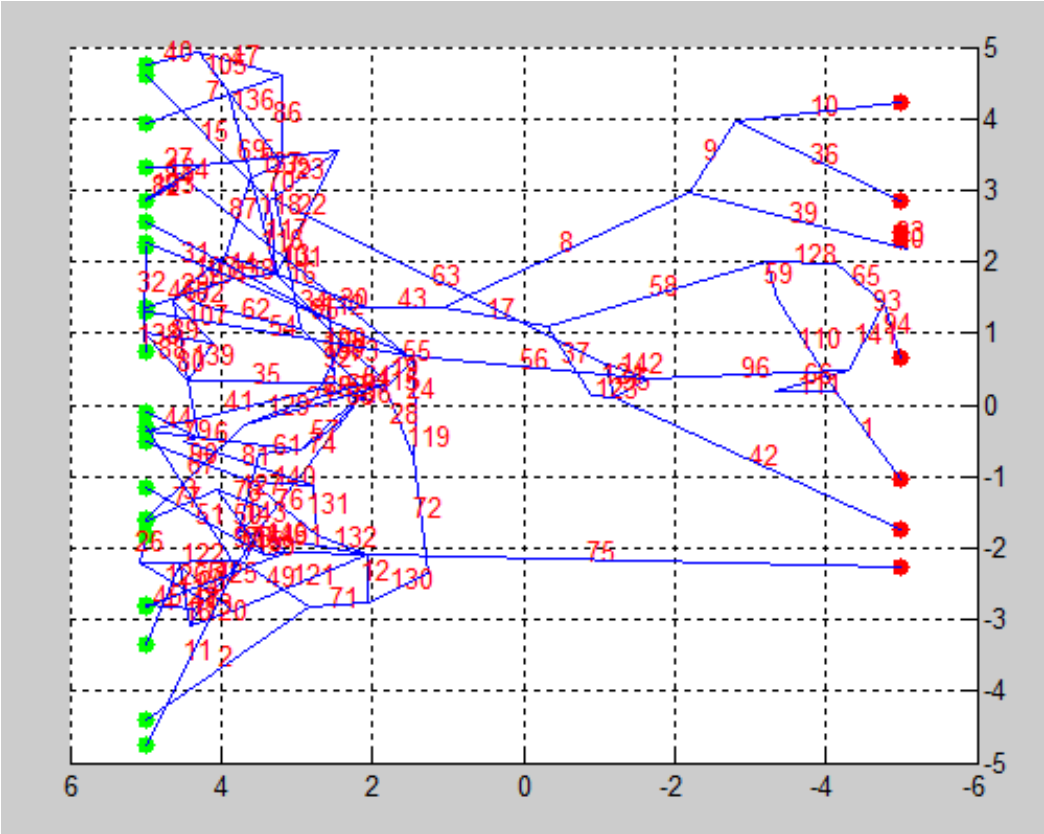

Figure 4.7 – Fracture paths system for simulation with κ=1, h=0.005 rotation

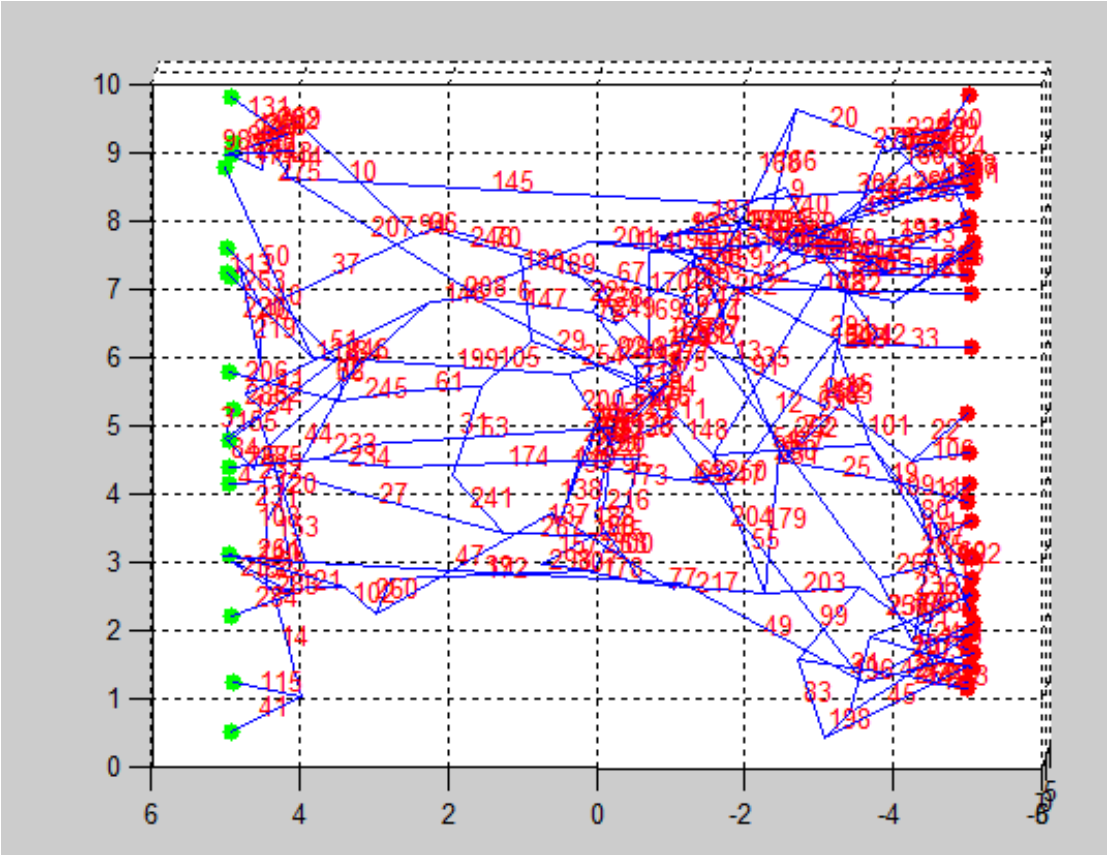

Figure 4.8 - Fracture paths system for simulation with κ=1, h=0.01 rotation

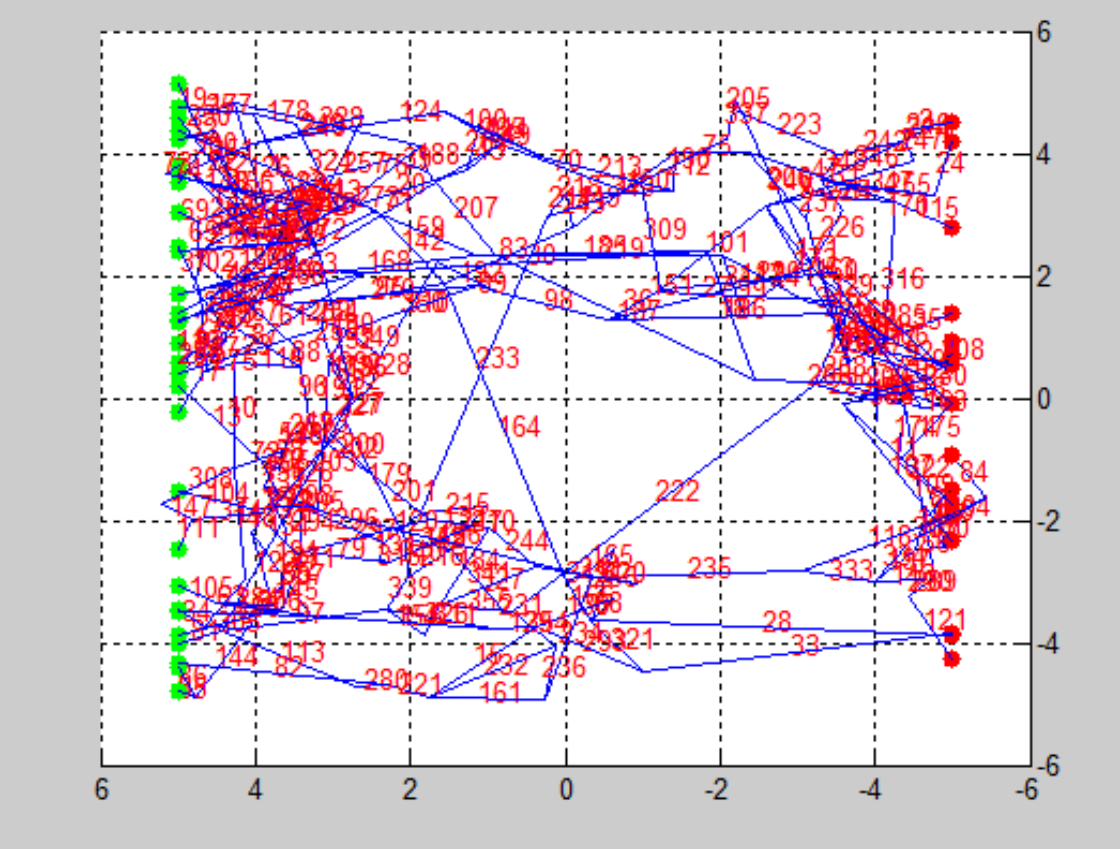

Figure 4.9 - Fracture paths system for simulation with κ=1, h=0.005 no rotation

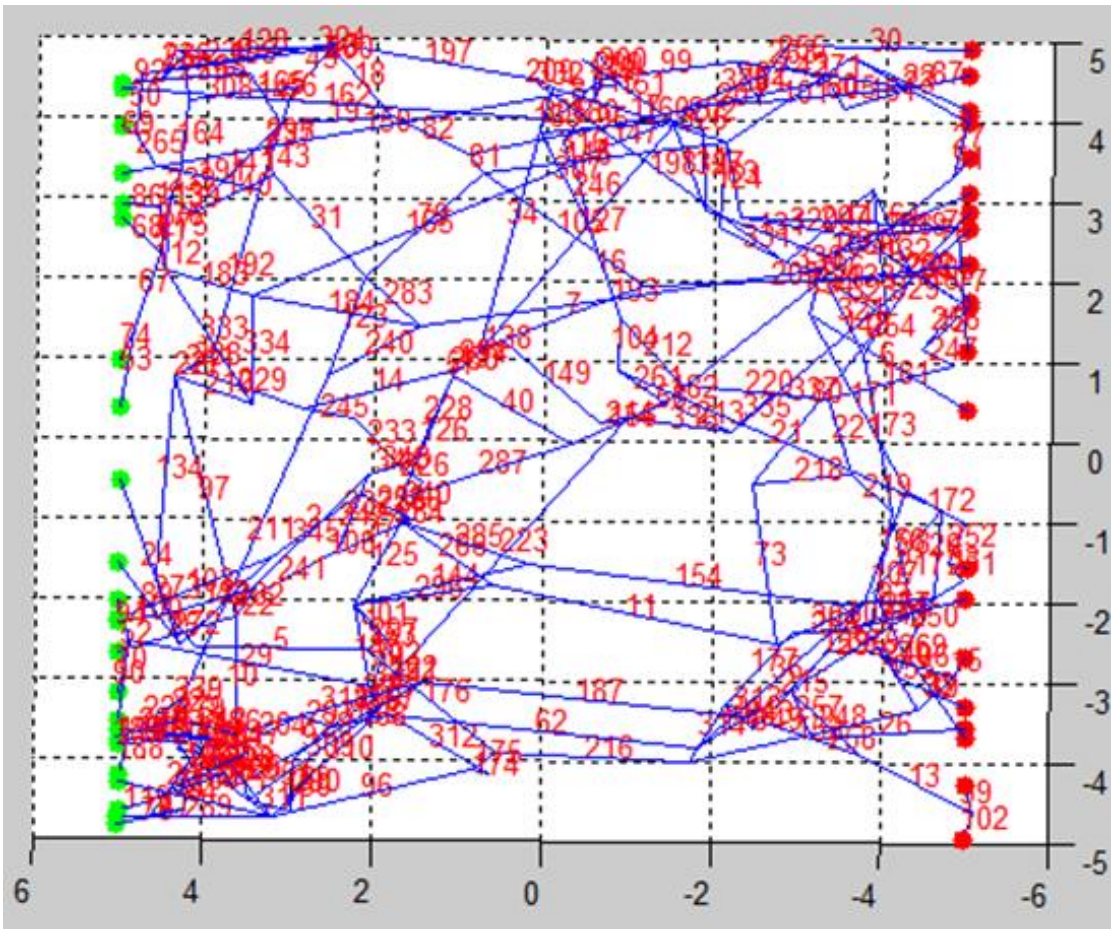

Figure 4.10 - Fracture paths system for simulation with κ =1, h=0.01 no rotation

- *Plots of the paths κ=40*

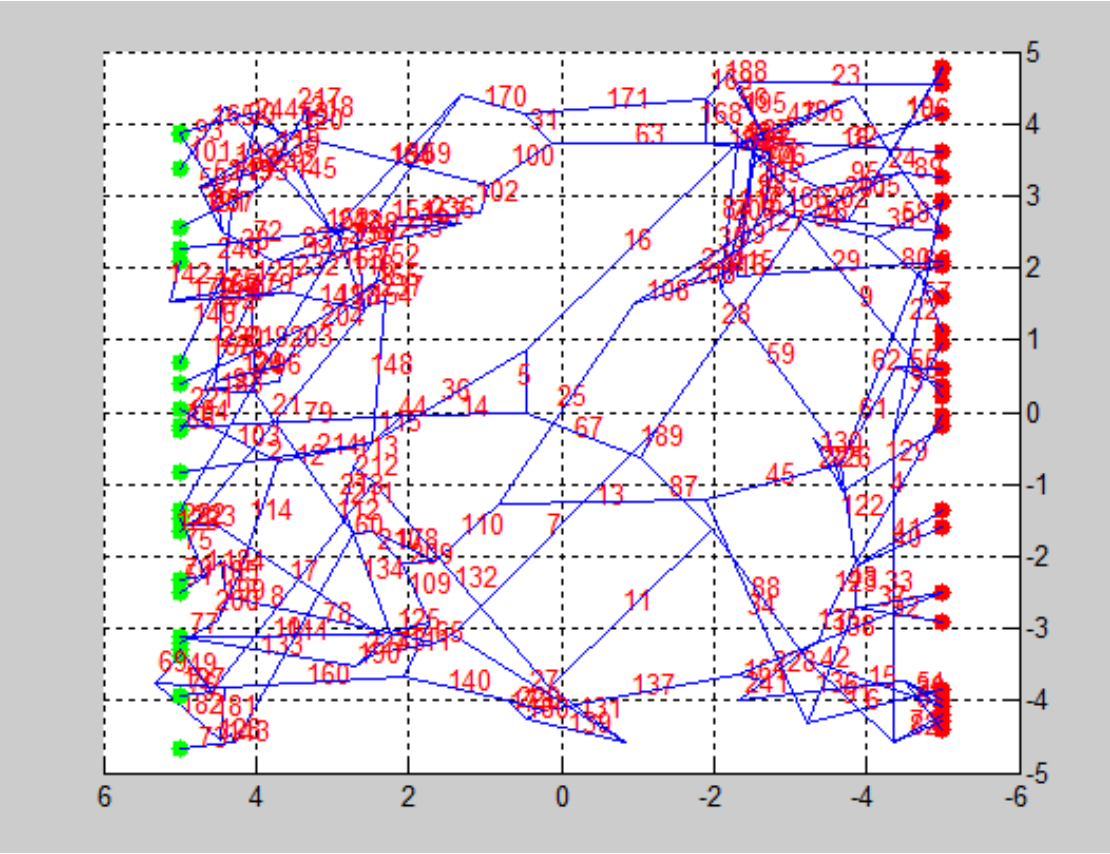

Figure 4.11- Fracture paths system for simulation with κ=40, h=0.005 rotation

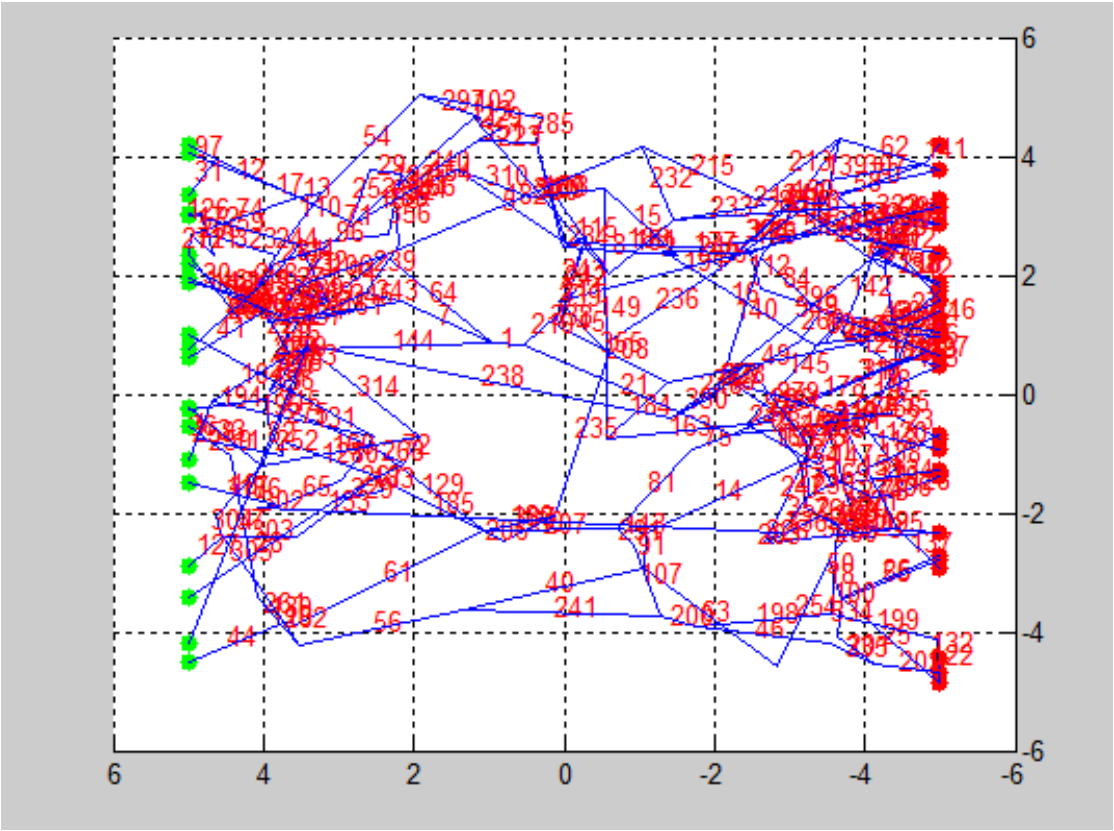

Figure 4.12 - Fracture paths system for simulation with κ =40, h=0.01 rotation

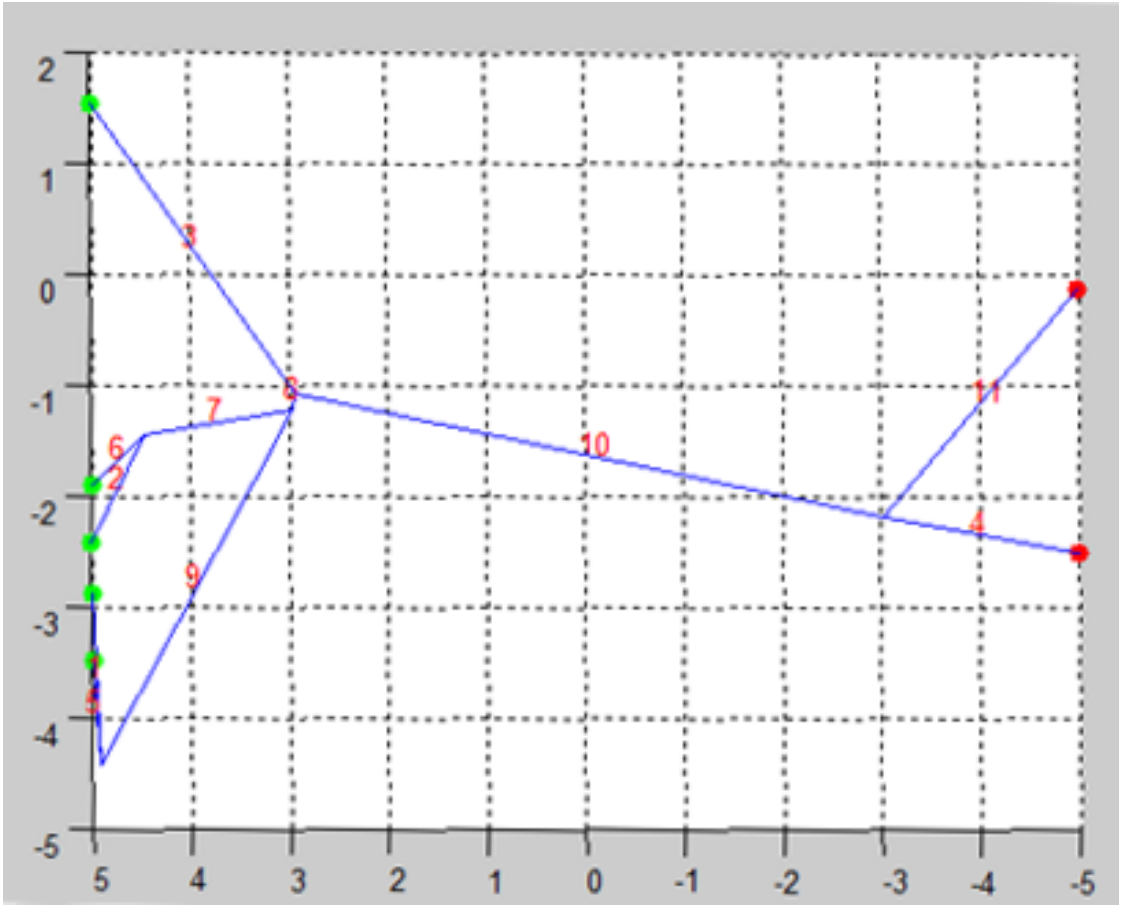

Figure 4.13- Fracture paths system for simulation with κ =40, h=0.005 no rotation

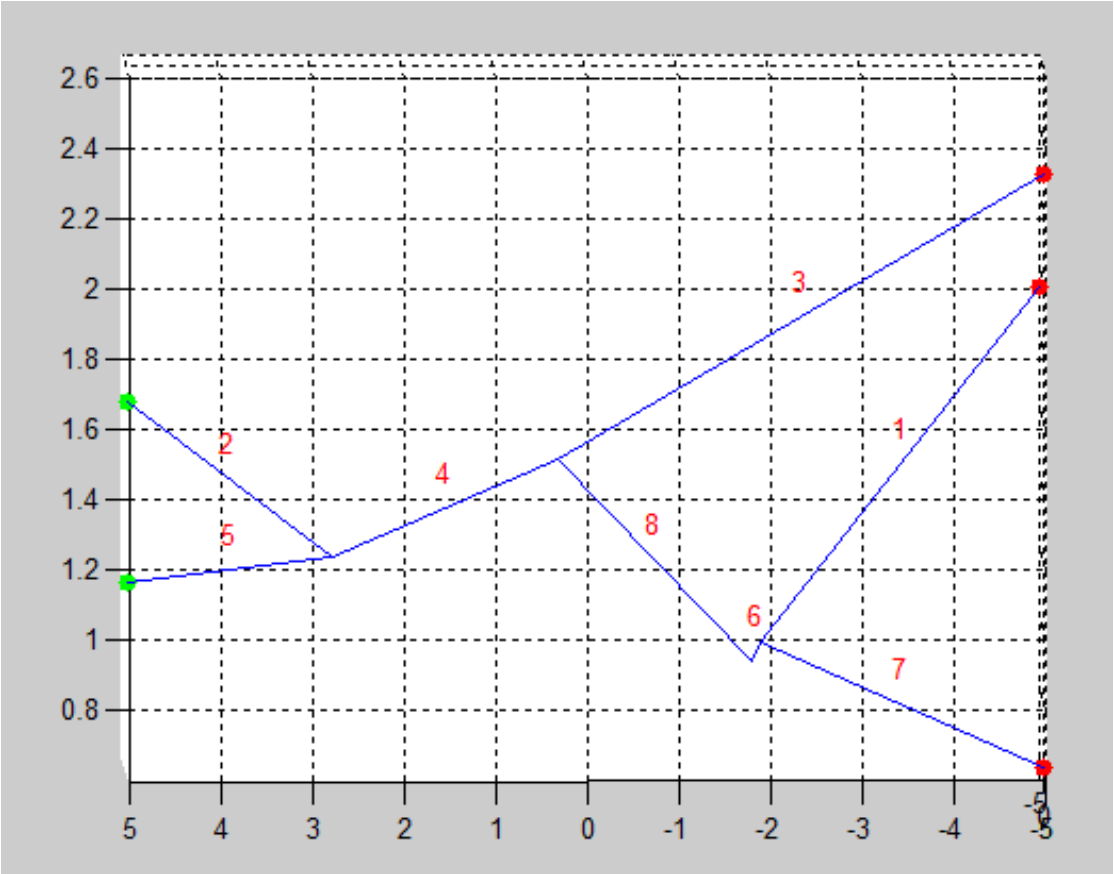

Figure 4.14 - Fracture paths system for simulation with κ =40, h=0.01 no rotation

The following interpretation can be offered: for κ = 1 (Figures 4.7 to 4.10) the number of paths in general is high. There are many fractures that intersect the two boundaries (green and red dots in the figures). Figure 4.7 (h=0.005, rotation) shows a somewhat odd behavior in that the number of paths decreases then increases again. This influences the flow, which in effect is smaller in this particular case. The h=0.01 m no rotation case (Figure 4.10) shows a higher number of paths and more branches compared to the other figures. This confirms the hypothesis made earlier that, with κ=1 the planes in the volume are randomly oriented, and this produces a large number of intersections between fractures.

The results for κ =40 paths are very consistent and clear. More branches occur in the rotation case (Figures 4.11 and 4.12) than in the no rotation case, (Figures 4.13 and 4.14) and as a consequence the number of paths is higher in the rotation case. As mentioned before the primary process for κ=40 generates planes almost parallel to each other and the rotation of the fractures in the tertiary process increases the probability of intersections.

4.2.3 Effect of fracture translation

In the tertiary process fractures are translated and can be rotated or not rotated. The effect of rotation was discussed above. It is worthwhile to investigate what effect translation may have. Figure 4.15 shows the possible overlaps of apertures if the fractures are translated and not rotated. Such an overlap can produce a fracture path. However, when we investigated Qout as a function of translation and rotation as shown in Figure 4.16 one can see that translation has no effect both in the rotation- and the no rotation case and that the Qout for no rotation is higher (for reasons explained earlier). A possible explanation for the lacking

effect of translation can be found with the numbers shown in Table 4.3. The minimum value of the translation is 0.016 m; so only few fractures with aperture h=0.01 m will overlap as shown in Figure 4.15.

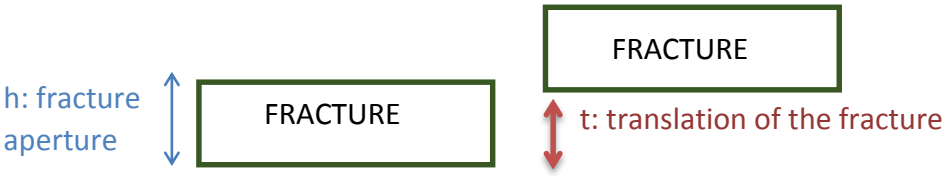

Figure 4.15 – Schematic representation of the translation between fractures

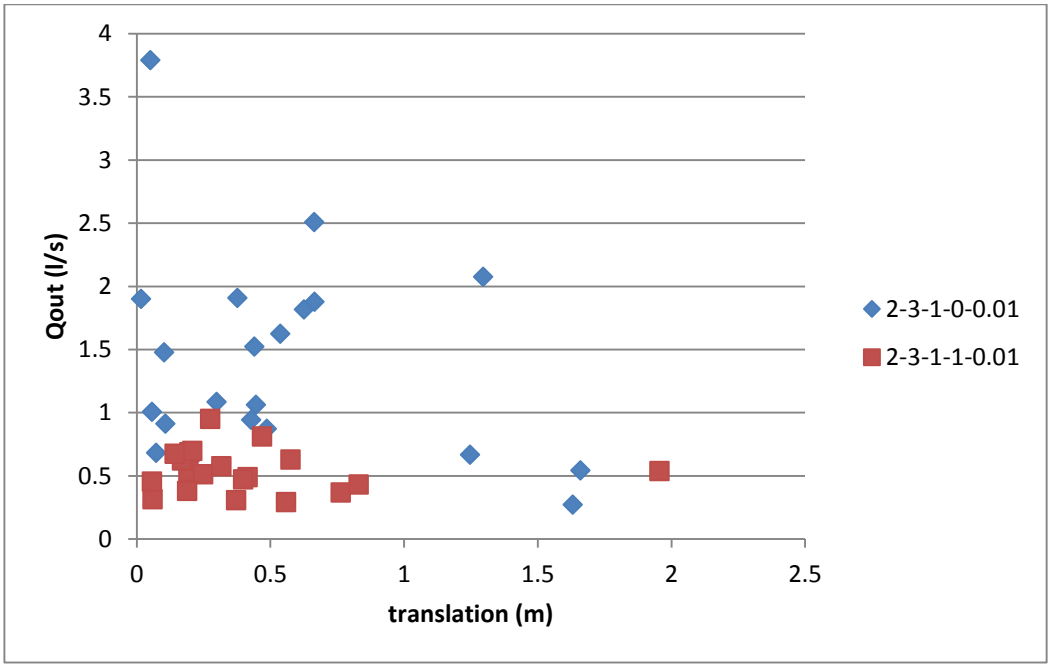

Figure 4.16 - Translation of the fractures vs Qout

Table 4.3 - Max and min values of the translation of the fractures

translation (m)	min	max
no rotation	0.016	1.659
rdm rotation	0.057	1.955

4.3 Conclusion

The parametric study demonstrates how aperture, the Fisher parameter and rotation of the fractures influence the production flow rate. As to be expected greater aperture produces greater flow. The effects of orientation are more complex as the effect of fracture plane orientation (Fisher parameter) and of rotation of individual fractures interact. For planes randomly generated the case with no rotation of the fractures and an aperture of 0.01 m generates greater flow than with rotation, while for parallel planes greater flow occurs in case of rotation of the fracture and aperture equal to 0.01 m.

This study of a simple synthetic case shows that the model is consistent but also that are some unexpected complexities affected by fracture orientation.

CHAPTER 5

BOREHOLE INTERSECTION

5.1 INTRODUCTION

Up to now the fracture and flow system was created and modeled starting from plane boundaries of the controlled volume (Figure 5.1). In order to apply GEOFRAC to model a geothermal reservoir, borehole[1] boundary conditions have to be implemented in the model. With this GEOFRAC allows the user to evaluate the flow just through the fractures that intersect the injection - and production wells. After the fracture system is modeled with plane boundaries, the model checks if fractures intersect the injection and the production wells (Figure 5.1).

[1] The term borehole will be used in this Chapter to represent geothermal wells

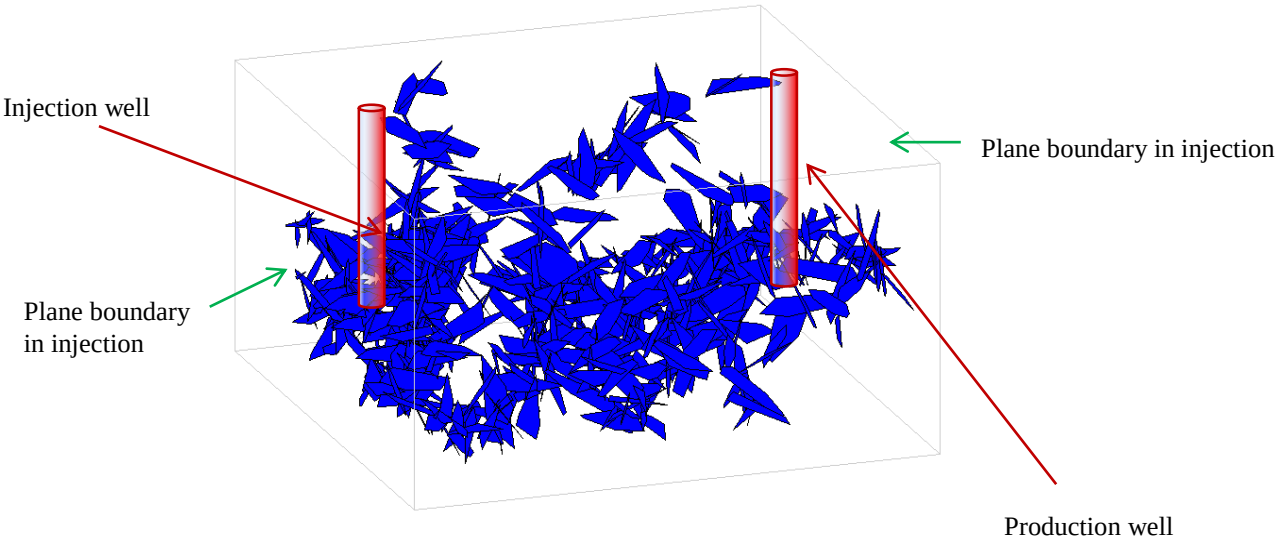

Figure 5.1 - Fracture systems intercepted by the two wells

5.2 INTERSECTION ALGORITHM

5.2.1 The MATLAB function *intersectBorehole*

In order to have the possibility to choose if the model considers the fractures system in the entire controlled volume or just the fractures that intersect the boreholes, a new function `intersectBorehole` was created.

```
function [frac, inter]=intersectBorehole(P0, d, rb, fractureSet)
```

This function takes the fracture set generated in the controlled volume, checks which fractures intersect the borehole (cylinder) and returns the intersections and the fractures that intersect the cylinder.

In more detail the inputs are:

PO: [X0, Y0, Z0], i.e. is the center of the borehole at the surface

d: depth of the borehole (m)

rb: radius of the borehole (m)

FRACTURESET: MATLAB structure folder containing all fractures and geometric characteristics. (Polygon vertex coordinates)

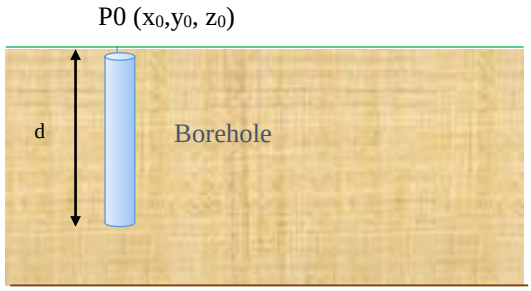

Figure 5.2 Schematic representation of geometric inputs for the Intersect Borehole function

The outputs are:

FRAC: array of fractures that intersect the borehole

INTER: array of intersections of the fractures with the borehole

From this point on GEOFRAC will take as input just the FRAC array in which fractures that intersect the borehole are stored.

In the Matlab file this intersection is done in three steps:

STEP 1: Clear polygons outside the interest volume (below the borehole zone)

From the computational point of view it is better to eliminate fractures that are below the borehole depth because one is certain that they will not intersect the borehole. This allows one to reduce the quantity of fractures that the code needs to check. The function that it is run at this point is `clearPolygonsBelowVolume`

```
[polygon, cs, rs]=clearPolygonsBelowVolume(polygon,center,P0,d);
```

Where

`polygon=fractureSet.polygonall;` this is the list of the fractures generated in the controlled volume

`center=fractureSet.Call;` it is the center of all fractures in the controlled volume

`cs, rs` are respectively the center and the radius of the spheres that enclose the polygons

See the end of this chapter for the code of the function `clearPolygonsBelowVolume.`

STEP2: Check which spheres that enclose polygons, resulting from step 1, intersect the borehole

In this step the intersections between the borehole and the spheres that enclose the polygons is checked and stored in C.

```
C = intersectBoreholeSphere(cb,cs,rb,rs);
```

See the end of this chapter for the function `intersectBoreholeSphere`

Figure 5.3 gives a visual representation in Matlab of an intersection between a cylinder and spheres.

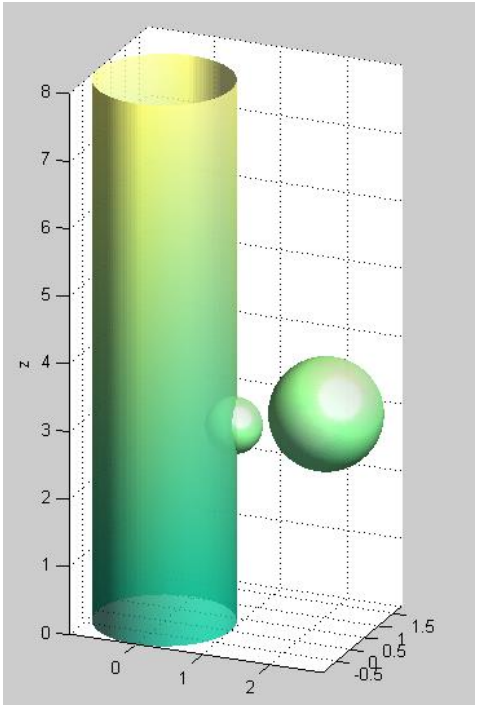

Figure 5.3- Matlab representation of intersection between a cylinder and spheres

STEP 3: Calculate if polygons (whose spheres intersect the borehole) actually intersect the well

In this step just the polygons, whose spheres intersect the borehole and that were stored in the preceding step are analyzed.

```
m=find(C==1);
```

`C==1` means that there is intersection and this information is stored in m.

The intersection between a sphere and a cylinder can be a circle, a point, the empty set, or a special type of curve. In order to ensure any possible intersection between polygon and cylinder, the following cases are taken into account:

- CASE 1- General case If at least one vertex is inside the cylinder, the polygon intersects the borehole (Figure 5.4)
-

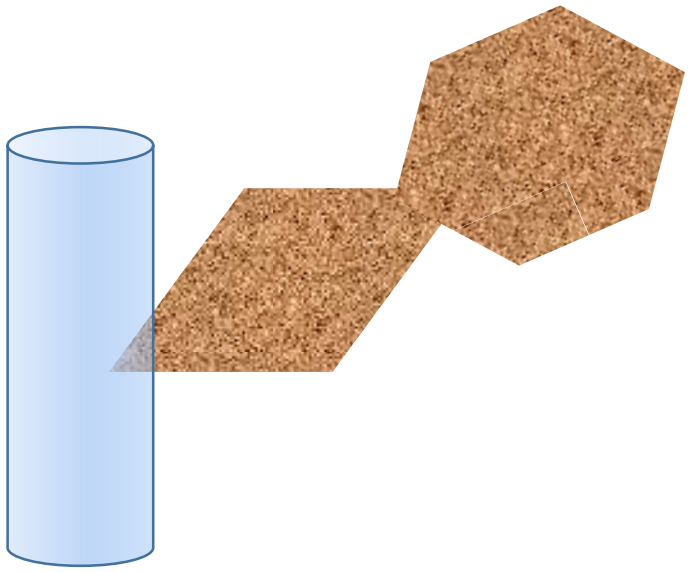

Figure 5.4 - Schematic representation of intersection between the borehole and one vertex of the fracture (polygon)

- CASE 2- Polygon inscribed into the cylinder. The way of modeling case 1 solves also the case of polygon inscribed into the borehole (Figure 5.5).

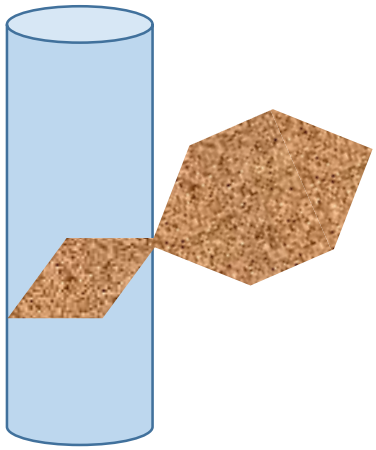

Figure 5.5 - Schematic representation of a fracture (polygon) inscribed into the borehole

- CASE 3 - All vertices outside the cylinder but a line between 2 vertices (i.e. v_1 and v_2 in Figure 5.6) intersects the cylinder.

  At this point of the code just the vertexes coordinates are stored in FRACTURESET, so lines between vertices are created in the code, and then the intersections between lines and the cylinder are calculated.

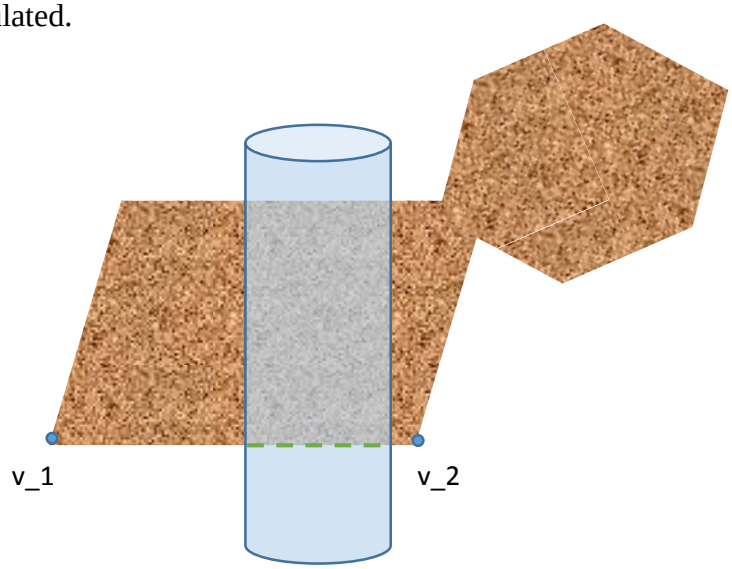

Figure 5.6- Schematic representation of an intersection between one side of a fracture and the cylinder

- CASE 4 - All vertices outside the cylinder, no line between vertices intersect the cylinder (Figure 5.7).

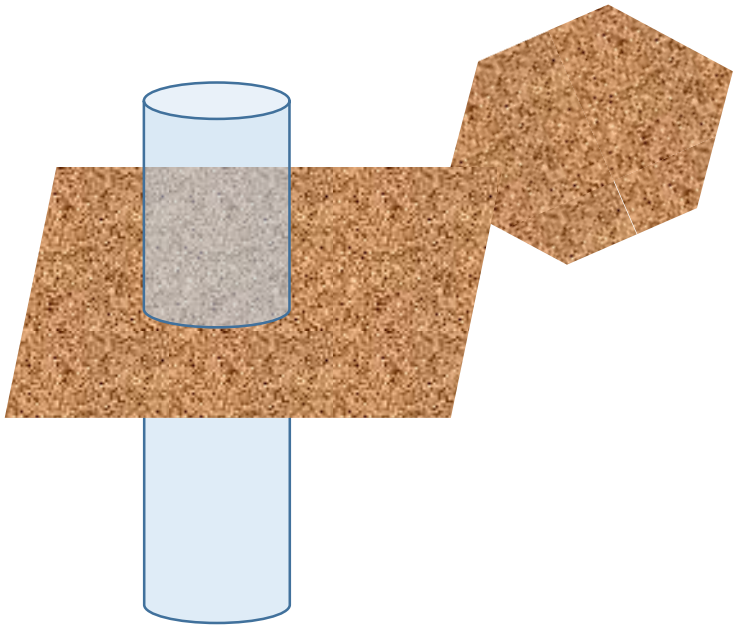

Figure 5.7- Schematic representation of intersection between a fracture (plane) and a borehole (cylinder)

CHAPTER 6

GEOFRAC GRAPHICAL USER INTERFACE

6.1 INTRODUCTION

Geofrac is a program written in the MATLAB computational environment, so one needs to run MATLAB in order to use GEOFRAC. GEOFRAC has been made accessible through a Graphical User Interface (GUI). The GUI allows the user to perform the complicated simulations of a geothermal basin without the need to understand the details of how the tasks are performed.

After starting MATLAB, one can use the GUI to enter input parameters, as described in more detail in section 6.2, and determine the computed fracture system, the output flow rate and the thermal energy extracted. How the outputs can be obtained, and how they are represented is explained in section 6.3.

6.2 INPUT PARAMETERS

In order to be able to use GEOFRAC one needs to open the GEOFRAC folder though the Matlab command *Open Folder*. In the GEOFRAC folder a file called *RunGeofrac.m* opens the window shown in Figure 6.1. The GUI is organized in sections:

- Geometric inputs
- Stochastic inputs
- Simulation
- Flow inputs
- Thermal inputs
- Borehole inputs

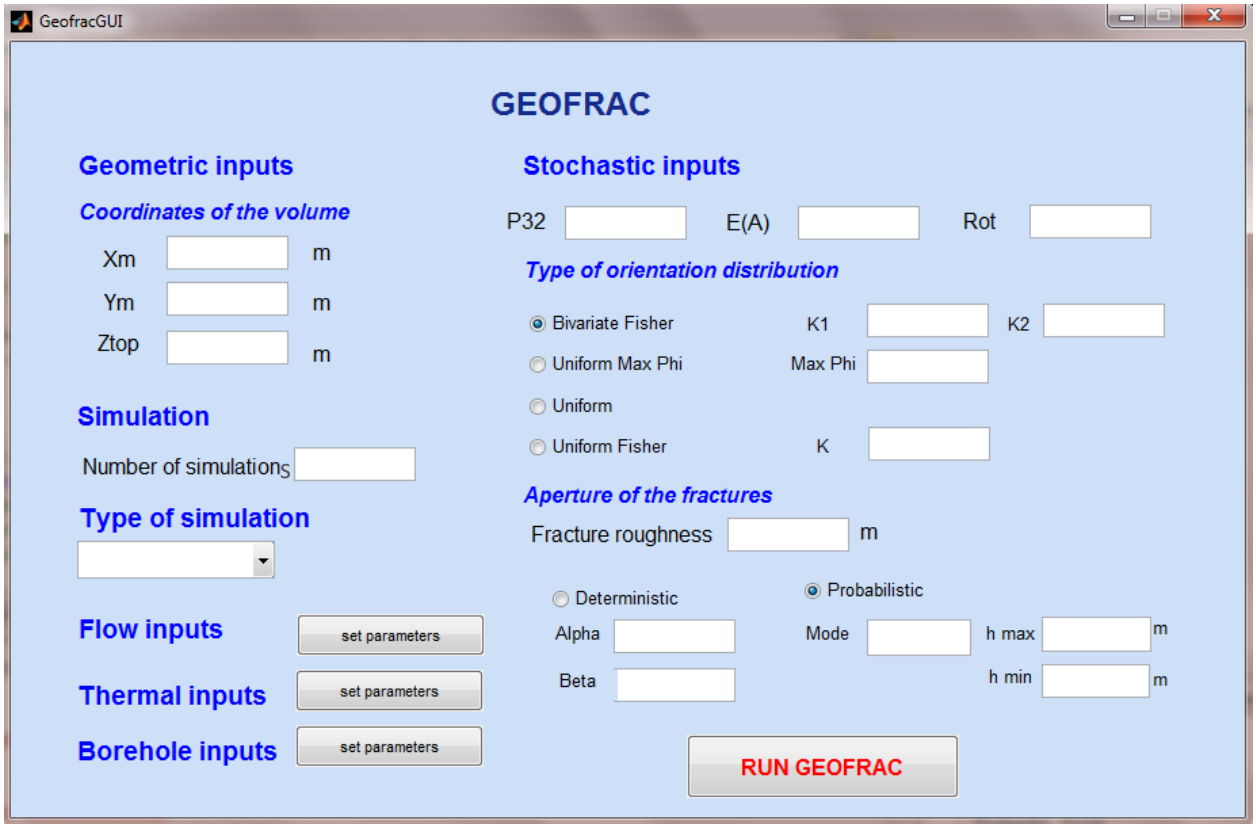

Figure 6.17 – GEOFRAC GUI (user's interface)

6.2.1 Geometric inputs

The geometric inputs (Figure 6.2) defines the reservoir dimensions.

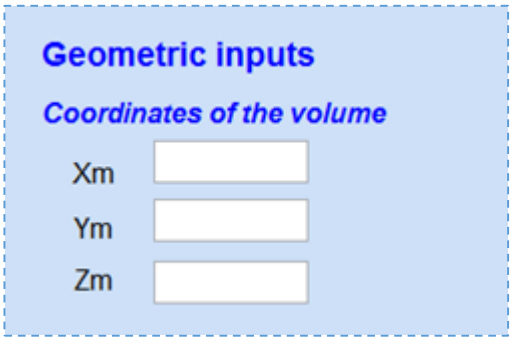

Figure 6.18 - Geometric dimensions of the reservoir to be modeled

Figure 6.3 shows how the coordinates are placed in the space. The coordinates of the controlled volume in GEOFRAC are defined in the following way:

Xm: half of the length of the area of interest (m)

Ym: half of the width of the area of interest (m)

Ztop: depth of the area of interest (m)

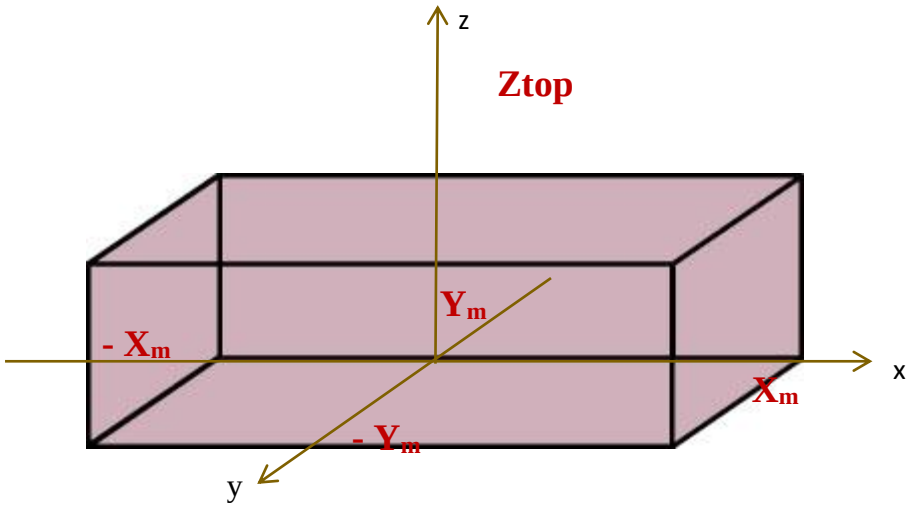

Figure 6.19 – Coordinates of the controlled volume according to GEOFRAC

The left and right sides of the controlled volume (Fig. 6.3) are taken in GEOFRAC as the boundaries from and to which the flow is respectively generated and collected.

At the end of this chapter, a section is dedicated to give some recomendations on how to simulate large reservoirs.

6.2.2 Stochastic inputs

GEOFRAC uses stochastic models to represent natural fracture systems based on available geological information. Figure 6.4 shows the stochastic parameters that need to be set in order to generate the fracture system. P_{32} and E(A) define the intensity and the mean area of

the fractures. The orientation distribution parameters define the orientation of the primary planes generated in the controlled volume and the aperture mode parameters define the type of distribution that one wants to use in order to generate the aperture of the fractures. The stochastic parameters are explained in more detail below.

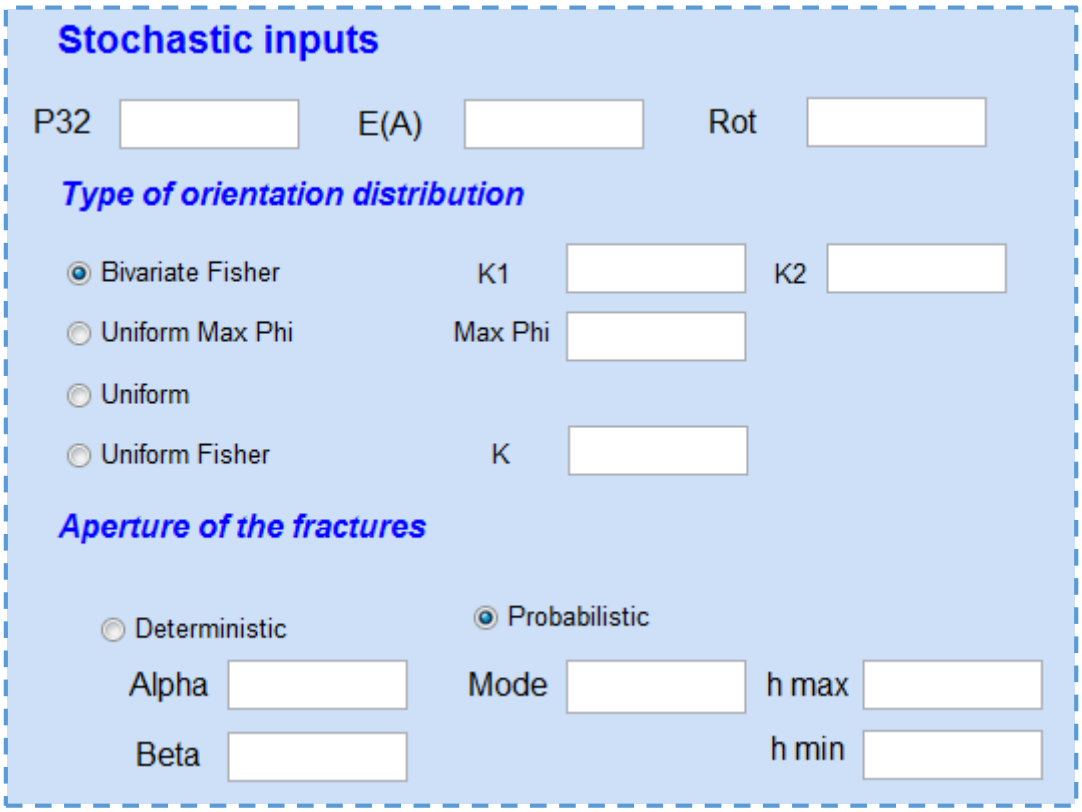

Figure 6.20 - Section of the stochastic inputs in the GUI.

P_{32}, E(A) and Rot

Three stochastic parameters in GEOFRAC are:

- P_{32}: fracture intensity (cumulative fracture area per rock volume), that can be calculated from:

$$P_{32} = \frac{\sum_{i=1}^{N} A_{f,i}}{V}$$

Where

$A_{f,i}$: fracture area of fracture f;

V: total volume of fractured rock mass.

- E(A): mean area of fractures
- Rot: rotation of the polygons in the tertiary process

P_{32}, as described in Dershowitz and Herda (1992) and used in Ivanova (1995), is the most appropriate description of the fracture intensity in 3D space. P_{32} can be obtained from borehole spacing information or observations on outcrops using the approach by Dershowitz and Herda (1992). E(A) can be obtained from fracture trace lengths on outcrops with suitable bias corrections as developed by Zhang et al. (2002).

Once the main fracture plane is established (see next section), the algorithm gives the possibility to randomly rotate the fractures in the space. Rot is a parameter that allows the user to rotate the polygons (fractures) or to not rotate them. The values in Rot that can be inserted are:

Rot = 1: rotation of the polygons

Rot = 0: no rotation of the polygons

Types of orientation distribution

The orientation of the planes in the so-called primary process of GEOFRAC can be modeled choosing among four types of orientation distribution as explained in Ivanova (1995), depending of the information available or the type of distributions that the user is most confident in. These four distributions and the parameters that need to be set are shown in Table 6.1.

Table 6.4- Types of orientation distributions in GEOFRAC and parameters that needs to be set

ORIENTATION DISTRIBUTION	PARAMETER
Bivariate Fisher	κ_1, and κ_2
Uniform Max Phi	max φ
Uniform	
Univariate Fisher	κ

Fracture apertures models

As explained in Chapter 2, there are numerous models to simulate the apertures of fractures. In GEOFRAC the user can decide between two methods: the deterministic and the probabilistic method.

The deterministic method is the one proposed by Ivanova et al. (2012) and assumes that fracture aperture may be correlated with fracture length by a power-law function (Equation 6.1):

$$h = \alpha(2\mathrm{R_e})^{\beta} \qquad \textit{Equation 6.1}$$

where R_e is the equivalent radius of the fracture polygon obtained in the secondary process as explained in Chapter 3, h is the aperture, and α and β are coefficients that depend on the site geology and that are measured on site or can be found in the literature.

The probabilistic model defined in Ivanova et al. (2012) assumes that the distribution of the fracture aperture can be represented by a truncated lognormal distribution (Equation 6.2):

$$f_{TR}(h) = \frac{f(h)}{\int_{\min}^{h_{\max}} f(h)d(h)}, h_{\min} \le h \le h_{\max} \qquad \textit{Equation 6.2}$$

where h_{min} and h_{max} are the minimum and the maximum aperture values and f(h) is the full lognormal distribution of the aperture h.

The methods for the aperture model and the parameter are shown in Table 6.2.

Table 6.5 - Types of methods for the fracture aperture and parameters that needs to be set

FRACTURE APERTURE METHODS	PARAMETER
Deterministic	α and β
Probabilistic	mode, h_{min} and h_{max}

6.2.3 Simulation

In GEOFRAC, and as shown in Figure 6.5, it is possible to specify the number of simulations in order to improve the accuracy of the results.

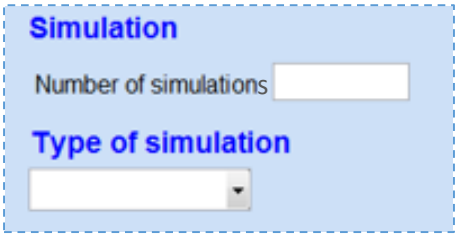

Figure 6.21 - Simulation parameter: number of simulations and type of simulation

'Type of simulation' is a pop-up menu and the user can decide to run:

- Fracture system
- Fracture system + Flow system
- Fracture system + Flow system + Thermal

This choice allows the user to use GEOFRAC just for the fracture system generation in order to use it for other applications, for example for slope stability analysis.

6.2.4 Flow inputs

The button “Flow inputs” in the main GUI window, allows one to set the fluid parameters if the flow simulation is chosen. (Figure 6.6).

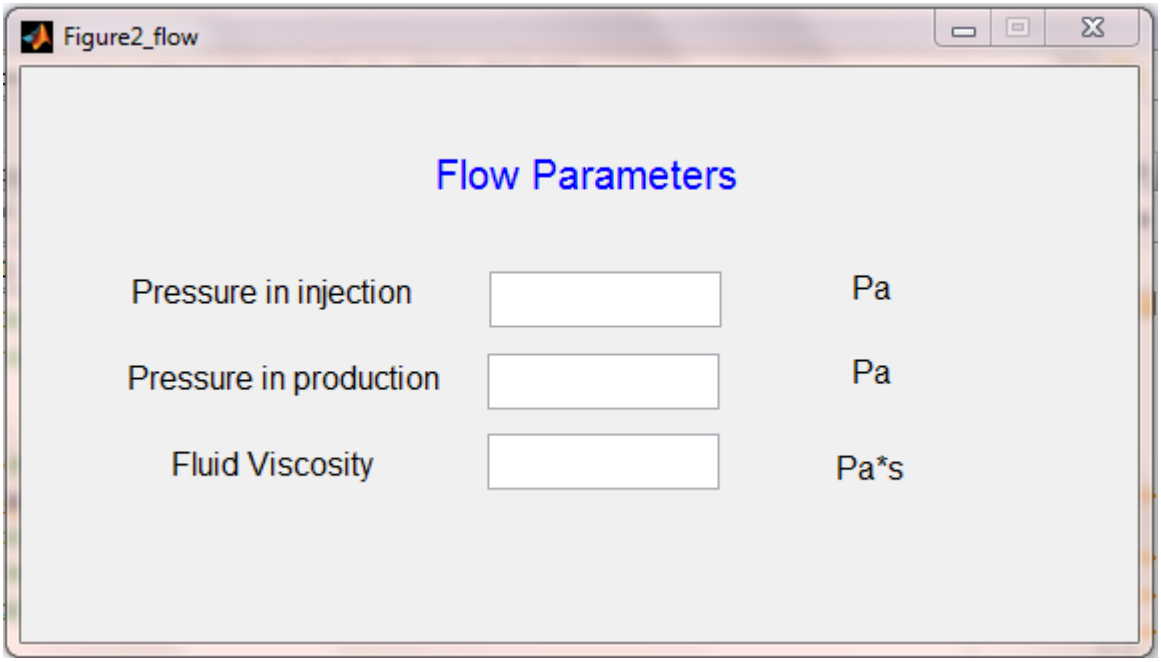

Figure 6.22 - Flow parameters in GEOFRAC

These parameters are:

P_i: injection pressure (Pa) of the fluid in the injection well

P_{out}: production pressure (Pa) of the fluid in the production well

Fluid dynamic viscosity (Pa*s)

6.2.5 Thermal parameters

The button “Thermal inputs” in the main GUI window, allows one to set the thermal parameters of the fluid and the surrounding rock. These options can be modified only if the Fracture + Flow or the Fracture + Flow+ Thermal simulation has been chosen (see section 6.2.4).

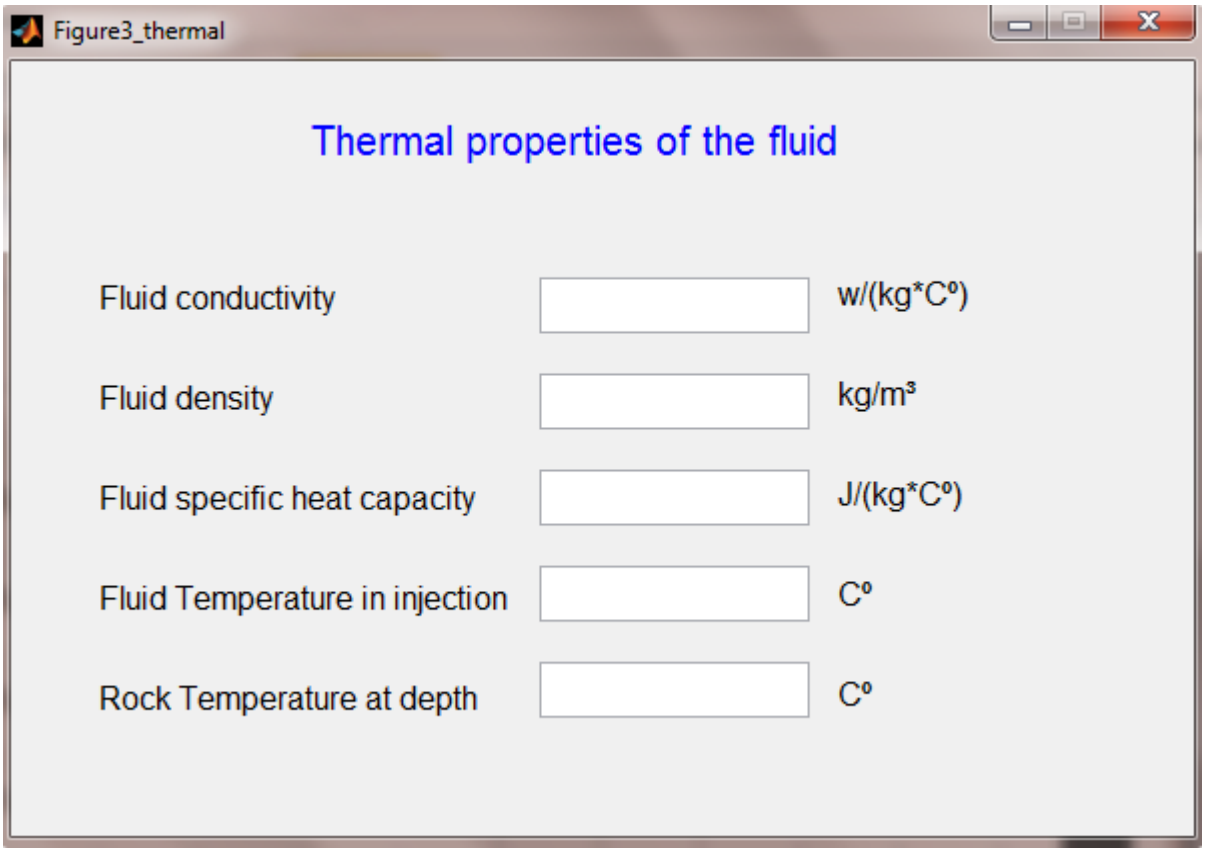

6.2.6 Borehole Parameters

The button “Borehole Inputs” in the main GUI window, allows one to set the geometric parameters of the geothermal well.

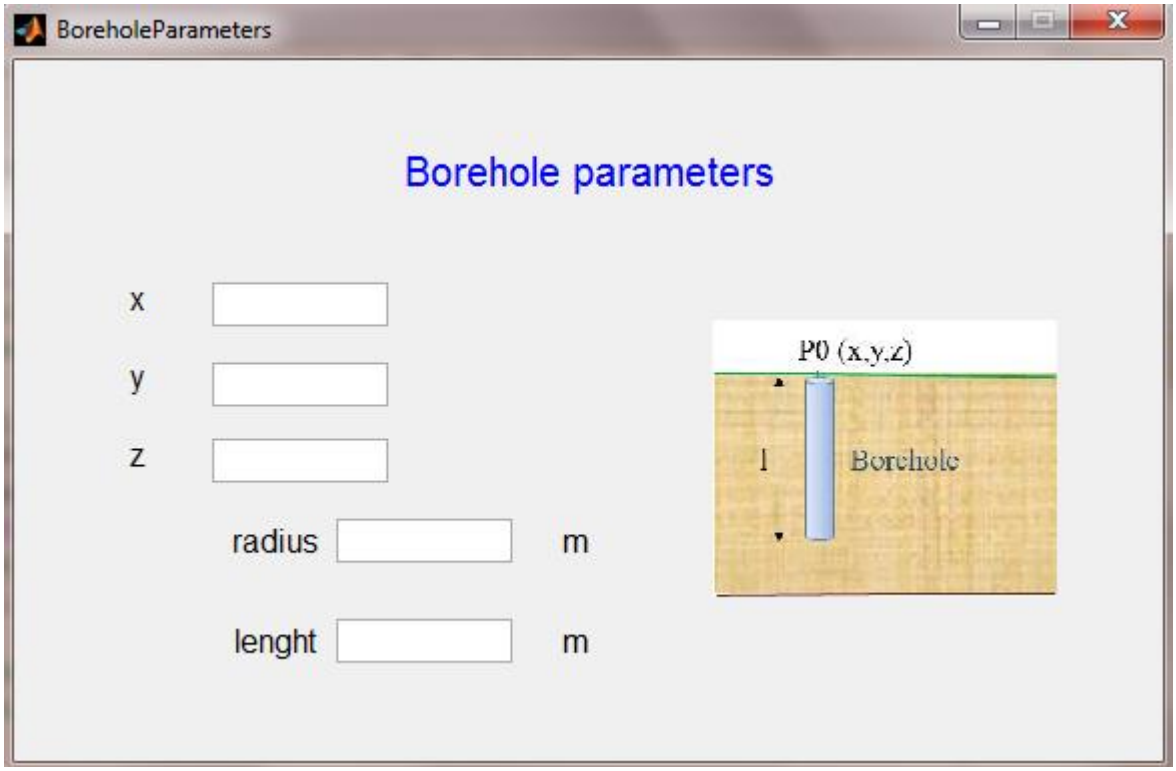

Po (x, y, z) define the center of the well respect to the volume simulated. Radius and length of the well need to be set as well.

6.3 RESULTS

After pressing the RUN GEOFRAC button, the simulations starts and it may take some time to obtain results, depending on the number of simulations and the size of the controlled volume. The resulting charts and numerical results can be personalized with simple coding based of the user's needs. Improvement of the results section is described in the conclusion section (Chapter 8).

If the flow simulation is chosen, GEOFRAC will display the fractures system as shown in Figure 6.7, and the pressure and the flow rate in the production well in the MATLAB workspace.

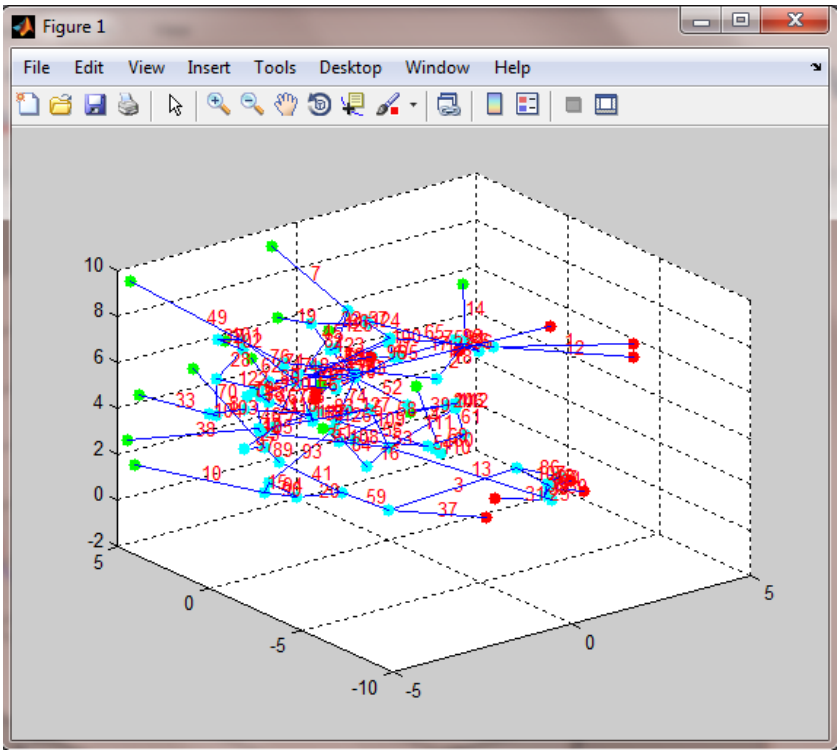

Figure 6.23 - Flow network system in the controlled volume

GEOFRAC generates also an excel file called `Results` (Table 6.3) with the results of selected parameters. The values in bold (last cells) are the mean values of those parameters.

Table 6.6- Excel file with the summary of some important results

	Numbers of Polygons	Numbers of paths	P_{32}mean	E(A)mean	Aperture Average (m)	Qout (l/s)	Re mean (m)
1	2109	1295	3.11474	1.47688	0.005	7.4877	0.6259
2	2009	910	2.831532	1.409423	0.005	5.7135	0.6084
3	1278	400	1.828845	1.431021	0.005	5.6685	0.6137
4	1833	1216	2.633562	1.43675	0.005	5.6866	0.6180
5	2086	868	2.961028	1.419476	0.005	6.2722	0.6128
6	2093	1760	2.996395	1.431627	0.005	9.7479	0.6131
7	1659	608	2.430787	1.465212	0.005	4.6046	0.6224
8	2120	875	3.084176	1.4548	0.005	6.6706	0.6225
9	2229	1404	3.179268	1.42632	0.005	7.7514	0.6170
10	2189	1188	3.146575	1.437449	0.005	7.5592	0.6198
Av.	**1784**	**821**	**2.566034**	**1.437124**	**0.005**	**6.2396**	**0.6172**

The values of Qout can be plotted using excel as shown in Figure 6.8.

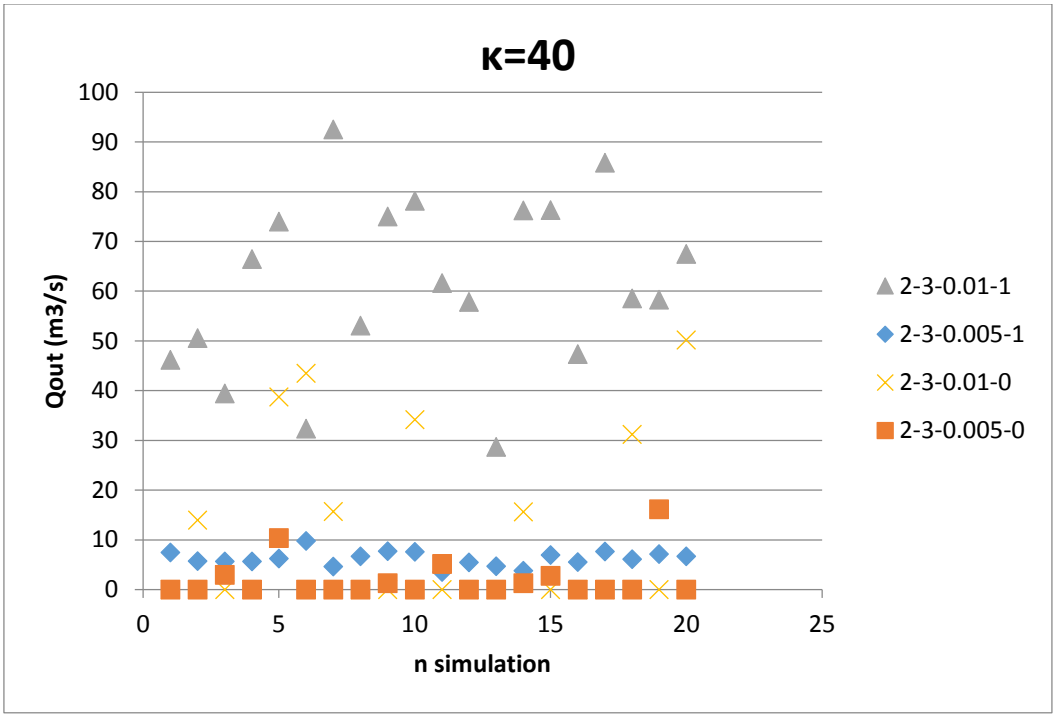

Figure 6.24- Example of representation of the Qout results

As shown previously, in GEOFRAC it is possible to select two types of aperture distribution. The following chart, Figure 6.9, shows a truncated log-normal distribution in which the minimum and the maximum aperture value and the mode were chosen.

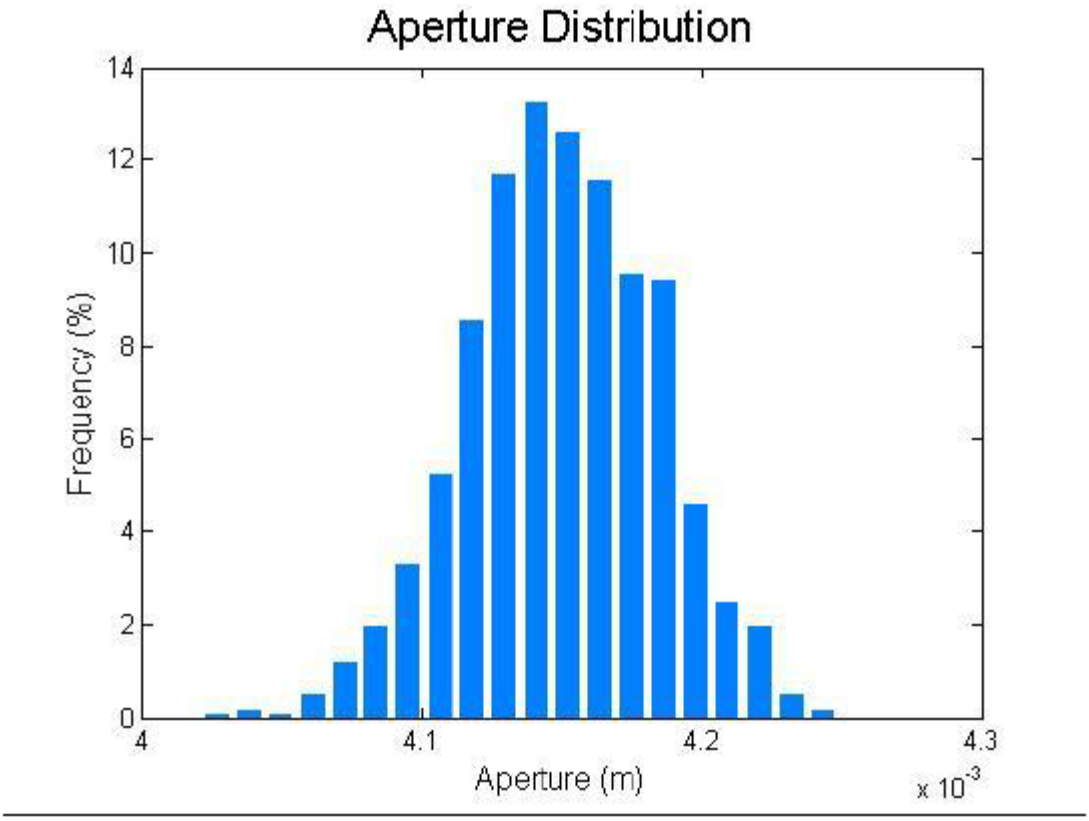

Figure 6.9 - Aperture distribution that follows a truncated lognormal distribution

System requirement for large reservoir simulations

The capacity of GEOFRAC packages simulating large geothermal reservoirs is mainly limited by the number of fractures and not by the reservoir volume. The time needed to run one simulation is mainly determined by the speed of the processor. For an ordinary desktop with less than 8GB ram and an Intel i3 processor, the number of fractures it can handle is less than 300. The 300-fracture reservoir takes about half an hour to finish. Work stations are able to handle larger number of fractures. For a work station with 32GB ram and a 3.5 GHz Intel i7 processor, the number of fractures can be as many as 2000, and it takes about 1 hour to finish the simulation.

In GEOFRAC it is not possible to enter the number of fractures directly because the inputs parameters of the algorithm are P_{32} and E(A). It is however possible, taking into consideration the definition of P_{32}, to obtain the cumulative fracture area per rock volume

$$P_{32} \times V = \sum E(A)$$

Once $\sum E(A)$ is obtained, it is possible to find the approximate number of fractures from

$$\sum E(A) / E(A) = \text{Number of fractures (approx.)}$$

In case of large reservoir it is also recommended not simulate the entire reservoir in order to not encounter problems of insufficient computer memory. To do so one should concentrate the calculation on the zone defined by the injection and production wells and their depth.

GEOFRAC: GUI – File list

RunGeofrac.m	Main file of the GUI. When running this file the GUI opens and it is possible to set the inputs before running Geofrac. It allows one to generate the fracture pattern and the flow pattern.
GeofracCallback.m	It contains the link formula between the GUI and the Geofrac function.
GeofracGUI.m	File generated automatically by MATLAB when one creates a new GUI

CHAPTER 7

APPLICATION OF GEOFRAC TO MODEL A GEOTHERMAL RESERVOIR: A CASE STUDY

The aim of this chapter is to present results of GEOFRAC tested with real data made generously available by the energy company, Landsvirkjun, Iceland. This allows us to verify the capability of this model for representation of hydrothermal reservoirs, to understand the limitations and to implement possible changes in the associated code.

The geological-hydro-thermal description of the geothermal field selected is presented in the first part of the chapter. The parameters selected for the simulation will be then presented and discussed. Then the results will end this chapter.

7.1 Hydro-Geological characterization of the Námafjall geothermal field

The Námafjall geothermal field is located in NE-Iceland about 5 km northeast of Lake Myvatn as shown in Figure 7.1. Precisely, it is located in the southern half of the Krafla fissure swarm and it is associated with the Krafla volcano. The Krafla geology is characterized by active rifting, forming a graben zone through its center, where volcanic craters, volcanic pyroclastics and lava flows, all of basaltic composition, dominate. The fissure swarm that intersects the Krafla central volcano (100 km long and 5 to 8 km wide) is

part of the neo-volcanic zone of axial rifting in N-Iceland (Figures 7.2 and 7.3), (Malimo, 2012). Figure 7.3 is a zoom out of the square red shape in Figure 7.2.

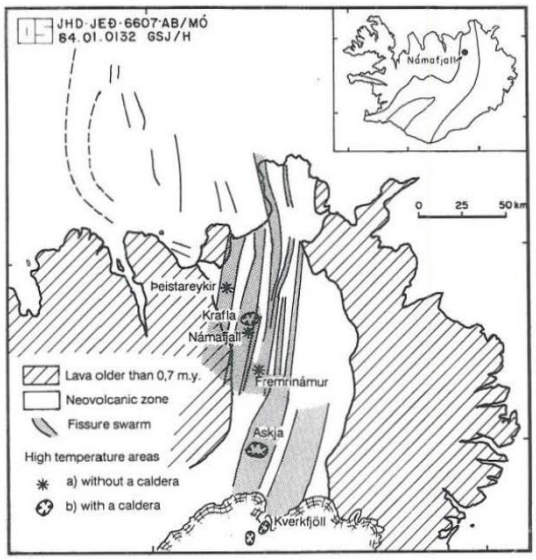

Figure 7.1 -The high temperature areas in North Iceland and location of the Namafjall geothermal reservoir (from Isabirye, 1994)

Magma from the Krafla caldera traveled horizontally in the SSW direction along the fissures and fractures all the way down to Námafjall, and it serves as the heat source for the hydrothermal system. The Námafjall field is characterized by the Námafjall ridge, about 0.5 km wide and 2.5 km long. (There are several fractures and faults in this area, such as the Krummaskard and Griótagjá, and often surface manifestations are clearly aligned with the fractures). The geological characteristics of the Námafjall field indicate that the Námafjall ridge is part of the Námafjall-Dalfjall-Leirhnjúkur ridge, which has an overall length of about 15 km and width of about 1 km (Ragnars et al., 1970).

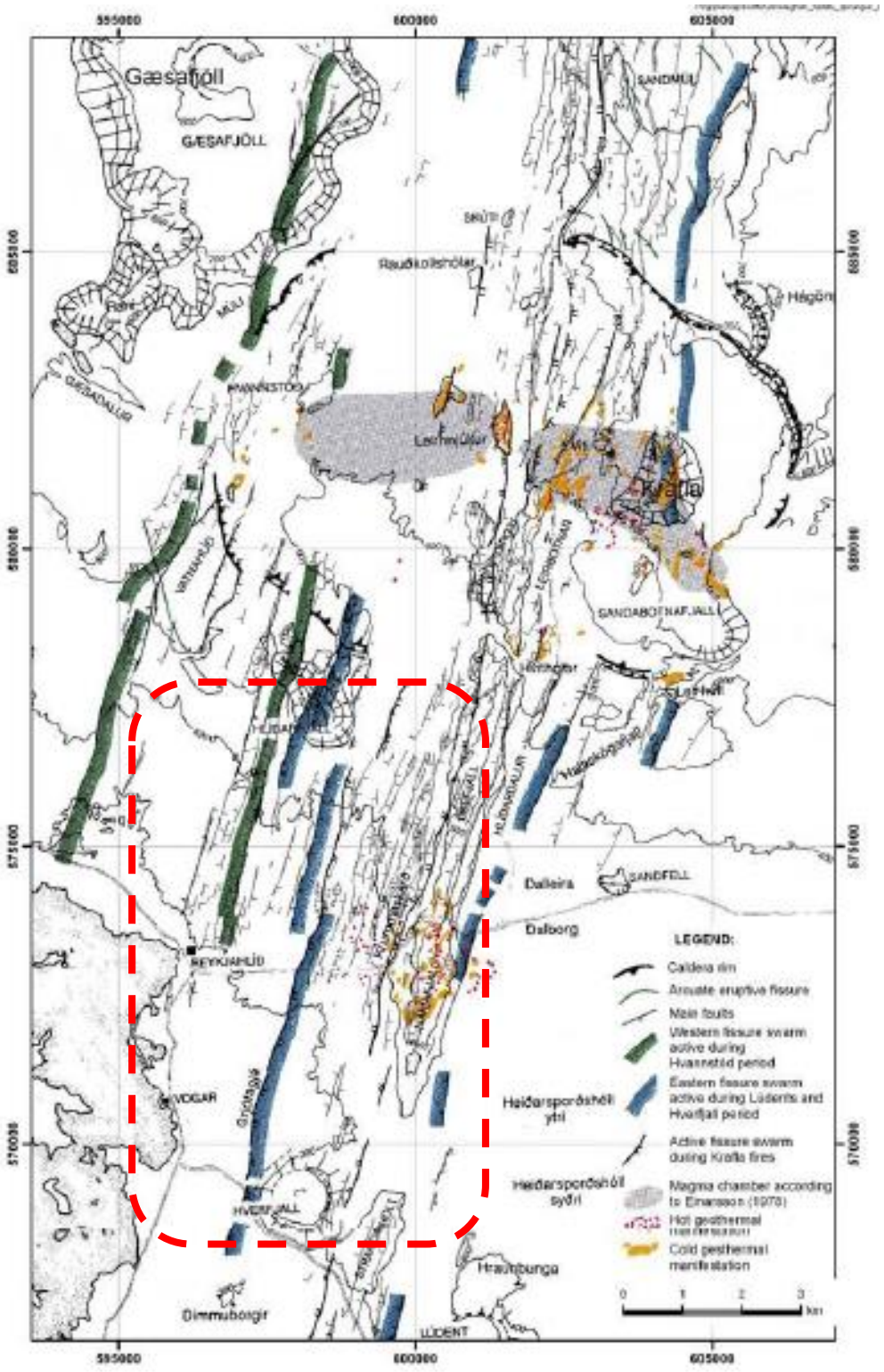

Figure 7.2 - Structural map of Krafla and Námafjall geothermal areas showing the Krafla caldera and associated fissure swarm. (from Sæmundsson, 1991).

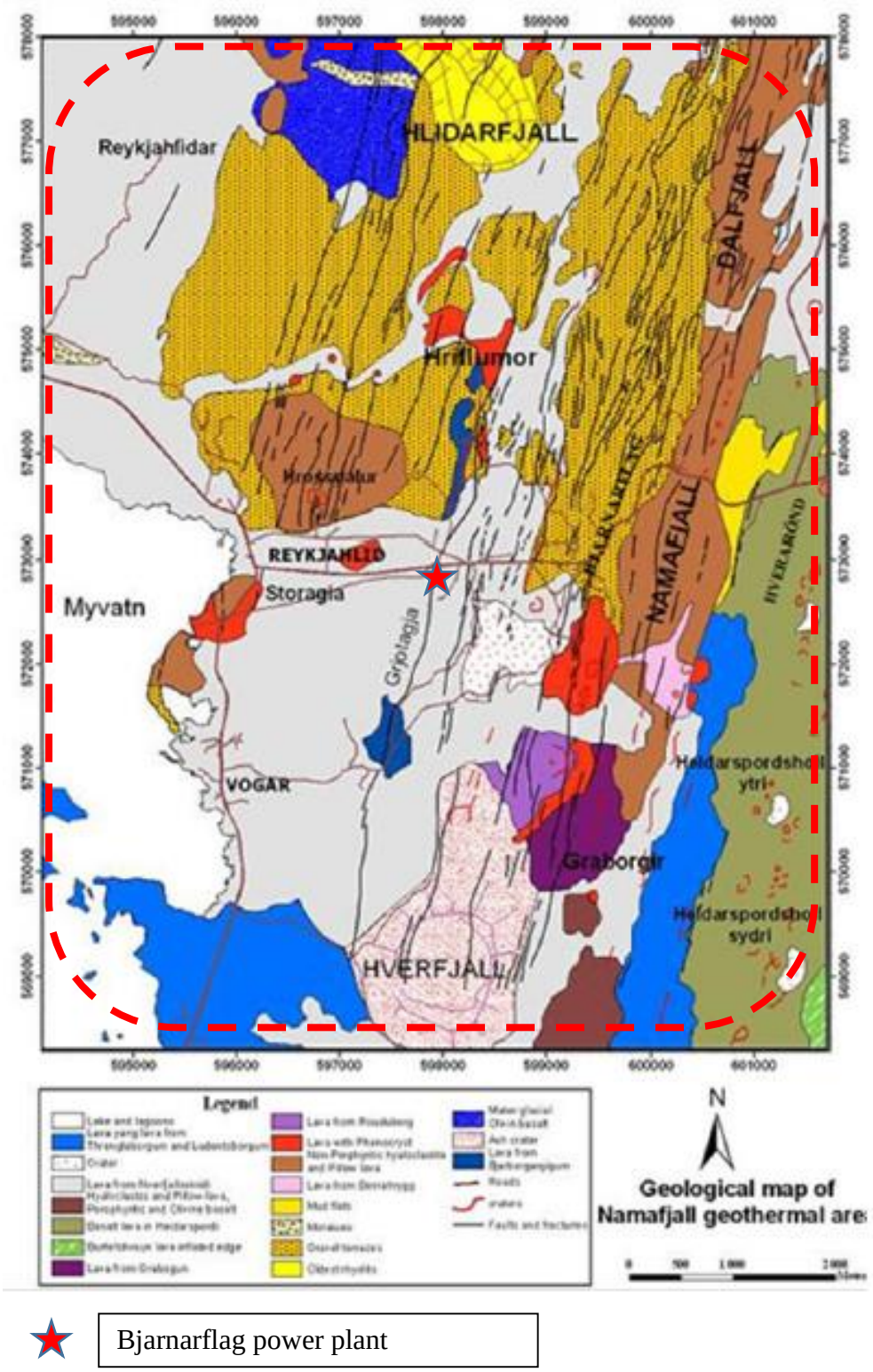

★ Bjarnarflag power plant

Figure 7.3 - Geological map of the Námafjall area. (from Sæmundsson, 1991).

The surface rocks in the study area are highly permeable. The postglacial lava flow acts as good aquifer. There are numerous open fissures and large active faults with a NNE/SSW strike, like Grjótagjá and Stóragjá (Ragnars et al. 1970) that add to the already permeable nature of the lavas. Figure 7.4 shows a possible groundwater flow model. There is a relation between the direction of the lava flows and the direction of groundwater flow probably caused by the fact that the fissures developed during the cooling of the lava, are mostly parallel to the direction of the lava flow.

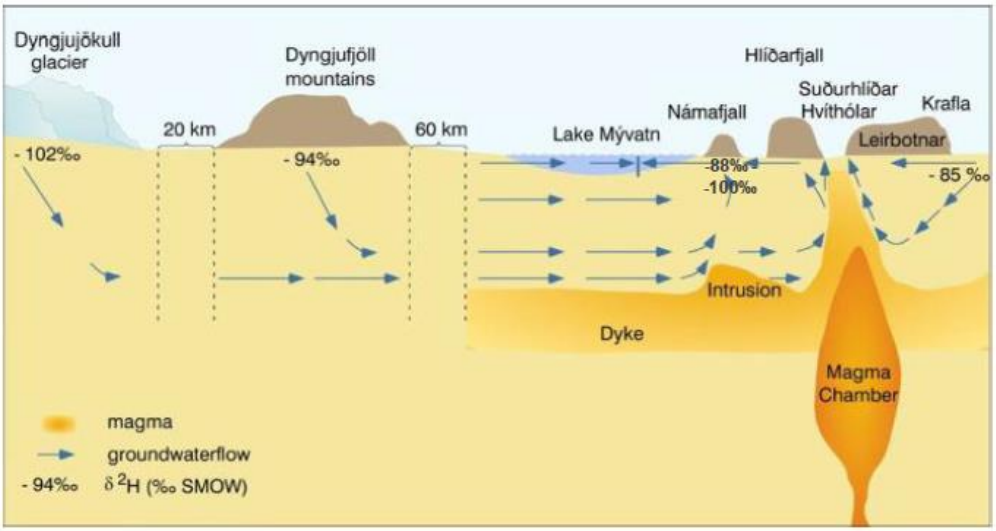

Figure 7.4 - Possible groundwater flow model to Námafjall and Krafla (Malimo, 2012).

7.2 Námafjall geothermal power plant project

The Námafjall project was launched in the early 50s for enhanced sulfur production. Shallow wells were drilled to increase the outflow of geothermal gas to the surface. The first geothermal research program in this area initiated in the 60s. Drilling continued in Námafjall

and Klafla. Volcanic activity then stopped the expansion and development of other areas. Directional drilling was adopted for the first time in Námafjall in 2006 and continued the following years. Figure 7.5 shows the location of the wells in the whole Bjarnarflag area, of which Námafjall is a subarea. Table 7.1 lists the wells in order of their completion time and reports also the damages that eventually occurred in some of these wells.

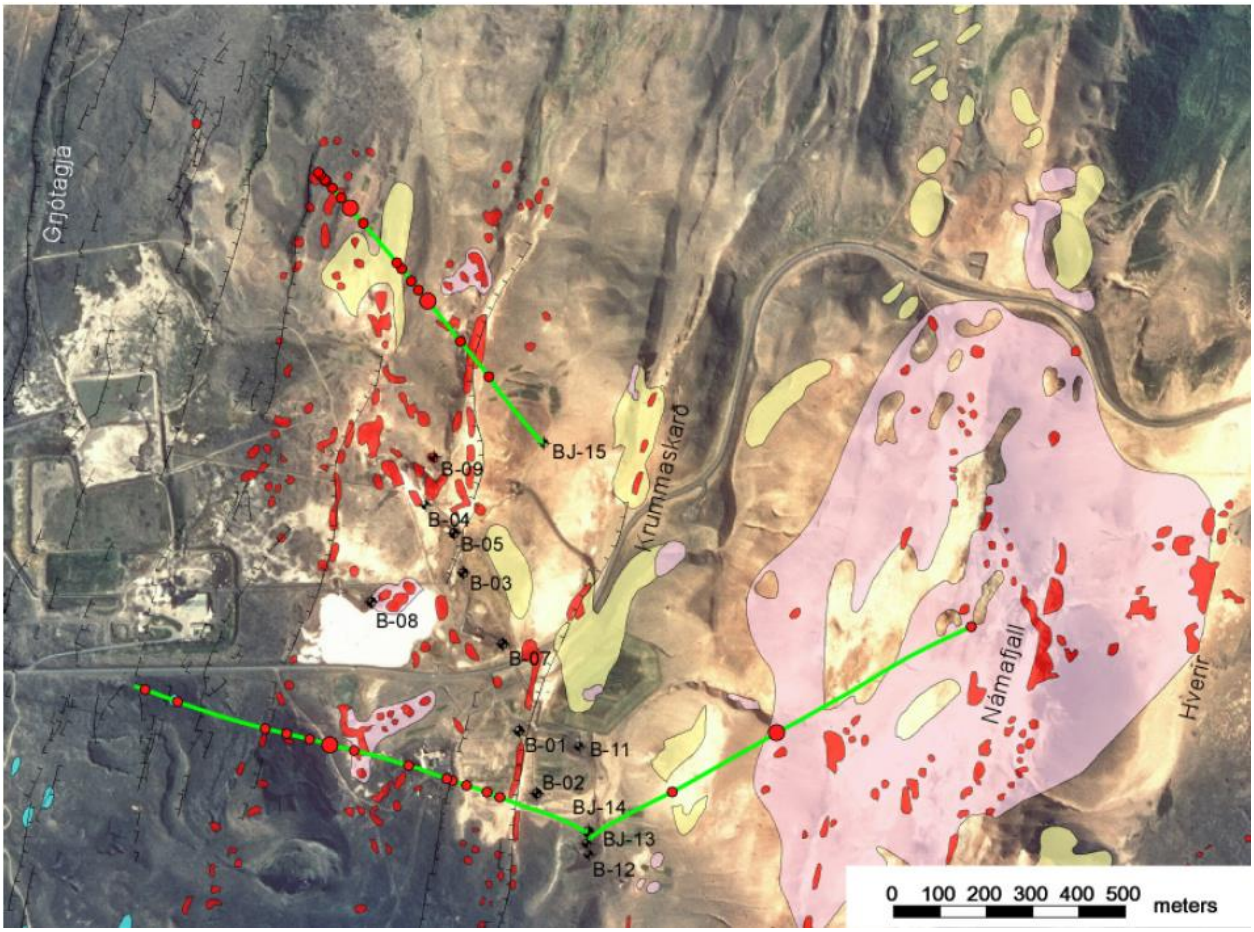

Figure 7.5 - Bjarnarflag – location of boreholes, well paths and feed zones (Gudmunddsson, 2010).

Table 7.7 - Boreholes in Bjarnarflag field (Gudmunddsson, 2010).

B-1	1963-1965	107	-	4 3/4	342*
B-2	1963-1965	207	-	4 3/4	492**
B-3	1966-1968	596	-	4 3/4	683
B-4	1968	625		6 ¼	630 (1138)***
B-5	1968-1969	478		8 3/4	638**
B-6	1969	577	550-953	6 ¼	1193*
B-7	1969	582		6 ¼	1206*
B-8	1970	537.5		6 ¼	1312*
B-9	1970	600	570-819****	6 ¼	843 (1311)
B-10	1975	598	558-1780	8 3/4	1809*
BJ-11	1979	619.6	604-1915	8 ½	1923
BJ-12	1980	686	631-1955	8 ½	1999
BJ-13	2006	851.7	816-2155	8 ½	2174 *****
BJ-14	2008	840.5	801.7-2479	8 ½	2506 *****
BJ-15	2008	846	806.9-2655.6	8 ½	2690 *****

*Collapsed 1977
**Monitoring well
***Lava intruded through the bottom aquifer
****Slotted linear 621-641 m
*****Directionally drilled

In 1969, Laxá Power Company built a geothermal power plant, and Landsvirkjun acquired Laxá Power Company and the power plant on 1983. Furthermore, the steam supply system at Bjarnarflag was bought by Landsvirkjun from the State Geothermal Services; this system provides steam to produce electricity, as well as supplying steam to a Diatomite Plant and the Mývatn district heating system. The size of the power plant is 3 MWe and the energy

generated by the Bjarnarflag station amounts to approximately 18 GWh per year. (Gudmunddsson, 2010). The location of the Bjarnarflag power plant is shown in Figure 7.3.

7.3 Inputs selected for the simulation in GEOFRAC

Deep drillings conducted in this area have provided important information on the sources and composition of geothermal fluids, thermal properties of the fluids, and the geology and fracture system of this geothermal area. Numerical models of the reservoir can help with the characterization and optimal use of the geothermal resources. In general, the parameters used in the application of GEOFRAC can be found from a preliminary survey and exploration: P_{32} can be obtained from fracture spacing information obtained in boreholes and on outcrops. Best estimate fracture size E(A) can be obtained from fracture trace lengths on outcrops with suitable bias corrections. Distribution and estimates of fracture size can also be obtained subjectively. The list of the inputs needed in GEOFRAC is shown in Figure 7.6.

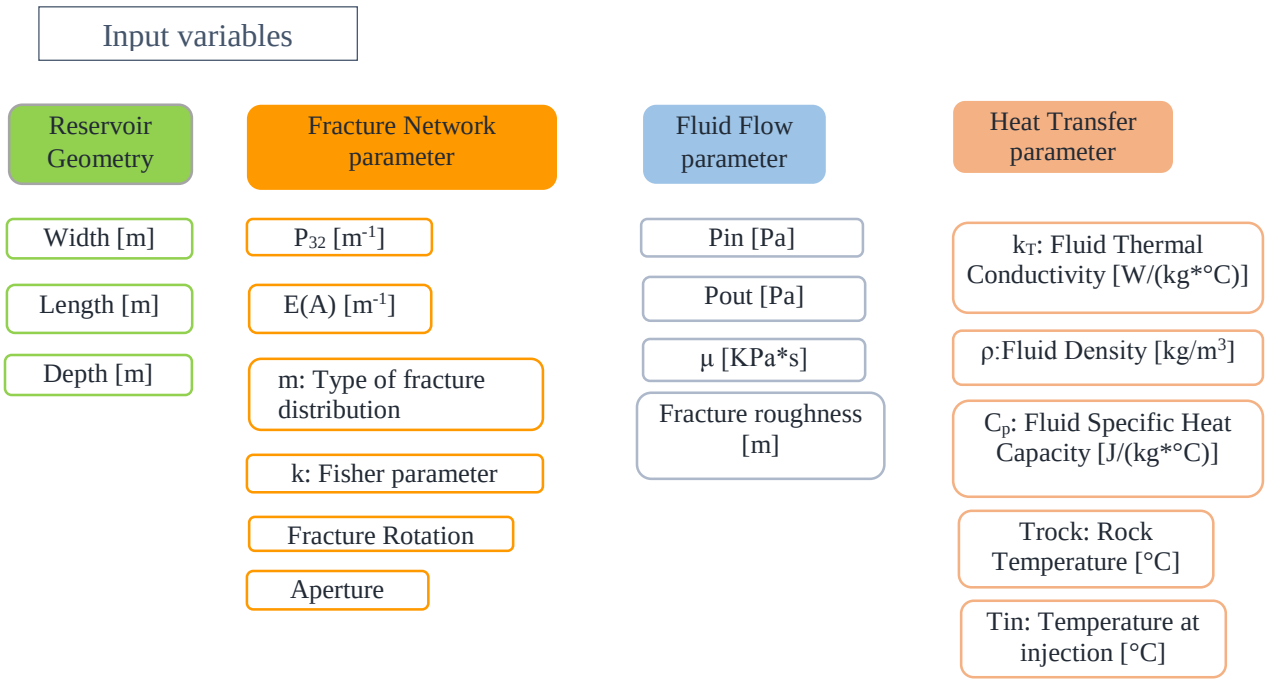

Figure 7.6 - Inputs for GEOFRAC

The inputs selected for the Námafjall simulation are reported and explained in the next sections. All the physical data described here were obtained from Rivera Ayala (2010), from boreholes and measurements given by Landsvirkjun, the Icelandic geothermal company, and from other references mentioned.

Reservoir geometry

The Namafjall geothermal field is a large reservoir formed by the Krafla caldera. It is about 10 km long and 5-8 km wide. The magma chamber is at a depth 3-7 km under the caldera. In our model the dimension X, Y, Z (Figure 7.7) express the size of the reservoir that we want to simulate. Z in particular refers to the injection depth. We conducted simulations on

the slice from 1000-2000m depth; this is in fact the fractured zone in this particular field (Isabirye, 1994). For our simulation we therefore assume:

X=1 km

Y= 2 km

Z= 1 km

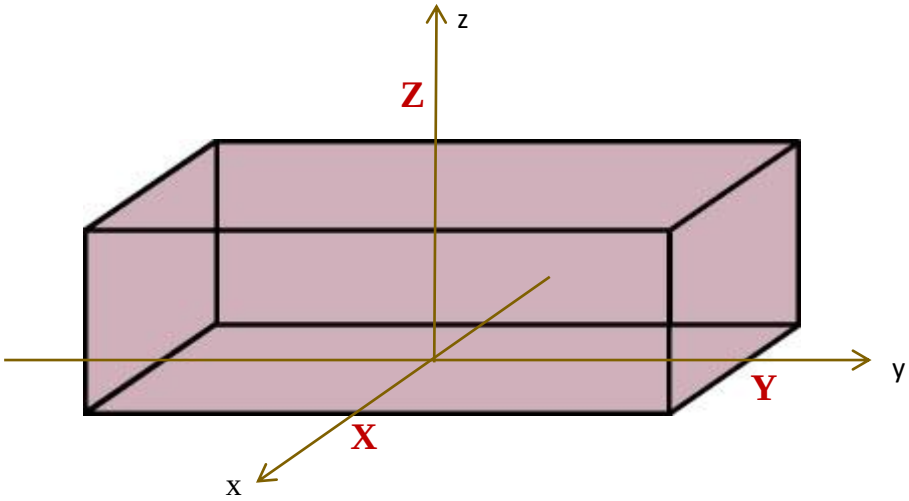

Figure 7.7- Coordinates of the controlled volume according to GEOFRAC

Fracture network parameters

In GEOFRAC fractures planes are generated in the volume V with a Poisson plane process of intensity μ where μ= P_{32}. P_{32} is given as sum of the areas of all fracture i ($A_{f,i}$) over the total modeled volume (Equation 7.1):

$$P_{32} = \frac{\sum_{i=1}^{N} A_{f,i}}{V} \qquad \textit{Equation 7.1}$$

The other fracture parameter E(A) is the mean area of fractures.

According to the geologic survey and boring logs, the hydrothermal reservoir is fractured by major fault related fissures and manifestations (Rivera Ayala, 2010). The boring data indicated very large spacings between the fractures. So a low value for P_{32} and high value for E(A) is chosen to simulate this geologic condition. The values are:

$P_{32} = 0.02\ m^{-1}$

$E(A) = 800000\ m^2$

The orientation of the planes generated with a stochastic process, can be specified with the Fisher distribution. Lower values of the Fisher parameter k indicates more randomly oriented planes; higher k indicates that the planes are mostly parallel to each other. From borehole data, the major planes in this area appear to be mostly parallel to each other; for this reason a k=20 was chosen for this simulation. The mean pole chosen of the major fractures is (π/2, 0), because the field data indicates that the fractures are mostly horizontal, as shown in Figure 7.8. These assumptions are made because, in general, it appears that the major permeable zones encountered by the Kafla wells are due to vertical fractures, that drive the flow into depth, and horizontal permeable zones between adjacent lava beds, as shown and explained in Figure 7.4.

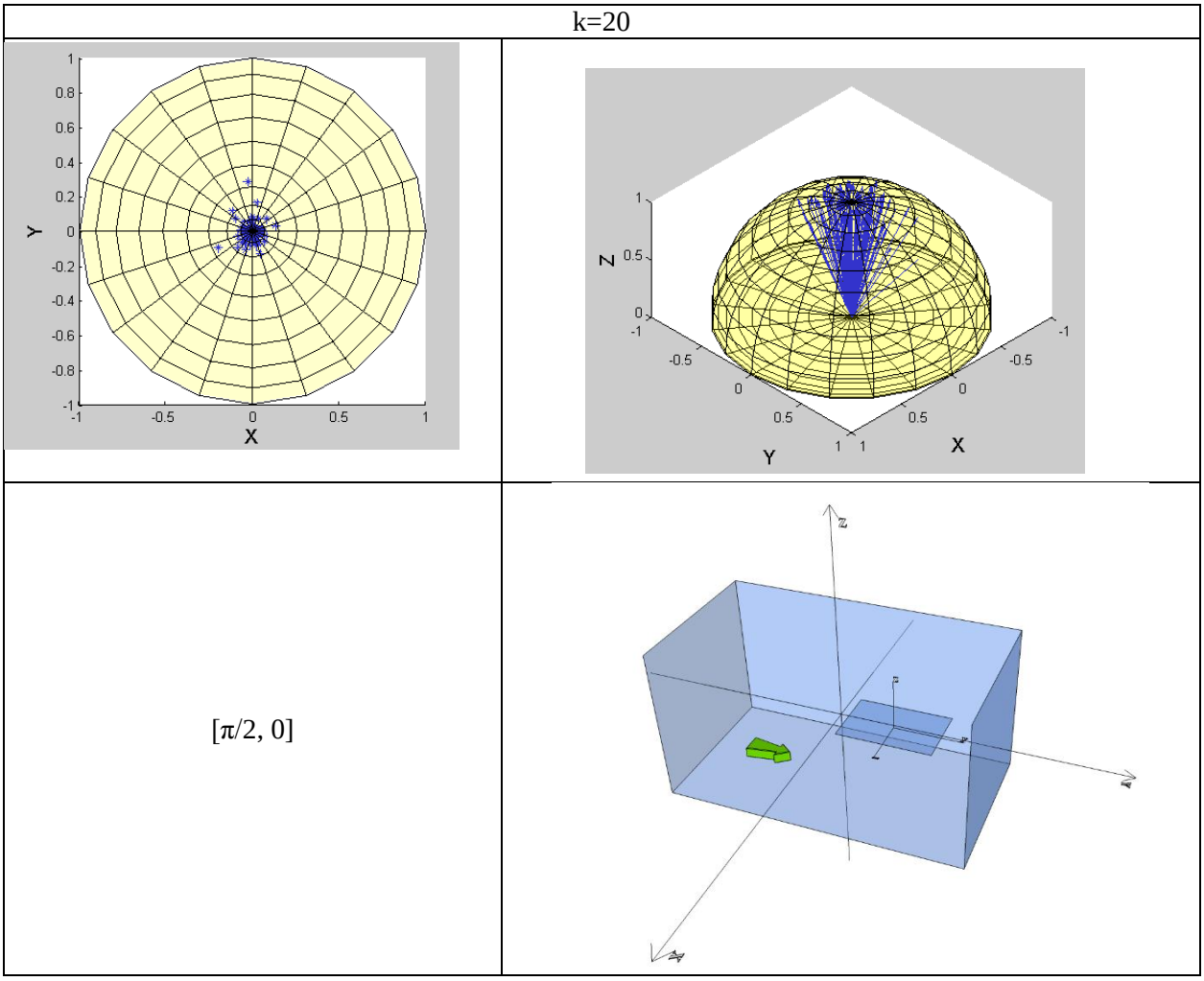

Figure 7.8 - Schematic representation of the mean orientation of the major fracture planes

Random translation and rotation (see Vecchiarelli, 2012) of the fractures (polygons) is performed to represent the local variation of fracture position and orientation of minor fractures. A new algorithm in GEOFRAC was added to the model to allow the user to model fractures with or without random rotation. Because the simulation presented here is concentrating on simulating the major planes, we assume that the fractures are all in the same plane and no rotation of the individual fractures is considered.

No data are available for the aperture of the fractures in this reservoir. GEOFRAC has three models available to be used in order to generate fracture aperture. For this case the probabilistic approach is used. According to the statistical study done by Dershowitz and Einstein, (1988), the apertures of fractures follow a truncated lognormal distribution:

$$f_{TR}(h) = \frac{f(h)}{\int_{\min}^{h_{\max}} f(h)d(h)}, h_{\min} \le h \le h_{\max} \qquad \textit{Equation 7.2}$$

Where h_{min} and h_{max} (in meters) are the minimum and the maximum aperture values. This relation is presented in Figure 7.9.

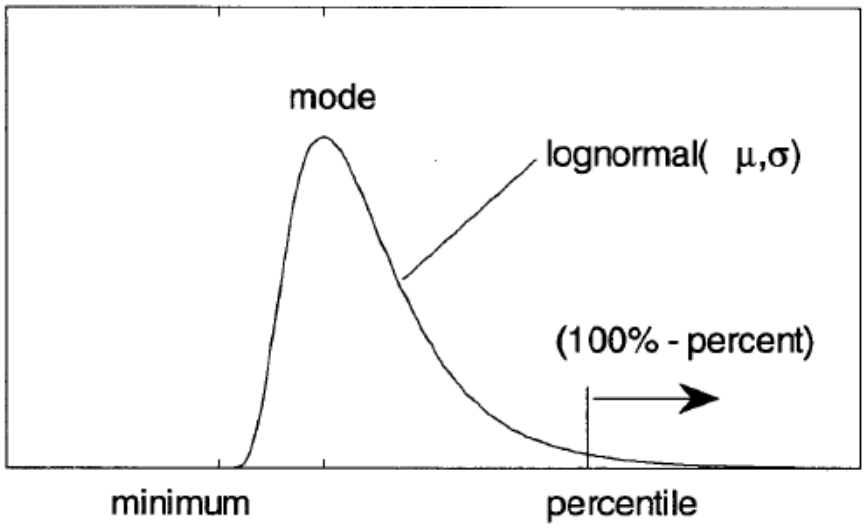

Figure 7.9 - Truncated lognormal distribution

For the simulation h_{min} = 0.00002 m, mode=0.004m and h_{max} = 0.01 m are used. The distribution of the apertures is shown in Figure 7.10.

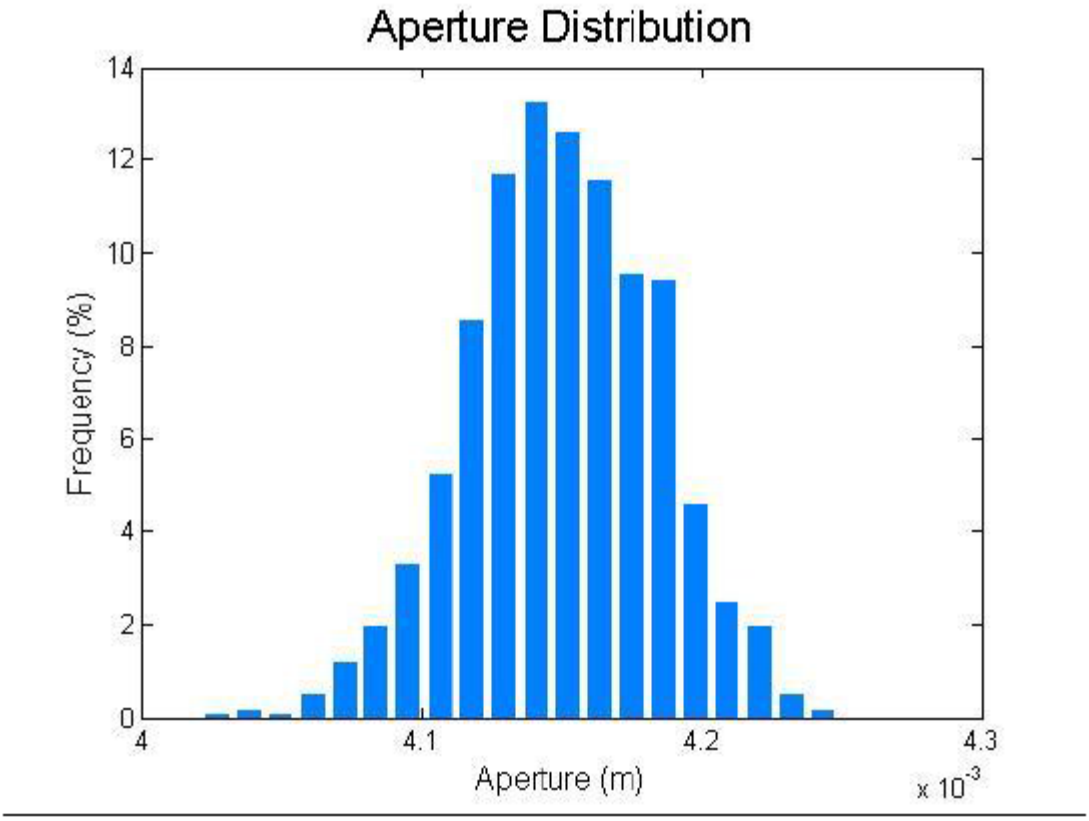

Figure 7.10 - Aperture distribution that follows a truncated lognormal distribution

Fluid flow parameters

The flow equations used to model the flow through the fractures are those for laminar flow between parallel plates (Equation 7.1).

$$q = \frac{wh^3 \Delta P}{12 \mu \Delta L} \qquad \textit{Equation 7.1}$$

Where:

q is the volumetric flow rate (m^3/sec) per unit width;

w is fracture width;

h is the aperture of the fracture in m;

μ is the fluid dynamic viscosity in Pa * s;

ΔP is the pore pressure change in Pa after the flow travels through distance ΔL.

The water flows only in the x direction between two parallel plates with the no-slip condition for viscous fluids forming the parabolic velocity profile in the y direction. The roughness of the fracture (as shown in Figure 7.11) considered in the simulation is ε = 0.4 m.

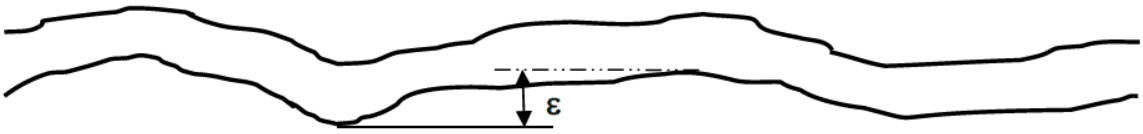

Figure 7.11 – Schematic representation of the roughness

The initial thermal condition of the water is assumed to be 60°C. So the value of the viscosity is $\mu=0.468\times10^{-3}$ Pa·s and the fluid density, ρ=983kg/m3.

Heat transfer parameters

Figure 7.12 shows selected temperature logs obtained in the well B-9 (see Figure 7.5 for location) in the period 1970 - 1993. In the first years, the logs near surface are influenced by cooling during drilling and thus do not show the real rock temperature. At 1300 m the

temperature was higher than 250 °C. Looking at all the temperature profiles the average temperature below 300 m is around 200-250 °C.

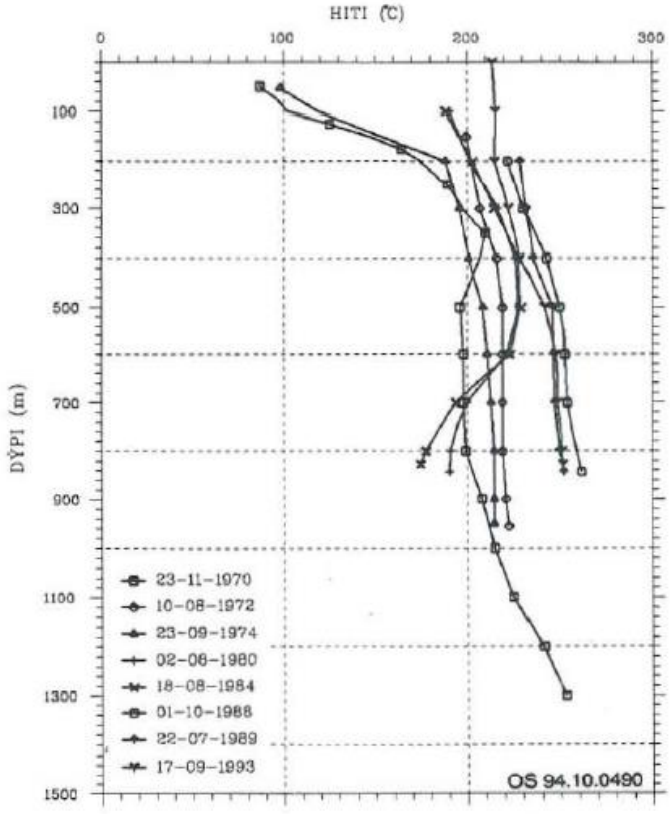

Figure 7.12 - Temperature measurements in well B-9, 1970-1993 (Isabirye, 1994)

In the area the majority of the wells predict temperatures of 240°C - 260°C (Rivera Ayala, 2010). For the simulation Trock= 250°C is used. The magma chamber is located below 3-7 km under the caldera, and it serves as a source of heat for the hydrothermal system; so the assumption of constant temperature of the surrounding rock is reasonable. In the simulation it is also assumed that at depth temperature of the geothermal fluid is equal to the rock temperature.

For a typical heat exchanger, the outlet temperature, which is also the temperature of the injected water, is around 60 °C, so the injection temperature is assumed to be 60 °C. The

thermal properties of the fluid at a small scale do not change much with temperature, so constant values are used:

Fluid Thermal Conductivity k_t=0.6546 w/(kg*°C)

Fluid Specific Heat Capacity, Cp = 4185 J/(kg*°C)

7.4 Results

Figure 7.13 is a schematic representation of the possible flow paths in one simulation. The purple numbers represent the temperatures (°C) in each branch while the blue numbers

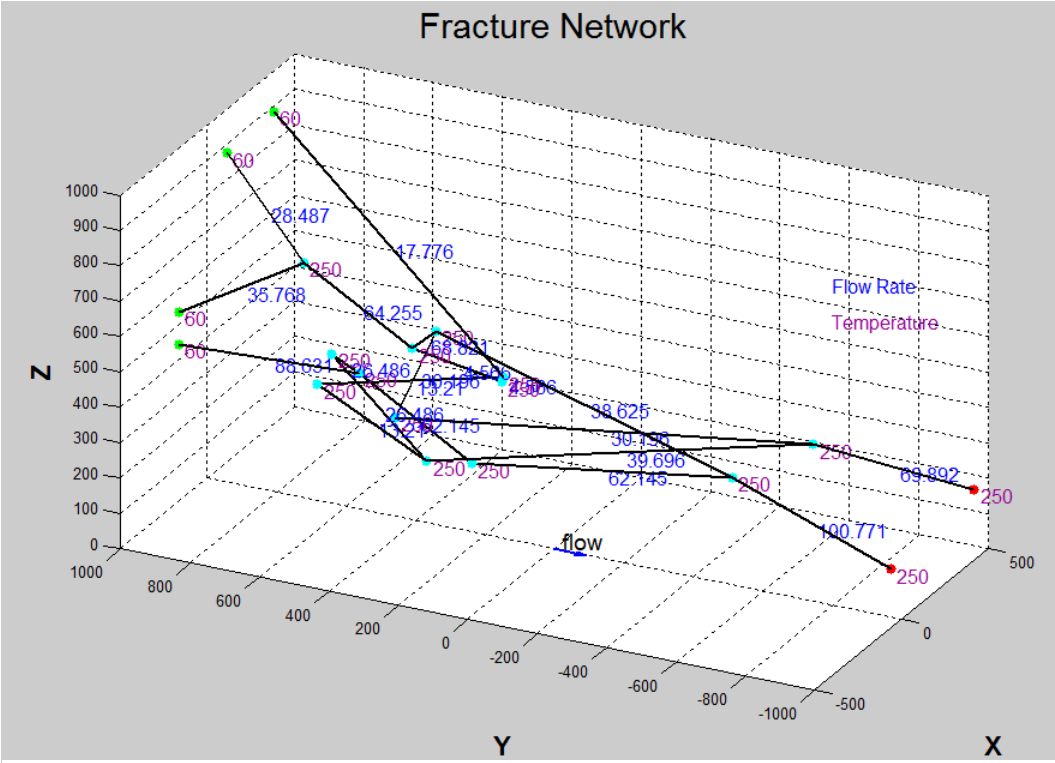

Figure 7.13 - Schematic representation of the fracture flow system obtained in one simulation

represent the flow rates (l/s). This figure shows that GEOFRAC, as a discrete fracture model, calculates the flow rates and temperatures explicitly.

Because of the stochastic processes used in GEOFRAC, the results are not deterministic. To draw reliable conclusions, a moderate number of simulations has to be run. Here, 20 simulations are run and analyzed as follows.

The average value of the total flow rates is 0.21 m3/s. This value is in line with the production flow this actual power plant is producing (ISOR, 2013). The Reynolds number of all the branches is checked to make sure that the assumption of laminar flow in the flow model is satisfied.

Because of the small apertures and large areas of the fractures, the heat transfer between the rock and the flow is very efficient. As we can see from Figure 7.12, the temperature of the water reaches that of the rock at the first node after the injection boundary. One has to keep in mind, however, that the thermal model in GEOFRAC assumes a constant rock temperature, so the results can only model the beginning stage of the injection. Still, the results indicate that the large area and small apertures of fractures are very helpful in extracting the heat from the underground.

The average energy extraction rate estimated by GEOFRAC is 116,224 KW; it is much higher than the capacity of the power plant, which is around 10 MW (Ragnars et al., 1970). This is quite understandable given that the energy conversion efficiency of a geothermal plant is often around 20%. In addition, the heat transfer model is based on the above mentioned assumption that the temperature of the rock is constant, but in reality, there is temperature drawdown in the rock. The heat extraction rate cannot be maintained for a long time. Although the results GEOFRAC overestimate the heat extraction rate, they provide the upper bound of the power. Future work on the thermal model is needed to produce a long term temperature prediction of the reservoir.

When the parameters used in GEOFRAC are varied, the changes in the results reflect the sensitivity of the model. We conducted such parametric studies (Vecchiarelli et al., 2012; Li et al. 2013) and these studies indicate that the fracture parameters such as fracture intensity, best estimate of fracture area, and orientation have a very large influence on the fracture network. The number of fractures, number of flow paths and their geometry are all dependent on these fracture parameters. Aperture plays a very important role in determining the flow rate and heat transfer mainly because the cube of the aperture appears in the governing equation. In other words the resulting flow rate is very sensitive to the aperture distribution. These parametric studies, therefore indicate that the choice of parameters has to be done extremely carefully.

The simulation of a real case with GEOFRAC, showed that this model can be used to represent a hydrothermal reservoir. When selecting the inputs in the model it is important to understand that the model is very sensitive to the aperture parameter as well as to the orientation of the fractures.

CHAPTER 8

CONCLUSIONS AND FUTURE WORK

8.1 Summary and conclusions

GEOFRAC is a discrete fracture pattern model, which combined with a fracture flow model can represent the fracture-flow system in a geothermal reservoir. Recent developments have made GEOFRAC more efficient by basing it on Matlab, and it has been expanded by including an intersection algorithm and a thermal-flow model.

In Chapter 2, models and software tools used to model fracture flow systems are presented. Each of them has some properties that make it difficult to model and to optimize a geothermal basin.

Chapter 3 describes the algorithm and the basic concept of GEOFRAC.

In Chapter 4 the results obtained from a parametric study with the fracture flow model GEOFRAC are analyzed and discussed. Specifically, the influence of fracture aperture and orientation on flow was investigated. The parametric study demonstrates how aperture, the Fisher parameter for fracture orientation and rotation of the individual fractures influence flow rate. As to be expected greater apertures produce greater flow. The effects of orientation are more complex as the effect of fracture plane orientation (Fisher parameter) and of rotation of individual fractures interact. For planes randomly generated the case with no rotation of the fractures and an aperture of 0.01 m

generates greater flow than with rotation, while for parallel planes greater flow occurs in the case of rotation of the fracture and aperture of 0.01 m. This study of a simple synthetic case shows that the model produces consistent results but also that there are some unexpected complexities affected by fracture orientation.

Chapter 5 presents the extension of GEOFRAC with an algorithm that allows the modeling of wells intersecting the fractured region.

In Chapter 6 a GUI that was created in order to simplify the work to the user is presented.

In Chapter 7 the analysis of a case study shows that GEOFRAC produces reasonably close results to the real geothermal conditions. The estimation of important factors such as flow rate and energy extraction rate are reasonably close to reality. However, GEOFRAC has still limitations that need to be further examined and that are described in the next section.

Another goal of this research was to understand the uncertainty of field predictions and to detect possible limitations and necessary improvements of GEOFRAC. The main limitation in the modelling effort was the lack of data regarding fracture intensity P32 and best estimate fracture area EA. Restrictive assumptions in the present GEOFRAC are the homogeneity of the parameters for the entire reservoir and the assumption of a single phase fluid.

In conclusion, GEOFRAC seems to accurately model the fracture flow system in a geothermal reservoir. The values of flow rates obtained in the parametric study are reasonably comparable to the ones found in the literature. The well intersection algorithm adds the possibility to properly include injection and production wells. (This feature can eventually be used to improve the location of the wells in order to obtain higher flow from the wells). The GUI presented in this report will allow any user to easily apply GEOFRAC.

8.2 Future research

Further improvements of GEOFRAC are possible:

- Implementation of an algorithm to obtain the optimum position of the injection and production wells. The borehole intersection algorithm presented in Chapter 5 can be used to evaluate the fractures that intersect the wells for a given position. One of the most important improvements in the code would be to implement an algorithm to select the optimum position of the borehole after the fracture flow system is generated; the optimization should be done considering the most fractured area, and the fracture zone with the greatest apertures. This will increase the flow rate in the production well and may reduce the cost associated with exploration and construction of the wells.
- Analysis of the change in porosity and permeability due to the cold fluid injection. The initial injection of water at 20° C may create a state of stress in the rock that induces more fractures in the system or, conversely, close some fractures.
- Fluid physical conditions (change of density, change of liquid phase to vapor). The assumption made up to now is a single phase fluid in its liquid state.
- Analysis of the temperature of the basin over a long period. Some studies show a reduction of the temperature over the long term. It would be useful to analyze this phenomenon and, if necessary, create an algorithm that will simulate the flow rate and temperature over time, and simulate this decrease in temperature.
- Geochemistry and reactive transport model.
- Matrix domain model (Double porosity model). Fluid flow through a geothermal system is dominated by flow through the fractures while heat transfer is controlled by the interaction

between the matrix and fracture. The amount of flow from the matrix to the fracture affects heat transfer.

- Improve the results section of the GUI. Create a sub-GUI that allows the users to decide which results and charts should be shown.

REFERENCE

Apuani T., Corazzato C., Cancelli A., Tibaldi A. (2005). Stability of a collapsing volcano (Stromboli, Italy): Limit equilibrium analysis and numerical modeling, *Journal of Volcanology and Geothermal Research 144 (2005) 191– 210.*

Clearwater J., Burnell J., Azwar L. (2012). Modelling the Ngatamariki geothermal system. *Proceeding, Thirty-Seventh Workshop on Geothermal Reservoir Engineering, Stanford University, Stanford, California, January 30 – February 1, 2012.*

Coates R. T. and Schoenberg M. (1995). Finite-difference modeling of faults and fractures, *Geophysics, VOL. 60, NO. 5 (September-October 1995); P. 1514-1526, 11 FIGS*

Deng S., Podgorney R., Huang H. (2011). Discrete Element Modeling of Rock Deformation, Fracture Network Development and Permeability Evolution Under Hydraulic Stimulation, *PROCEEDINGS, Thirty-Sixth Workshop on Geothermal Reservoir Engineering Stanford University, Stanford, California, January 31 - February 2, 2011*

Dershowitz W. S. and Einstein H.H (1988). Characterizing rock joint geometry with joint system models, *Rock Mechanics and Rock Engineering 21, 21-51 (1988).*

Dershowitz W. S. and Herda (1992). Interpretation of fracture spacing and intensity, Rock Mechanics, Tillerson & Wawersik (eds), 1992 Balkema, Rotterdam.

Dershowitz, W.S. (2006). Hybrid Discrete Fracture Network and Equivalent Continuum Model for Shaft Sinking, *ARMA/USRMS 06-1029*

Diodato D.M. (1994). A Compendium of Fracture Flow Models *Work sponsored by U.S. Department of Defense, United States Army, Europe, Combat Maneuver Training Center, Hohenfels, Germany 1994.*

Einstein H.H. and Locsin J.Z. (2012). Modeling Rock Fracture Intersections and application to the Boston area, *Journal of geotechnical and geoenvironmental engineering, ASCE, November 2012.*

Gudmundsson Á., Mortensen A. K, Hjartarson A., Karlsdóttir R. and Ármannsson H. (2010). Exploration and utilization of the Námafjall high temperature area in n-iceland. *Proceedings World Geothermal Congress 2010 Bali, Indonesia, 25-29 April 2010.*

Hatton C. G., Main I. G., Meredith P. G. (1994). Non-universal scaling of fracture length and opening displacement, *Nature, Vol. 367, 13 January 1994.*

Hicks T. W., Pine R. J., Willis-Richards J., Xu S., Jupe A. J., Rodrigues N. E. V. (1996). A Hydro-thermo-mechanical Numerical Model for HDR Geothermal Reservoir Evaluation, *Int. J. Rock Mech. Min. Sci. & Geomech. Abstr. Vol. 33, No. 5, pp. 499-511, 1996*

Hong Shen, Herbert Klapperich, Syed Muntazir Abbas, Abdelazim Ibrahim (2012). Slope stability analysis based on the integration of GIS and numerical simulation, *Automation in Construction 26 (2012) 46–53.*

Illman W. A., Hughson D. L. (2005). Stochastic simulations of steady state unsaturated flow in a three-layer, heterogeneous, dual continuum model of fractured rock, *Journal of Hydrology 307 (2005) 17–37*

Isabirye E. (1994). Borehole geology and hydrothermal alteration in well B-9, Namafjall geothermal field, NE-Iceland. *Geothermal training programme Orkustofnun, Grensasvegur 9, Reykjavik, Iceland, Reports 1994 Numbers 5.*

Ivanova V. (1995). Three-dimensional stochastic modeling of rock fracture systems, *Master thesis.*

Ivanova V., Sousa R., Murrihy B., Einstein H.H. (2012). Mathematical algorithm development and parametric studies with the GEOFRAC three-dimensional stochastic model of natural rock fracture systems.

Jing L. (2003). A review of techniques, advances and outstanding issues in numerical modelling for rock mechanics and rock engineering, *International Journal of Rock Mechanics & Mining Sciences 40 (2003) 283–353.*

Johnston J. D. and McCaffrey K. L. W. (1995). Fractal geometry of vein systems and the variation of scaling relationship with mechanism, *Journal of Structural Geology, Vol. 18, Nos 2/3, pp. 349 to 358, 1996.*

Li W., Yost K., Sousa R. (2013). Heat transfer between fluid flow and fractured rocks. *GRC annual meeting, 2013*

Malimo S. J. (2012). Aquifer fluid modeling and assessment of mineral-gas-liquid equilibria in the Námafjall geothermal system, NE-Iceland. *Thesis.*

Mancktelow, N.S., (1999). Finite-element modelling of single-layer folding in elasto-viscous materials: the effect of initial perturbation geometry. *Journal of Structural Geology 21, 161±177.*

Newson J., Mannington W., Sepulveda1 F., Lane R., Pascoe R., Clearwater E., O'Sullivan M. J. (2012). Application of 3d modelling and visualization software to reservoir simulation: Leapfrog geothermal and Tough2. *Proceeding, Thirty-Seventh Workshop on Geothermal Reservoir Engineering,* Stanford University, Stanford, California, January 30 – February 1, 2012.

Ólafsson M., Ármannsson H. (2013). The Námafjall high temperature system, NE Iceland; chemical characteristics of the fluid for a power plant. *Procedia Earth and Planetary Science 7 (2013) 640 – 643.*

Podgorney R., Huang H., Gaston D. (2010). Massively parallel fully coupled implicit modeling of coupled thermal-hydrological-mechanical processes for enhanced geothermal system reservoirs. *Proceeding, Thirty-Firth Workshop on Geothermal Reservoir Engineering,* Stanford University, Stanford, California, February 1-3, 2010.

Podgorney R., Lu C., Huang H. (2012). Thermo-hydro-mechanical modeling of working fluid injection and thermal energy extraction in EGS fractures and rock matrix. *Proceeding, Thirty-Seventh Workshop on Geothermal Reservoir Engineering,* Stanford University, Stanford, California, January 30 – February 1, 2012.

Ragnars K., Saemundsson K., Benediktsson S. and Einarsson S. S. (1970). Development of the Namafjall area. Northern Iceland. *U. N. Symposium on the Development and Utilization of Geothermal Resources, Pisa 1970. Vol. 2 Part 1.*

Reichenberger V., Jakobs H., Bastian P., Helmig R. (2005). A mixed-dimensional finite volume method for two-phase flow in fractured porous media, *Advances in Water Resources 29 (2006) 1020–1036.*

Rivera Ayala M. A. (2010). Coupled geothermal reservoir-wellbore simulation with a case study for the Namafjall field, N-Iceland. *Geothermal Training Programme Report 2, December 2010*

Sousa, R. (2013). Three-Dimensional discrete fracture flow model. *Research report, Massachusetts Institute of Technology, Cambridge, MA (draft).*

Staub I. (2002). Models for the geometry of fractures, *Golden Associates AB report, May 2002.*

Stone D. (1984). Sub-surface fracture maps predicted from the Eye-Dashwa Pluton, Atikokan, Canada, *Int. J. Rock Mech. Min. Sci. & Geomech. Abstr. Vol. 21, No. 4, pp. 183-194, 1984.*

Tezuka K. and Watanabe K. (2000). Fracture network modeling of Hijiori hot dry rock reservoir by deterministic and stochastic crack network simulator (D/SC), *Proceedings World Geothermal Congress 2000 Kyushu - Tohoku, Japan, May 28 - June 10, 2000.*

Vecchiarelli, A., Sousa, R., and Einstein, H. H. (2013). Parametric study with GEOFRAC: A Three-dimensional Stochastic fracture flow model. *Proceedings: 38th Geothermal Reservoir Engineering.*

Veneziano D. (1978). Probabilistic model of joints in rock, *Research Report, Dept. of Civil Engineering, June 1978.*

Vermilye J. M. and C. H. Scholz (1995). Relation between vein length and aperture, *Journal of Structural Geology, Vol. 17, No. 3, pp. 423-434, 1995.*

Watanabe K. and Takahashi H. (1995). Fractal geometry characterization of geothermal reservoir fracture networks, *Journal of Geophysical research, Vol. 100, B1, pages 521-528, January 10, 1995.*

Willis-Richards J. and Wallroth T. **(1995)**. Approaches to the modelling of hdr reservoirs: a review, *Geothermics Vol. 24, No. 3, pp. 307-332, 1995.*

Zhang L. and Einstein H.H. (2000). Estimating the intensity of rock discontinuities, *International Journal of Rock Mechanics and Mining Sciences 37 (2000) 819-837.*

Zhang Y., Mancktelow N.S., Hobbs B.E., Ord A., Muhlhaus H.B. (2000). Numerical modeling of single-layer folding: clarification of an issue regarding the effect of computer codes and the influence of initial irregularities, *Journal of Structural Geology, v. 22, p. 1511–1522.*

Zhang, Y., Hobbs, B.E., Ord, A., Muhlhaus, H.B., (1996). Computer simulation of single-layer buckling, *Journal of Structural Geology 18, 643±655.*

RECOVERY ACT – DECISION AIDS FOR GEOTHERMAL SYSTEMS

PROJECT ID: DE-EE0002743

Final Report

Numerical and Analytical Modeling of Heat Transfer between Fluid and Fractured Rocks

---

Wei Li

Herbert Einstein

Massachusetts Institute of Technology

May 2014

Numerical and Analytical Modeling of Heat Transfer between Fluid and Fractured Rocks

Executive Summary

This final report in the context of the research project, "Recovery Act – Decision Aids for Geothermal Systems", puts everything together in the form of an integrated "fracture pattern-fracture flow-fracture heat transfer" model, which is then applied to and checked against a case. The basis for all this is the discrete fracture network model, GEOFRAC, that has been substantially extended and made more user friendly as described in the report, "Further Development and Application of GEOFRAC-FLOW to Geothermal Reservoirs".

This report, " Numerical and Analytical Modeling of Heat Transfer between Fluid and Fractured Rocks", first reviews (Chapters 1, 2) the basic processes in heat transfer (conduction, convection, radiation) and how they are analytically expressed. Fluid flow in porous media and fractures is also briefly reviewed. This forms the basis for a review of heat transfer between a fluid and the rock mass in which both analytical and numerical models are commented upon, and this for continuum-, discrete- and hybrid models.

In Chapter 3 the discrete fracture network model, GEOFRAC, and the fracture fluid model, GEOFRAC-FLOW are used to develop GEOFRAC-THERMAL. (Note that GEOFRAC-FLOW was also developed in the context of this research and was reported in the report, "Decision Aids for Geothermal Systems – Fracture Flow Modeling"). An extensive parametric study was then conducted with GEOFRAC-THERMAL in which the effect of geometric-, flow- and heat characteristics were investigated. Most importantly, the model was then applied to the Fenton Hill case, and the model results showed good coincidence with the measured values in the initial operating phase. However, at this stage of the research it was not possible to model temperature drawdown in the rock.

As a consequence, additional work on drawdown (coupled) models was done. The first (0-d or lumped thermal capacity) model assumes uniform temperature distribution in the rock; for this, an analytical solution was formulated and successfully compared to the Fenton Hill case now properly considering rock temperature drawdown. In the next step a simplified coupled 1-D solution (only

transverse heat conduction in the rock, neglected fluid velocity profile and fluid heat conduction) was developed. This was satisfactorily compared to a numerical solution.

To conclude, one can state, that with GEOFRAC-THERMAL combined with the simple thermal drawdown analysis, one can produce practically useful results. This has been shown through the application to a real case. Nevertheless, more work in the direction of a more sophisticated thermal drawdown models is desirable.

Table of Contents

List of Figures

List of Tables

1. Introduction

1.1. Context

With the expected depletion of available fossil fuels in the foreseeable future, alternative energy resources have been intensively investigated to ensure the security of energy supply for the long term. Geothermal energy, as a renewable energy option, has provided some base-load electricity around the world for more than a century. Conventional geothermal resources are limited in their location and ultimate potential for supplying electricity. Beyond these conventional resources are Enhanced (Engineered) Geothermal Systems (EGS, also termed as Hot Dry Rock system, HDR) with an enormous potential for primary energy extraction using heat-mining technology, which is designed to extract and utilize the earth's stored thermal energy.

Modeling of heat transfer between fluid and fractured rocks is of particular importance for energy extraction analysis in EGS, and therefore represents a critical component of EGS design and performance evaluation. In conventional fracture dominated geothermal systems with reinjection, this modeling process is also helpful for understanding how the thermal front migrates and optimizing of reservoir management strategies.

In order to improve the energy productivity but also the performance of the geothermal systems, a better understanding of the heat transfer between fluid and fractured rocks is important.

1.2. Research Objectives

The purpose of this research is to develop a model which predicts the temperature profile of both the water and the rock, so that better decisions can be made regarding the geothermal system, when information on the underground conditions are limited.

The challenge of modeling this heat transfer process comes from the complex geometry of the rock fracture networks, variation of rock and fluid properties, and uncertainty of these underground conditions. Also, the large scale and long time period that need to be modeled require intensive computational efforts.

To achieve the research objectives, both numerical and analytical approaches are utilized in the modeling of heat transfer between fluid flow and fractured rocks. In the numerical approach,

GEOFRAC, a 3-D geology-based stochastic Discrete Fracture Network (DFN) model, is used to simulate the fracture networks in the geothermal reservoirs. GEOFRAC-FLOW, a flow model based on GEOFRAC, is used to explicitly calculate the flow rate in each fracture. On the basis of the two, a heat transfer model GEOFRAC-THERMAL is developed to calculate the temperature of water at each node in the network. Comprehensive parametric studies with the three models are conducted to demonstrate the capabilities of the models. A thermal drawdown model based on the result of GEOFRAC-THERMAL is proposed and studied.

In the analytical approach, governing equations are formulated and solved for the temperature profile of the fluid and the rock. Influence of the factors in the governing equations are analyzed for the case of water and granite. Solutions with necessary simplifications, for example the 0-D and 1-D solutions, are presented.

A case with fluid flow and fractured rocks in a simple geometric configuration is constructed to compare the fluid temperature calculation between the numerical and analytical approaches.

2. Background

The process of heat transfer between fluid flow and fractured rocks is complex. This chapter provides an overview of the basic heat transfer mechanisms. First, a discussion is given of the fundamental concepts and equations used to describe heat and mass transfer, with a particular focus on geothermal systems. Next, a brief summary is given of previous numerical modelling efforts focused on heat transfer in fractured media. Finally, a literature review of analytical modelling efforts is presented.

2.1.Heat Transfer

There are three distinct modes of heat transfer to consider in any thermal model: conduction (the transfer of energy through the interaction of molecules), convection (heat transfer due to the movement of molecules within a fluid), and radiation (energy transfer through some sort of wave phenomenon, most typically electromagnetic waves).

2.1.1. Conduction

The transfer of heat by conduction is perhaps the simplest and most direct form of heat transfer. Conductive heat transfer occurs at the molecular scale, by means of collisions and interactions between molecules at different energy states. In nonmetallic solids these interactions typically take the form of lattice vibrational waves. Heat may also be conducted by the movement of free electrons, this behavior being characteristic of metals (Incropera & DeWitt, 2002). Rigorous quantitative studies of heat conduction began with Joseph Fourier's 1822 publication of The Analytical Theory of Heat (Fourier, 1955). In this work Fourier presented the basic law concerning the rate of heat movement at a steady state, now known as Fourier's Law of heat conduction:

$$q_{hx} = -k_x \frac{dT}{dx} \tag{2.1}$$

where:

q_{hx} is the heat flux in the x direction;

$\frac{dT}{dx}$ is the temperature gradient in the x direction;

k_x is the thermal conductivity in the x direction.

k is a physical constant whose value depends upon the material. A highly conductive material, like copper, may have a k value of 386 W/(m·K), while an insulating material, like cork, has a value of around 0.04 W/(m·K) –a ten-thousand fold difference. Solids tend to have much higher *k* values than liquids because the molecules of solids are more tightly bonded than those of liquids. Like the specific heat capacity, thermal conductivity is often assumed to be a constant, though in many cases it exhibits a dependence on temperature.

A general heat conduction equation to describe the transient heat conduction can be constructed by using the energy conservation principle and Fourier's law of heat conduction on an infinitesimal control volume, as shown in Figure 2.1.

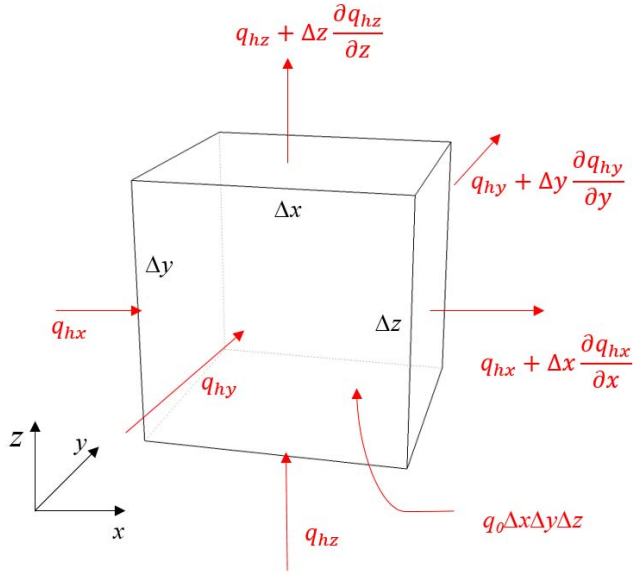

Figure 2.1 Energy Conservation in the Infinitesimal Control Volume

The energy conservation principle leads to Equation 2.2:

$$-\left(\frac{\partial q_{hx}}{\partial x} + \frac{\partial q_{hy}}{\partial y} + \frac{\partial q_{hz}}{\partial z}\right) + q_0 = \rho C_p \frac{\partial T}{\partial t} \tag{2.2}$$

Equation 2.2 can also be rewritten into a more compact form:

$$-\nabla \cdot \boldsymbol{q_h} + q_0 = \rho C_p \frac{\partial T}{\partial t} \tag{2.3}$$

where:

q_{hi} represents the heat flux in the i direction;

$\boldsymbol{q_h}$ is the heat flux tensor;

q_0 represents the internal energy generation, such as radioactive decay;

ρ is the density;

C_p is the specific heat capacity.

By applying Fourier's law of heat conduction, Equation 2.3 can be rewritten as:

$$\frac{\partial}{\partial x}\left(k_x \frac{\partial T}{\partial x}\right) + \frac{\partial}{\partial y}\left(k_y \frac{\partial T}{\partial y}\right) + \frac{\partial}{\partial z}\left(k_z \frac{\partial T}{\partial z}\right) + q_0 = \rho C_p \frac{\partial T}{\partial t} \tag{2.4}$$

In more compacted form:

$$\nabla \cdot (k \nabla T) + q_0 = \rho C_p \frac{\partial T}{\partial t} \tag{2.5}$$

If the medium is isotropic and homogeneous, having a spatially constant value of thermal conductivity, then the equation may be further simplified:

$$\frac{\partial^2 T}{\partial x^2} + \frac{\partial^2 T}{\partial y^2} + \frac{\partial^2 T}{\partial z^2} + \frac{q_0}{k} = \frac{\rho C_p}{k}\frac{\partial T}{\partial t} = \frac{1}{\alpha}\frac{\partial T}{\partial t} \tag{2.6}$$

where α represents the thermal diffusivity, the ratio of thermal conductivity to volumetric heat capacity:

$$\alpha = \frac{k}{\rho C_p} \tag{2.7}$$

2.1.2. Convection

Strictly speaking, convection is the transport of energy by motion of a medium. In convection, heat transfer is a two-step process involving a moving fluid in contact with a solid at some interface between them. The first step is an exchange of heat between the solid and fluid at their interface, and the motion of the affected fluid molecules from the interface. The second step is conduction, both within the solid, as well as between the displaced fluid molecules and the remainder of the

fluid (Mills, 1999). As shown in Figure 2.2, the heat is conducted from the bottom solid to the fluid, the hot fluid brings the heat to the cold fluid so that heat is transferred.

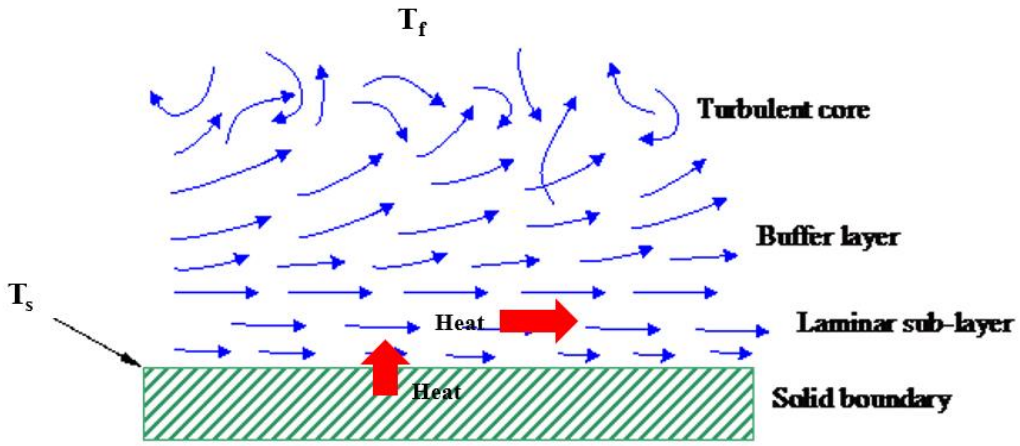

Figure 2.2 An Example of Heat Convection

The convective heat flux is directly proportional to the mechanical mass flux of the fluid. When a fluid moves with a constant mass flux, the effects of forced convection can be modelled by the addition of this convective flux into the energy conservation Equation 2.3. As shown in Figure 2.3 colored in blue, the mass flow q_{mi} in the i direction brings the convective flux $q_{mi}C_pT$ to the infinitesimal control volume, the divergence $\nabla \cdot (\boldsymbol{q_m} C_p T)$ of this convective flux is the energy taken away by this flux.

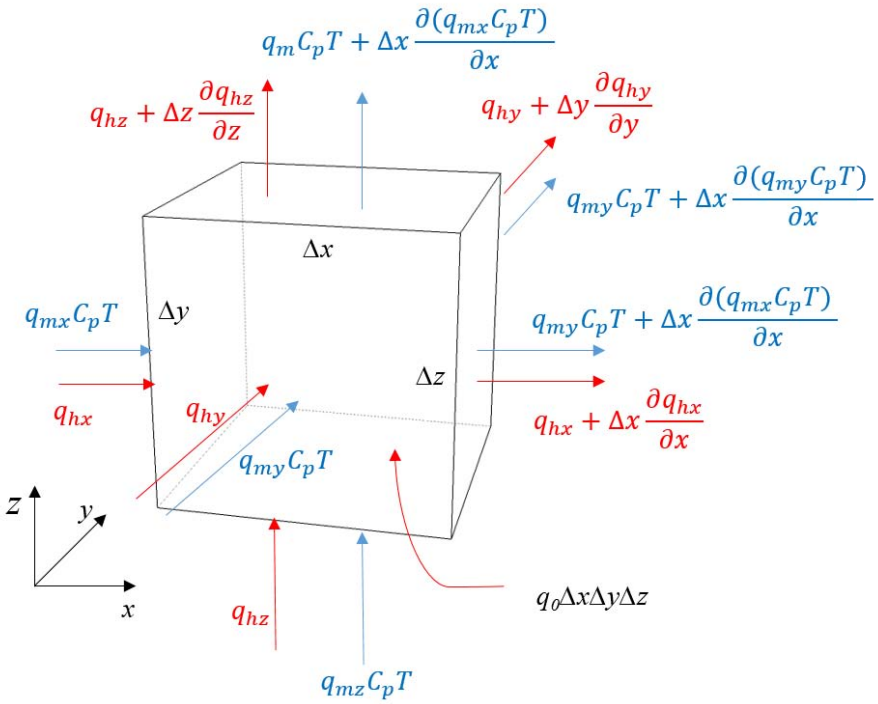

Figure 2.3 Energy Conservation in the Infinitesimal Control Volume

$$\nabla \cdot (k\nabla T) - \nabla \cdot \left(\boldsymbol{q_m} C_p T\right) + q_0 = \rho C_p \frac{\partial T}{\partial t} \quad (2.8)$$

Where:

$\boldsymbol{q_m}$ is the mass flux of the fluid;

$\boldsymbol{q_m} C_p T$ is the convective heat flux.

The rate of heat transfer by convection is usually a complicated function of surface geometry and temperature, the fluid temperature and velocity, and fluid thermal properties. In an external forced flow, the rate of heat transfer is approximately proportional to the difference between the surface temperature T_s and temperature of the free stream fluid T_f. The constant of proportionality is called the convective heat transfer coefficient h_c:

$$q_h = h_T(T_s - T_f) \quad (2.9)$$

h_T is a physical constant whose value depends upon the material (as it was with k), but also the conditions of the convection (whether the flow is laminar or turbulent and so on).

2.1.3. Radiation

Thermal radiation is energy emitted by matter as electromagnetic waves, due to the pool of thermal energy in all matter with a temperature above absolute zero. All objects constantly emit energy as electromagnetic radiation, of an intensity determined by the object's temperature and surface characteristics. This energy can be absorbed by other objects, also as a function of their temperature and surface characteristics. The transfer of heat by electromagnetic radiation is termed radiative heat transfer (Mills, 1999).

Not all electromagnetic radiation that reaches a body is absorbed. The energy may be either absorbed, reflected, or transmitted through the body, at fractions described by the absorptance Θ, reflectance Λ, and transmittance Ω. These coefficients, whose sum must equal unity, will vary depending on the wavelength of the incoming radiation.

The Stefan-Boltzmann law describes the maximum amount of energy that may be emitted from a body at a given temperature. The law, which is valid for a theoretical “black body" having Θ = 1, predicts a maximum energy flux (q_h) of:

$$q_h = BT^4 \quad (2.10)$$

where:

T is the surface temperature;

B is the proportionality constant, which is referred to as the Stefan-Boltzmann constant and is equal to 5.67×10^{-8}W/(m^2·K).

When radiation is exchanged between two objects, the rate of heat transfer is a function of the difference in the fourth power of their temperatures. The heat flux from object 1 to object 2 is given by $q_h(T_1)$, while the heat flux from object 2 to object 1 is given by $q_h(T_2)$. The net heat flux from object 1 to object 2 is thus described by:

$$q_h(T_1) - q_h(T_2) = B(T_1^4 - T_2^4) \tag{2.11}$$

The actual rate of heat transfer from object 1 to object 2 is a function of the heat fluxes of the two objects, the area through which heat is emitted and absorbed, and their configuration in space. The rate can be calculated according to:

$$q_h = A_1 F_{1-2} B(T_1^4 - T_2^4) \tag{2.12}$$

where:

A_1 is the area from which radiation is emitted and absorbed;

$F_{1\text{-}2}$ is the configuration factor, a function of the emittances and absorptances of the two objects, as well as their arrangement in space.

The heat transfer processes between fluid flow and fractured rock are mainly conduction and convection. Radiation in this configuration only transfers a negligible amount of heat. In the rock, where there is fluid flow in the interconnected pores, heat conduction in the rock and fluid, and heat convection in the fluid are the mechanisms that transfer heat. In fractures, heat is transferred by both conduction and convection in the fluid. The fluid and rock system, thus form a 3-D coupled heat transfer system.

2.2.Mass Transfer

There are mainly two modes of fluid mass transfer in the fractured rocks. They are fluid flow in interconnected rock pores and fluid flow in rock fractures. These two modes have significantly different contact areas between the fluid and the solid, thus need to be considered separately. A combined mode of the two is also possible when fluid flows in fractured porous rocks.

2.2.1. Fluid Flow in Rock Pores

Fluid flowing in the interconnected rock pores is very common in the field of groundwater hydrology and petroleum engineering. In 1856, the French engineer Henry Darcy performed several experiments concerning water flow through sand (Darcy, 1856). His observation can be summarized as the Darcy's law:

$$q_{vol} = KA\frac{h_2 - h_1}{l} \tag{2.13}$$

where:

q_{vol} is the volumetric flow rate;

A is the cross-sectional area of the tube;

h_1 and h_2 are the hydraulic head at the measurement points;

l is the distance between the measurement points;

K is the hydraulic conductivity.

The hydraulic head is given as:

$$h = \frac{p}{\rho g} + z_{el} \tag{2.14}$$

where:

p is the fluid pressure;

ρ is the density of the fluid;

g is the gravitational constant;

z_{el} is the elevation head, which is the distance to the datum.

The proportionality constant K in Darcy's relation is referred to as the hydraulic conductivity. The property of hydraulic conductivity is a measure of how easily the fluid is conducted through the porous medium. Hydraulic conductivity is influenced by four factors: the dynamic viscosity and density of the fluid, gravitation, and the transmitting property of the material the fluid is flowing through. This last property is called permeability, which we denote by κ. Permeability has units m^2, but in practice, the unit Darcy (D) is usually used. 1D is defined as the permeability of a fluid with viscosity 1 cP flowing at the rate of 1 cm/s under a pressure gradient of 1 atm/cm, that is 1D

$\approx 9.869\times10^{-13}$ m^2. The hydraulic conductivity K and permeability κ can be related by Equation 2.15:

$$K = \frac{\kappa \rho g}{\mu} \tag{2.15}$$

where:

μ is the dynamic viscosity.

Generally, the hydraulic conductivity and permeability are tensors. Darcy's law can be written in the differential form:

$$u = -\frac{1}{\mu} K(\nabla p - \rho g) \tag{2.16}$$

Where:

u is the volumetric flux called Darcy velocity.

The Darcy velocity is not the actual velocity at the pore scale, but rather an averaged macroscopic volume flux. It is the volume flowing over the entire cross section, including both fluid and matrix. The actual velocity, U, is only the flow through the cross section of the fluid. The two velocities are hence related by Equation 2.17.

$$U = \phi u \tag{2.17}$$

where:

ϕ is the porosity of the porous medium.

The velocity U is called the intrinsic velocity, as it describes the actual velocity. This velocity is important because it is the velocity of fluid that transports heat.

2.2.2. Fluid Flow in Rock Fractures

Fractures and faults provide permeable pathways for fluids at a variety of scales, from great depth in the crust to flow through fractured aquifers. Fracture-dominated flow is important in many situations of technical or scientific interest, such as in naturally-fractured petroleum reservoirs, and most geothermal reservoirs.

The simplest model of flow through a rock fracture is the parallel plate model. This is the only fracture model for which an exact calculation of the hydraulic conductivity is possible; this calculation yields the well-known cubic law. The derivation of the cubic law begins by assuming

that the fracture walls can be represented by two smooth, parallel plates, separated by an aperture δ, as shown in Figure 2.4.

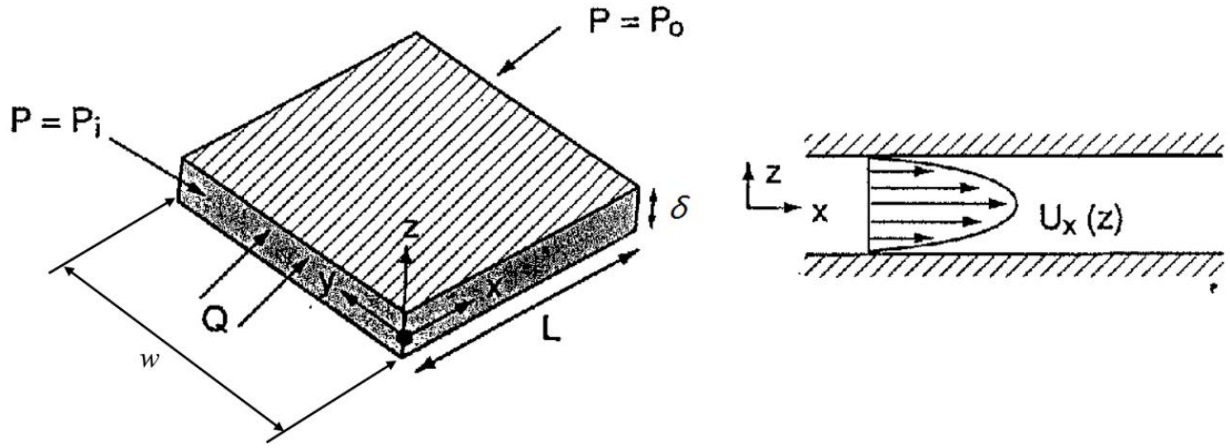

Figure 2.4 Fluid Flow between Two Parallel Plates

As the problem is 2-D, fluid velocity in the Y and Z direction is zero. The assumption that the flow is laminar means the streamlines are parallel, i.e. $u_z=0$. The Navier-Stokes Equation in the X direction is:

$$\frac{\partial u_x}{\partial t} + u_x \frac{\partial u_x}{\partial x} + u_z \frac{\partial u_x}{\partial z} = f_{bx} - \frac{1}{\rho}\nabla p + \frac{\mu}{\rho}\nabla^2 u_x \tag{2.18}$$

Because it is steady condition, laminar flow condition and there is no body force on the fluid. Equation 2.18 can be simplified as:

$$0 = -\frac{1}{\rho}\nabla p + \frac{\mu}{\rho}\left(\frac{\partial^2 u_x}{\partial z^2}\right) \tag{2.19}$$

Thus,

$$\frac{1}{\mu}\frac{\partial p}{\partial x} = \frac{\partial^2 u_x}{\partial z^2} \tag{2.20}$$

The boundary conditions are:

$$u_x = 0 \; at \; z = \frac{\delta}{2} \; and \; z = -\frac{\delta}{2}$$
$$\frac{\partial u_x}{\partial z} = 0 \; at \; z = 0 \tag{2.21}$$

The solution of this differential equation is:

$$u_x(y) = -\frac{1}{2}\frac{1}{\mu}\left(\frac{\partial p}{\partial x}\right)\left[\left(\frac{\delta}{2}\right)^2 - z^2\right] \tag{2.22}$$

The negative sign means the direction of the flow is opposite to that of the pressure gradient. Because the flow is steady, the pressure gradient in the x direction is uniform. Assume the pressures at the inlet and outlet of the fracture are p_i and p_o, respectively; the length of the fracture is L. Equation 2.22 can be rewritten as:

$$u_x(y) = -\frac{1}{2}\frac{1}{\mu}\left(\frac{p_0 - p_i}{L}\right)\left[\left(\frac{\delta}{2}\right)^2 - z^2\right] \tag{2.23}$$

As shown in Equation 2.23, the velocity profile across the fracture is parabolic. Usually, the bulk velocity is used as the average velocity across the fracture, as defined in Equation 2.24.

$$\overline{u_x} = \frac{\int_{-\frac{\delta}{2}}^{+\frac{\delta}{2}} u_x dy}{\int_{-\frac{\delta}{2}}^{+\frac{\delta}{2}} dy} = \frac{\delta^2}{12\mu}\left(\frac{p_i - p_o}{L}\right) \tag{2.24}$$

Assume the width of the fracture is w, the cross sectional area is A, then the flow rate is:

$$Q_x = \overline{u_x}A = \overline{u_x}w\delta = \frac{w\delta^3}{12\mu}\left(\frac{p_i - p_o}{L}\right) \tag{2.25}$$

Because of the aperture cube term, Equation (2.23) is called the cubic law (named Poiseuille law for cases with circular cross-section) (Witherspoon et al., 1980). When the cubic law is applied to calculate the flow rates in the fractures, reduction factors are often introduced to account for the surface roughness of the fractures. These reduction factors are produced by fitting test data with the cubic law. Different type of rocks often have different reduction factors.

Fundamentally, the above two modes of fluid transfer in the rock mass have a lot in common, for example, the flow rates are controlled by fluid viscosity, and the flow rates are proportional to the

pressure gradient. These similarities are one of the reasons why equivalent hydraulic conductivity can be used to calculate fluid flow in rock fractures. However, when it comes to heat transfer, the significantly different contact areas of the two modes might make the two mass transfer modes perform differently. This will be covered in the following.

2.3. Analytical Approaches

Modeling the heat transfer between fluid and fractured rocks in the geothermal systems falls into the 'data limited' class of Starfield & Cundall (1988). This means that we are unable to characterize the system well enough to determine the actual geometry. A simplified geometric representation of the fractures is necessary for analytical approaches. The fracture systems in the rocks are usually represented by a continuum if the fractures are uniformly distributed in the rock mass, or by discrete fractures if there is only a small number of fractures and they can be represented individually. When both of the fractures and the porosity of the rock are considered, the models are called hybrid models.

2.3.1. Continuum Models

In the world of mechanics, a continuum is defined as a volume of material whose properties can be represented by one point or one infinitesimal element. The discrete behavior of individual fractures is represented by an average property over a representative elementary volume (REV). Because the flow in rock fractures and rock pores are both proportional to the pressure gradient, equivalent hydraulic conductivity can be used. Then, the fractured rock can be modeled using the same approach as that of the porous media.

Because of the extensive research in underground hydrology and petroleum engineering, the conduction and advection in porous media have been well formulated for solute transport. Similar mechanisms drive the heat transfer in porous media, so the problem of heat transfer is often solved in the similar way to that of solute transport.

The continuum models often assume the fluid moves in a confined rock stratum, which can also be equivalent to porous medium. Heat transfer happens between the confining impermeable rock, the fractured rock and the fluid. Lauwerier (1955) published the first and perhaps the most widely known solution for the temperature distribution due to injection of a hot fluid in a reservoir, which includes heat losses to the impermeable strata surrounding the reservoir. Malofeev (1960) has

shown that Lauwerier's solution is also applicable in the radial flow case. Avdonin (1964) considered a non-zero value for the thermal conductivity within the reservoir in the horizontal direction. Chen and Reddell (1983) developed analytical solutions of temperature distribution for thermal injection into a confined aquifer, with a cap rock of finite thickness.

Figure 2.5 shows the sketch of a continuum model developed by Ascencio et al. (2014). The injected fluid is incompressible and flows through the permeable fractured stratum, which is treated as a confined aquifer between the underlying rock and overlying impermeable stratum. The flow in the fractured rock stratum is radial and goes to the horizontal infinity. Cylindrical coordinates (r, θ, z) are used in this case. The material properties of the rock and the water are assumed to be constant without changing with temperature. The confining rock and the fractured rocks are homogeneous, isotropic and of infinite horizontal extent.

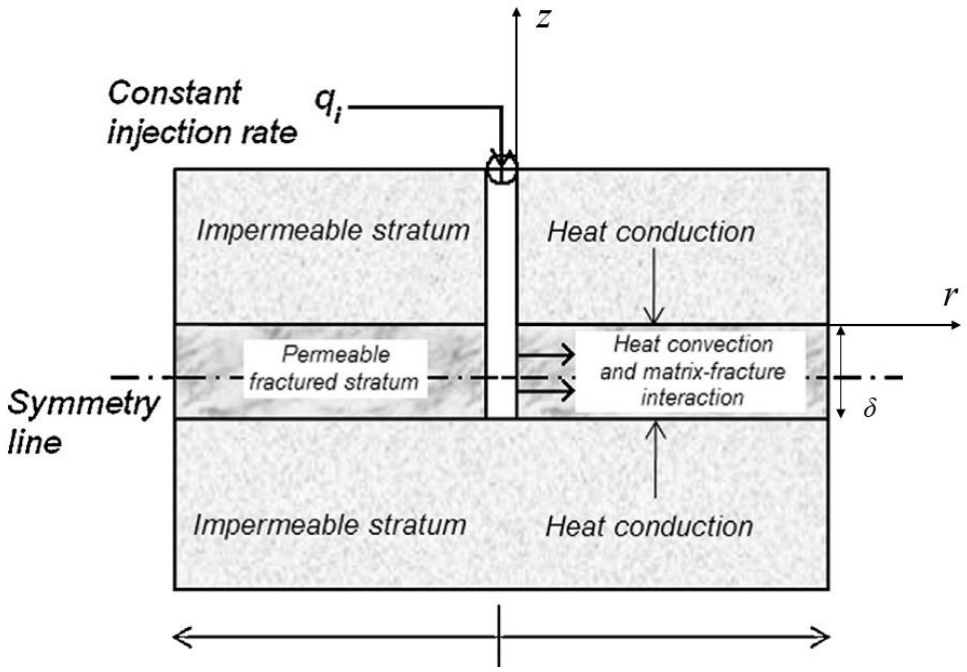

Figure 2.5 A Sketch of the Conceptual Model developed by Ascencio et al. (2014)

The model only considers the vertical heat conduction in the impermeable stratum, thus the energy equation for the confining rock is given by Equation 2.26:

$$\rho_r C_{pr} \frac{\partial T_{cr}}{\partial t} = k_r \frac{\partial^2 T_{cr}}{\partial z^2}, (0 < r, 0 < z < \infty, 0 < t) \tag{2.26}$$

where:

"T_{cr}" represents temperature of the confining impermeable stratum.

The fractured confined rock stratum is represented by porous medium with equivalent porosity ϕ, which is the volume of fractures over the total volume. The energy balance equations for the fluid and the fractured rock are written as Equations 2.27 and 2.28:

$$\phi\rho_f C_{pf}\frac{\partial T_f}{\partial t} = \phi k_f\frac{\partial^2 T_f}{\partial z^2} - \frac{\rho_f C_{pf} q_i}{2\pi\delta r}\frac{\partial T_f}{\partial r} + q^*\left(t, \overrightarrow{x_f}\right), (0 < r, -\frac{\delta}{2} < z < 0, 0 < t) \quad (2.27)$$

$$(1-\phi)\rho_r C_{pr}\frac{\partial T_r}{\partial t} = (1-\phi)k_r\frac{\partial^2 T_r}{\partial z^2} - q^*\left(t, \overrightarrow{x_f}\right), (0 < r, -\frac{\delta}{2} < z < 0, 0 < t) \quad (2.28)$$

where:

the subscript "*r*" represents the fractured rock;

the subscript "*f*" represents the fluid in the fracture;

r is the radius of the cylindrical coordinate;

δ is the fracture aperture;

q_i is the injection rate;

$q^*(t, \overrightarrow{x_f})$ is the heat flow from the fractured rock to the fluid in the fractures.

The boundary conditions are:

$$T_f \neq T_{cr};\ T_r = T_{cr}, (z = 0) \quad (2.29)$$

$$-\phi k_f\frac{\partial T_f}{\partial z} = \phi h\left(T_f - T_{cr}\right), (z = 0) \quad (2.30)$$

$$(1-\phi)k_r\frac{\partial T_r}{\partial z} = k_{cr}\frac{\partial T_{cr}}{\partial z} + \phi h\left(T_f - T_{cr}\right), (z = 0) \quad (2.31)$$

$$\frac{\partial T_r}{\partial z} = \frac{\partial T_f}{\partial z} = 0, (z = -\frac{\delta}{2}) \quad (2.32)$$

Equation 2.29 reflects the continuous temperature from the confining rock to the fractured rock. Equation 2.30 is the energy conservation between the confining rock and the fluid. Equation 2.31

reflects the continuous heat flux between the impermeable stratum and the fractured stratum. Equation 2.32 is the symmetry of the system about the $z = -\frac{\delta}{2}$ axis.

In the fractured rock stratum, a uniform temperature profile is assumed in the Z direction, so Equation 2.27 and 2.28 can be integrated with respect to the vertical coordinate z, within the limit $-\frac{\delta}{2}$ and 0. Laplace transform is used to solve the equations and numerical inverse Laplace transform is used to plot the temperature-time curve and migration of the thermal front.

This analytical model makes several assumptions and simplifications, nevertheless, keeps many of the important features of the geothermal systems. It characterizes the heat transfer between the confining rock, fractured rock and the fluid. The results provide a very useful insight into how the thermal front migrates and how the temperature of the fluid changes, which is very important in design the reinjection strategies for the geothermal systems.

However, this model does not account for the existence of the production well, which influences the flow direction. The assumption of a uniform velocity profile and temperature profile in the fractured stratum in the Z direction may omit the important heat transfer in the fluid. In addition, the parameters *h* and *q** in Equation 2.27 and 2.30 are difficult to characterize since the system is an non-steady system, i.e. *h* and *q** vary with time and space.

2.3.2. Discrete Models

In discrete fracture models, the geometry of each fracture is considered. However, analytical models of heat transfer between fluid and fractured rocks have to rely on a number of simplifications to make the differential equations and boundary conditions solvable. Abstracted geometric configurations are often used to represent the fractures in the geothermal systems.

Gringarten and Sauty (1975) developed an analytical model for heat extraction in geothermal systems. Their model is a linear model involving an infinite series of parallel, equidistant, vertical fractures of uniform aperture, separated by blocks of homogeneous and isotropic, impermeable rock. A similar configuration, but horizontal fractures are assumed in the model developed by Bödvarsson and Tsang (1982). McFarland and Murphy (1976) use one disk shaped, uniform aperture, vertical fracture to represent the underground fracture. One vertical fracture in an unbounded domain is modeled by Cheng et al. (2001).

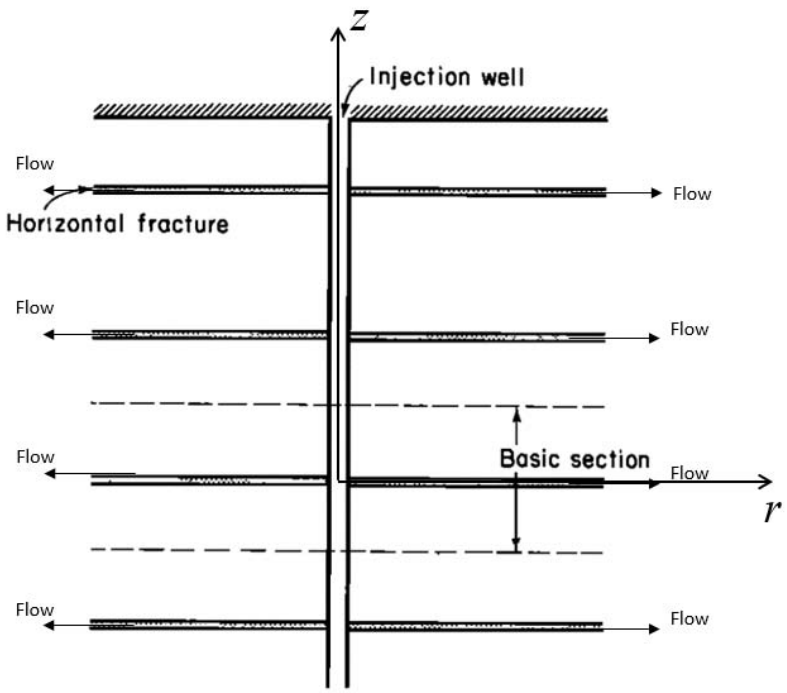

Figure 2.6 Cross-section of the Analytical Model developed by Bödvarsson and Tsang (1982)

A schematic of the analytical model developed by Bödvarsson and Tsang (1982), is shown in Figure 2.6. The injection well penetrates into a reservoir with an infinite series of parallel, equidistant, horizontal fractures of uniform aperture, separated by blocks of homogeneous and isotropic, impermeable rock. Similar to the model developed by Ascencio et al. (2014), steady and radial flow is assumed in the horizontal fractures and cylindrical coordinates *(r, θ, z)* are used for convenience. Because of the symmetry about the dashed lines in Figure 2.6, one basic section of the fracture system is analyzed, as shown in Figure 2.7.

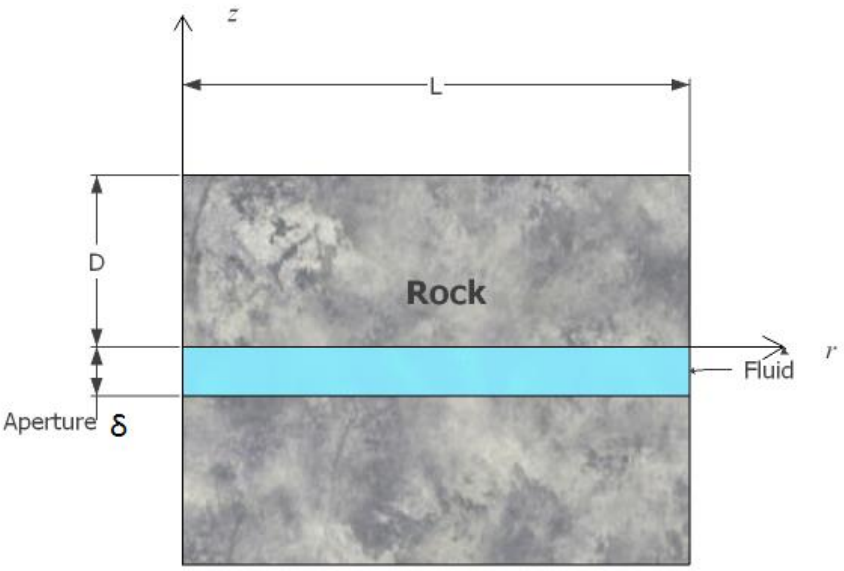

Figure 2.7 One Basic Section of the Fracture System in Figure 2.6

Only the heat conduction in the vertical direction is considered. The temperature in the rock is governed by the heat conduction in the Z direction:

$$\frac{\partial^2 T_r}{\partial z^2} = \frac{\rho_r C_{pr}}{k_r}\frac{\partial T_r}{\partial t}, (0 < z < D) \tag{2.33}$$

The differential equation governing the fluid temperature in the fracture can be derived by performing an energy balance in an infinitesimal control volume in the fracture. The temperature and velocity profile of the fluid in the Z direction (transverse direction) is assumed to be uniform.

$$\rho_f C_{pf}\frac{\partial T_f}{\partial t} + \frac{\rho_f C_{pf} q_i}{2\pi\delta r}\frac{\partial T_f}{\partial r} - \frac{2k_f}{\delta}\frac{\partial T_f}{\partial z}|_{z=0} = 0, (-\delta < z < 0) \tag{2.34}$$

The initial and boundary conditions can be expressed as:

$$T_f = T_r = T_0, (t = 0) \tag{2.35}$$

$$T_f = T_i, (r = 0) \tag{2.36}$$

$$T_f = T_r, (z = 0) \tag{2.37}$$

$$\left.\frac{\partial T_f}{\partial z}\right|_{z=D} = 0 \tag{2.38}$$

Equation 2.35 indicates that the water and fracture has the same temperature T_0 before injection. Equation 2.36 describes that the temperature of the injected fluid is T_i. The temperature of the solid at the interface with the fluid is the same as that of the fluid, as indicated in Equation 2.37. Because of the symmetry of the basic section, there is no heat flow through the section boundary, as described in Equation 2.38.

This model uses Laplace transform to solve the partial differential equations. Numerical inverse Laplace transform is used to transform the solution into the time and space domain. This model is capable of calculating the temperature profile of the fluid and rock at any time. It can also calculate the migrating of thermal front.

However, this model greatly simplified the geometry of the fracture network, which may not capture the complexity of the underground conditions. Also, without considering the existence of the production well, the velocity profile of the fluid is not close to reality. In addition, diffusion in the longitudinal direction is neglected which may cause a certain amount of inaccuracy in the result. More realistic cases need to be considered, which will be covered in Chapter 4.

2.3.3. Hybrid Models

The models capturing the heat transfer between fluid and fractured porous rocks are known as hybrid models in this context. These models have to consider both the heat conduction and convection in the fluid in both the porous rocks and the fractures. Convection terms have to be put in the energy balance equations for both porous rock and fluid in the fractures. Analytical solutions are nearly impossible to be found without simplifications. Martínez et al. (2014) used similar methods as for solute transport in fractured porous rocks by Roubinet et al. (2012), which is to neglect the convection in the porous rock due to the slow velocity relative to the velocity in the fracture. The formulation of the problem is then similar to that in section 2.3.2. Instead of the radial coordinate, two dimensional Cartesian coordinates in the X-Z direction are used for fluid flowing in the X direction, as shown in Figure 2.8.

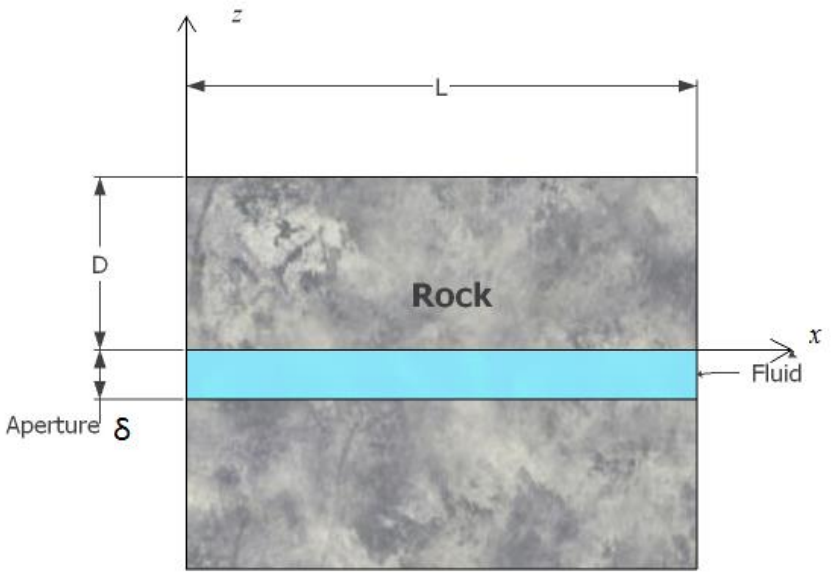

Figure 2.8 Analytical Model Developed by Martinez et al. (2013)

Since the heat convection is neglected, heat conduction is the only mechanism that drives the heat in the porous rock. Because the porous rock has both solid and fluid, the diffusion coefficient *D* is used. To account for the anisotropy of the porous rock, the superscript of *D* indicates the direction of the diffusion. The temperature in the porous rock matrix is governed by the heat diffusion in the X and Z directions:

$$\frac{\partial T_r}{\partial t} = D_r^x \frac{\partial^2 T_r}{\partial x^2} + D_r^z \frac{\partial^2 T_r}{\partial z^2}, (0 < z < D) \tag{2.39}$$

The fluid temperature in the fracture can be derived by performing an energy balance in an infinitesimal control volume in the fracture. The different velocities in the X and Z direction, u_x and u_z, will end up with different diffusion coefficients in the fluid, D_f^x and D_f^z, respectively, as shown in Figure 2.9.

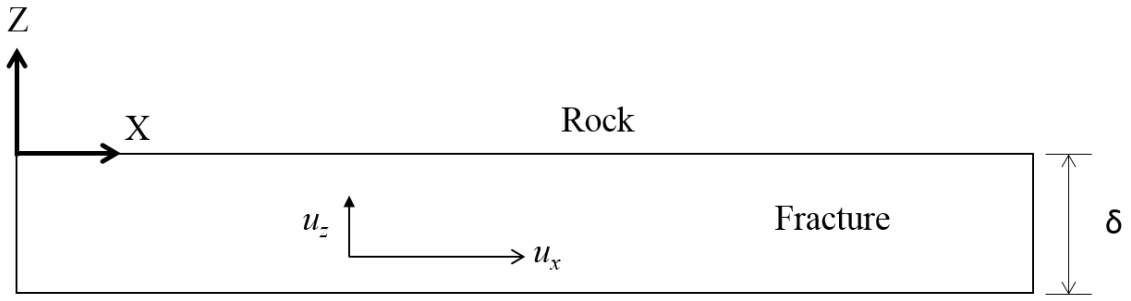

Figure 2.9 Flow Condition in the Fracture

The convection in the X direction is expressed as the convection term: $u_x \frac{\partial T_f}{\partial x}$.

$$\frac{\partial T_f}{\partial t} + u_x \frac{\partial T_f}{\partial x} = D_f^x \frac{\partial^2 T_f}{\partial x^2} + D_f^z \frac{\partial^2 T_f}{\partial z^2}, (-\delta < z < 0) \tag{2.40}$$

Similar to Section 2.3.2, the initial and boundary conditions can be expressed as:

$$T_f = T_r = T_0, (t = 0) \tag{2.41}$$

$$T_f = T_i, (x = 0) \tag{2.42}$$

$$T_f = T_r, (z = 0) \tag{2.43}$$

$$\left.\frac{\partial T_f}{\partial z}\right|_{z=D} = 0 \tag{2.44}$$

The temperature and velocity profile of the fluid in the Z direction is assumed to be uniform so that Equation 2.40 can be easily integrated in the Z direction. The temperature of the solid at the interface with the fluid is the same as that of the fluid, as indicated in Equation 2.43. Because of the symmetry of the basic section, there is no heat flow through the section boundary (z=D), as described in Equation 2.44. The advantages of this model are that both the longitudinal and transverse heat diffusion are considered in the porous rock and that the longitudinal heat diffusion and convection are considered in the fracture. This model is expected to be more accurate and general if the diffusion term D_r for the porous rock and diffusion term D_f for the fluid can be well provided.

Analytical solutions, such as those mentioned above, provide significant physical insight into these transport phenomena and act as an invaluable component in field-scale screening and management (decision support) models. Yet they rely on a number of simplifying assumptions that might not be valid in a specific application.

2.4.Numerical Approaches

Except in some simple and idealized cases, the partial differential equations and corresponding initial and boundary conditions cannot be solved analytically. To take the complexities of the

geothermal systems into consideration, numerical approaches are often used. The development of modern computational technology greatly advanced the numerical modeling technique for physical processes. Some of the most popular methods for the type of problems we are considering are the Finite Difference Method (FDM), the Finite Element Method (FEM), the Finite Volume Method (FVM) and the Boundary Element Method (BEM).

The methods mentioned above have many applications. However, for geothermal systems, it is a challenge to use these methods to model the complex geometry of the fracture networks, the variation of rock and fluid properties, and the uncertainty of these underground conditions in a large scale and long time. Simplifications have to be made to make the numerical models computationally possible, but still capture the important physical processes. Similar to the analytical models, continuum models can be categorized into three categories, they are continuum models, discrete models and hybrid models.

2.4.1. Continuum Models

Similar to the analytical continuum models, the fractured rocks can be treated as a continuum, to which finite element method can be well applied. The question remaining is how to characterize the fractured rocks as continuum so that the heat and mass transfer processes can be modeled.

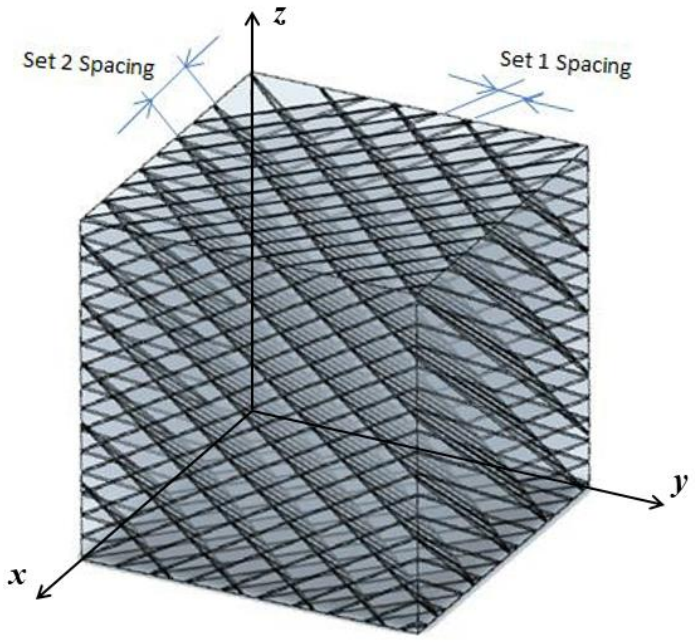

Figure 2.10 Sketch of Fracture Network in the Rock

Figure 2.10 shows the continuum model developed by Reeves (2006). In many cases, there are two predominant sets of sub-vertical fractures orthogonal to each other and three or more sets are observed in some cases (Kalinina et al., 2013). Due to the nature of these scenarios, the continuum model characterizes fracture sets using the strike, dip, aperture, and spacing of parallel fractures in the system. Both natural fractures and fractures created by hydro-fracturing can be represented by parallel plane sets in the rock mass. This approach can be used to model fluid flow in the fractured rock mass, thus generating the hydraulic conductivity tensor.

When simulating the flow process, because the fractures may not be parallel to the flow path, the hydraulic conductivity tensor of one fracture set needs to be transformed:

$$k_{ij} = \frac{g\delta^3}{12\mu L}T \tag{2.45}$$

where,

k_{ij} is the permeability tensor in the i=x, y, z and j=x, y, z direction, caused by a particular set of fractures;

δ is the fracture aperture;

L is the spacing between the fractures;

μ is the dynamic viscosity;

T is the transform matrix:

$$T = \begin{bmatrix} n_2^2 + n_3^2 & -n_1 n_2 & -n_1 n_3 \\ -n_1 n_2 & n_1^2 + n_3^2 & -n_2 n_3 \\ -n_1 n_3 & -n_2 n_3 & n_1^2 + n_2^2 \end{bmatrix} \tag{2.46}$$

$$n_1 = cos\varphi sin\omega \qquad n_2 = cos\varphi cos\omega \qquad n_3 = -sin\varphi$$

where,

φ is the fracture pole plunge (90°-dip);

ω is the fracture pole trend (strike-90°).

φ and ω are shown in Figure 2.11.

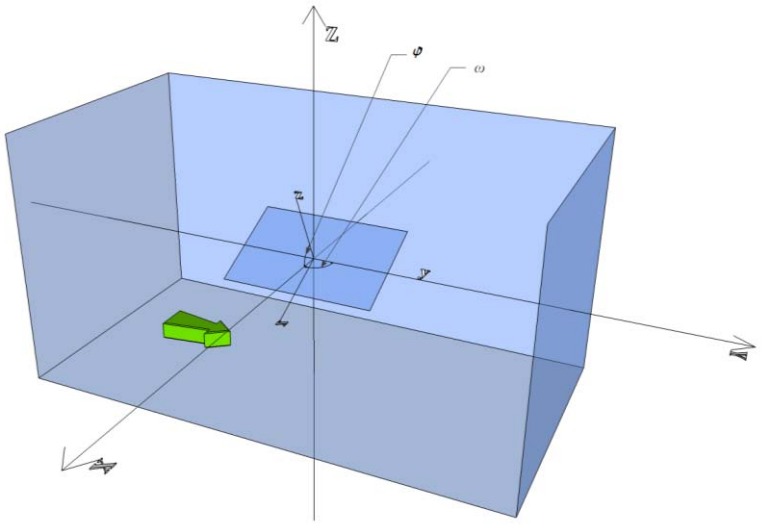

Figure 2.11 Fracture Pole Plunge φ and Pole Trend ω

For multiple fracture sets, the hydraulic conductivity tensor is the sum of the hydraulic conductivity tensors of all the individual fracture sets:

$$k_{ij} = \sum_{m=1}^{N} k_{ij}^{m} \tag{2.47}$$

where,

N is the number of fracture sets;

k_{ij}^{m} is the hydraulic conductivity tensor.

After the permeability tensor is built for the rock mass, the rock mass is treated as a homogeneous anisotropic porous medium. This is a simplification that makes the process very convenient for numerical modeling. In the model developed by Reeves (2006), the Finite Element Heat and Mass Transfer code (FEHM) developed by Zyvoloski et al. (1988) is used. This code was written to simulate 3-D mass and heat transfer in porous rock. It considers two fluid phases, gas and liquid. The mass transfer is governed by Darcy's law, and heat transfer is governed by Fourier's law of heat conduction (Zyvoloski et al., 1988).

2.4.2. Discrete Models

Discrete fracture models refers to the fracture models that explicitly account for the physical process of each fracture. These models are often computationally intensive because the models

have to deal with the information of all the fractures, the number of which is in the thousands. However, with the development of more powerful computers and more efficient numerical methods, the computational efforts seem to be less of a problem.

In the context, stochastic methods are often used to generate fracture networks based on the statistical data from the field. The stochastic discrete fracture models provide information of the geometry of the fractures and their intersection. Heat and mass transfer is often calculated by numerical methods such as the finite element method with adaptive meshing (Smith et al., 2013) or finite difference method (Fu et al., 2013). Below is an example of the discrete models to capture the heat transfer between the fluid and fractured rock, which was developed by Smith et al. (2013).

As shown in Figure 2.12, a stochastic fracture network model is generated using the commercial software FRACMAN. The geometry information of all the fractures are plotted.

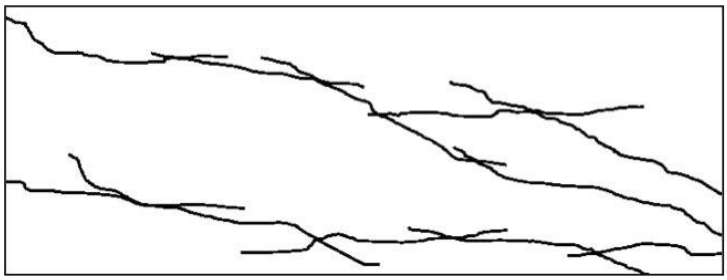

Figure 2.12 2-D Stochastic Fracture Network Generated by FRACMAN

Then, Cartesian mesh is used and refined near the fractures, as shown in Figure 2.13. The refining scheme is called adaptive meshing, since it makes the mesh finer around the discontinuity (the fractures) and coarser away from the discontinuity. The elements in the fracture are assigned with a significantly higher permeability, and the elements off the fracture are assigned with very low permeability or zero permeability if the rock is impermeable.

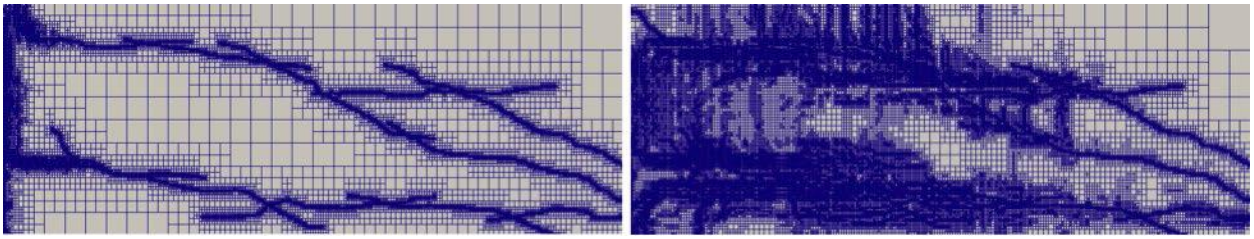

Figure 2.13 Adaptive Meshing in 2-D

Adaptive meshing can also be applied to 3-D discrete fracture networks, as shown in Figure 2.14.

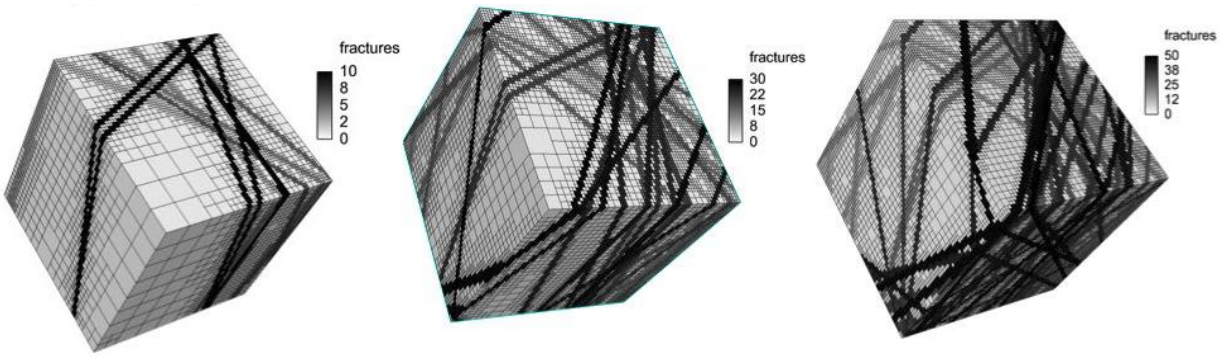

Figure 2.14 Adaptive Meshing in 3-D

The finite element method is used to calculate the heat and mass transfer between the fluid and fractured rocks after the mesh is generated and refined. Other processes can be coupled to this model since the finite element model has already been built. Mechanical processes such as the deformation of fractures due to thermal stress can be coupled into this model.

In the discrete models, the quality of the discrete fracture network is of great importance. Although the fracture network is stochastically generated, how close the generation processes are to the reality determines the reliability of the fracture network. Adaptive meshing is very helpful with capturing the geometry of the fractures and increasing the efficiency of the finite element method. But for the geothermal system with a large scale and long life time, the computational efforts required to model the entire geothermal system with reasonable accuracy may still be problematic.

2.4.3. Hybrid Models

In the field of underground hydrology, petroleum engineering, and underground environmental engineering, many heat and mass transfer models are already available. By mapping the hydraulic conductivity from a discrete fracture network to an existing heat and mass transfer continuum model, a hybrid model was developed by Hao et al. (2012). The model has been proven to be very powerful in predicting the thermal drawdown induced by flow channeling in fractured geothermal reservoirs.

A 2-D stochastic discrete fracture network model is firstly used to generate a fracture network, as shown in Figure 2.15a, the first picture. Then, the Cartesian grid is overlaid on the fracture network map to calculate the grid-based effective hydraulic conductivity. The effective hydraulic conductivity of a single fracture is calculated according to the Cubic Law, as shown in Equation 2.48.

$$K_f^n = \frac{\rho g \delta^3}{12 \mu L} \tag{2.48}$$

The conceptual schematic for grid-based effective hydraulic conductivity calculation is shown in Figure 2.15b.

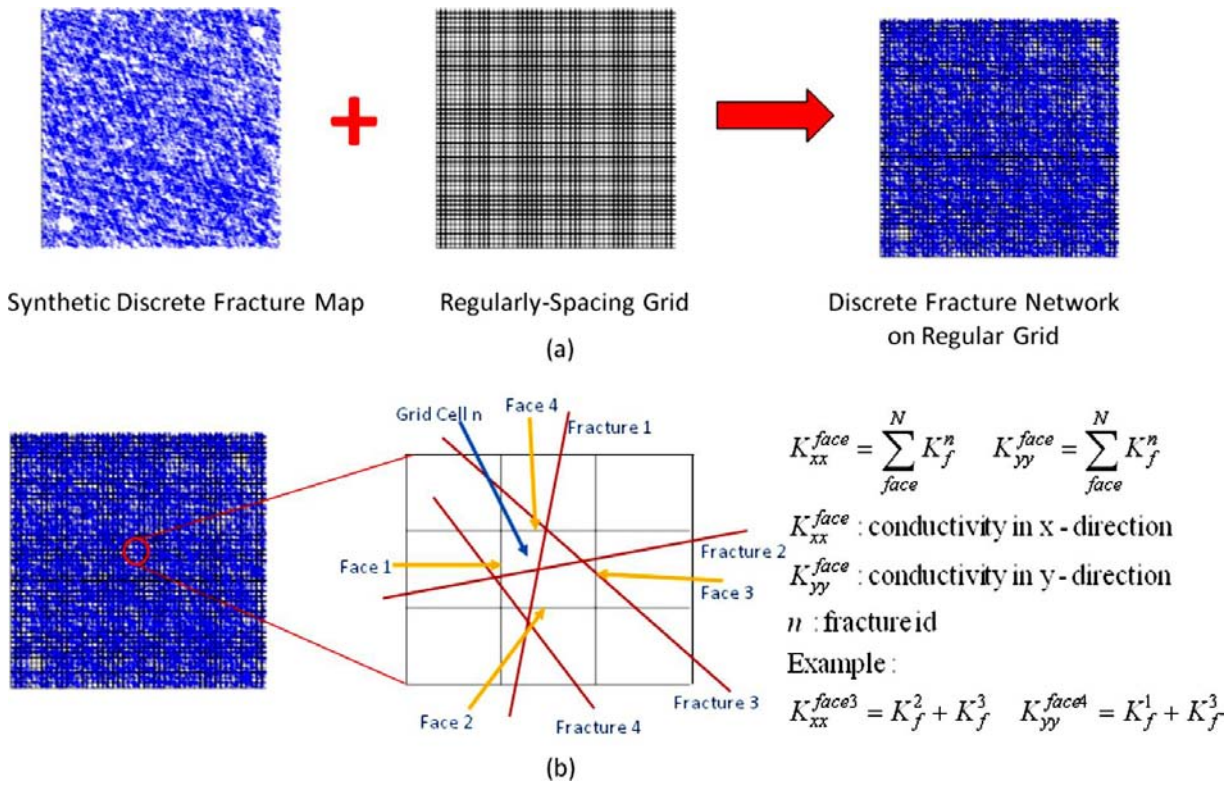

Figure 2.15 Schematic for Grid-based Effective Hydraulic Conductivity Calculation

After the hydraulic conductivity grid is mapped out, the coupled fracture flow and heat transfer simulations are performed using the Nonisothermal Unsaturated-Saturated Flow and Transport code, NUFT (Nitao, 1998; Hao et al., 2012). The NUFT code, which is based on Darcy's flow approximation, represents a current state-of-the-art in modeling multiphase, multicomponent heat and mass flow and reactive transport in unsaturated and saturated porous media. An integrated finite difference method is used for numerical discretization.

Similar to the discrete models, other models can be implemented in order to address various flow-, heat transfer- and mechanical processes. In this hybrid model, the discrete 2-D fracture network is the basis of the conductivity calculation. How this 2-D discrete fracture network model simulates the real fracture network determines the reliability of the model. The grid based effective hydraulic conductivity calculation is a valid approximation for the flow calculation. The accuracy of the flow

calculation depends on the resolution of the grid, which will further affect the accuracy of the heat transfer calculation.

3. Numerical Approach using GEOFRAC

Geometric and mechanical characterization of rock fractures is the basis for most of the work of engineering geologists, civil and mining engineers when dealing with rock masses (Dershowitz and Einstein, 1988). However, the complete description of fractures is difficult because of their three-dimensional nature and the limited information we can get from outcrops, borings, tunnels, tracer logs, and micro seismic events. Researchers from Lawrence Livermore National Laboratory, depicted a realistic fracture network based on their observation of fractures in rock masses, as shown in Figure 3.1 (Settgast et al., 2012) .

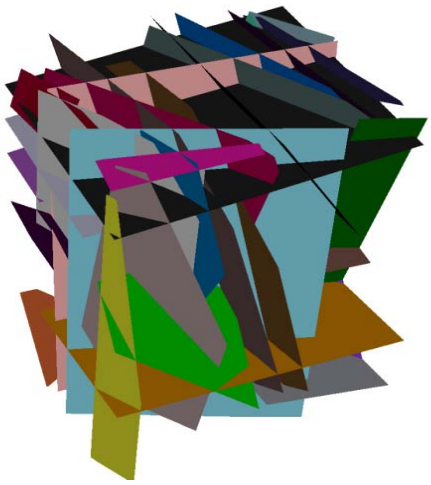

Figure 3.1 A realistic Fracture Network Derived from Experimental Data (Settgast et al., 2012)

Also, the analysis of micro seismic events data can be used to depict the fracture networks near an exploration borehole. Figure 3.2 shows a picture of fracture network near the Habanero-1 exploration well in the Cooper Basin, Australia (Barton et al., 2013). The two examples show that the DFN models, by considering each fracture separately, can adequately capture the actual geometries of the factures. With the fast development of computational power, the DFN models have received more and more attentions.

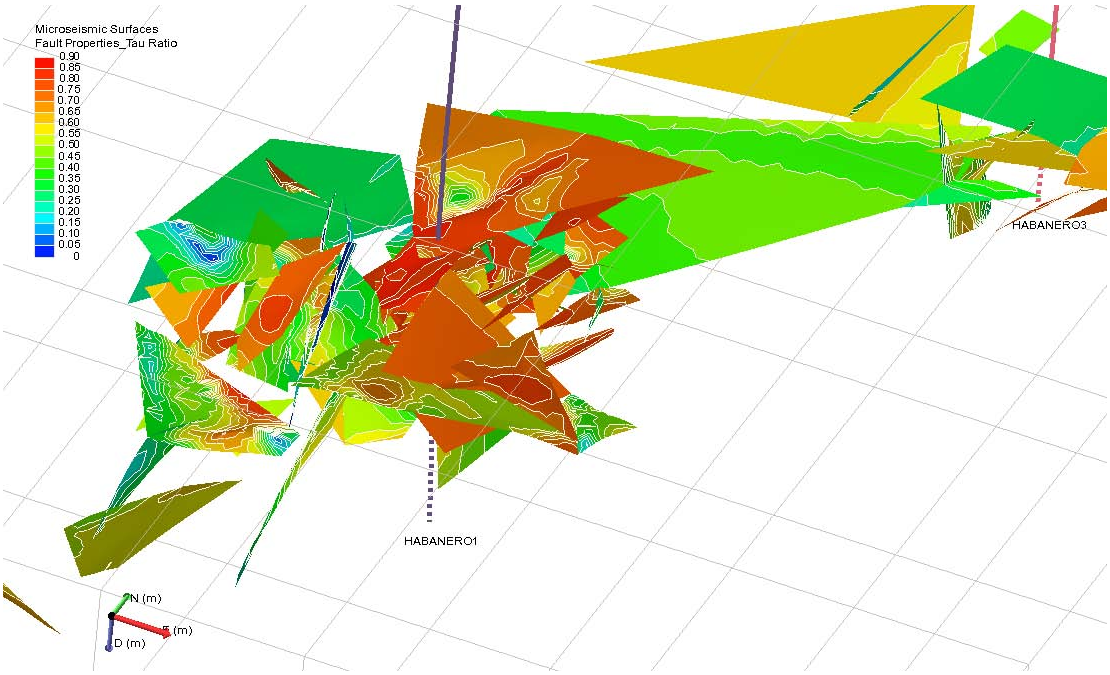

Figure 3.2 Network of Fractures Local to Habanero 1 Viewed from the Southeast. Color Indicates Proximity of the Fractures to Frictional Failure (Barton et al., 2013)

To reproduce the fracture network, one needs to rely on stochastic models. To provide parameters for this stochastic approach, statistical procedures have to be used to characterize the fracture orientations, shape, size, spacing and intensity. Researchers have proposed a number of statistical distributions for the fracture geometric characteristics, and a number of stochastic DFN models.

This chapter first introduces the stochastic DFN model, GEOFRAC; the recent development of the fluid flow model, GEOFRAC-FLOW; and heat transfer model, GEOFRAC-THERMAL. Comprehensive parametric studies with the three models are conducted to assess the effects that changing certain parameter can have on the results. Case studies on two geothermal projects are presented to show the capability and accuracy of these models.

3.1. GEOFRAC

3.1.1. Algorithm

With the help of statistical studies on the fractures, stochastic discrete fracture models were developed, e.g. Veneziano (1979), Dershowitz (1985), Ivanova (1995). This modeling approach has been applied in software such as Fracman and GEOFRAC, which can operate on different platforms. The following is a brief summary of the new GEOFRAC model using MATLAB.

GEOFRAC is a three-dimensional (3D), geology-based, geometric-mechanical, hierarchical, stochastic model of natural rock fracture systems (Ivanova et al., 2012). The model represents fracture systems as 3D networks of intersecting polygons, generated through spatial geometric algorithms that mimic the mechanical processes of rock fracturing in nature. The fracture generation process is visualized in Figure 3.3.

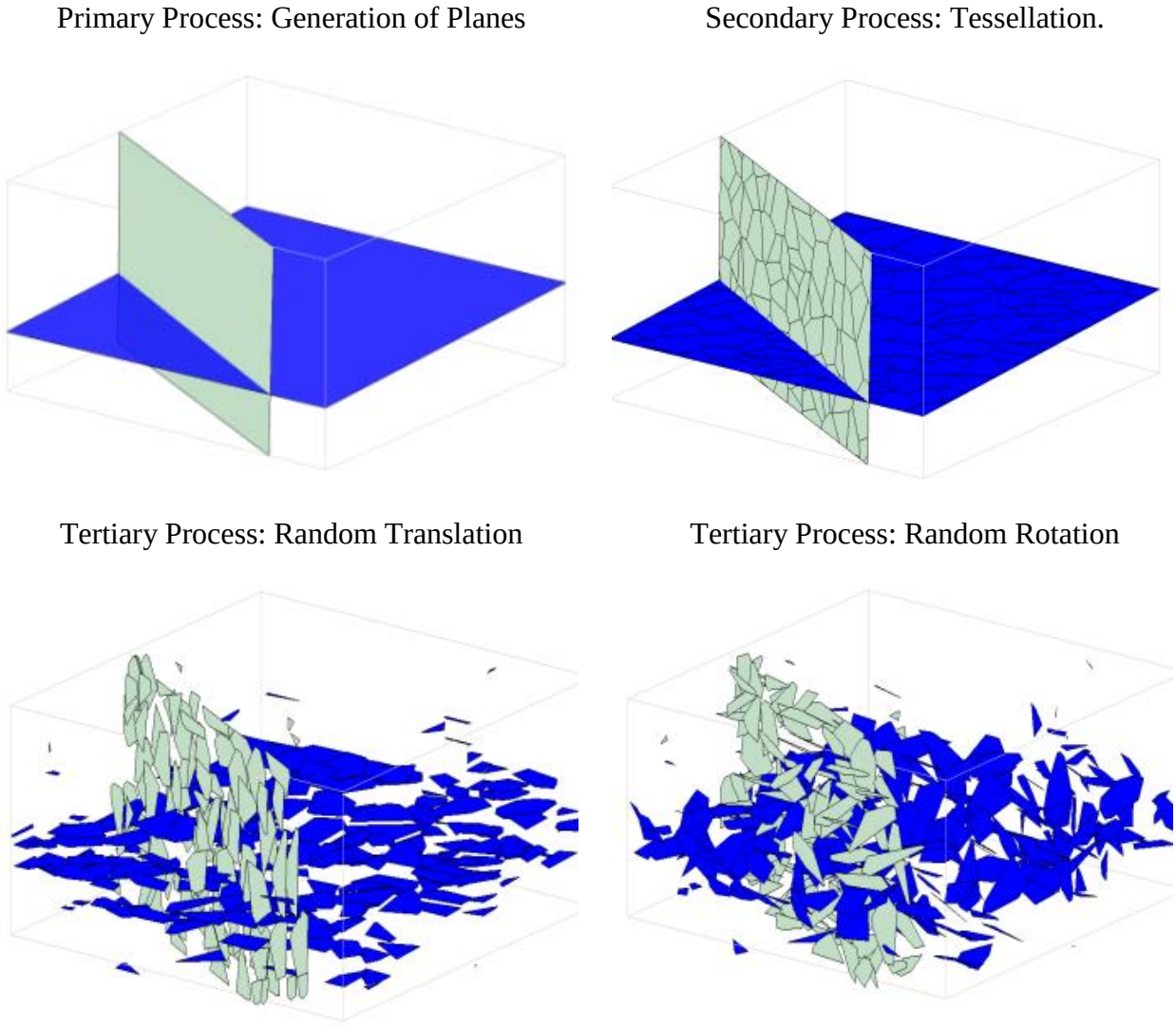

Figure 3.3 Three Fracture Generation Processes (V. Ivanova et al., 2012)

In GEOFRAC, stochastic processes are used to determine the fracture size, aperture, tessellation, and rotation. Detailed information can be found in Ivanova et al. (2012). With the help of built-in probability functions in MATLAB, these stochastic processes can be implemented easily. Geometric information on all the fractures is produced by the model. Validation of this fracture model was done by Sousa et al. (2012), who analyzed the connectivity of fracture networks.

3.1.2. Inputs

"X", "Y", "Z" are the dimensions of the rock volume being modeled, as shown in Figure 3.4. This volume is a cuboid and does not have to be the whole dimension of the reservoir, instead, one can choose to model only the volume of interest. For the later need of introducing GEOFRAC-FLOW, the direction of flow is also denoted in Figure 3.4. The fluid pressure is applied on the two surface that is perpendicular to the Y axis.

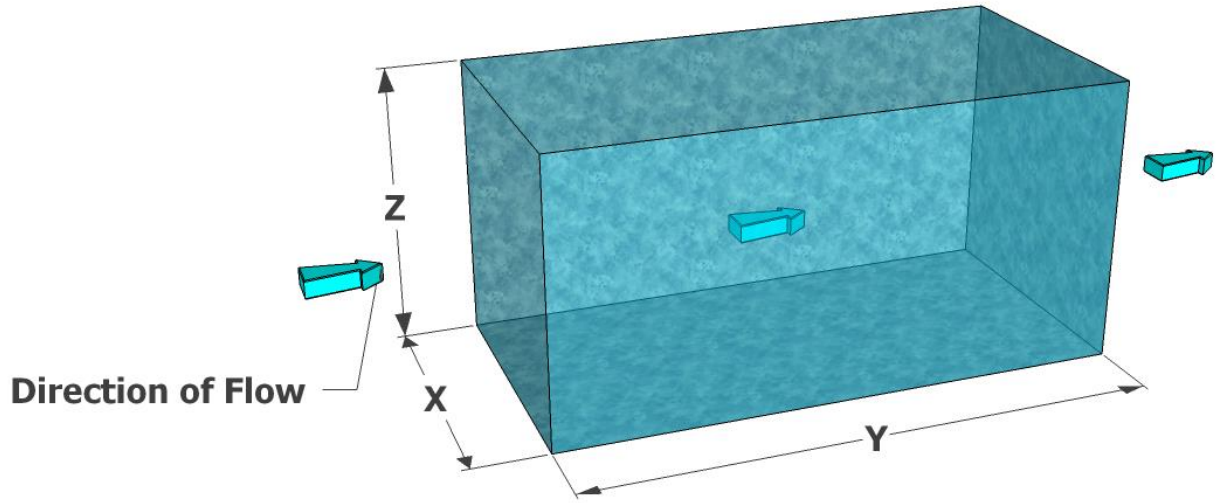

Figure 3.4 Dimensions of the Modeled Volume

"mu" is the fracture intensity in GEOFRAC, and is defined as:

$$mu = \frac{Total\ Fracture\ Area}{Volume\ of\ Rock} = P_{32} \tag{3.1}$$

P_{32} is a very commonly used fracture intensity parameter in engineering practice.

"EA" is the expected area of fractures. In GEOFRAC, fracture areas are assumed to be exponentially distributed, and EA is the mean of the distribution.

"m" is the type of orientation distribution in the primary process of GEOFRAC. "k" is the orientation distribution parameter. GEOFRAC has four choices for the distribution type. They are the uniform distribution, the uniform maxphi distribution, the Fisher distribution and the bivariate Fisher distribution. Figure 3.5 is an example of how a uniform distribution looks like in 3-D (3.5a) and in an equal-area projection (3.5b). For the detailed description of the orientation distributions, please refer to Appendix A.

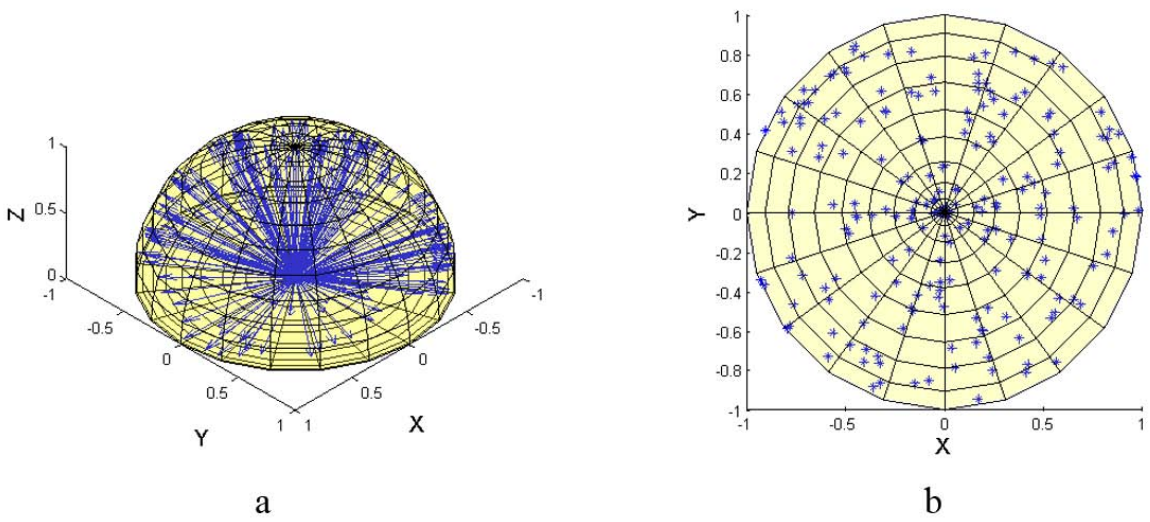

Figure 3.5 Uniform Orientation Distribution

"mPole" is the mean orientation of the pole of the fractures. This parameter controls how the fractures are oriented relative to the rock mass. Figure 3.6 shows how mPole=(θ, ϕ), is defined. For detailed definitions and examples, please refer to Appendix B.

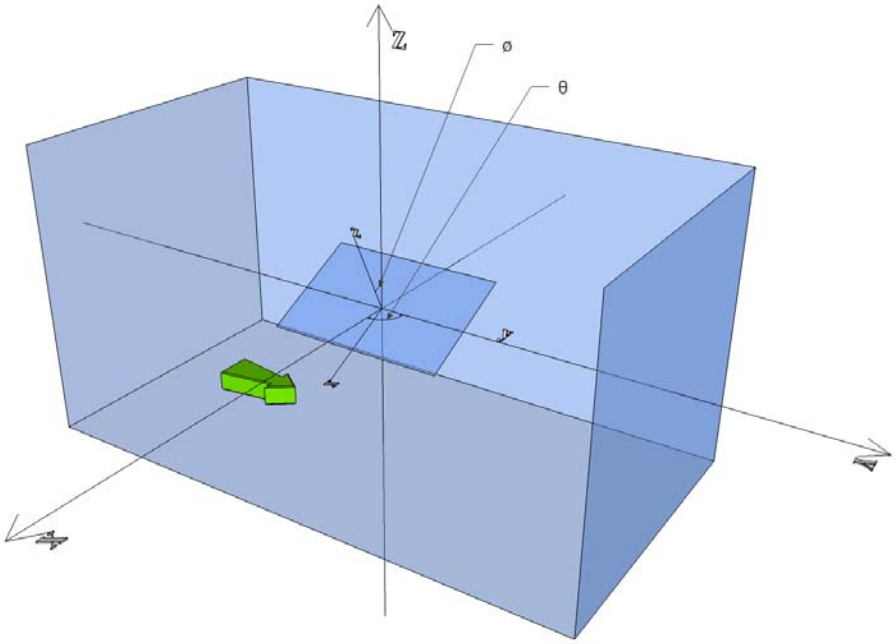

Figure 3.6 Definition of mPole

"rot" is the rotation of fractures in the tertiary process in GEOFRAC. When rot=1, the fractures will be randomly rotated based on a uniform orientation distribution. When rot=0, the fractures will not be randomly rotated.

"fvalue" is the aperture of the fractures. In GEOFRAC, fracture apertures can be generated using both deterministic method and probabilistic method. The deterministic method directly assign all the fractures one value for apertures. The probabilistic methods generates the apertures that follows a truncated log normal distribution.

3.1.3. Outputs

"NON" (Number of Nodes) and "NOB" (Number of Branches) are used to indicate the complexity of the fracture network. They are the total number of nodes and branches in the one simulation, respectively. Higher values of "NON" and "NOB" indicate more complex fracture networks.

"Flow Existence" is an indicator of the probability of having a reservoir with fluid flowing through it. It equals the ratio of the number of cases with flow to the number of all the cases. It is an output associated with GEOFRAC-FLOW (see Section 3.2), but as it reflects the conductivity of the fluid, it is considered to be a fracture network parameter.

"Graphic Results" are the plots of all the fractures after the simulation is done. They provide a graphic impression of the fracture network. Figure 3.7 is an example of the graphic output provided by GEOFRAC.

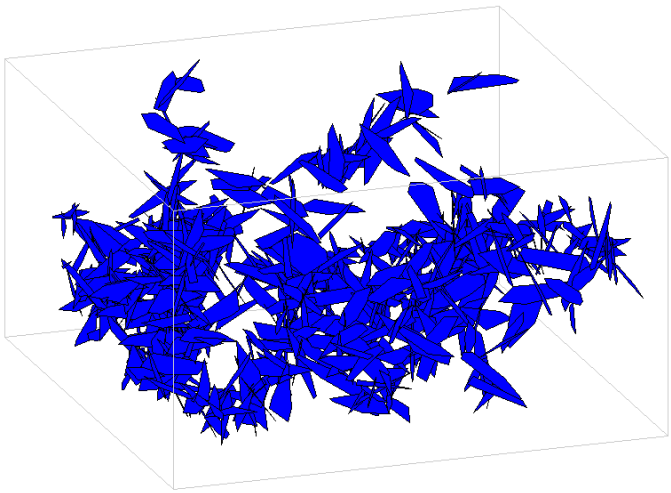

Figure 3.7 Graphic Output Generated by GEOFRAC

3.2.GEOFRAC-FLOW

3.2.1. Algorithm

On the basis of the DFN generated by GEOFRAC, a flow model was developed by Sousa et al. (2012). Because this discrete fracture model accounts for individual fractures, fluid flow is calculated explicitly in each fracture. As derived in Section 2.2.2, the flow rate in each fracture is:

$$Q = \frac{w\delta^3 \Delta P}{12\mu\Delta L} \tag{3.2}$$

where,

Q is volumetric flow rate;

w is fracture width;

μ is fluid dynamic viscosity;

δ is aperture of the fracture;

$\Delta P/_{\Delta L}$ is pressure gradient.

This equation is an idealized case. In reality, flow through fractures differs from the cubic law because of the following four factors:

1. Surface roughness of the fractures.
2. Flow path tortuosity. The path in the fracture is not straight; the direction changes cause water head loss.
3. Surface contact in a rock fracture. The aperture of a fracture is not constant; there are regions where the two fracture surfaces contact each other.
4. Local water head loss at fracture intersections.

Witherspoon et al. (1980) modified Equation 3.2 to account for roughness of the fracture surfaces to the form of Equation 3.4.

$$Q = \frac{w\delta^3 \Delta P}{12f\mu\Delta L} = \frac{w\delta^3 \Delta h_L \gamma}{12f\mu\Delta L} \tag{3.3}$$

$$f = 1 + 6(\frac{\varepsilon}{\delta})^{1.5} \tag{3.4}$$

where,

f is a reduction factor (Witherspoon et al., 1980);

ε is the surface roughness (Jones, Wooten, & Kaluza, 1988), as illustrated in Figure 3.8;

$\Delta h_L / \Delta L$ is fluid head loss;

γ is the unit weight of the fluid.

Figure 3.8 Surface Roughness of Fractures

This modified form has been validated by Witherspoon et al. (1980) in their experiments, and is used in GEOFRAC-FLOW to govern the fluid flow in fractures.

For flow in fracture networks, mass and energy conservation equations are used as governing equations. The fluid head loss along a fracture can be calculated with:

$$\Delta h_L = f \frac{12\mu \Delta L}{\gamma w \delta^3} Q \tag{3.5}$$

As shown in Equation 3.5, head loss is proportional to the length of the fracture, reciprocal to the width and the aperture cubed. Aperture is treated as constant; width is stochastically distributed, so the length of the flow path determines the head loss in of the flow. Fluids tend to flow in the direction which has the greatest pressure gradient, and travel along the paths causing smallest head loss. In the model, paths are chosen as the shortest connection between the inlet fracture and outlet fracture. These connections can be found by using the Dijkstra's algorithm (Dijkstra, 1959). After the paths are found, a flow path network is built as shown in Figure 3.9 below:

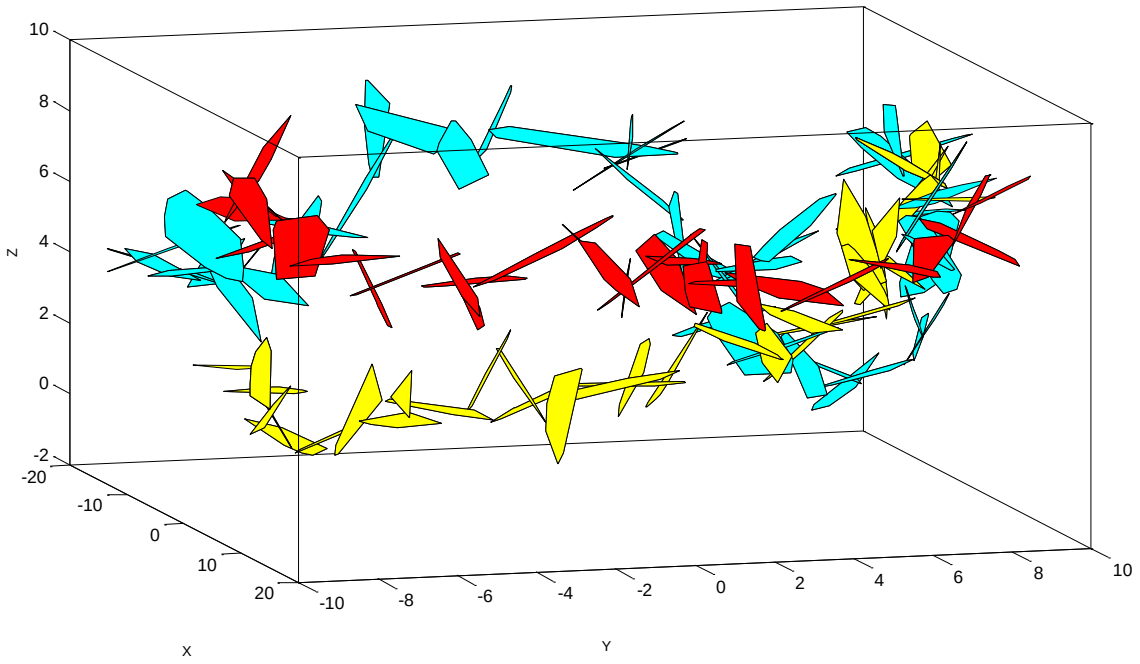

Figure 3.9 Example of Flow Network (Sousa, R.L 2012)

In Figure 3.10, each fracture is represented by a single line, so that the geometry of the fracture network can be better presented.

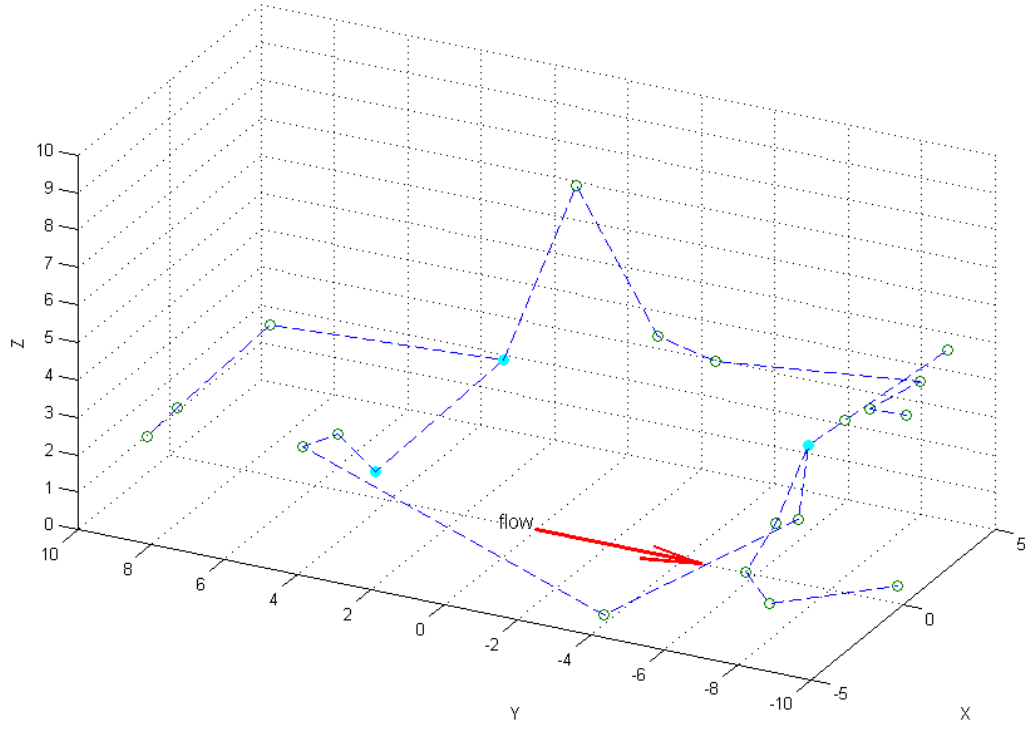

Figure 3.10 Simplified Flow Network

To reduce computational cost, the fracture network is simplified by using one branch to equivalently represent the fractures from one node (intersection) to another. The equivalent fracture aperture, length, and width are expressed below.

$$\delta_{eq} = \frac{1}{\sqrt[3]{\sum_{i=1}^{n} \frac{l_i}{l}\left(\frac{1}{\delta_i^3}\right)}} \tag{3.6}$$

$$l_{eq} = \sum_{i=1}^{n} l_i \tag{3.7}$$

$$w_{eq} = \frac{\sum_{i=1}^{n} w_i l_i}{\sum_{i=1}^{n} l_i} \tag{3.8}$$

where,

l_i is the length of the i^{th} fracture;

δ_i is the aperture of the i^{th} fracture;

l is the total length of the series of fractures.

w_i is the width of the i^{th} fracture.

The mass and energy conservation equations are solved at the nodes in the network to calculate the flow rate in all the branches. The final result of the flow model is shown in Figure 3.11. The size of the simulated reservoir is 10*20*10 m^3, the blue colored values indicate the flow rate (*L/s*). The maximum Reynolds number of all the flows in the 8 branches is 1086.24, satisfying the laminar flow assumption very well.

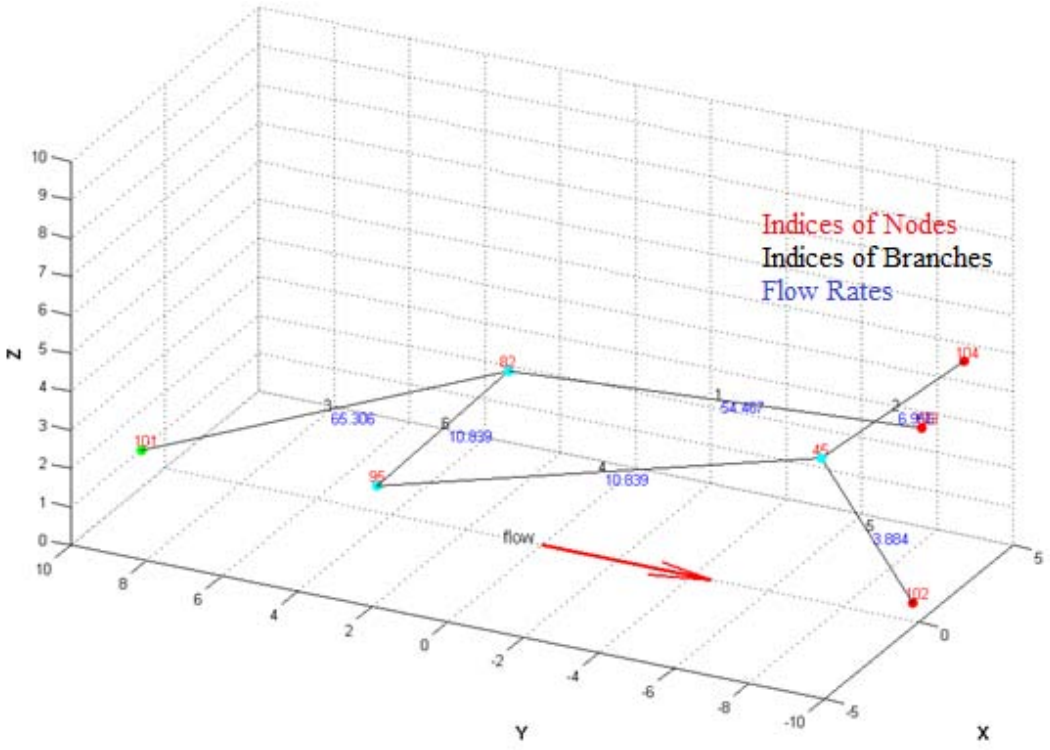

Figure 3.11 Results of GOFRAC-FLOW

3.2.2. Inputs

"Pin" and "Pout" are the injection and production well pressures. The flow rate is dependent on the difference between the two pressures, but it is necessary to keep both of them because the wells need a certain pressure to keep the water in a liquid phase.

"μ" is the fluid dynamic viscosity. Because it does not change much with temperature, this parameter is assumed to be constant in the model. The dynamic viscosity of water at a temperature of 60°C is used, which is 0.468×10^{-3}Pa·s.

"ε" is the roughness of the fracture surfaces. It is used as a flow model parameter because it accounts for the interaction between fluid and the rough facture surfaces.

3.2.3. Outputs

"Qout" is the total flow rate through the fractured rock mass. The since the flow rate can be calculated explicitly for each boundary, "Qout" will be the sum of the flow rates which go into the production well.

"Re" is the Reynolds Number which is used to check the validity of the results. The assumption of laminar flow has to be valid so that the cubic law can be used to calculate the flow rates.

3.3. GEOFRAC-THERMAL

3.3.1. Algorithm

Based on the fracture and flow models, a heat transfer model was developed by Yost and Einstein (2013). For the fluid in each fracture, the heat transfer problem is simplified as uniform wall temperature (UWT) problem and is governed by the UWT heat convection equation for flow between two parallel plates. A sketch of this model is shown in Figure 3.12. The model has the following assumptions:

1. The rock temperature is uniform and constant.
2. The fluid flows between two parallel plates is laminar and steady.

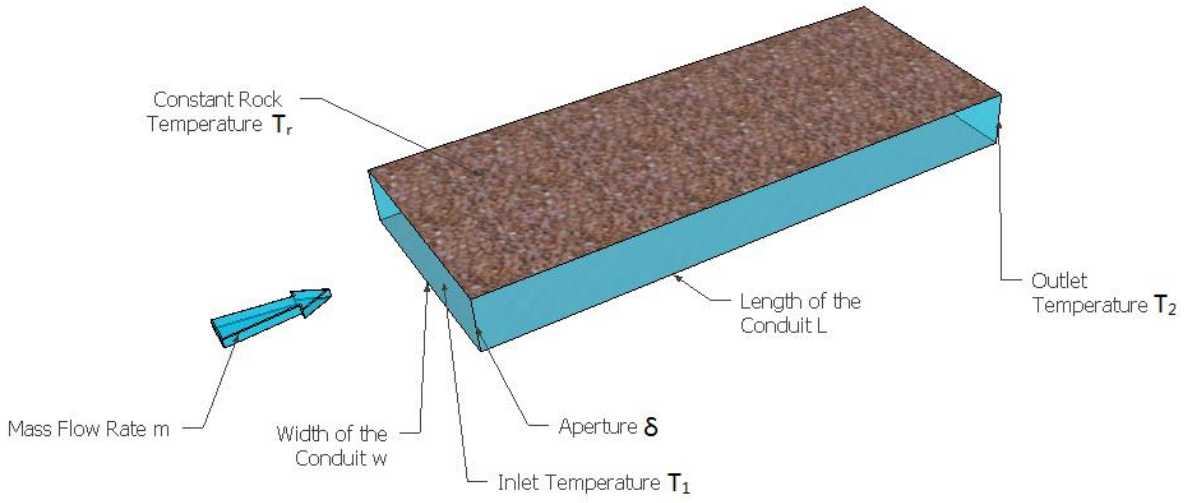

Figure 3.12 Heat Transfer of Fluid Flowing between Two Parallel Plates

$$T_2 = T_r - (T_r - T_1)\exp(-\frac{h_T PL}{\dot{m} C_{Pf}}) \tag{3.9}$$

$$h_T = \frac{Nu \times k_f}{D_h} \tag{3.10}$$

where，

T_1 and T_2 is the temperature of the fluid at the inlet and outlet, respectively;

T_r is rock temperature, in this model it is an constant;

h_T is heat convection coefficient;

P is perimeter 2(δ+w);

L is the fracture length;

$\dot{m}$ is the mass flow rate;

C_{pf} is the specific heat capacity;

k_f is the fluid heat conductivity;

D_h is the hydraulic diameter of the conduct.

Nu is Nusselt number, which is the ratio of convection to pure conduction heat transfer:

$$Nu = \frac{h_T L_C}{k_f} \tag{3.11}$$

where, L_C is the characteristic length, it is the hydraulic diameter in equation 3.12.

Nu is related to flow state, and the dimensions of the parallel plates. Laminar flow between two isothermal parallel plates, usually have long thermal entrance length L_{eh}. L_{eh} is defined as the distance required for the Nusselt number to decrease to within 5% of its fully developed value $N_{u\infty}$.

$$L_{eh} = 0.017 Re_D Pr D_h \tag{3.12}$$

where，

R_{eD} is the Reynolds Number, for laminar flow, R_{eD}<2300;

Pr is the Prandtl number, $Pr = \frac{C_p \mu}{k} = \frac{4200 \times 0.001}{0.58} = 7.24$;

To simplify the calculation, average Nusselt number is used(Mills, 1995).

$$\overline{Nu_{D_h}} = 7.54 + \frac{0.03(D_h/L) Re_{D_h} Pr}{1 + 0.016[(D_h/L) Re_{D_h} Pr]^{2/3}} \tag{3.13}$$

$$Re_{D_h} \leq 2800 \tag{3.14}$$

This model explicitly calculates the heat transfer in each fracture and obtains the temperature of each node by weight averaging the temperature of the inflowing branches. Although the assumptions idealize the physical process, the model can capture the basic heat transfer problem between the rock and the fluid. Figure 3.13 is an example of the results produced by the heat transfer model. In addition to the results from the fracture network model GEOFRAC and flow

model GEOFRAC-FLOW, the heat transfer model calculated the temperature of the fluid at each node, as indicated in purple in Figure 3.13.

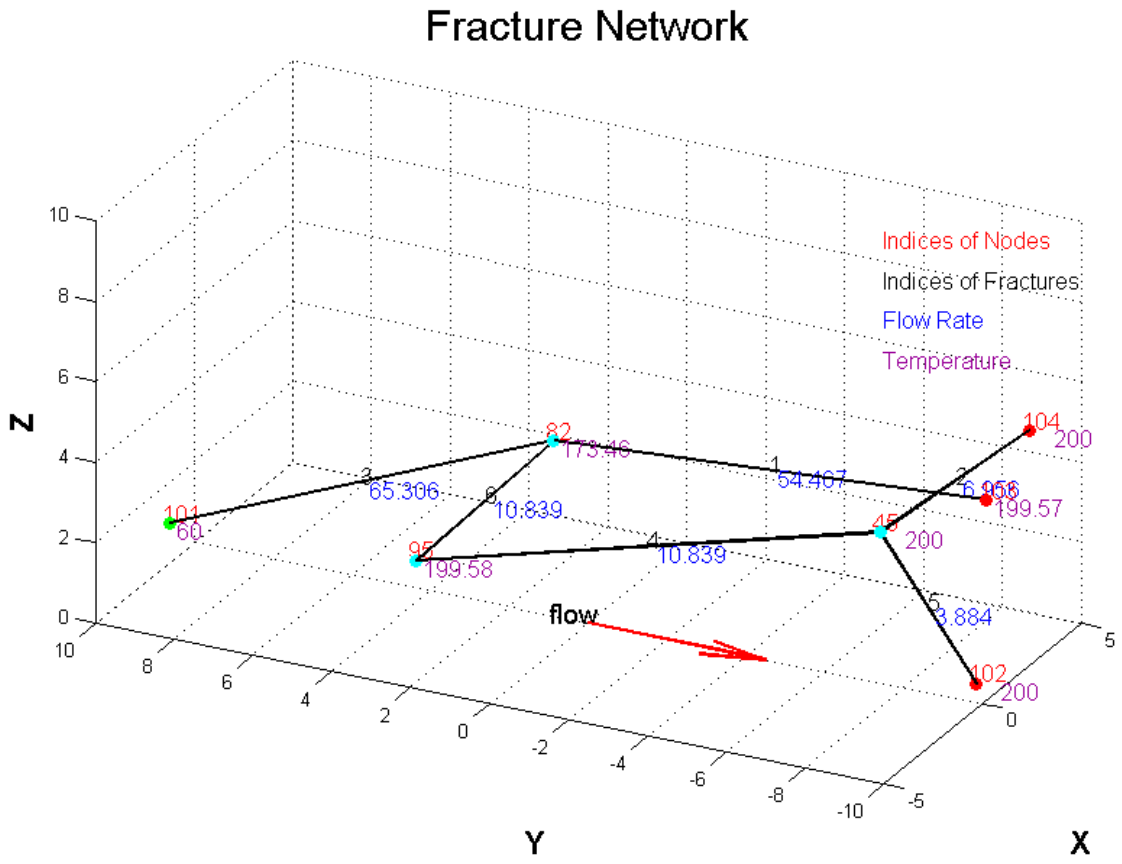

Figure 3.13 Example of the Results Produced by GEOFRAC-THERMAL

3.3.2. Inputs

"kt", the thermal conductivity of water; "ρ", the density of water; "Cp", the heat capacity of water are material properties that do not change much with temperature. In the model they are all constants, kt=0.58W/(m·°C), $\rho=10^3 kg/m^3$, Cp=4.168J/(kg·°C).

"Trock" is the rock temperature. Since the heat transfer problem is simplified as a uniform wall temperature problem, only one temperature is assigned to the model as the uniform wall temperature.

"Tin" is the injection water temperature. In a heat exchanger-based EGS plant, temperature of the water out of the exchanger is then reinjected in the reservoir, so "Tin" is often in a small range of temperature.

3.3.3. Outputs

"Tout" is the production well temperature. It can reflect the efficiency of the heat transfer between the fluid and the rock. In a geothermal plant, it is one of the factors that determine the type of energy converter. For high temperature production wells, steam engines are often used. For low temperature production wells, binary heat exchangers are often used.

"Eout", energy extraction rate, is the thermal energy extracted by the water circulation per unit time, as defined in Equation 3.15. It is one of the factors that determine the capacity of the electricity plant.

$$Eout = (Tout - Tin) \times Qout \times \rho_f \times C_{pf} \tag{3.15}$$

where,

ρ_f is the density of the water;

C_{pf} is the specific heat capacity of the water.

3.4. Parametric Study with the Three Coupled Models

3.4.1. Scheme of Parametric Study

The three models are built to simulate the heat and mass transfer in the fractured geothermal reservoir. The hierarchy of the three coupled models is shown in Figure 3.14. For now, the three models are not fully coupled, which means a change of parameters at a lower level will affect the result at the higher level, but changes of parameters at a higher level will not affect the result at the lower level.

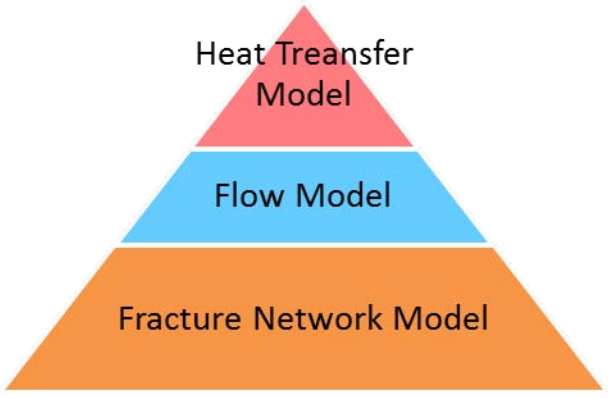

Figure 3.14 The Hierarchy of Three Coupled Model

The three coupled models have a total of 19 parameters. They control the inputs related to reservoir geometry, fracture network, flow, and heat transfer. The following map (Figure 3.15) is a structure of the inputs (on the left side) and outputs (on the right side) of the models.

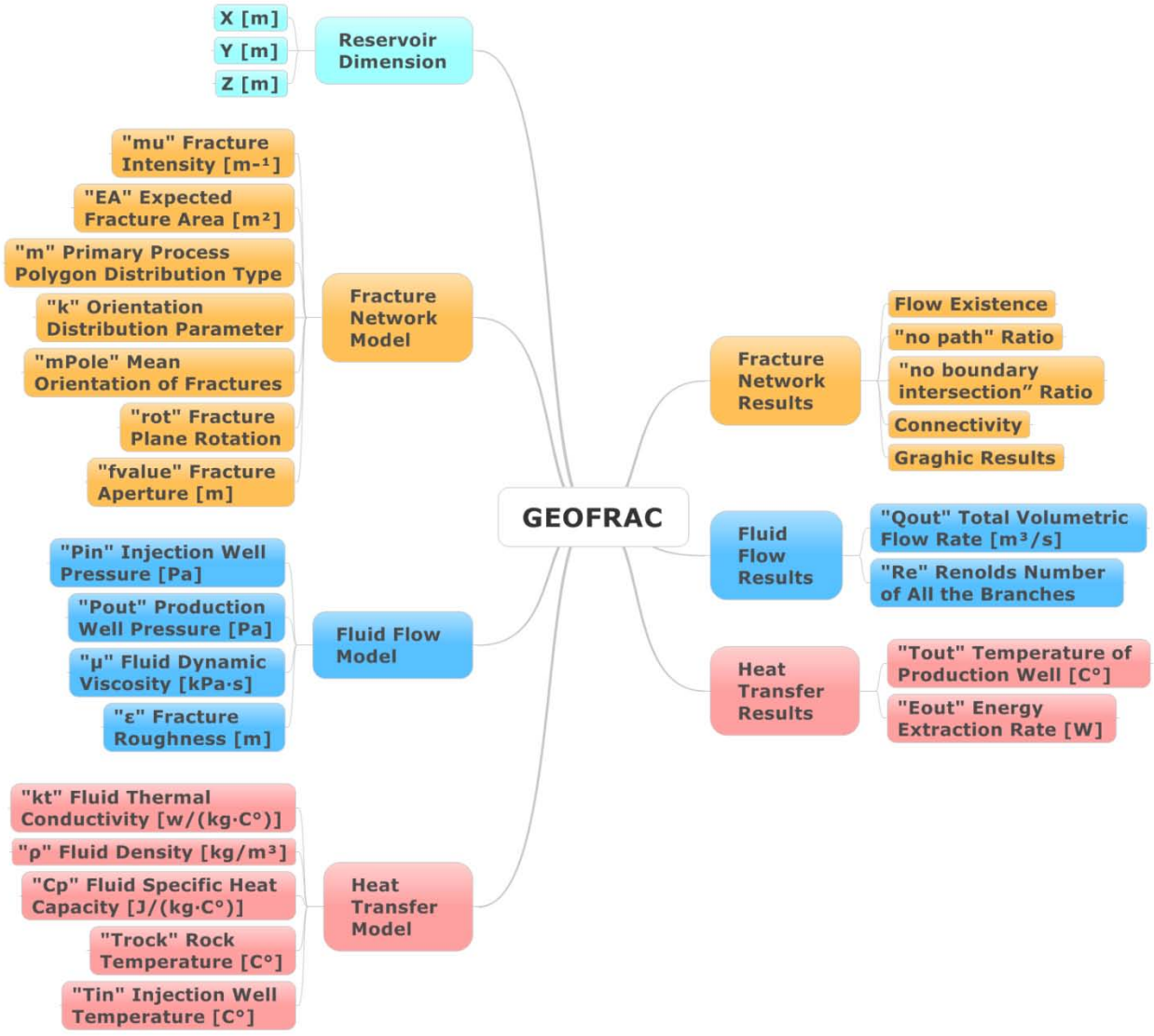

Figure 3.15 Structure of Parameters

With so many inputs for the models, it is necessary to systematically conduct parametric studies with the models. Parametric studies can assess the effects that changing certain parameters can have on the results. They can help the model developer to check the validity of the model, and also help the model user to better understand the models.

Because the models represent a stochastic process, one result for each parameter combination is not representative. In the parametric studies, 20 flow rate results are used to produce a mean value

for flow rates. Because some of the simulation runs cannot generate a result with a flow path for a particular parameter combination, there can be more than 20 simulations to generate 20 flow rates. 20 results may not be representative, but can reflect a trend. A study on the proper number of simulations that should be run is included in Appendix C.

The parametric studies with the three models are conducted in the following way. A set of reference parameter is chosen, and one parameter is varied each time to see how the results will differ from that with the reference parameter.

Table 3.1 shows the reference parameters.

Table 3.1 Reference Parameters

mu (m^{-1})	EA(m^2)	m	k	mPole	rot	fvalue (m)	ε	X (m)
1.5	5	4	1	[π/2, π/2]	0	0.0005	0.0005	10
Y (m)	Z (m)	ΔP (Pa)	μ (Pa·s)	kt (W/m·K)	ρ (kg/m^3)	Cp (J/kg·K)	Tr (C°)	Tw (C°)
20	10	5000	0.468×10^{-3}	0.6546	983	4185	200	60

3.4.2. Fracture Intensity "mu"

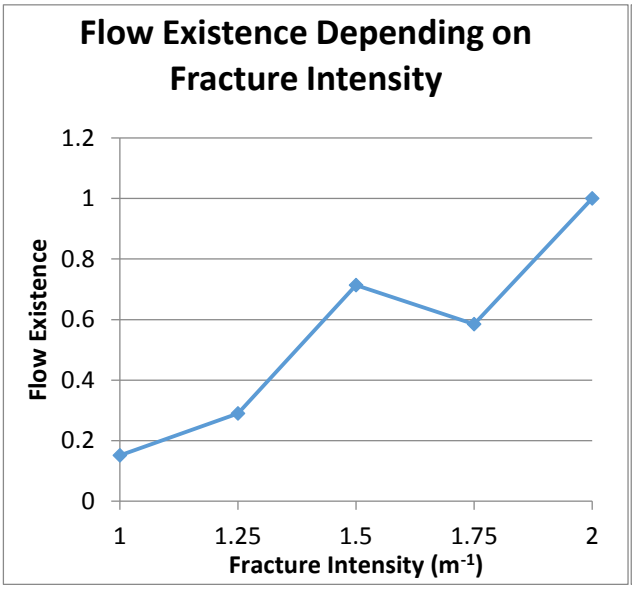

Figure 3.16 Flow Existence

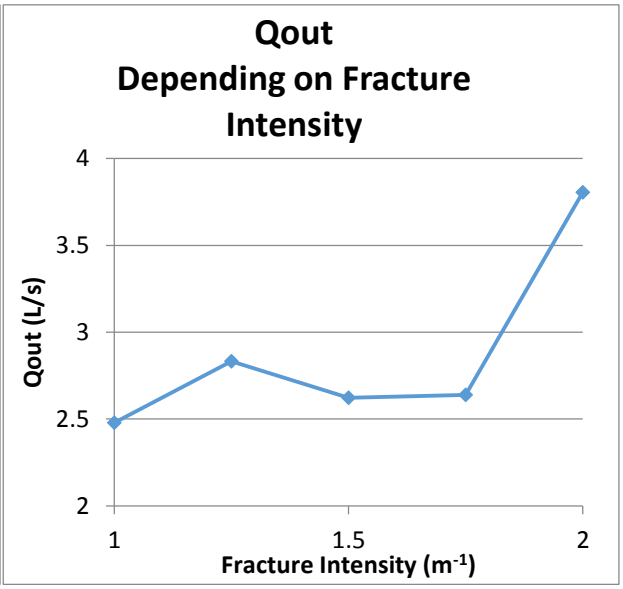

Figure 3.17 Total Flow Rate

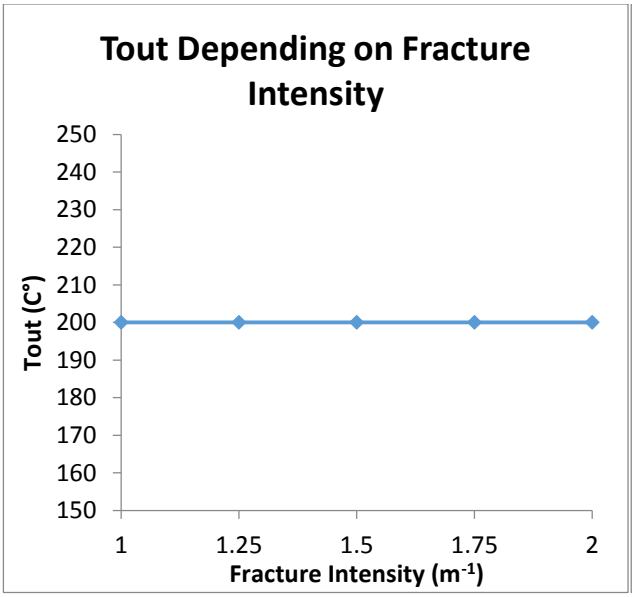

Figure 3.18 Production Well Temperature

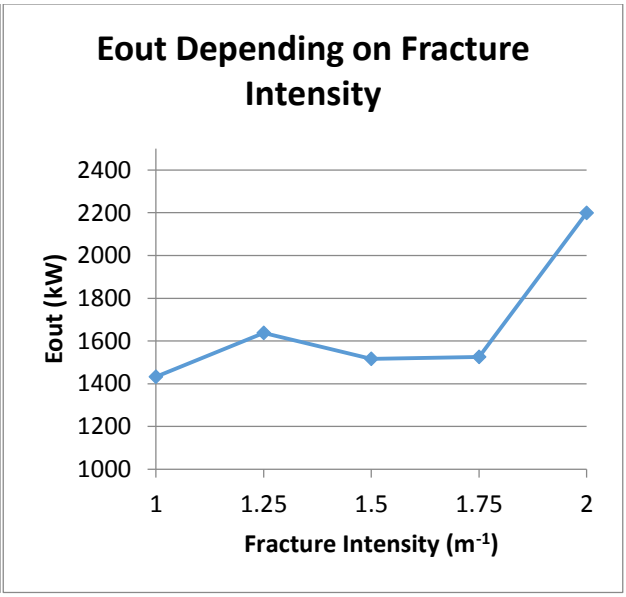

Figure 3.19 Energy Extraction Rate

With higher fracture intensity, it is more likely to have paths in the reservoir; and the flow rates are also higher. Figure 3.16 and 3.17 somehow show this trend, but not exactly because of the limited number of simulations for each parameter combination. The output temperature is the same as that of the rock, as shown in Figure 3.16; this is so because of the high efficiency of heat transfer. As the temperature is the same as that of the rock, the heat extraction rate is proportional to the flow rate, as shown in Figure 3.17 and Figure 3.19.

3.4.3. Expected Area "EA":

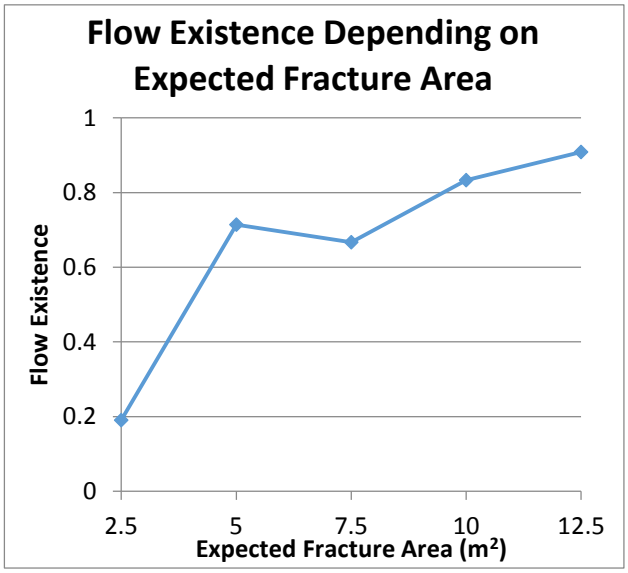

Figure 3.20 Flow Existence

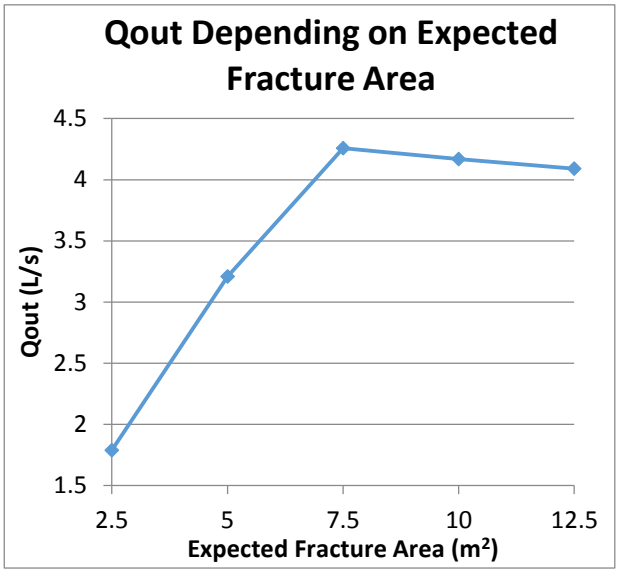

Figure 3.21 Total Flow Rate

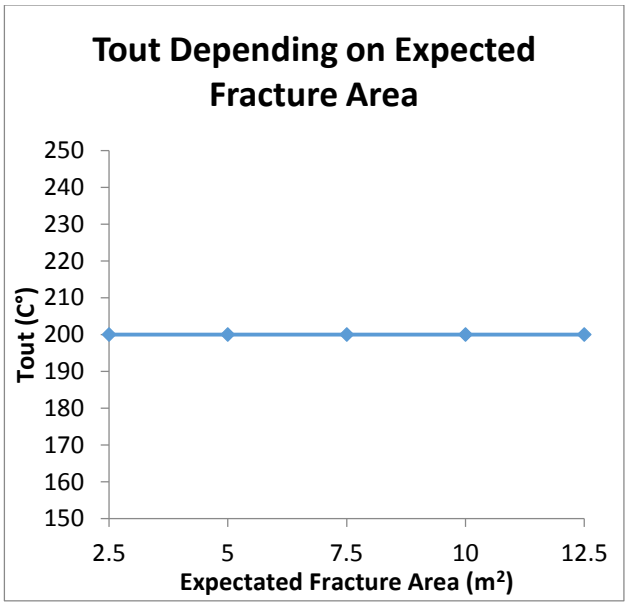

Figure 3.22 Production Well Temperature

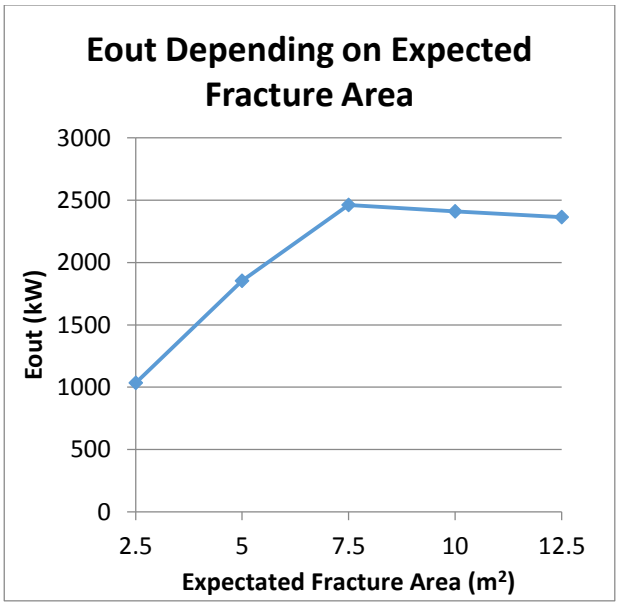

Figure 3.23 Energy Extraction Rate

When the fracture intensity is fixed while varying EA, larger EA would produce a smaller number of fractures. Smaller fractures are less likely to intersect with each other, and flow paths are hardly created. Larger fractures are more likely to intersect with each other, but because of the small number of them, fewer flow paths are created. These characteristics indicate that the curve in Figure 3.20 should be increasing and the curve in Figure 3.21 should be concave downward. Figure

3.21 matches the prediction very well, but Figure 3.20 does not, probably because of the limited number of simulations. “Tout” and “Eout” are similar to section 3.4.2.

3.4.4. Mean Orientation and Orientation Distribution:

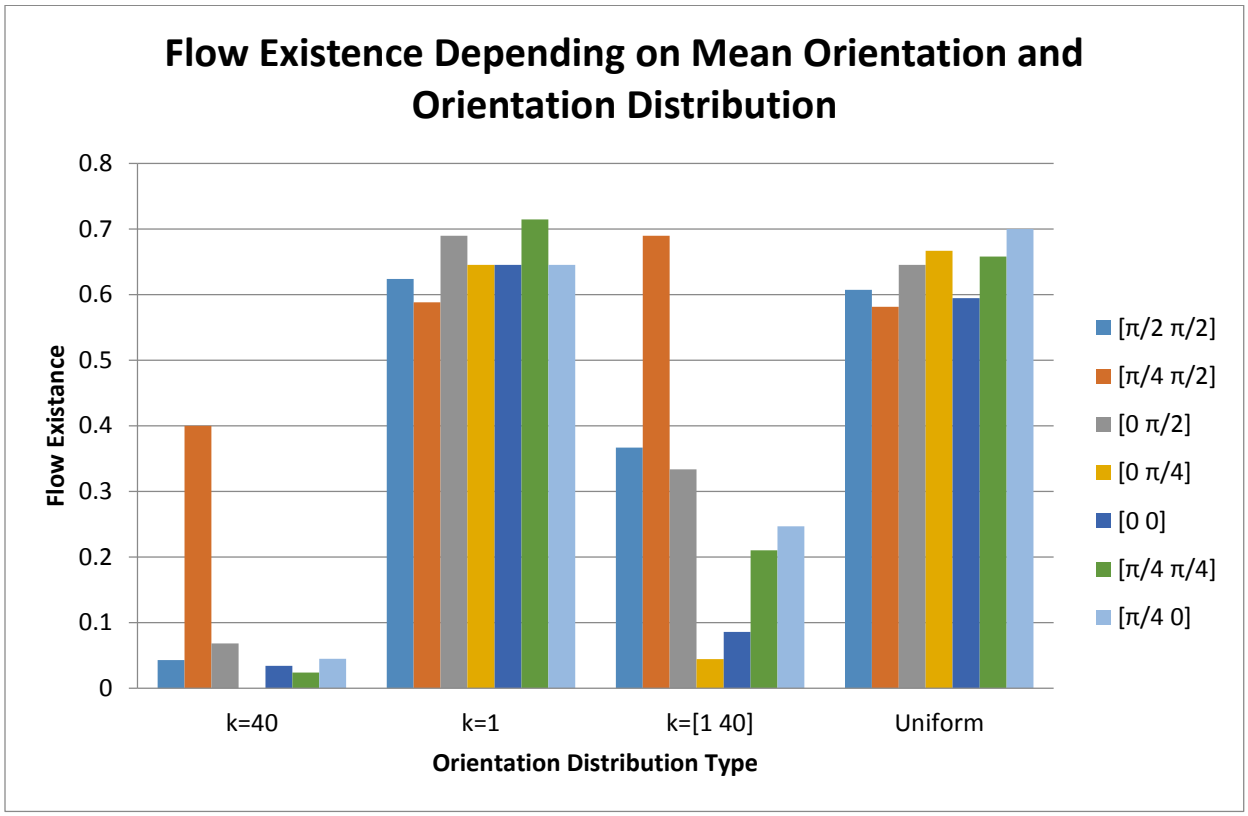

Figure 3.24 Flow Existence

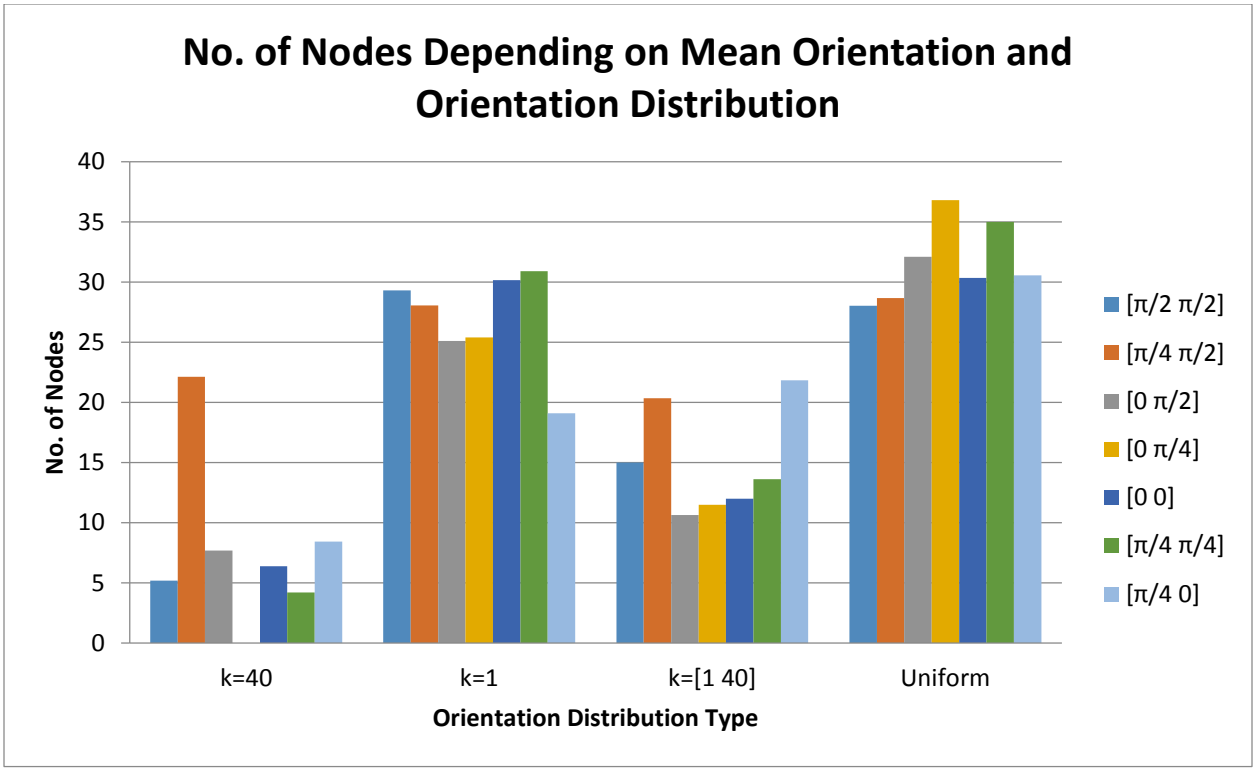

Figure 3.25 Number of Nodes

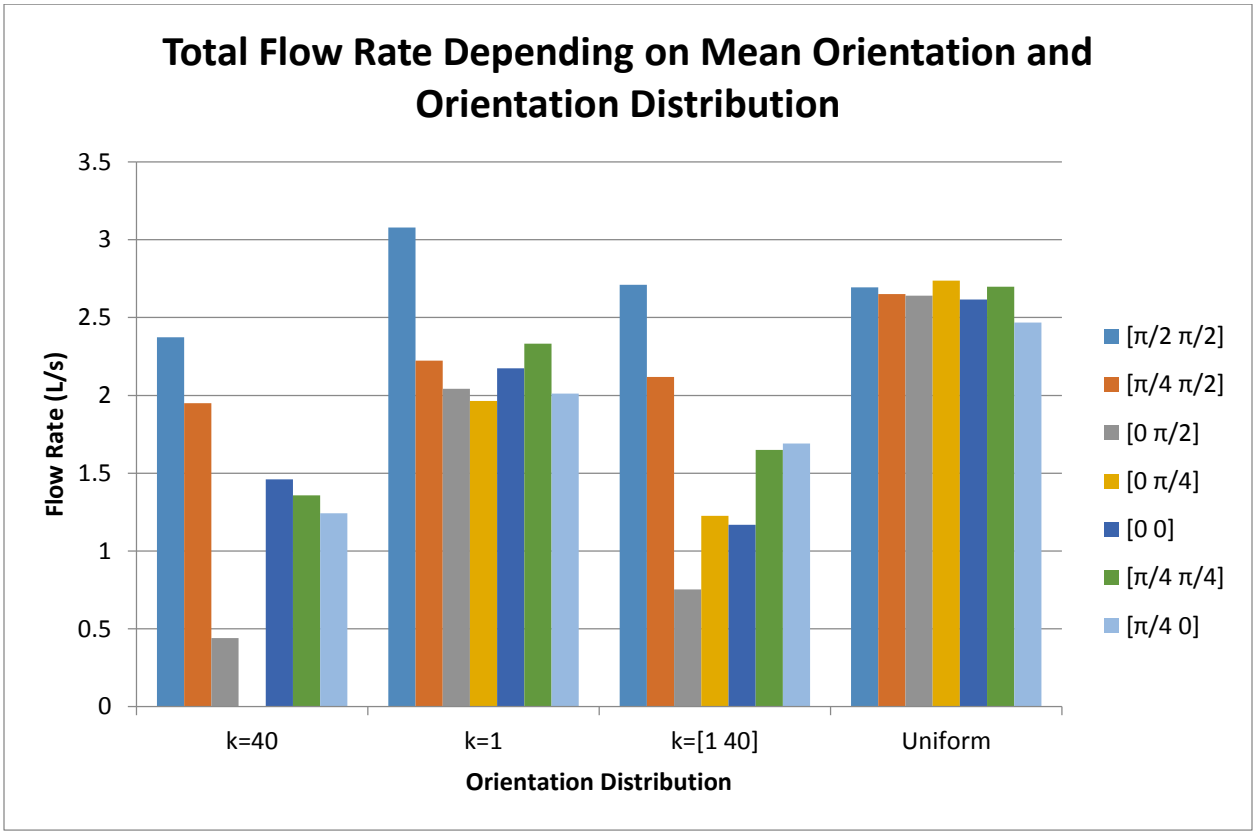

Figure 3.26 Total Flow Rate

Effect of Orientation Distribution

1. Figure 3.24 shows that, generally, the Fisher distribution with k=1 has the highest chance of having flow paths in a reservoir. The uniform distribution is second, followed by bivariate Fisher with k= [1, 40]. This can be explained by looking at the orientation distribution (Appendix A). A more uniform distribution of orientation has greater chances to have flow paths.
2. When the orientation distribution is more uniform, it will result in a smaller difference among the 7 mean orientations, as shown in Figure 3.24 and 3.25.
3. Figure 2.25 shows that with more uniform orientation distributions the model produces more complex fracture networks.
4. In Figure 3.26, the flow rates of different mean orientations have significant deviations even for the uniform distribution. It is hard to see any trend. But fracture networks with more uniform orientations tend to have higher flow rates.

Effect of Mean Orientation

1. Mean orientation has an influence on the Flow Existence, especially when the orientation distribution is not uniform. For definition of mean orientations and how it affects the results, please refer to Appendix B. As shown in Figure 3.24, when k=40 or k= [1, 40], the mean orientation [$\pi/4$, $\pi/2$] has a high Flow Existence.
2. As for complexity of the fracture network, the mean orientation [$\pi/4$, $\pi/2$] has a higher chance of forming a complex fracture network, as shown in Figure 3.25. This phenomenon possibly results from the geometry of the reservoir. The reservoir can accommodate more fractures if the fractures' mean orientation is [$\pi/4$, $\pi/2$].
3. In terms of flow rate, fractures with mean orientation [$\pi/2$, $\pi/2$] are more likely to have high flow rates. This can be explained by considering the length of flow path. Fractures oriented [$\pi/2$, $\pi/2$], are vertical fractures that are parallel to the direction of pressure gradient.

3.4.5. Random Rotation:

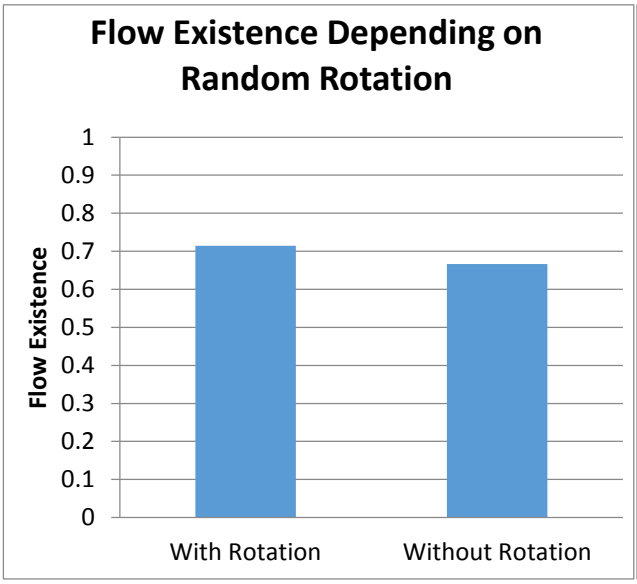

Figure 3.27 Flow Existence

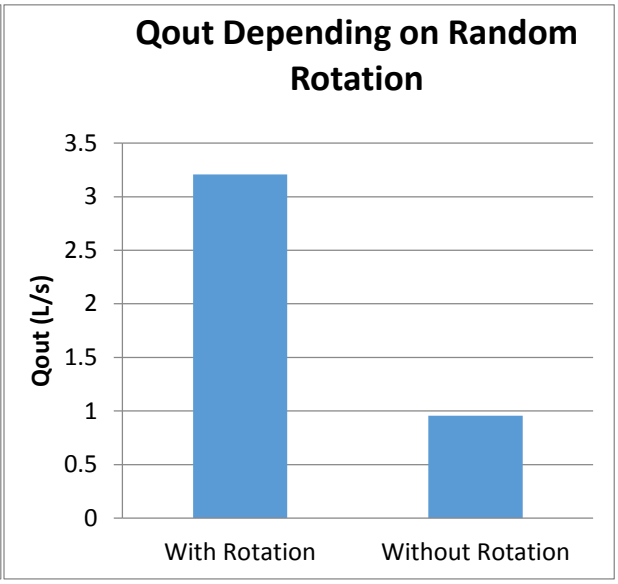

Figure 3.28 Total Flow Rate

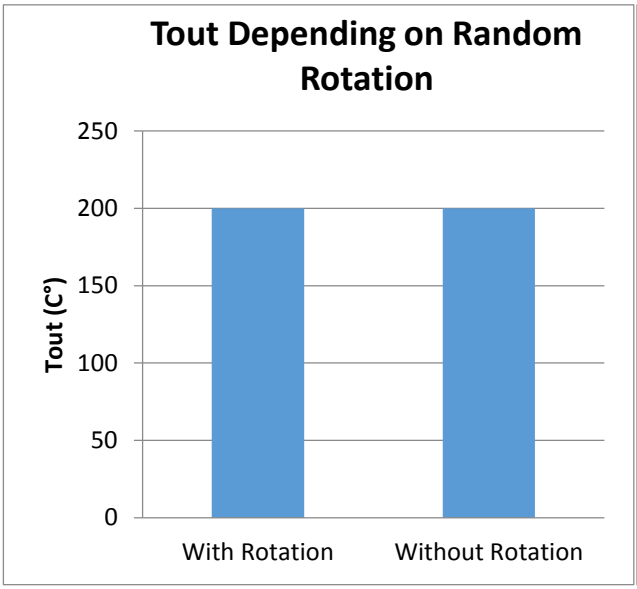

Figure 3.29 Production Well Temperature

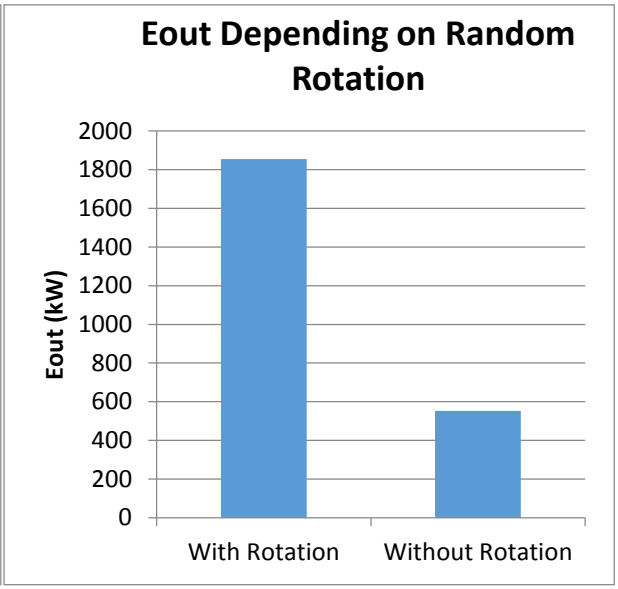

Figure 3.30 Energy Extraction Rate

Fractures with random rotation in the tertiary process are more likely to intersect with each other, have higher Flow Existence, and Qout, as shown in Figure 3.27 and 3.28. Because the random rotation has little influence on the heat transfer efficiency, Tout and Eout are similar to section 3.4.2. The heat transfer efficiency is so high that the temperature of the production well, Tout, is the same as that of the rock, the energy extraction rate Eout is then proportional to the flow rate Qout.

3.4.6. Fracture Aperture:

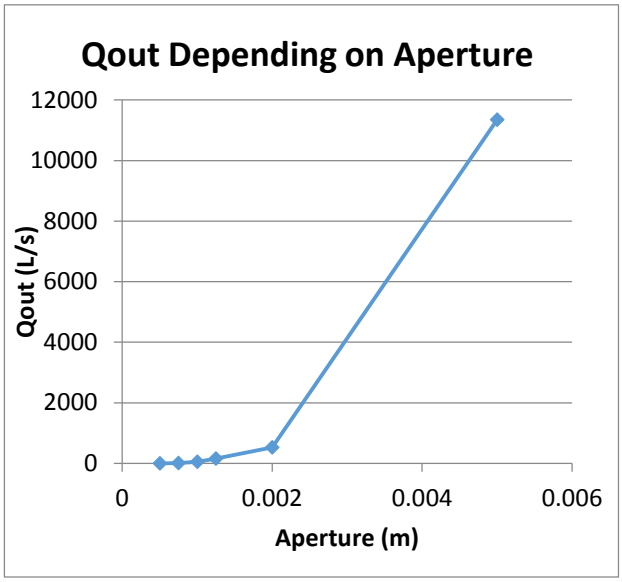

Figure 3.31 Total Flow Rate

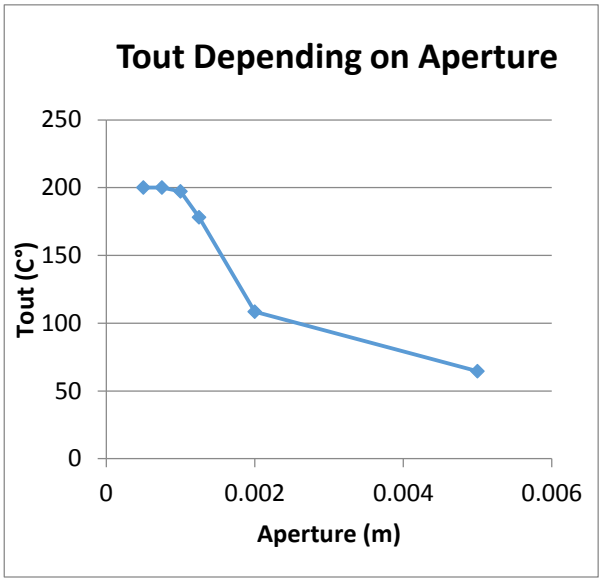

Figure 3.32 Production Well Temperature

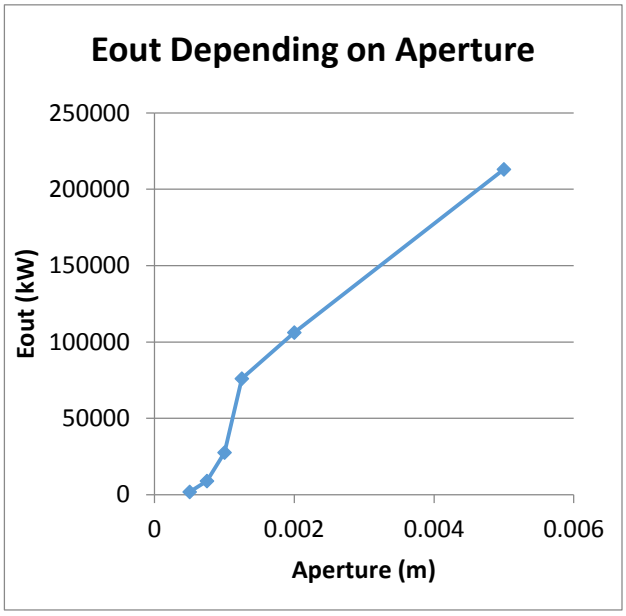

Figure 3.33 Energy Extraction Rate

Fracture Aperture is a variable that is independent of the three fracture generation processes. In theory it should not affect the fracture network variables such as Flow Existence and Number of Branches, but it has a dramatic influence on the flow rates as shown in Figure 3.31. When the aperture becomes wider, the flow rate increases, and the production well temperature decreases, as shown in Figure 3.32. However, the energy extraction rate will still increase because of the high flow rate, as shown in Figure 3.33.

3.4.7. Pressure Difference:

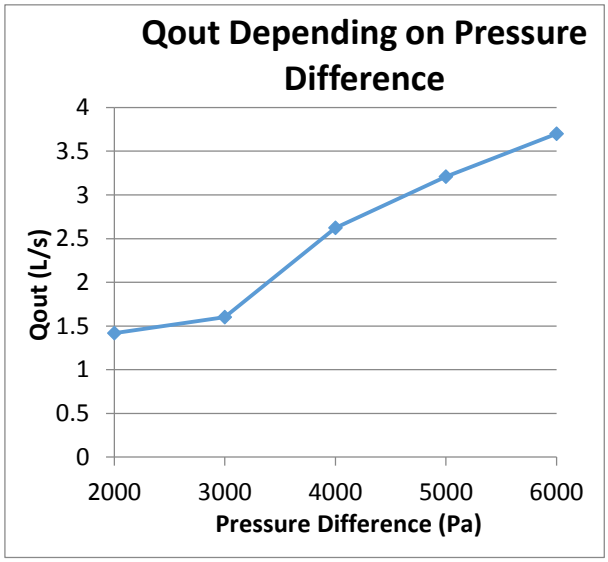

Figure 3.34 Total Flow Rate

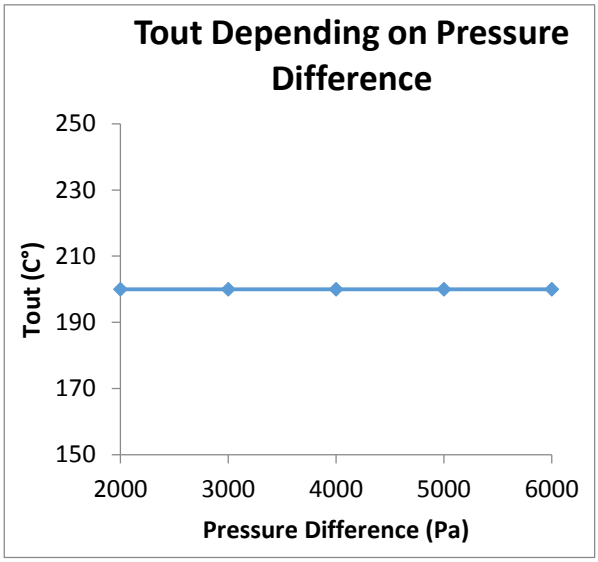

Figure 3.35 Production Well Temperature

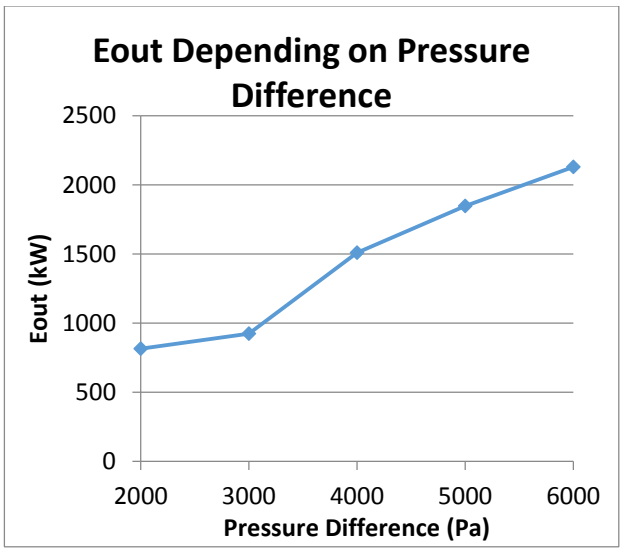

Figure 3.36 Energy Extraction Rate

Figure 3.34 shows that higher pressure results in higher flow rate. This is reasonable because in the modified Cubic Law (Equation 3.3), the flow rate is proportional to the pressure difference. "Tout" is the same as that of the rock even if flow rate increases, as shown in Figure 3.35. This is because of the high heat transfer efficiency and relatively long flow path. As the temperature is the same as that of the rock, Eout, is proportional to the flow rate, Qout, as shown in Figure 3.36.

3.4.8. Rock Temperature:

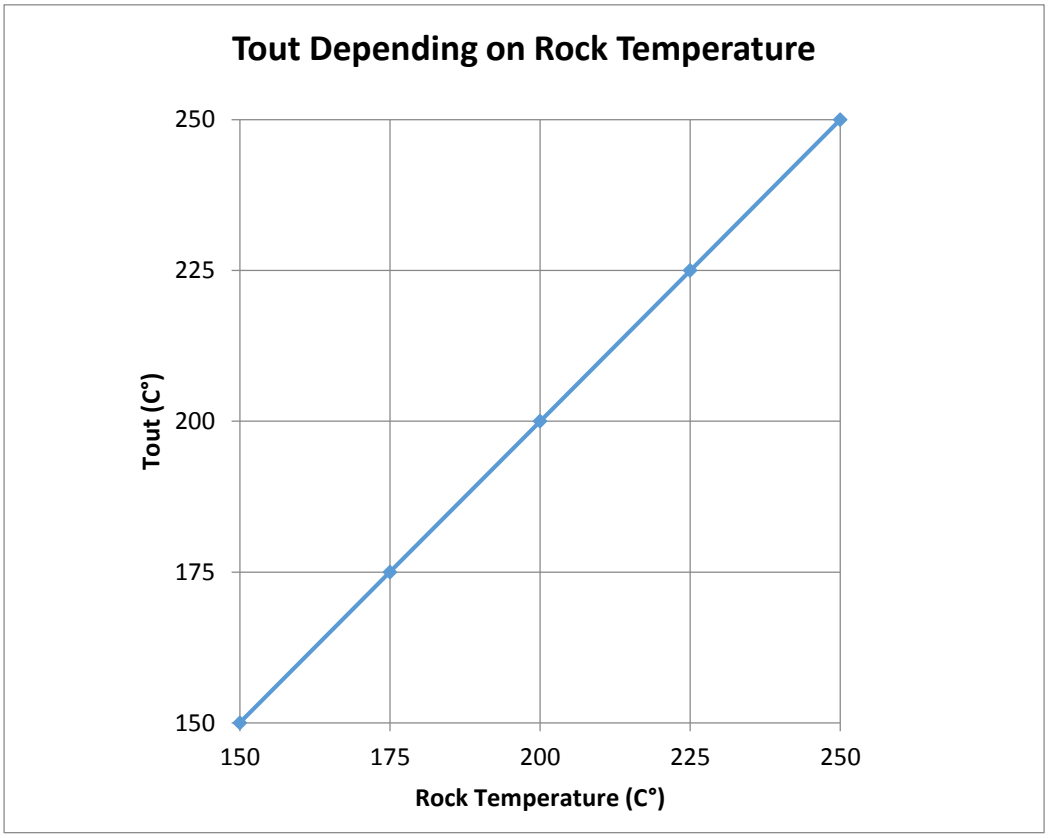

Figure 3.37 Production Well Temperature

As the aperture of the fracture is quite small for base case, the heat transfer process is very efficient; the production well temperature will be the same as that of the rock, as shown in Figure 3.37.

3.5. Case Study with GEOFRAC on the Fenton Hill Project

3.5.1. Project Description

The project at Fenton Hill was the first attempt anywhere to work with a deep, full-scale HDR reservoir. The site – on the edge of the Valles Caldera at the northern end of the Rio Grande rift zone in north-central New Mexico – was chosen for its heat and rock characteristics, as well as its proximity to the Los Alamos National Laboratory where the project was conceived. The purpose of the project was to develop methods to extract energy economically from HDR systems located in crystalline, granitic/metamorphic basement rock of suitably high temperature.

The R&D program was roughly divided into two major phases. Phase I, started with drilling the deep wells GT-2, EE-1, GT-2A and GT-2B in 1974 and completed in 1980. It dealt with field

development and associated research on a 3 km deep reservoir with a temperature of about 200°C. Phase II followed in 1979, with the drilling of EE-2 and EE-3 into a deeper (4.4 km), hotter (300°C) reservoir. Figure 3.36 shows a map of the site with testing wells and the trajectory of the wells before 1979.

Full-scale operation of the loop occurred from January 27 to April 13, 1978 (75 days in total). This part of Phase I was referred to as Segment 2 and was designed to examine the thermal drawdown, flow characteristics, water losses, and fluid geochemistry of the system in detail. In addition, the experimental area was closely monitored for induced seismic activity.

3.5.2. Project Data

The test was done in the 70's, useful data for GEOFRAC was found in the technical report written by Tester and Albright (1979). The plan view of the R&D site is shown in Figure 3.38. The Injection well EE-1 is at the top of the map and the major production well GT-2B is at the bottom of the map.

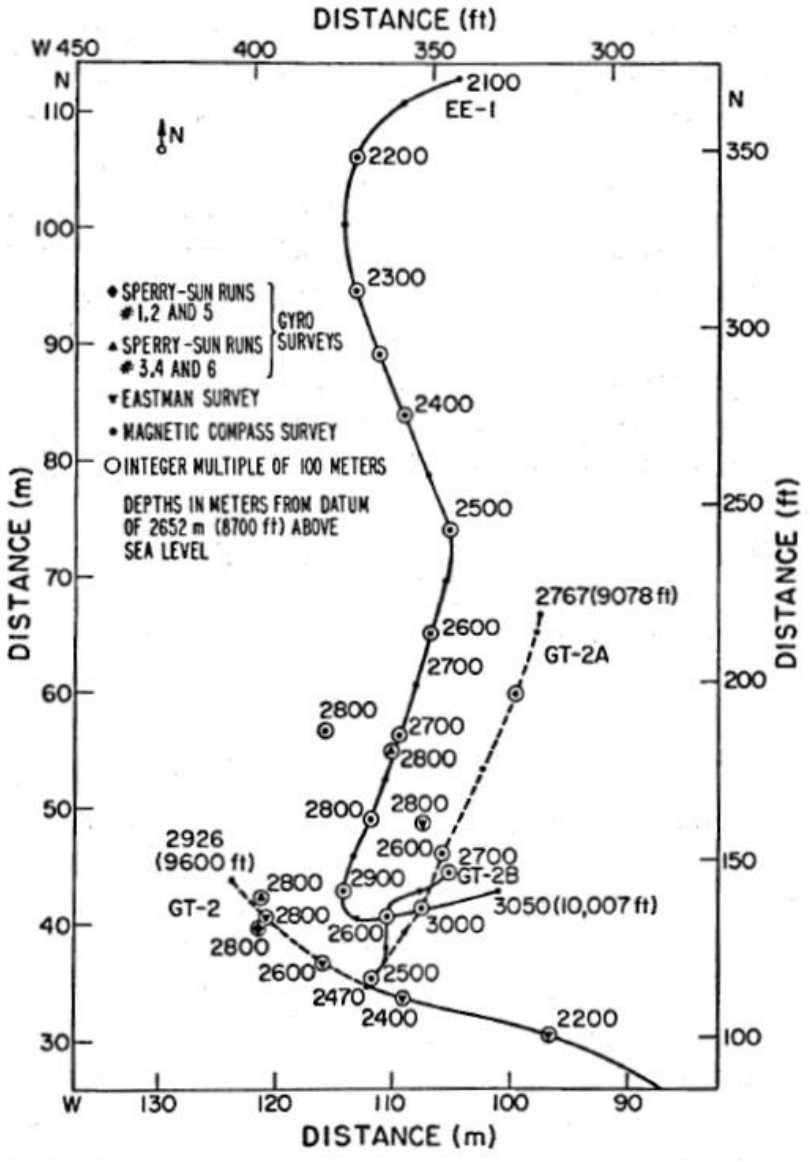

Figure 3.38 Plan View of the Lower Section of the GT-2 and EE-1 Wellbores.

The impedance of the reservoir, which is defined in Equation 3.15, decreased during the circulation. This is why the injection pressure was not maintained, as shown in Figure 3.39 and 3.40.

$$\text{Impedance} = \frac{\text{Injection Well Pressure} - \text{Production Well Pressure}}{\text{Volumetric Flow Rate}} \tag{3.16}$$

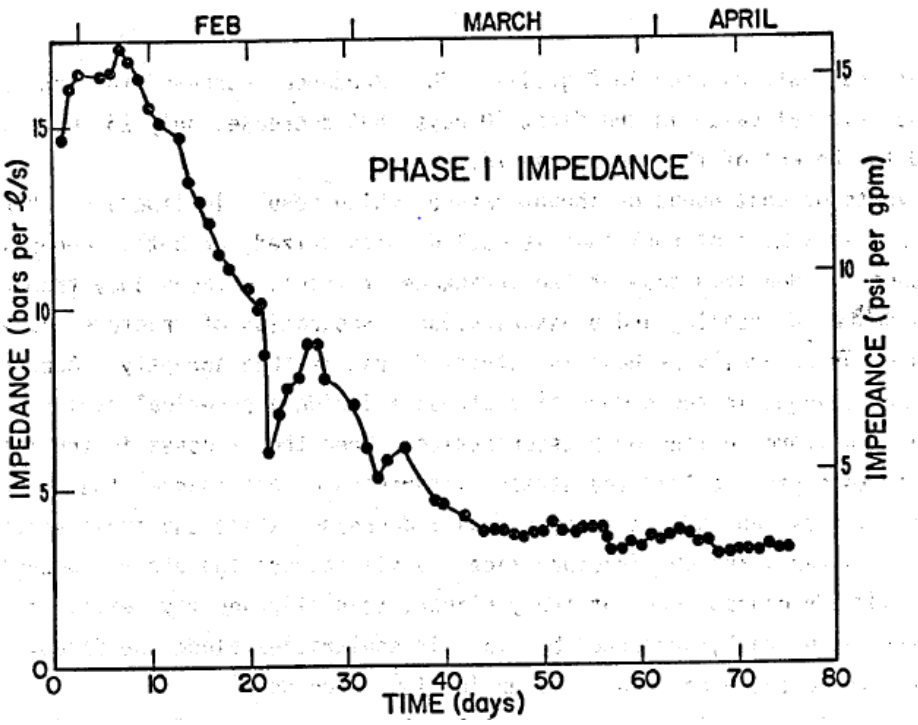

Figure 3.39 Impedance of Fenton Hill Geothermal Reservoir

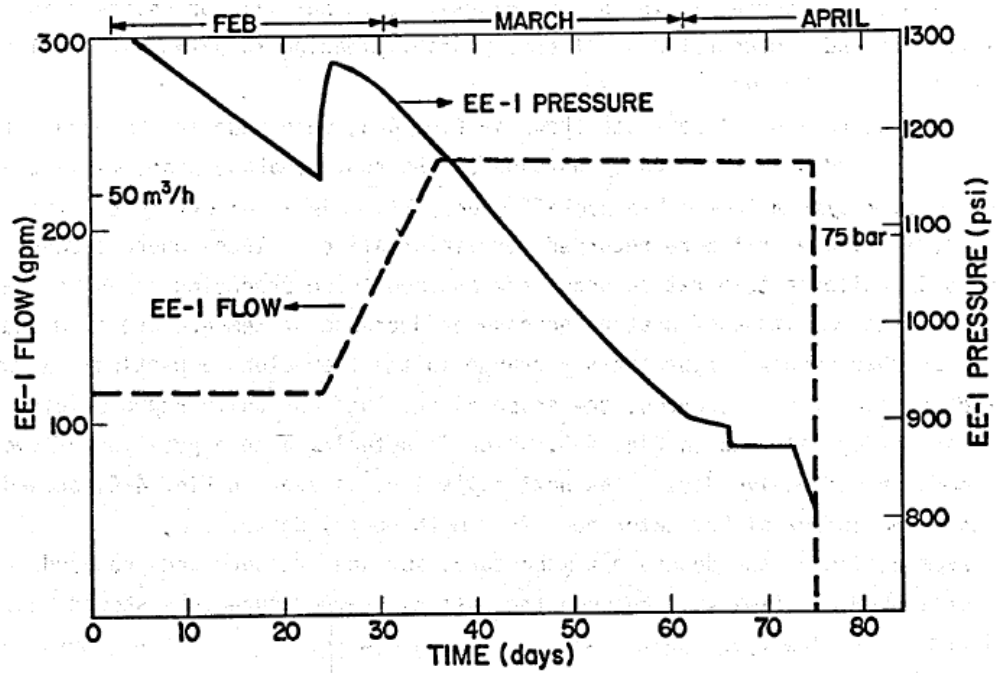

Figure 3.40 Pressure and Flow Rate of the Injection Well

During the injection test, water loss was observed to decrease, as marked in a red loop in Figure 3.41. One explanation was that the decrease of water loss was caused by saturation of the rock, so it is reasonable to assume that there is no water leakage from the reservoir.

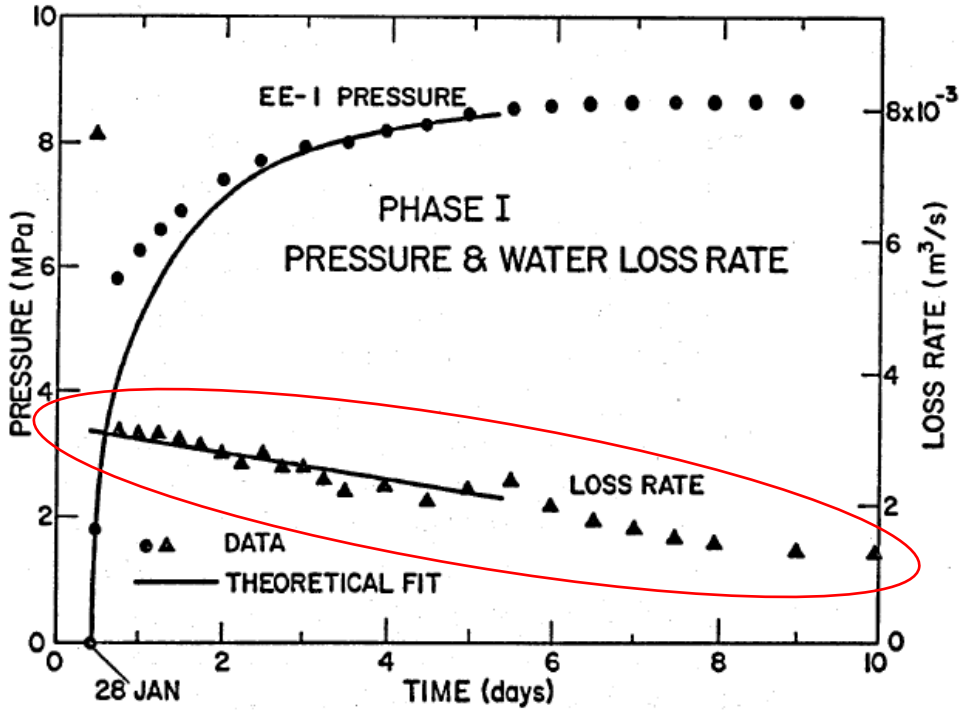

Figure 3.41 Pressure and Water Loss

Thermal drawdown of the production well was also monitored as shown in Figure 3.42 with dots. A single circular fracture thermal drawdown model (Harlow & Pracht, 1972) was used to simulate the thermal drawdown, and the results are shown with the continuous curve in Figure 3.41.

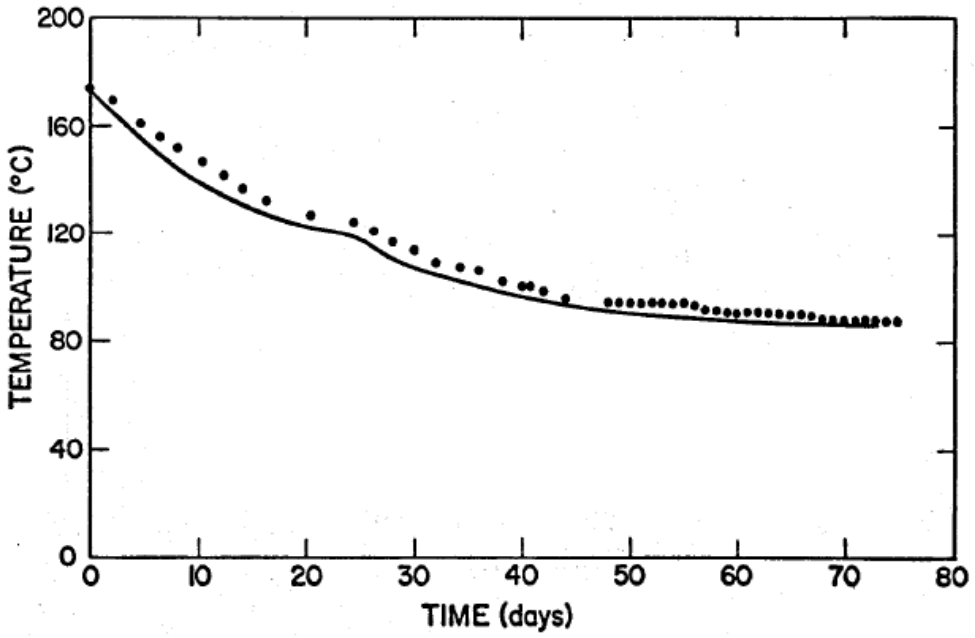

Figure 3.42 Measured and Modeled Thermal Drawdown of Production Well

In Figure 3.43, the thermal power (the same as energy extraction rate) of the closed loop test is plotted. Although thermal drawdown was observed as shown in Figure 3.42, the increasing flow rate maintained the high heat extraction rate after the day 50 as shown in Figure 3.43.

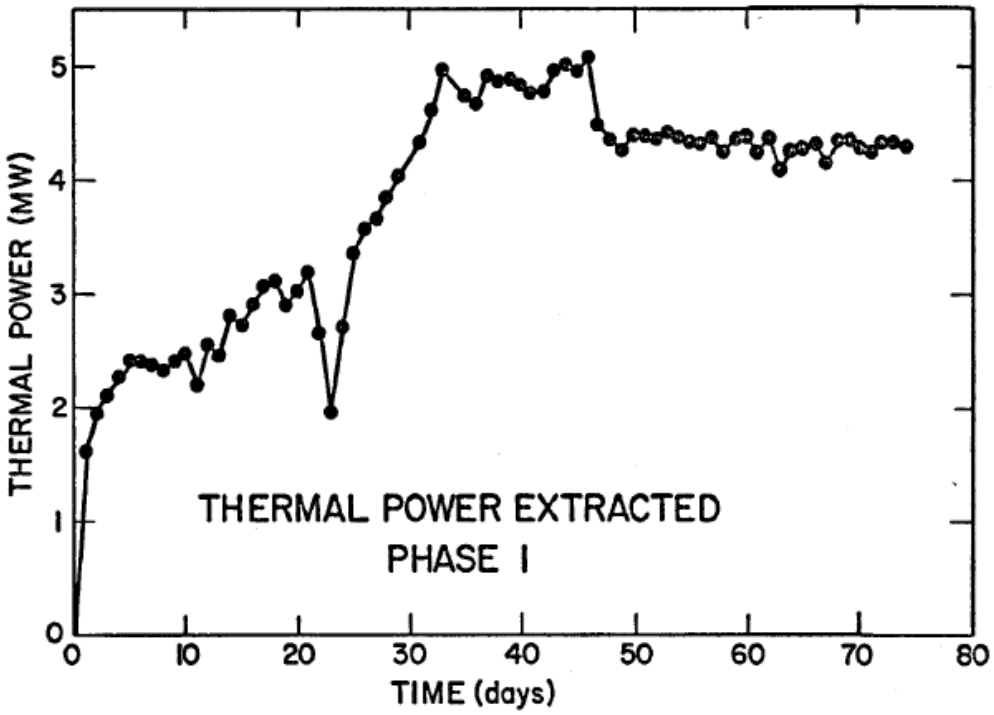

Figure 3.43 Heat Extraction Rate

The main production well is GT-2B; 90% of the production is from this well. Thus, the reservoir can be simplified as a two-well system, which can be modeled by the current GEOFRAC models.

Rock temperature was not measured directly. However, the initial water temperature in the well was measured, and was close to that of the rock and could be used as rock temperature.

The fracture network might consist of several major fractures connecting the injection and production well, as judged by the researchers of the project. As shown in Figure 3.44, the temperature profile had some sudden jumps, each of which indicated that there was a fracture conducting fluid at this depth, making the measured temperature non-continuous.

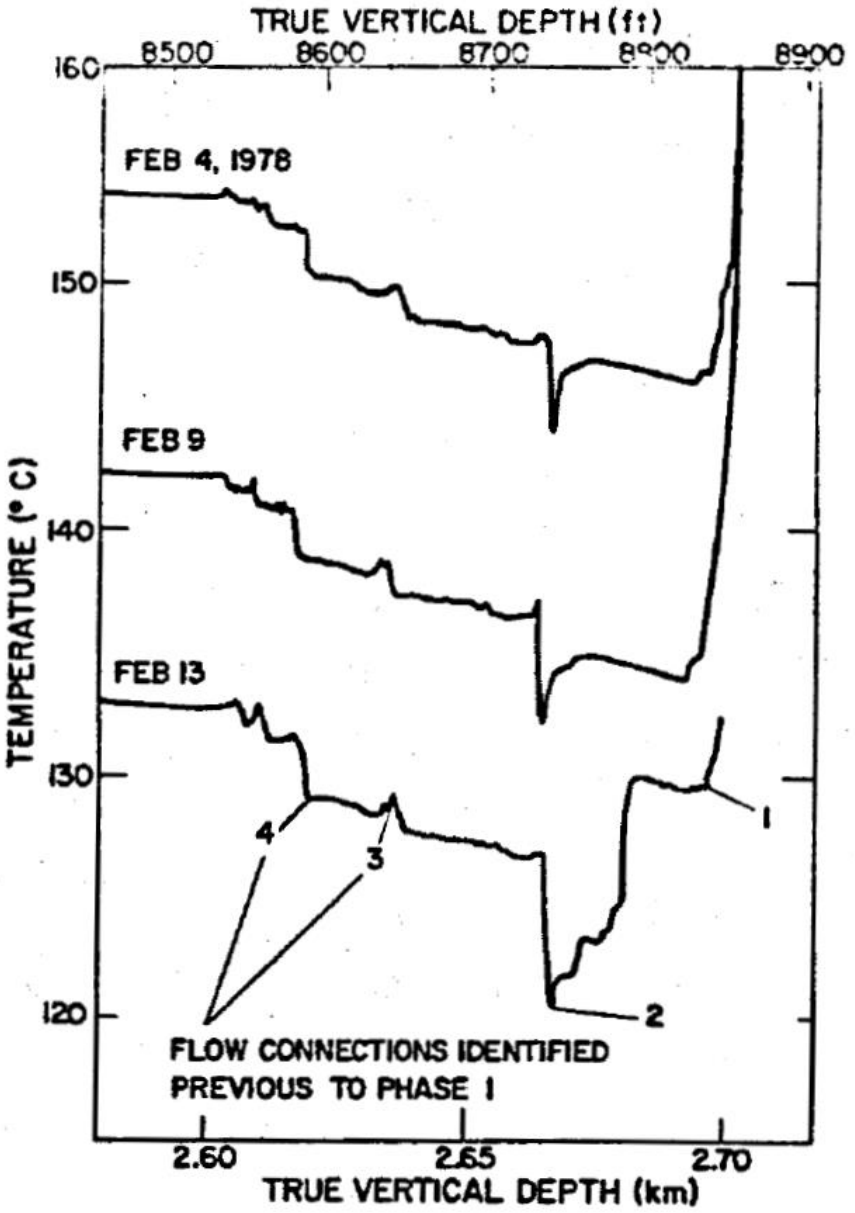

Figure 3.44 Temperature Profile of the Production Well

The horizontal distance between the injection and production wells was about 100m. The estimated effective heat transfer area was 8000m^2 by Tester and Albright, (1979). No estimated reservoir volume was reported. The flow rate was in the range of 5~30L/s. The impedance of the reservoir was in the range of 4-21bar-l/s. There were no data on fracture aperture; 0.2mm was assumed in the simulation done by Tester and Albright, (1979).

The above is a brief summary of the project. For detailed information, please refer to the project report by (Tester & Albright, 1979).

3.5.3. GEOFRAC Simulation with the Fenton Hill Data

Inputs for GEOFRAC, GEOFRAC-FLOW and GEOFRAC-THERMAL are chosen based on project report. Assumptions and estimations are made for some parameters that are not mentioned in the report. The reason for choosing some of the parameters are listed below.

Table 3.2 Summary of the Input Parameter for GEOFRAC Simulation

X (m)	Y (m)	Z (m)	mu (m^{-1})	EA(m^2)	m	k	mPole	rot
40	100	80	0.2	1000	4	20	[π/2, 0]	0
fvalue (m)	ε (m)	ΔP (Pa)	μ (Pa·s)	kt (W/m·K)	ρ (kg/m^3)	Cp (J/kg·K)	Trock (°C)	Tin (°C)
0.0002	0.001	1MPa	0.468×10^{-3}	0.6546	983	4185	180	60

Dimension of the reservoir X, Y and Z is shown in Figure 3.4. According to the footprint (Figure 3.36) of the project, the X and Y dimensions are 40m and 100m respectively. According to the temperature profile of the production well shown in Figure 3.42, the fluid came out from a section of well about 80 meters long, therefore, the Z dimension is estimated to be 80 meters.

"mu" is the fracture intensity. 0.2 is chosen because the geological description in the report indicates that there are only a small number of major fractures conducting water.

"EA" is the expected area of fractures. In the Fenton Hill report, it is likely that the two wells were connected by some large-area fractures or even only one single fracture. So the fracture area is then estimated to be large, i.e. ¼ XY.

"m", "mPole" and "k" in this simulation were picked according to the geological description. As the injection and production wells are connected by some major fractures and the stress history of the site is relatively simple, the fractures are expected to be more or less parallel to each other. A relatively high parameter k=20 is chosen for the Fisher distribution. The fractures are more or less horizontal so the mean orientation of the fracture poles, "mPole" is set to [π/2, 0].

"fvalue" is the aperture of the fracture. In the project report, the simulation was done by using 0.2mm aperture, so the same value is used as input for GEOFRAC.

"ε" is the roughness of the fracture. According to Jones et al., (1988), roughness can be several times the value of the aperture if the rock is inhomogeneous. In this case 5 times the value of the aperture is used.

“ΔP” is the pressure difference between the injection and production wells. As shown in Figure 3.40, pressure is not maintained high in the circulation test. A relatively low pressure difference is used to simulation the steady state of the fluid circulation.

“Trock” and “Tin” are the temperature of the rock and the injected water. They can be found from the temperature log of the production well, as shown in Figure 3.42 and 3.44. The initial temperature 180°C measured in the production well can be used as temperature of the rock since the temperature of the water was the same as that of the rock before injection. The injected water temperature depends on the heat exchanger on the ground and is given in the report as 60 °C.

The rest of the inputs for the simulations are material properties that are assumed to be constant with temperature. Typical values are chosen and the summary of the values is shown in Table 3.2. Because of the stochastic processes used in GEOFRAC, the results are not deterministic. To draw reliable conclusions, a moderate number of simulations has to be run. Here, 20 simulations are run and analyzed below.

Figure 3.47 is a schematic representation of the possible flow paths in one simulation. The purple numbers represent the temperatures (°C) at each node while the blue numbers represent the flow rates (l/s) in each branch. This figure shows that GEOFRAC, as a discrete fracture model, calculates the flow rates and temperatures explicitly.

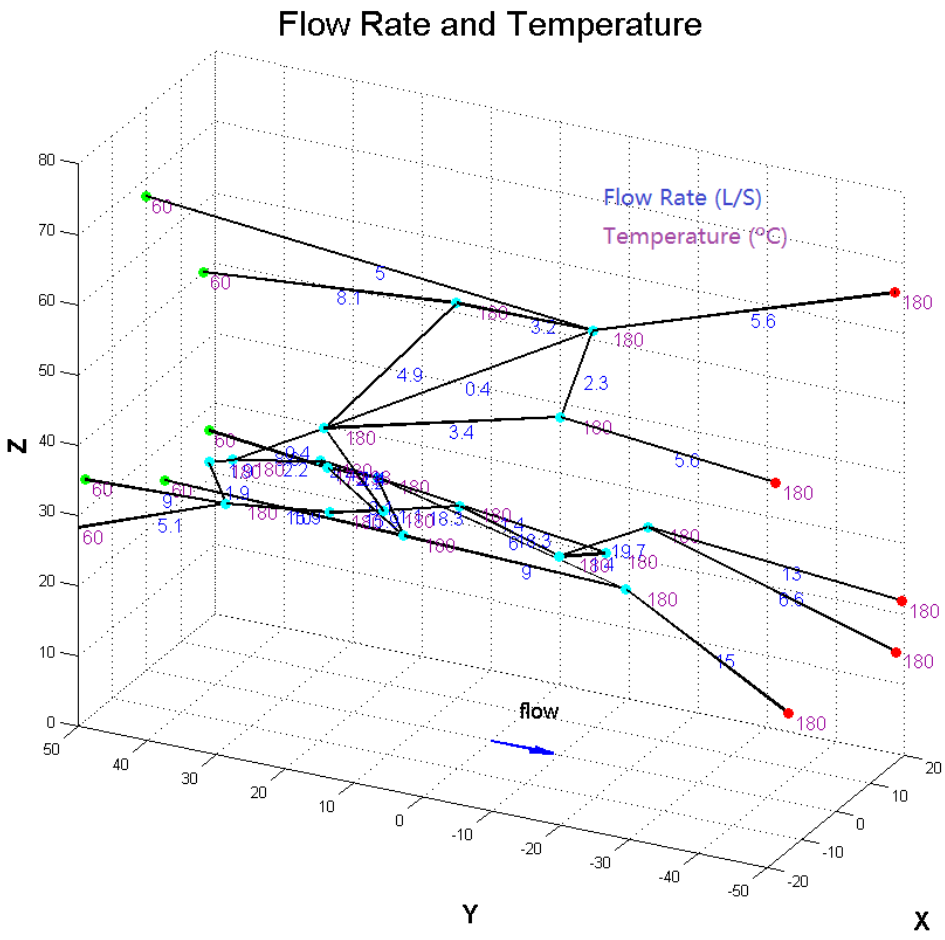

Figure 3.45 Schematic Representation of the Possible Flow Paths Obtained in One Simulation

The average total flow rate of the 20 simulations is 11.3L/s. This value is in line with the flow rate of the production well. The standard deviation of the results is 9.05L/s, which indicates that GEOFRAC can provide results that do not deviate much from the real data. The Reynolds number of all the branches is checked to make sure that the assumption of laminar flow in the flow model is satisfied.

Because of the small apertures and large areas of the fractures, the heat transfer between the rock and the flow is very efficient. As we can see from Figure 3.45, the temperature of the water reaches that of the rock at the first node after the injection boundary. One has to keep in mind, however, that the thermal model in GEOFRAC assumes a constant rock temperature, so the results can only model the beginning stage of the injection. Still, the results indicate that the large area and small apertures of fractures are very helpful in extracting the heat from the underground.

The energy extraction rate estimated by GEOFRAC is 5.72 MW; it is quite close to the measured data as shown in Figure 3.43. The result produced by GEOFRAC is a steady state result, both flow rate and temperature do not change with time. However, the measured data indicate increasing flow rate and decreasing production well temperature, as shown in Figure 3.40 and 3.42. The two compensate each other, providing a relatively constant energy extraction rate. This is the reason why the result of GEOFRAC is close to that of the measured.

This case study with GEOFRAC shows that this model can be used to model the heat and mass transfer in a geothermal reservoir. However, the constant temperature assumption for the rock limited the capability of this model to simulating only the beginning stage of the injection. Future work on the thermal model is needed to produce a long term temperature prediction of the reservoir.

4. Analytical Approach for Discrete Fracture Model in 2-D

4.1.Introduction

Heat transfer in fractured media is difficult to model analytically. Separate governing equations are used for the rock matrix and the fracture, where heat is both conducted and convected. The two domains are coupled by a Cauchy boundary condition (simultaneous Type I and II) that assumes thermal equilibrium and conservation of energy between the two domains. The current analytical approaches have both to fully analytical (closed-form solutions) as well as semi-analytical solutions (in which an inverse Laplace transform is performed numerically, etc.)

Although solutions of the equations are tractable only for very simple geometries, analytical solutions provide rapid and exact calculations of temperature for these cases. Consequently, analytical solutions have an important application in sensitivity analysis and are indispensable for determining the governing parameters in a particular system. Further, they provide a reliable solution against which numerical solutions can be verified.

Several analytical solutions have been developed for the problem of heat exchange between water in a single fracture and an impermeable matrix. These solutions do not consider heat generation within the rock matrix; the system under consideration is typically cold water flowing through hot rock.

For the case of a single discrete fracture, solutions are provided in 2D Cartesian coordinates by Lauwerier (1955), Bodvarsson (1969), Yang et al. (1998), and Kocabas (2004). Some examples are the approximate solution of Alishaev (1979) and the semi-analytical solution of Heuer et al. (1991), who developed solutions for an arbitrary flow field in a planar fracture. In addition, solutions can be readily adapted from the equivalent problem of matrix solute diffusion; such solutions are provided by Grisak and Picken (1981) and Tang et al. (1981). Solutions to the heat transport problem were found in radial coordinates by Bödvarsson (1972) and to the equivalent solute transport problem by Feenstra et al. (1984)

Extension of the problem to a series of equally-spaced parallel fractures was presented first in the geothermal literature by Gringarten et al. (1975) and Lowell (1976), who developed Laplace-space solutions to the problem using Cartesian coordinates in two dimensions. Bödvarsson and Tsang

(1982) solved the problem in Laplace space using radial coordinates. Sudicky and Frind (1982) presented a solution to the equivalent solute problem, using Cartesian coordinates.

This chapter presents the partial differential equations used to describe the fully coupled heat transfer problem between fluid flow and fractured rocks. Assumptions are made to simplify the equations so that the solutions can be found analytically. A case study is used to show the how the model works in predicting the temperature drawdown of a geothermal reservoir.

4.2.Problem Formulation

The conceptual geothermal reservoir model is shown in Figure 4.1. The injection well and production well are connected by a series of equally-spaced parallel fractures. The fractures are assumed to be planar, so X-Z Cartesian coordinates are used. One basic section is extracted for analysis, as shown in Figure 4.2. When the half fracture spacing D extends to infinity, the solution can also be used to analyze the single-fracture reservoir case.

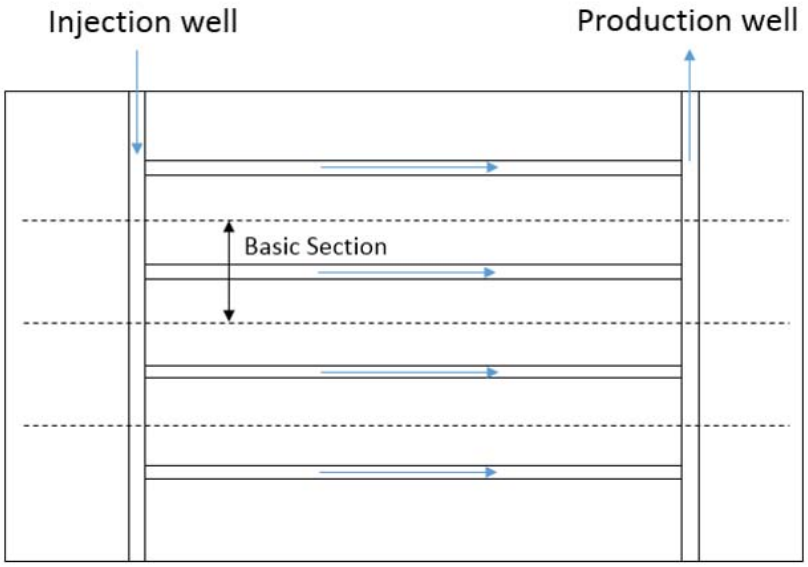

Figure 4.1 Single Planar Fracture

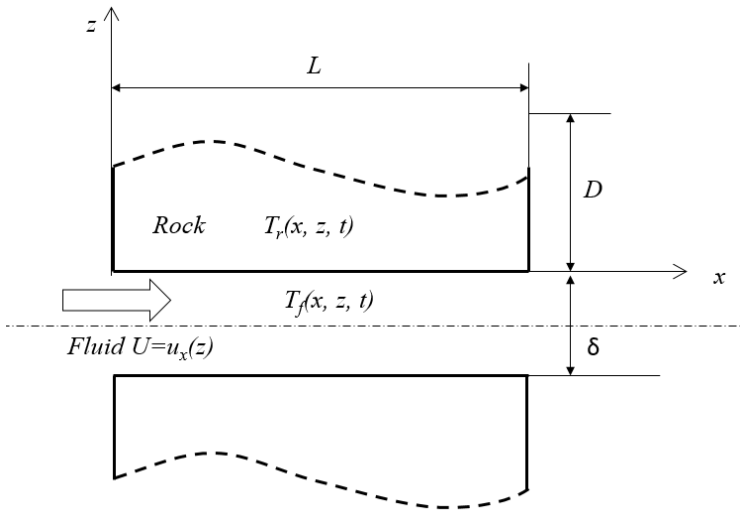

Figure 4.2 One Basic Section

The following assumptions are made to formulate the heat transfer problem.

1. The rock associated with the fracture is impermeable, therefore only the effects of thermal conduction are present.
2. The flow in the fracture is to be steady-state, single-phase, incompressible, laminar flow. Gravity effect is negligible, and the fracture walls are smooth and parallel to each other.
3. The material properties: density, specific heat capacity and thermal conductivity are assumed to be constant.
4. Initially, the temperature is T_0 everywhere in the system. At t=0, the temperature of the injected water is fixed at T_i.

The governing equation for the fluid and rock temperatures can be derived based on the energy balance in the control volume:

$$\frac{\partial T_f}{\partial t} - \alpha_{fT}\frac{\partial^2 T_f}{\partial z^2} - \alpha_{fL}\frac{\partial^2 T_f}{\partial x^2} + u(z)\frac{\partial T_f}{\partial x} = 0, (-\frac{\delta}{2} \le z \le 0, x \ge 0) \tag{4.1}$$

$$\frac{\partial T_r}{\partial t} = \alpha_{rT}\frac{\partial^2 T_r}{\partial z^2} + \alpha_{fL}\frac{\partial^2 T_r}{\partial x^2}, (0 \le z \le D, x \ge 0) \tag{4.2}$$

where:

T_f is the temperature of the fluid in the fracture, because of the symmetry of the system about the $z = -\frac{\delta}{2}$ axis, only half of the fracture is considered. The temperature of the fluid is a function of both location and time, i.e. $T_f = T_f(x, z, t)$.

T_r is the temperature of the rock. The temperature of the rock is a function of both location and time, i.e. $T_r = T_r(x, z, t)$.

α is the thermal diffusivity. As defined in Equation 2.7, $\alpha = \frac{k}{\rho C_p}$. The subscripts "*r*" and "*f*" represent the rock and the fluid, respectively. The subscripts "*L*" and "*T*" represent the longitudinal and transverse directions, respectively. It should be noted that the thermal diffusivity of fluid α_f includes the effect of both thermal conduction and dispersion.

u(z) is the fluid velocity in the x direction. In this 2-D case, only the flow in the x direction is considered. The velocity distribution varies with flow mode. Laminar flow has parabolic velocity distribution in the Z direction, while turbulent flow has a more uniform velocity distribution.

Equation 4.1 and 4.2 are subject to initial conditions that the fluid and rock are at the same temperature before injection happens at t=0, as expressed in Equation 4.3

$$T_f(x, z, 0) = T_r(x, z, 0) = T_0 \tag{4.3}$$

Equation 4.1 is subject to boundary conditions that the fluid temperature at *x=0* is the injected fluid temperature T_i, and that the fracture is symmetric about the axis $= -\frac{\delta}{2}$, as experessed in Equation 4.4 and 4.5:

$$T_f(0, z, t) = T_i \tag{4.4}$$

$$\left.\frac{\partial T_f}{\partial z}\right|_{z=-\frac{\delta}{2}} = 0 \tag{4.5}$$

Equation 4.2 is subject to the boundary condition that there is no heat flux at the boundary of the section because of the symmetry in the rock, as expressed in Equation 4.6:

$$\left.\frac{\partial T_r}{\partial z}\right|_{z=D} = 0 \tag{4.6}$$

At the fluid-rock interface z=0, both the temperature and the heat flux are continuous, which are Cauchy type I and II boundary conditions:

$$T_r|_{z=0} = T_f|_{z=0} \tag{4.7}$$

$$k_r \left.\frac{\partial T_r}{\partial z}\right|_{z=0} = \left.\frac{\partial T_f}{\partial z}\right|_{z=0} \tag{4.8}$$

The set of Equations 4.1-4.8 is a boundary value problem that cannot be solved easily. Simplifications have to be made to make the problem solvable either analytically or semi-analytically. As discussed in Section 4.1, great efforts have been made by researchers to simplify and solve the boundary value problem. In what follows, two solutions are presented with simplifications made to the boundary value problem. The 0-D and 1-D solutions are named after the number of directions in which heat conduction in the rock is considered. These terms are used in Chen et al., (2001) and Martínez et al., (2013), so for consistency, the same terms are used in the analysis in Sections 4.3 to 4.5. For example, the 2-D solution means that the heat conduction in both the longitudinal and transverse direction is considered in the solution.

4.3.0-D Solution and Results

If the heat transfer in the rock is so efficient that the temperature distribution is nearly uniform, we may ignore the small differences of temperature within the rock. This approximation leads to the lumped thermal capacity model, which is also called 0-D model because the heat conduction process is assumed to happen instantaneously. The assumption of a uniform temperature is justified when the thermal resistance to conduction in the solid is small compared to the thermal resistance to convection. With this assumption, the temperature of the rock will only be a function of time, i.e. $T_r=T_r(t)$.

In the parametric study of GEOFRAC-THERMAL, another important conclusion is drawn that the temperature of the fluid at the outlet of the fracture is the same as that of the rock, when the aperture of the fracture is relatively small. Due to the assumption of uniform rock temperature, Equation 3.9-3.14 can be used to calculate the fluid temperature at the outlet after flowing through two

isothermal parallel plates. When the aperture is small, the heat convection coefficient is so high that the temperature of the fluid reaches that of the rock without travelling in the fracture for a long distance, as shown in Figure 4.3, for water as the fluid.

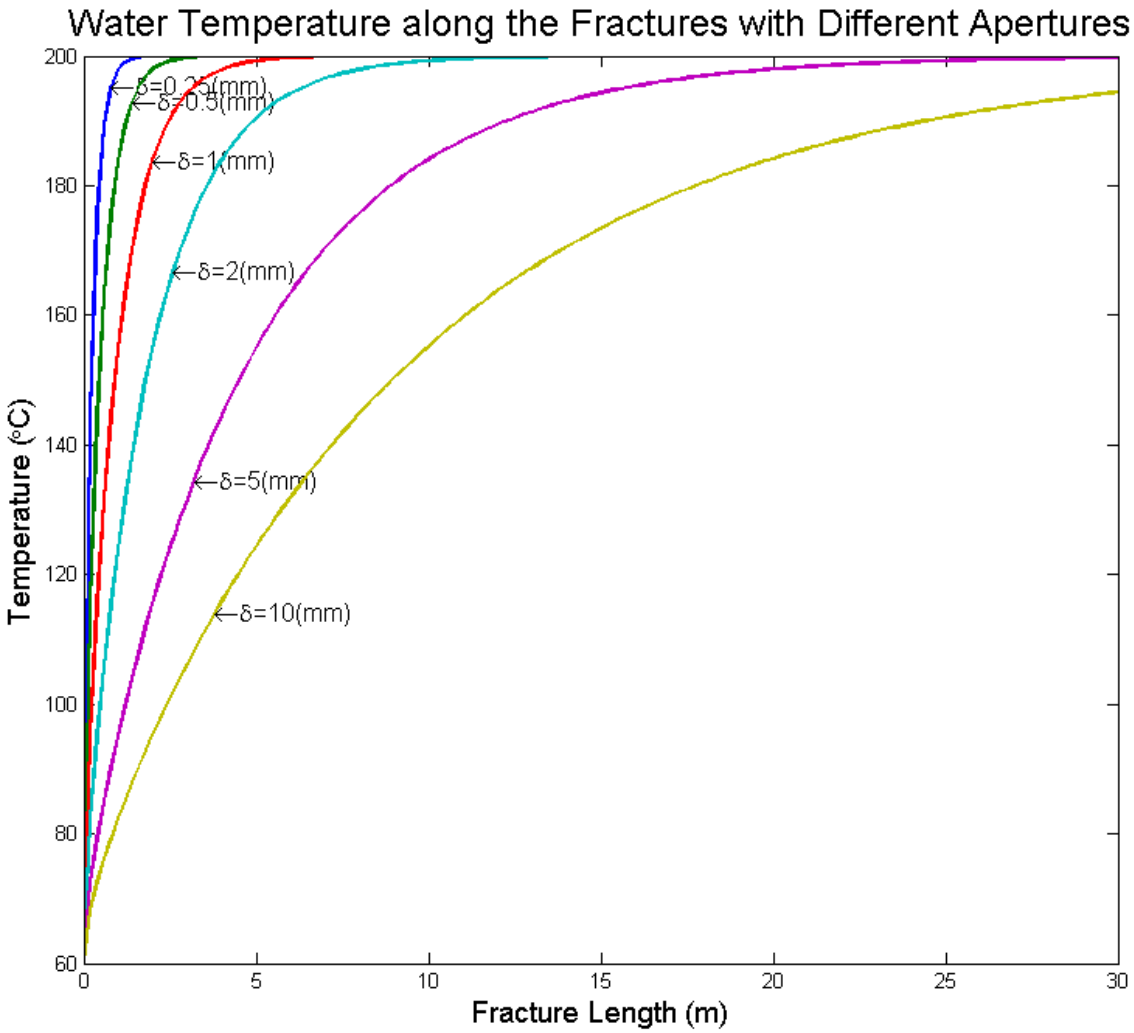

Figure 4.3 Increase of Fluid Temperature along the Fractures with Different Fracture Apertures (δ)

From the above analysis, we can see that the fluid temperature at the outlet is very likely to be the same as that of the rock. In fact, the flow path in a geothermal reservoir is much longer than 30m, and the aperture of the fracture is usually very small due to the high underground pressure, so it is valid to assume that the fluid temperature at the outlet is the same as that of the rock.

Besides the two assumptions discussed above, the following assumptions are made:

1. There is no water leakage in the reservoir;
2. The heat transfer process happens in a finite volume of rock mass.

3. Constant underground heat flux Q_0 goes into the reservoir.

Under these assumptions, energy balance can be performed to derive the governing equations for the temperature of the fluid and the rock:

$$\frac{dT_R}{dt} V_R \rho_R C_{PR} = -(T_f - T_i) Q \rho_f C_{Pf} + Q_0 S_R \tag{4.9}$$

Equation 4.9 is subject to the initial condition:

$$T|_{t=0} = T_{R0} \tag{4.10}$$

where,

T_i and T_f are the temperature of fluid at inlet and outlet, respectively;

T_R is the temperature of rock;

Q is the fluid flow rate;

Q_0 is the underground heat flux;

V_R is the volume of the geothermal reservoir;

ρ_R *and* ρ_f is the density of rock and fluid, respectively;

C_{Pf} and C_{PR} is the specific heat capacity of rock and fluid, respectively;

S_R is footprint area of the geothermal reservoir

With the temperature of the fluid at the outlet equal to that of the rock, i.e. T_f=T_r, the solution to Equation 4.10 is obtained:

$$T_R = D_3 e^{-D_1 t} + \frac{D_2}{D_1} \tag{4.11}$$

where,

$D_1 = \frac{Q \rho_W C_{PW}}{V_R \rho_R C_{PR}}$;

$D_2 = \frac{Q_0 S_R + T_w Q \rho_W C_{PW}}{V_R \rho_R C_{PR}}$;

$D_3 = T_{R0} - T_w - \frac{Q_0 S_R}{Q \rho_W C_{PW}}$;

Equation 4.11 shows that, if the flow rate is constant, the thermal drawdown of the rock follows an exponential curve. A parametric study is conducted to analyze the sensitivity of the thermal drawdown equation. The case with flow rate Q=0.01m^3/s and Volume=1000*500*500m^3 is used

as the base case for comparison, which is indicated with thick red lines in Figures 4.4 and 4.5. Figure 4.4 shows the effect flow rate has on the thermal drawdown of the reservoir. With higher injection rate, the reservoir cools down faster.

From the thermal drawdown equation, we can also see that the temperature drawdown is also sensitive to the volume of the reservoir, as shown in figure 4.5. The drawdown time is longer for larger thermal reservoirs.

Reservoir size and flow rate are the two main factors that determine the service life of a geothermal reservoir, the smaller the injection rate and the larger the reservoir, the longer the service life. The equation also implies that the effect of underground heat flux is negligible for most practical reservoirs, because the terms $\frac{Q_0 S_R}{V_R \rho_R C_{PR}}$, and $\frac{Q_0 S_R}{Q \rho_W C_{PW}}$ are negligible in comparison with the others.

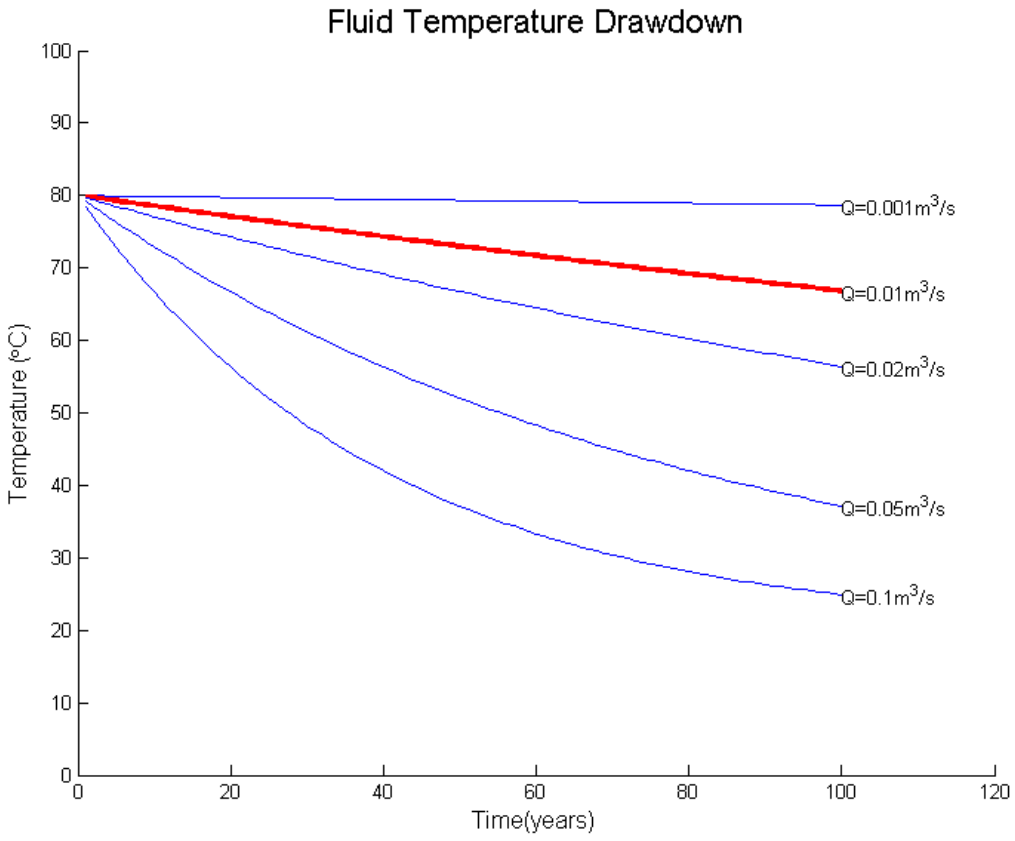

Figure 4.4 Temperature Drawdown with Different Flow Rates (Q)

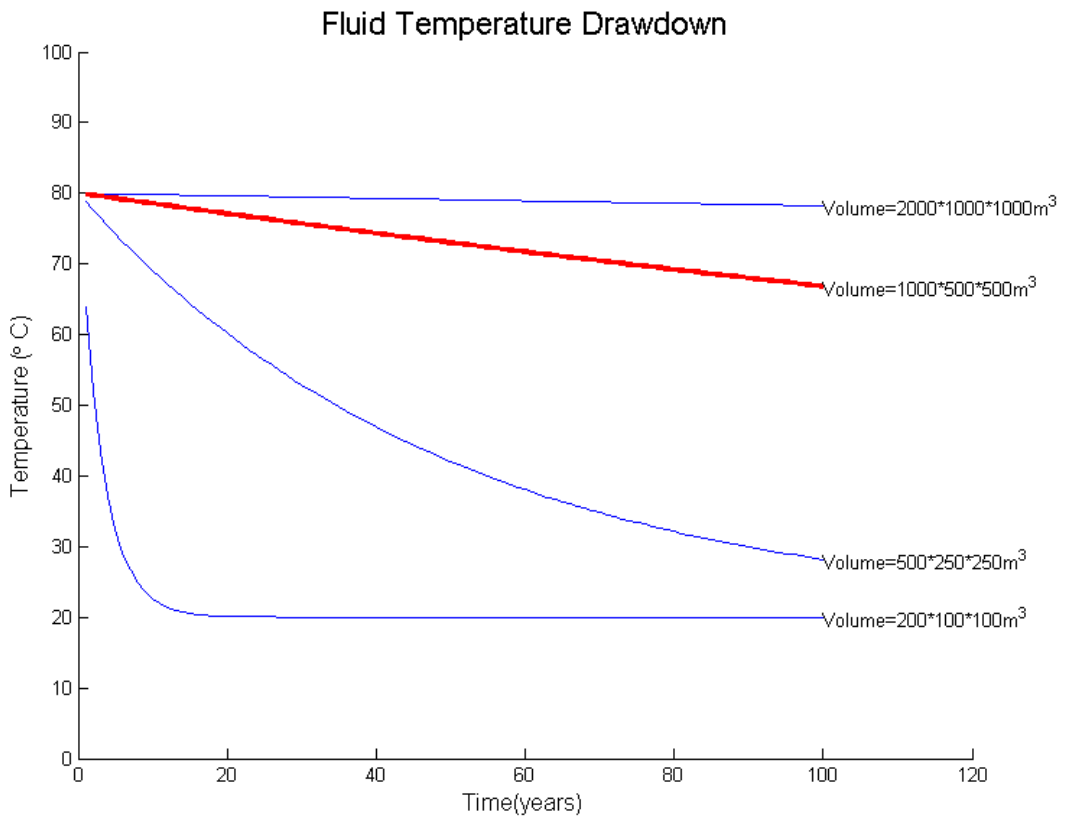

Figure 4.5 Temperature Drawdown with Different Reservoir Volumes

The thermal drawdown equation derived from this 0-D model provides a very simple and quick approach to evaluate the service life of a geothermal reservoir. However, there are two factors to consider when thinking about how the results of this simplified model will deviate from reality. One factor is that when a reservoir is cooling down, the rock near the production well tends to have higher temperature than that in the injection well. The other factor is that the rock located near the flow paths will be cooler than rock located far away from the flow paths. The deviation between our simplified approach and a more complex approach depends largely on the conductivity of the rock relative to the rate of energy extraction from the reservoir and the average distance between the flow paths. Highly conductive rock, with a low rate of removal, and with short distances between the flow paths will see a relatively uniform temperature in the reservoir and results consistent with the lumped thermal capacitance model, while less conductive rock with high energy extraction rate and long distances between the flow paths are more likely to deviate in their results.

4.4. A Case Study with 0-D Model

Despite the simplification and assumptions of the 0-D model, it provides a preliminary assessment of the temperature drawdown and service life of a geothermal reservoir. A case study has been done on the Fenton Hill geothermal project.

As described in Section 3.5, the data of the Fenton Hill project has been found in the project report (Tester & Albright, 1979), and a brief summary for the case study of the 0-D model is as the follows. The distance between the injection and main production well is around 100m; the initial rock temperature is 178 °C, measured by a sensor in the production wells; and the injection rate is around 20L/s. The measured thermal drawdown of the production well is shown with dots in Figure 4.6. At that time, the researchers used the single circular fracture thermal drawdown model (Murphy et al., 1981) to predict the drawdown of the reservoir, as shown with continuous curve in Figure 4.5. For detailed information about the model, please refer to the project report (Tester, J., 1978).

Most of the inputs for the model, such as temperature and flow rates data are directly from the project report. The volume of the reservoir is estimated from the project plan view and geology description. The input parameters are summarized in Table 4.1. The results of the model match very well with reality, as shown in Figure 4.6. There are some sudden turns in the series of dots because of the changing of injection rate during the operation. Except for these sudden turns, the thermal drawdown of the reservoir predicted by the 0-D model matches the measurements.

Table 4.1 the Parameters Used in the 0-D Model

X (m)	Y (m)	Z(m)	*Tw (C°)*	T_{r0} (°C)	Q (L/s)
100	40	80	83	178	20
Q_0 (W/m^2)	ρ_W (kg/m^3)	ρ_r (kg/m^3)	C_{PW} (J/kgC°)	C_{PR} (J/kgC°)	
0.06	1000	2700	4200	780	

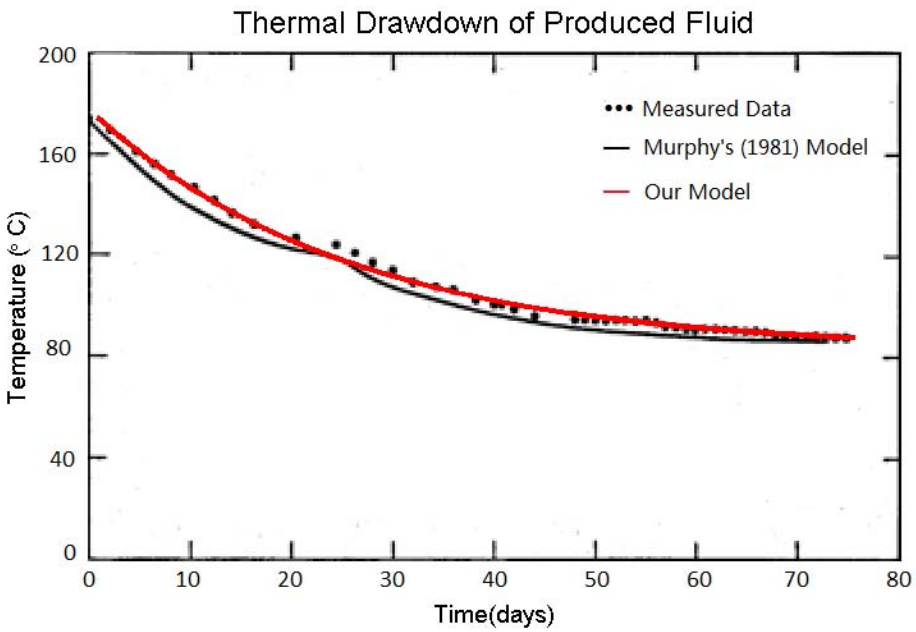

Figure 4.6 Thermal Drawdown of Fenton Hill Geothermal Reservoir

The 0-D model is a very simple lumped thermal capacitance model. The assumptions limit the application of the model, making it applicable for some simple geometries. In a real project, the temperature distribution cannot be uniform in the rock; no bounded volume is defined for a reservoir in reality, and also water leakage may not be negligible. The fracture networks will also add complexity to the thermal drawdown. The reason why the thermal drawdown curve matches the measurement is that the circulation test was done on a small scale and the flow paths and layout of the wells were relatively simple.

Due to the low heat conductivity of the rock, the non-uniform rock temperature profile will make the actual thermal drawdown of the geothermal reservoir different from the model proposed above. A new model taking into account the rock temperature distribution is needed for a more advanced analysis on the thermal drawdown of the reservoir.

4.5.1-D Solution and Results

The 1-D solution is the solution that takes only the transverse heat conduction in the rock into consideration. This simplification is valid because the temperature gradient in the transverse direction is much greater than that in the longitudinal direction. There exist a number of solution efforts in this 1-D solution category. Bödvarsson and Tsang, (1982) provided a solution for a set of parallel fractures in radial coordinates. Because of the symmetry of the system, the longitudinal

dimension z is finite, i.e. $0 \leq z \leq D$. Gringarten et al., (1975) provided a solution for a set of parallel fractures in planar coordinates. This solution is based on the assumption of a constant temperature gradient because the fractures are assumed to be vertical. Similarly, the longitudinal dimension is finite. Cheng et al., (2001), provided a solution for a single fracture in an infinite rock mass, i.e. $0 \leq z \leq +\infty$.

In what follows, the 1-D solution for a set of parallel horizontal fractures in planar X-Z coordinates is presented. Because the fractures are horizontal, the temperature of the rock is uniform initially. The same coordinate system as in Figure 4.2 is used. Since the solution is 1-D, the heat transfer in the transverse direction is considered in the rock. In the fluid, because of the small opening of the fracture, the fluid velocity and temperature is assumed to be constant in the transverse direction. Equation 4.1 and 4.2 is then simplified as:

$$\delta \frac{\partial T_f}{\partial t} + q_{vol} \frac{\partial T_f}{\partial x} - 2\alpha_{rT} \frac{\partial T_r}{\partial z}\Big|_{z=0} = 0, (-\frac{\delta}{2} \leq z \leq 0, x \geq 0) \tag{4.12}$$

$$\frac{\partial T_r}{\partial t} = \alpha_{rT} \frac{\partial^2 T_r}{\partial z^2}, (-0 \leq z \leq D, x \geq 0) \tag{4.13}$$

where，

T_f, temperature of the fluid, is only a function of x and t, because it is integrated in the Z direction, i.e. $T_f=T_f(x,t)$.

T_r, temperature of the rock, is a function of x, z and t, although the heat conduction in the x direction is not considered, i.e $T_r=T_r(x, z, t)$.

q_{vol} is the flow rate in the fracture. Because of the assumption of uniform velocity and temperature of the fluid in the transverse direction, the velocity and temperature are integrated in that direction. After integration, velocity becomes flow rate and temperature becomes bulk temperature, which is the average of the temperature in the transverse direction.

Equation 4.12 and 4.13 are subject to the initial condition:

$$T_f(x, z, 0) = T_r(x, z, 0) = T_0 \tag{4.14}$$

Equation 4.12 is subject to boundary conditions that the fluid temperature at $x=0$ is the injected fluid temperature T_i, as expressed in Equation 4.15:

$$T_f(0,t) = T_i \tag{4.15}$$

Equation 4.12 is subject to boundary condition that there is no heat flux at the boundary of the section because of the symmetry in the rock, as expressed in Equation 4.17:

$$\left.\frac{\partial T_r}{\partial z}\right|_{z=D} = 0 \tag{4.16}$$

At the fluid-rock interface z=0, both the temperature is continuous, which is Cauchy type I boundary condition:

$$T_r|_{z=0} = \left.T_f\right|_{z=0} \tag{4.17}$$

To make the solution process easier, the dimensionless forms are used. The dimensionless parameters are defined as the follows:

$$\zeta = \frac{\alpha_{rT}\delta}{qD^2}x \tag{4.18}$$

$$\eta = \frac{z}{D} \tag{4.19}$$

$$\tau = \frac{\alpha_{rT}t}{D^2} \tag{4.20}$$

$$T_D = \frac{T - T_0}{T_i - T_0} \tag{4.21}$$

$$\theta = \frac{\rho_f C_{pf}\delta}{\rho_r C_{pr} D} \tag{4.22}$$

Equation 4.12 and 4.13 is then simplified as:

$$\frac{\partial T_{Df}}{\partial \tau} + \frac{\partial T_{Df}}{\partial \zeta} - \frac{2}{\theta}\left.\frac{\partial T_{Dr}}{\partial \eta}\right|_{\eta=0} = 0 \tag{4.23}$$

$$\frac{\partial T_{Dr}}{\partial \tau} = \frac{\partial^2 T_{Dr}}{\partial \eta^2} \tag{4.24}$$

Initial and boundary conditions is also simplified as:

$$T_{Df}(\zeta, 0) = T_{Dr}(\zeta, \eta, 0) = 0 \tag{4.25}$$

$$T_{Df}(0, \tau) = 1 \tag{4.26}$$

$$T_{Df}(\zeta, \tau) = T_{Dr}(\zeta, 0, \tau) \tag{4.27}$$

$$\left.\frac{\partial T_{Dr}}{\partial \eta}\right|_{\eta=1} = 0 \tag{4.28}$$

Laplace transform is performed on the dimensionless time τ, i.e. τ in the Laplace domain is p. The temperature of the fluid and rock, T_f and T_r, in the Laplace domain are: u and v.

$$u = \int_0^\infty e^{-p\tau} T_{Df}(\zeta, \tau) d\tau \tag{4.29}$$

$$v = \int_0^\infty e^{-p\tau} T_{Dr}(\zeta, \tau) d\tau \tag{4.30}$$

Then, Equation 4.23 and 4.24 in the Laplace domain will be:

$$\frac{\partial^2 v}{\partial \eta^2} = pv \tag{4.31}$$

$$pu + \frac{\partial u}{\partial \zeta} - \left.\frac{2}{\theta}\frac{\partial v}{\partial \eta}\right|_{\eta=0} = 0 \tag{4.32}$$

Because the initial condition is already included in Equation 4.31 and 4.32, only the following boundary conditions are remained.

$$u(0, p) = 1/p \tag{4.33}$$

$$u(\zeta, p) = v(\zeta, 0, p) \tag{4.34}$$

$$\left.\frac{\partial v}{\partial \eta}\right|_{\eta=1} = 0 \tag{4.35}$$

Partial differential equations 4.31 and 4.32 can be solved in the Laplace domain:

$$u = \frac{1}{p} exp\left[-\left(p + \frac{2}{\theta}\sqrt{p} tanh\sqrt{p}\right)\zeta\right] \tag{4.36}$$

$$v = u\left[cosh\left(\sqrt{p}\eta\right) - tanh\sqrt{p}\sinh\left(\sqrt{p}\eta\right)\right] \tag{4.37}$$

Performing inverse Laplace transform is difficult for Equation 4.36 and 4.27, so numerical Laplace inversion is used. This numerical approximation of the inverse Laplace transform is based on the paper written by Valsa and Brancik, (1998). The method is written into a MATLAB code, with the copyright from Juraj Valsa. Figure 4.7 is an example of the result of the 1-D solution.

In this example, the spacing between two fractures is 2D=20m, the length of the fracture is L=50m. The aperture of the fracture is δ=5mm. The velocity of the water in the fracture is 0.2m/s. The initial rock temperature is 80 °C, and the injection temperature is 20 °C. As shown in Figure 4.7, the temperature of the fluid at outlet decreases with time after a short period when the temperature of the fluid is the same as that of the rock.

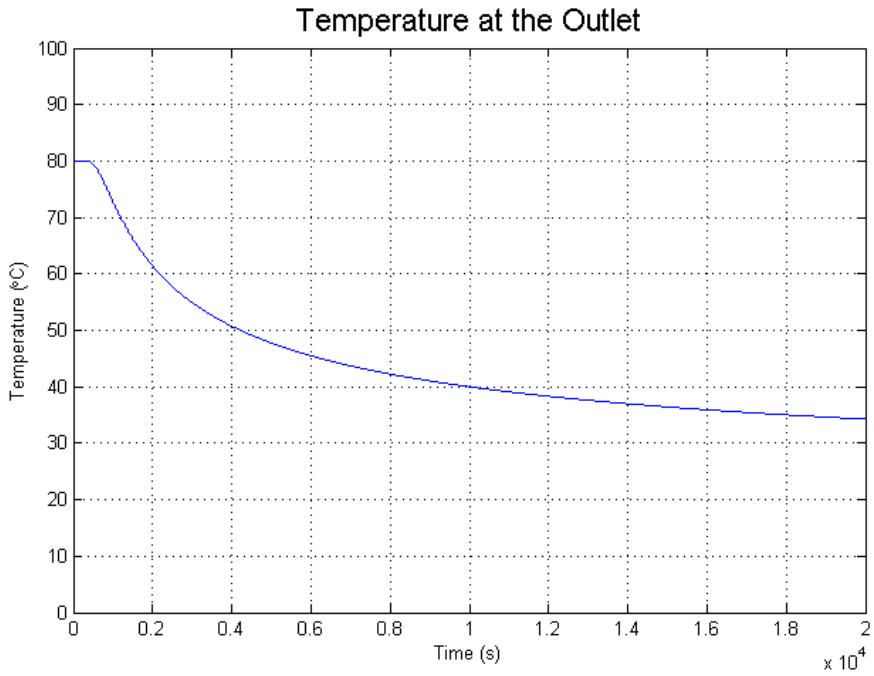

Figure 4.7 An Example of the 1-D Solution

Figure 4.8 to 4.10 present a parametric study on this 1-D solution. The set of parameters used in Figure 4.7 are used as a basis, which is plotted using the thick red curve, then one parameter is varied at a time. Some useful conclusions can be drawn from this parametric study.

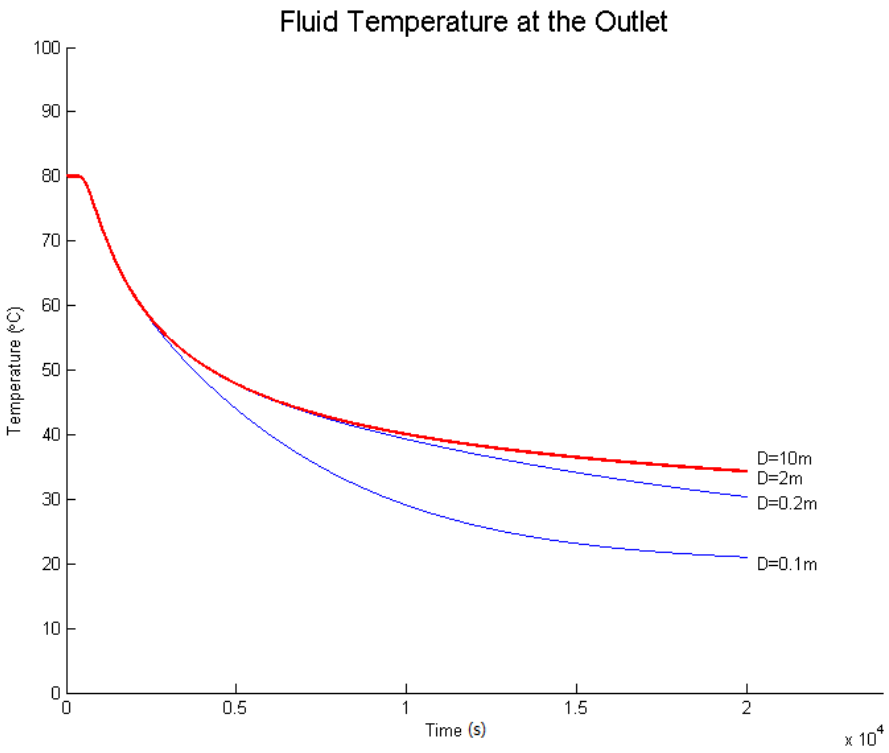

Figure 4.8 Temperature Drawdown with Different Fracture Spacings (D)

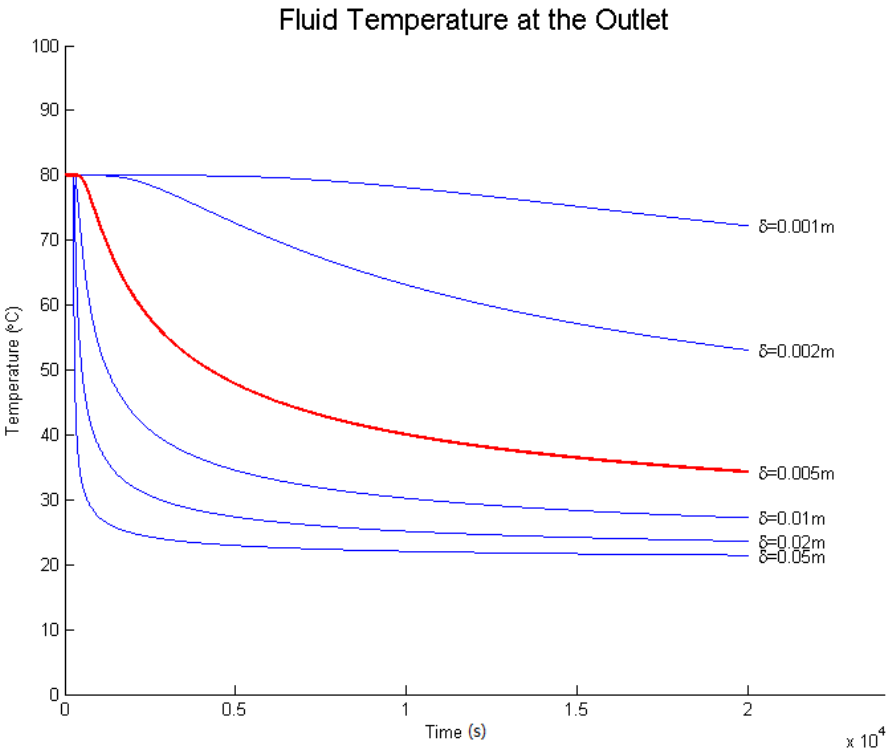

Figure 4.9 Temperature Drawdown with Different Apertures (δ)

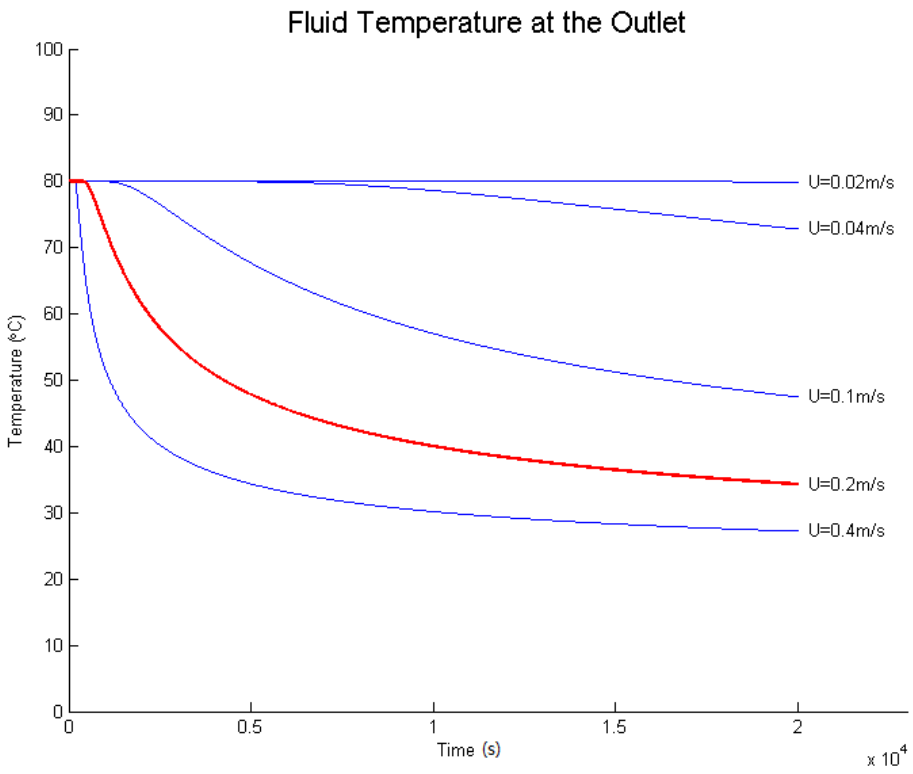

Figure 4.10 Temperature Drawdown with Different Velocity (U)

Figure 4.8 shows that when the fracture spacing is small, the fluid temperature at the outlet draws down more quickly than the cases when the fracture spacing is large. When the spacing is large enough, the temperature drawdown curves overlap with each other, as the curves with D=2m and D=10m do. This happens because when the cold front migrates in the Z direction, before it hits the boundary Z=D, the heat transferred to the fluid will not change; this is why when D is large enough, the thermal drawdown curves of different fracture spacings are the same.

Figure 4.9 shows that when the aperture of the fracture increases, the fluid temperature at the outlet draws down more quickly. This make sense because the greater aperture conveys more fluid, which helps the heat extraction. When more heat is extracted, the temperature of the rock draws down more quickly, thus the fluid temperature at the outlet draws down more quickly.

Figure 4.10 shows that when the fluid velocity increases, the fluid temperature at the outlet draws down more quickly. This make sense because the higher fluid velocity will convey more fluid, which help the heat extraction. When more heat is extracted, the temperature of the rock draws down more quickly, thus the fluid temperature at the outlet draws down more quickly.

The 1-D solution presented above is a simplified case of the Equation 4.1 and 4.2. It neglects the velocity profile and heat conduction in the fluid and longitudinal heat conduction in the rock. However, it provides a useful insight into the temperature reaction of the fluid and rock after cold water is injected. It is also very useful in determining the sensitivity to the factors associated with the geothermal reservoir. To obtain more accurate results, more complicated analytical or semi-analytical methods have to be used.

5. Comparison between the Numerical and Analytical Approaches

5.1. A Simply Configured Heat Transfer Problem

In section 4.5, the 1-D solution has provided a very useful insight into the temperature reaction of the fluid and rock after cold water is injected. However, it is necessary to find out if the assumptions used in the 1-D solution are valid and how these assumptions affect the results. A finite element simulation is run on a heat transfer problem with simple geometry to provide a reference to compare with the 1-D solution. The simple configuration is shown in Figure 5.1.

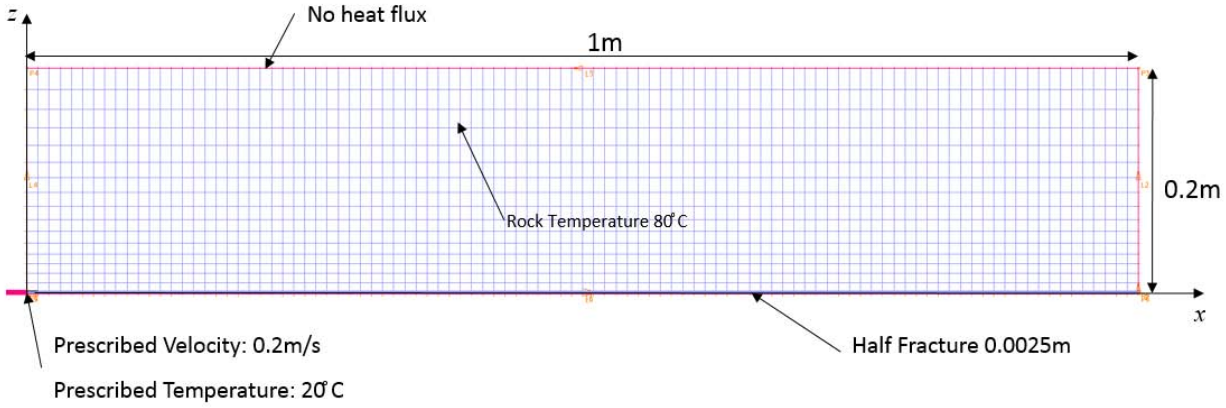

Figure 5.1 Finite Element Model

The finite element method has been proved reliable in modeling the physical process of the nature and has been widely used in the industry. To make sure that the results are reliable and accurate, very fine mesh needs to be applied on the domain, which in turn limits the length of time steps. In this case, the aperture of the fracture is 0.005m. Because of the symmetry of the system, half of the fracture is simulated. To capture the parabolic fluid velocity profile discussed in Section 2.2.2, the fracture is divided into 100 subdivisions in the X direction and 8 subdivisions in the Z direction. The rock is divided into 100 subdivisions in the X direction and 16 subdivisions in the Z direction. To make sure the result is stable, 0.1-second time steps are used to calculate the temperature change in 500s. Table 5.1 summarizes the input parameters for the finite element simulations. Material properties are chosen from typical values and remain constant during the simulation.

Table 5.1 Input Parameters for the Finite Element Simulation

T_0 (°C)	T_f (°C)	k_R(W/m/°C) (granite)	k_f(W/m/°C) (water)	ρ_R (kg/m^3) (granite)	ρ_f (kg/m^3)
80	20	3	0.58	2700	1000
C_{pR} (granite) (J/kg/°C)	C_{pf} (J/kg/°C)	μ (Pa·s)	L (m)	D (m)	δ (m)
790	4186	0.001	1	0.2	0.005

The 1-D solution does not consider the fluid velocity profile, neither does it consider the temperature profile in the transverse (Z) direction. The finite element simulations provide cases with uniform velocity profile and parabolic velocity profile as reference to show how the velocity and temperature profiles in the transverse direction matter. The same bulk velocity 0.02m/s is used in both cases and this bulk velocity (as defined in Section 2.2.2) is consistent with that used in the 1-D solution so that the results can be comparable.

The finite element simulation is able to provide the temperature and velocity of every node at the end of each time step. An example of the simulation result is shown in Figure 5.2. The temperature profile in the rock at t=100s shows that the temperature gradient in the Z direction is much greater than that in the X direction. This result indicates the validity of the assumption that the heat conduction in the longitudinal direction is negligible.

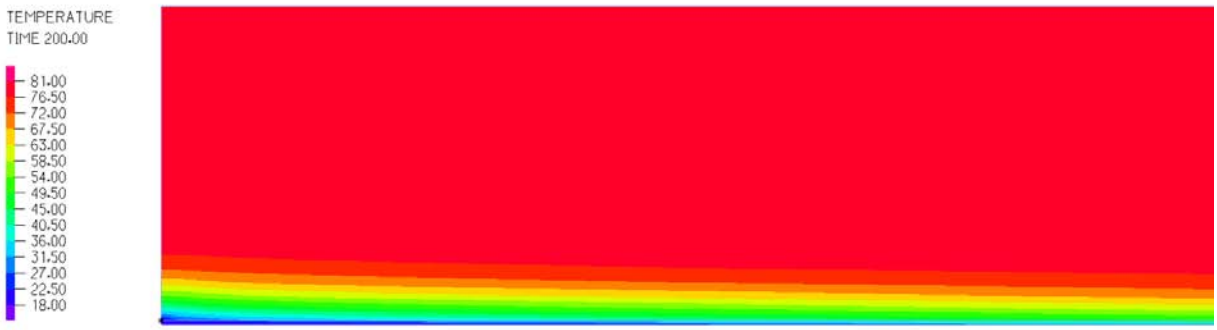

Figure 5.2 Temperature Profile of the Rock and Fluid

5.2. Comparison of the Results

In a geothermal project, the temperature of the fluid in the production well is a very important factor in determining the design life, and operation scheme. So in this comparison, the main interest is in the change of temperature of the fluid at the outlet of the fracture.

The finite element results can provide us the temperature and velocity of every node at the end of each time step. To compare with the results of the analytical solutions, bulk velocity and temperature at the outlet should be used. As discussed in Section 2.2.2, the bulk velocity is defined as:

$$\overline{u_x} = \frac{\int_{-\frac{\delta}{2}}^{0} u_x dz}{\int_{-\frac{\delta}{2}}^{0} dz} \tag{5.1}$$

The bulk temperature, as defined in Equation 5.2, reflects the energy conveyed by the fluid.

$$T_f = \frac{\int_{-\frac{\delta}{2}}^{0} u_x T_f dz}{\int_{-\frac{\delta}{2}}^{0} u_x dz} \tag{5.2}$$

The 1-D solution is based on the assumption of uniform velocity and temperature in the transverse direction of the fracture. In reality, the fluid velocity profile is parabolic if it is laminar flow. Turbulent flow velocity is more uniform in the transverse direction, but not strictly uniform. The temperature profile in the transverse direction is also not strictly uniform even though the fracture aperture is very small. In the following comparison, the results of the 1-D solution, the finite element simulation with a parabolic velocity profile and the finite element simulation with a uniform velocity profile are compared.

Figure 5.3 shows the fluid velocity profile in the Z direction in the fracture. The result of the Cubic Law is also plotted as a reference showing that finite element simulation is able to simulate the velocity profile of laminar flow.

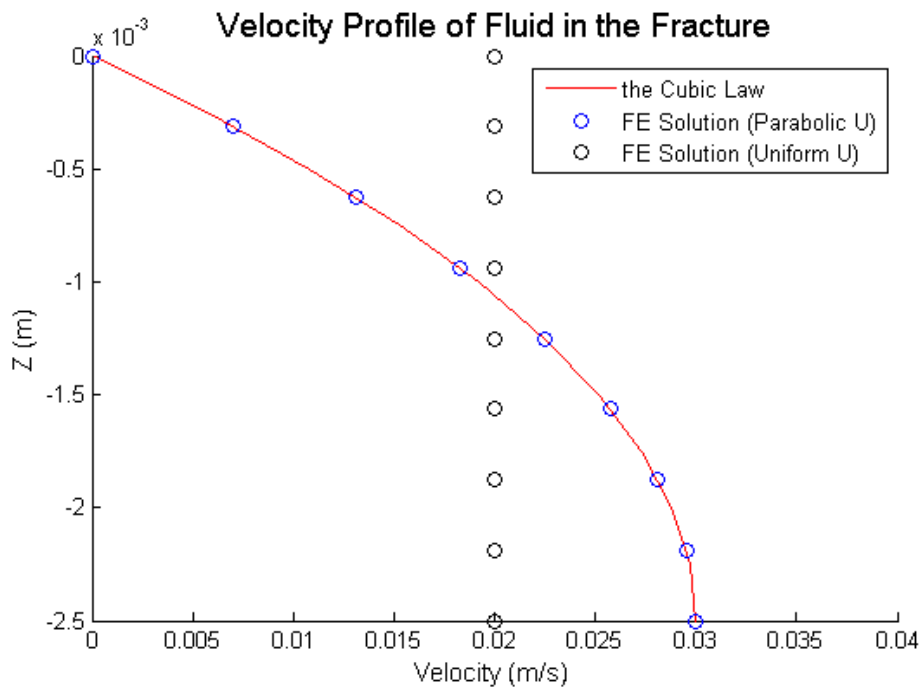

Figure 5.3 Velocity Profile in the Z Direction

Figure 5.4 shows the temperature profile of the fluid at the outlet when t=500s. This figure indicates that when the fluid laminar, a higher temperature gradient is expected in the fluid in the transverse direction.

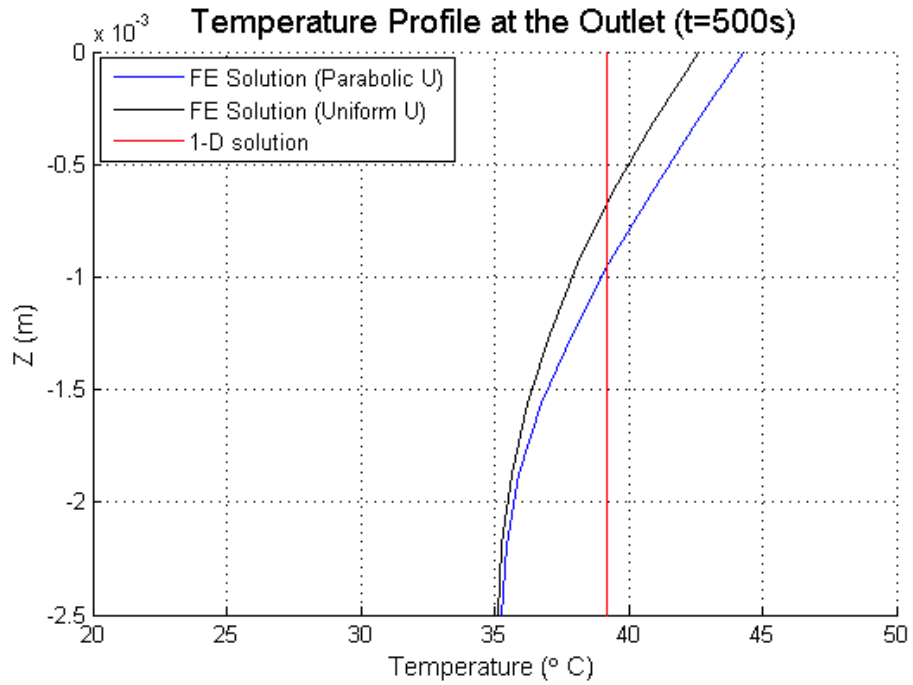

Figure 5.4 Fluid Temperature Profile in the Fracture

Figure 5.5 is the temperature drawdown curve of the fluid at the fracture outlet.

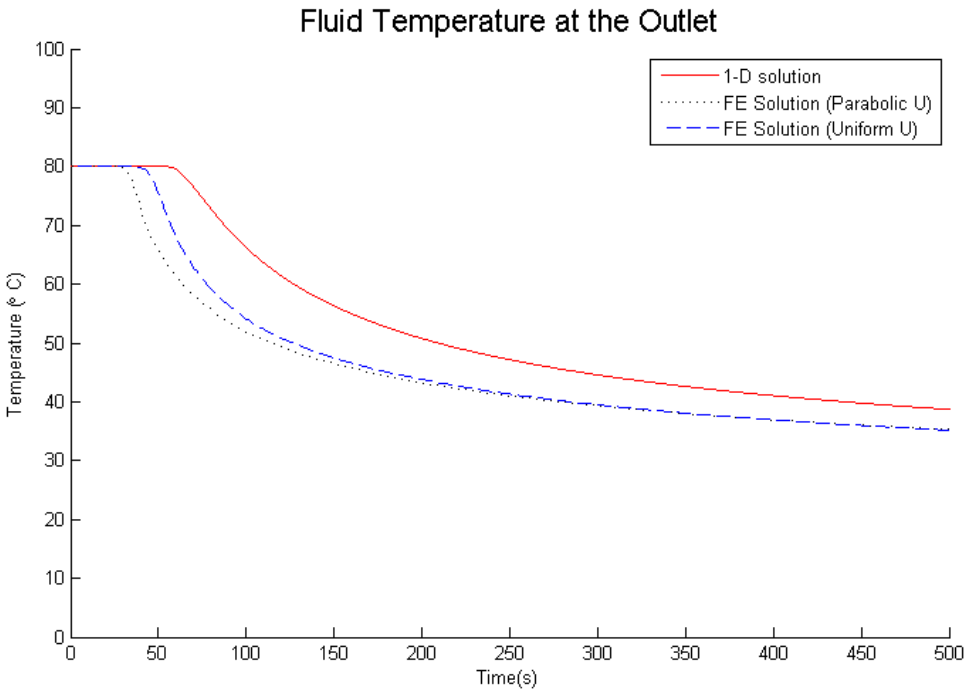

Figure 5.5 Fluid Temperature at the Outlet

The influence of the velocity profile can be seen by comparing the two finite element results. The finite element result with a uniform velocity profile shows higher heat transfer efficiency than the one with a parabolic velocity profile. This happens because the velocity profile determines the rock-fluid contact condition. When the velocity is uniform, the injected cold fluid will have more chance to interact with the rock and get heated up. However, for the case of the fluid with a parabolic velocity profile, the heated fluid near the rock flows slower than the fluid near the center, which is cooler. When hot fluid flows slower and cool fluid flows faster, the bulk temperature tends to be lower.

The influence of the temperature profile can be seen by comparing the 1-D solution with the finite element result with the uniform fluid velocity. As shown in Figure 5.5, the 1-D solution results in higher fluid temperature than the one with the uniform velocity profile. When the fluid temperature profile is uniform, the temperature of the fluid will become the boundary condition of the rock, as expressed in Equation 4.17. The heat conduction in the fluid is not accounted for, thus the system will show a higher heat transfer efficiency.

6. Conclusions

6.1. Summary and Main Findings

The purpose of this research is to develop a model, which predicts the temperature profile of both the water and the rock, so that better decisions can be made regarding the geothermal system. To achieve this purpose, both numerical and analytical approaches are used.

A literature review briefly describes the fundamental physical laws and models that are used in modeling the heat transfer process between the fluid and the fractured rocks. Numerical and analytical models are reviewed to provide a general sense of the current state of the art.

In the numerical approach, a stochastic discrete fracture network model, GEOFRAC, is used to generate a fracture network. GEOFRAC-FLOW, is then used to calculate the flow path in the fracture network and flow rate in each fracture. On the basis of the two models, a heat transfer model, GEOFRAC-THERMAL, is developed. Parametric studies with the three models show the sensitivity of the three models to the input parameters. A case study with the three models on the Fenton Hill project demonstrates the capability of the three models in modeling the heat and mass transfer in the initial operation of the geothermal reservoir.

In the analytical approach, a conceptual geothermal reservoir model is introduced. The heat transfer process in the fluid and the fractured rock is formulated based on energy conservation. Based on the assumption of uniform rock temperature, the 0-D solution is obtained. Useful conclusions are drawn based on the parametric study with the 0-D solution. A case study with the 0-D solution on the Fenton Hill project is conducted. The case study shows a very good match between the measured temperature drawdown and the predicted temperature drawdown for long-term operation. Based on the assumption of heat conduction only in the transverse direction of the rock, the 1-D solution is obtained. The 1-D solution shows an even more realistic prediction of the fluid temperature by showing a constant temperature at the beginning of injection. Parametric studies are conducted with the 1-D solution and useful conclusions are obtained.

To study the accuracy of the 1-D solution, a finite element analysis is conducted to provide a reference to compare with. The comparison of the temperature profiles at the outlet shows that the temperature gradient in the transverse direction in the fracture is not negligible. The comparison of the temperature-time curves at the outlet shows that the velocity profile and temperature profile

in the transverse direction will influence the calculation of temperature at the fracture outlet. These comparisons not only provide an insight into the accuracy of the analytical solutions, but also indicate the limitations of the current research and possible directions for the future work.

6.2.Limitations and Future Work

The modeling of heat transfer between fluid and fractured rocks is a complicated problem because of the physical processes involved and the complex geometry of the fractures. Both a numerical approach and an analytical approach were used. In the numerical approach, only heat convection is considered because of the assumption of constant rock temperature. However, the complex geometry of the fractures is well captured using the stochastic fracture network model, GEOFRAC. In the analytical approach, both heat conduction and convection are considered in the system. However, the geometry of the fracture system is significantly simplified to a series of equally-spaced parallel fractures.

For the numerical approach using GEOFRAC, heat conduction in the rock needs to be considered so that the temperature calculation can be more realistic. Also, with the temperature profile of the rock solved, more mechanisms can be coupled, such as the thermal contraction of the rock and the fracture propagation due to the contraction of the rock. Based on these couplings, a more realistic and powerful model can be developed to represent the complex physical process during the operation of a geothermal system.

For the analytical approach using the conceptual geothermal reservoir model, the velocity profile in the transverse direction in the fracture should be considered, as analyzed in Section 5.2. The heat conduction in the longitudinal direction both in the rock and in the fractures may also be of importance. A full dimensional analysis is needed to evaluate the importance of these factors. Solutions for more complicated fracture networks are other possible directions of future work.

Reference

Alishaev, M. (1979). Calculation of the temperature field of a porous stratum when fluid is injected for plane flow. *Fluid Dynamics*, *14*(1), 49–56.

Ascencio, F., Samaniego, F., & Rivera, J. (2014). A heat loss analytical model for the thermal front displacement in naturally fractured reservoirs. *Geothermics*, *50*, 112–121.

Avdonin, N. A. (1964). Some formulas for calculating the temperature field os a stratum subject to thermal injection. *Neft'i Gaz*, *3*, 37–41.

Barton, C. A., Moos, D., Hartley, L., Baxter, S., Foulquier, L., Holl, H., … Field, H. (2013). Geomechanically Coupled Simulation of Flow in Fractured Reservoirs. In *Proceedings: 38th Geothermal Reservoir Engineering*.

Bödvarsson, G. (1969). On the temperature of water flowing through fractures. *Journal of Geophysical Research*, *74*(8).

Bödvarsson, G. (1972). Thermal problems in the siting of reinjection wells. *Geothermics*, *1*(2), 63–66.

Bödvarsson, G., & Tsang, C. (1982). Injection and thermal breakthrough in fractured geothermal reservoirs. *Journal of Geophysical Research*, *87*, 1031–1048.

Chen, C.-S., & Reddell, D. L. (1983). Temperature distribution around a well during thermal injection and a graphical technique for evaluating aquifer thermal properties. *Water Resources Research*, *19*(2), 351–363.

Cheng, a. H.-D., Ghassemi, a., & Detournay, E. (2001). Integral equation solution of heat extraction from a fracture in hot dry rock. *International Journal for Numerical and Analytical Methods in Geomechanics*, *25*(13), 1327–1338.

Darcy, H. (1856). *Les Fontaines Publiques de la ville de Dijon*. Paris.

Dershowitz, W. S. (1985). *Rock Joint Systems*. *PhD thesis*. Massachussets Institute of Technology.

Dershowitz, W. S., & Einstein, H. H. (1988). Characterizing Rock Joint Geometry with Joint System Models. *Rock Mechanics and Rock Engineering*, *51*, 21–51.

Dijkstra, E. W. (1959). A Note on Two Problems in Connexion with Graphs. *Numerische Mathematik*, (1), 269–271.

Feenstra, S., Cherry, J., Sudicky, E., & Haq, Z. (1984). Matrix diffusion effects on contaminant migration from an injection well in fractured sandstone. *Ground Water*, *22*(3), 307–316.

Fourier, J. (1955). *The Analytical Theory of Heat*. New York: Dover.

Gringarten, A. C., & Sauty, J. P. (1975). A theoretical study of heat extraction from acquifers with uniform regional flow, *80*(35).

Grisak, G., & Picken, J. (1981). An analytical solution for solute transport through fractured media with matrix diffusion. *Journal of Hydrology*, *52*, 47–57.

Hao, Y., Fu, P., Johnson, S. M., & Carrigan, C. R. (2012). Numerical studies of coupled flow and heat transfer processes in hydraulically fractured geothermal reservoirs. In *GRC Transactions* (Vol. 36).

Harlow, F. H., & Pracht, W. E. (1972). Study of Geothermal Energy Extraction. *Journal of Geophysical Research*, *77*(35), 7038–7048.

Heuer, N., Küpper, T., & Windelberg, D. (1991). Mathematical model of a hot dry rock system. *Geophysical Journal International*, *105*, 659–664.

Incropera, F. P., & DeWitt, D. P. (2002). *Fundamentals of Heat and Mass Transfer* (5th ed.). New York: John Wiley & Sons.

Ivanova, V. M. (1995). *Geologic and Stochastic Modeling of Fracture Systems in Rocks*. PhD thesis. Massachussets of Institute of Technology.

Ivanova, V., Sousa, R., Murrihy, B., & Einstein, H. H. (2012). Mathematical Algorithm Development and Parametric Studies with the GEOFRAC Three-Dimensional Stochastic Model of Nature Rock Fracture Systems. *Submitted*.

Jones, T. A., Wooten, S. O., & Kaluza, T. J. (1988). Single-Phase Flow Through Natural Fractures. *Society of Petroleum Engineers Journal*.

Kalinina, E., Klise, K., Mckenna, S. A., Hadgu, T., Lowry, T. (2013). Applications of the Fractured Continuum Model (FCM) to EGS Heat Extraction Problems. In *Proceedings: 38th Geothermal Reservoir Engineering*.

Kocabas, I. (2004). Thermal transients during nonisothermal uid injection into oil reservoirs. *Journal of Petroleum Science and Engineering*, *42*, 133–144.

Lauwerier, H. A. (1955). The transport of heat in an oil layer caused by the injection of hot fluid. *Applied Scientifc Research*, *5*(2-3), 145–150.

Malofeev, G. E. (1960). Calculation of the temperature distribution in a formation when pumping hot fluid into a well. *Neft'i Gaz*, *3*(7), 59–64.

Martínez, Á. R., Roubinet, D., & Tartakovsky, D. M. (2014). Analytical models of heat conduction in fractured rocks. *J. Geophys. Res. Solid Earth*, *119*, 83–98.

McFarland, R. D., & Murphy, H. D. (1976). Extracting energy from hydraulically fractured geothermal reservoirs. In *Proceedings of 11th Intersociety Energy Conversion Engineering Conference*. State Line, Nevada.

Mills, A. F. (1995). *Heat and Mass Transfer* (pp. 271–274). Richard D. Irwin, INC., 1995.

Mills, A. F. (1999). *Heat and Mass Transfer* (2nd ed.). Upper Saddler River, N.J.: Prentice Hall.

Nitao, J. J. (1998). *User's manual for the USNT module of the NUFT code, version 2 (NP-phase, NC-component, thermal)*. Livermore, California.

Reeves, P. C. (2006). Fractured Continuum Approach to Stochastic Permeability Modeling. *Computer Applications in Geology*, *5*, 173–186.

Roubinet, D., de Dreuzy, J.-R., & Tartakovsky, D. M. (2012). Semi-analytical solutions for solute transport and exchange in fractured porous media. *Water Resources Research*, *48*(1), W01542.

Settgast, R., Johnson, S., Fu, P., Walsh, S. D. C., & Ryerson, F. (2012). Simulation of hydraulic fracture networks in three dimensions. *Proceedings: 37th Geothermal Reservoir Engineering*.

Smith, K., Plummer, M., Bradford, J., & Podgorney, R. (2013). Adaptive Mesh Refinement and Time Stepping Strategies for Incorporating Discrete Fracture Networks Into a High Performance Computing Framework for Geothermal Reservoir Simulation. In *GRC Transactions* (Vol. 37).

Sousa, R., Ivanova, V., Murrihy, B., & Einstein, H. H. (2012). *Decision Aids for Engineered Geothermal Systems: Fracture Pattern Modeling*. Research Report, MIT, Cambridge.

Starfield, A., & Cundall, P. (1988). Towards a methodology for rock mechanics modelling. *International Journal of Rock Mechanics, Mining Science and Geomechanics*, *25*(3).

Sudicky, E., & Frind, E. (1982). Contaminant transport in fractured porous media: analytical solutions for a system of parallel fractures. *1Water Resources Research*, *18*(4), 1634–1642.

Tang, D., Frind, E., & Sudicky, E. (1981). Contaminant transport in fractured porous media: Analytical solution for a single fracture. *Water Resources Research*, *17*(3), 555–564.

Tester, J. W., & Albright, J. N. (1979). *Hot Dry Rock Energy Extraction Field Test : 75 Days of Operation of a Prototype Reservoir at Fenton Hill*. Project Report.

Veneziano, D. (1979). *Probabilistic Model of Joints in Rock.* Research Report, MIT, Cambridge.

Witherspoon, P. a., Wang, J. S. Y., Iwai, K., & Gale, J. E. (1980). Validity of Cubic Law for Fluid Flow in a Deformable Rock Fracture. *Water Resources Research*, *16*(6), 1016–1024.

Yang, J., Latychev, K., & Edwards, R. (1998). Numerical computation of hydrothermal fluid circulation in fractured earth structures. *Geophysics Journal International*, *135*, 627–649.

Yost, K., & Einstein, H. H. (2013). *Decision Aids for Enhanced Geothermal Systems-Heat Transfer Model*. Cambridge.

Zyvoloski, G., Dash, Z., & Kelkar, S. (1988). *FEHM : Finite Element Heat and Mass Transfer Code*.

Nomenclature

Symbol	Units	Description
A	m^2	Area
B	$W/(K \cdot m^2)$	Stefan-Boltzmann constant, 5.67×10^{-8}
C_p	$J/(kg \cdot °C)$	Specific heat capacity
D_h	m	Hydraulic Diameter
EA	m^2	Expected area of fractures
F		Configuration Factor
f		Reduction factor
g	m^2/s	Gravitational constant, 9.81
h_T	$W/(°C \cdot m^2)$	Heat convection conefficient
h	m	Hydraulic head
K	m/s	Hydraulic conductivity
k_i	$W/(°C \cdot m)$	Thermal conductivity in the i direction
L	m	Fracture length
mu or P_{32}	m^{-1}	Fracture intensity
Nu		The Nusselt number
Pr		The Prandtl number
P	m	perimeter
p	Pa	pressure
Q	m^3/s	Volumetric flow rate
q_0 or Q_o	W/m^3	Internal energy generation
q_{hi}	W/m^2	Heat flux in the i direction
q_m	$kg/(s \cdot m^2)$	Mass flux
q_{vol}	m^3/s	Volumetric flow rate
Re		The Reynolds number
r	m	Radial coordinate

T	°C	Temperature
U	m/s	Bulk velocity
u_i	m/s	Velocity in the i direction
w	m	Fracture width
x, y, z	m	Cartesian coordinates
z_{el}	m	Elevation head
α	m^2/s	Thermal diffusivity
γ	kN/m^3	Unit weight
δ *or fvalue*	m	Fracture aperture
ε	m	Fracture surface roughness
κ	m^2	Permeability
ϕ		porosity
ρ	kg/m^3	Density
μ	Pa·s	Dynamic viscosity
φ	°	Fracture pole plunge
ω	°	Fracture pole trend

Appendix A

Table A01 shows how the orientation distributions look like when projected on a hemisphere.

Table A01 Orientation Distributions

Fisher k=1	
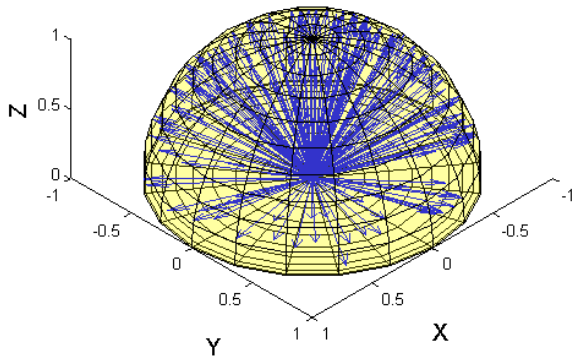	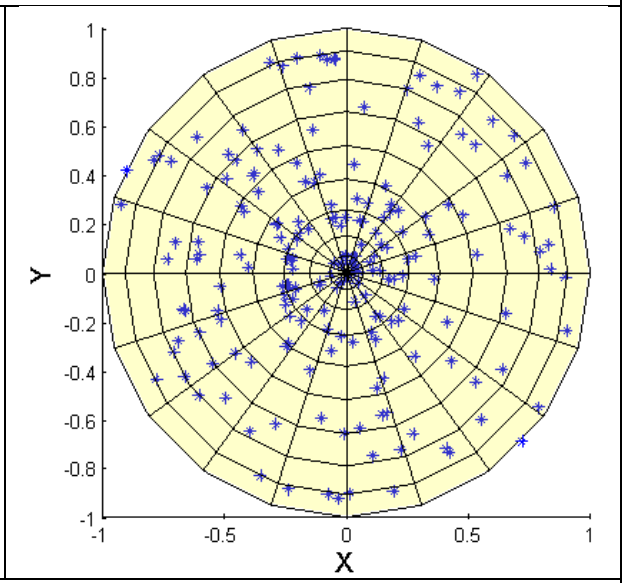
Fisher k=40	
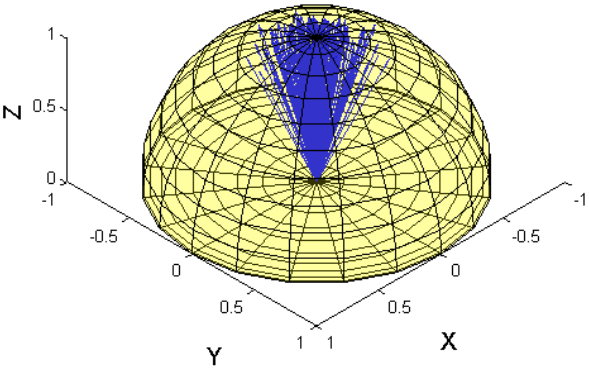	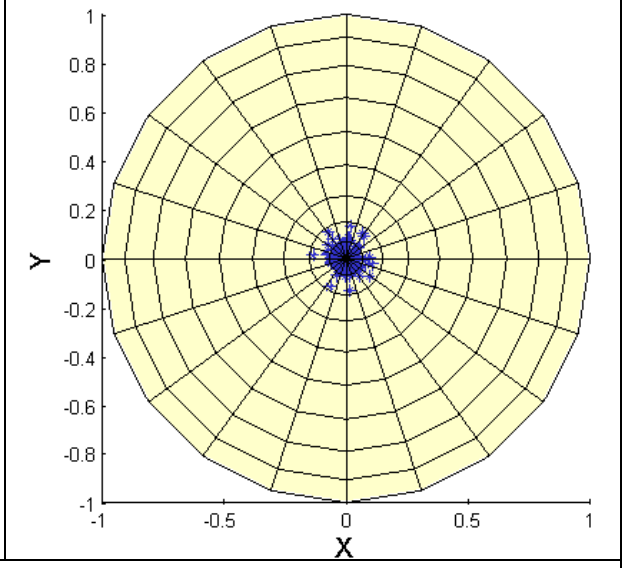
Bivariate Fisher k=[1 40]	

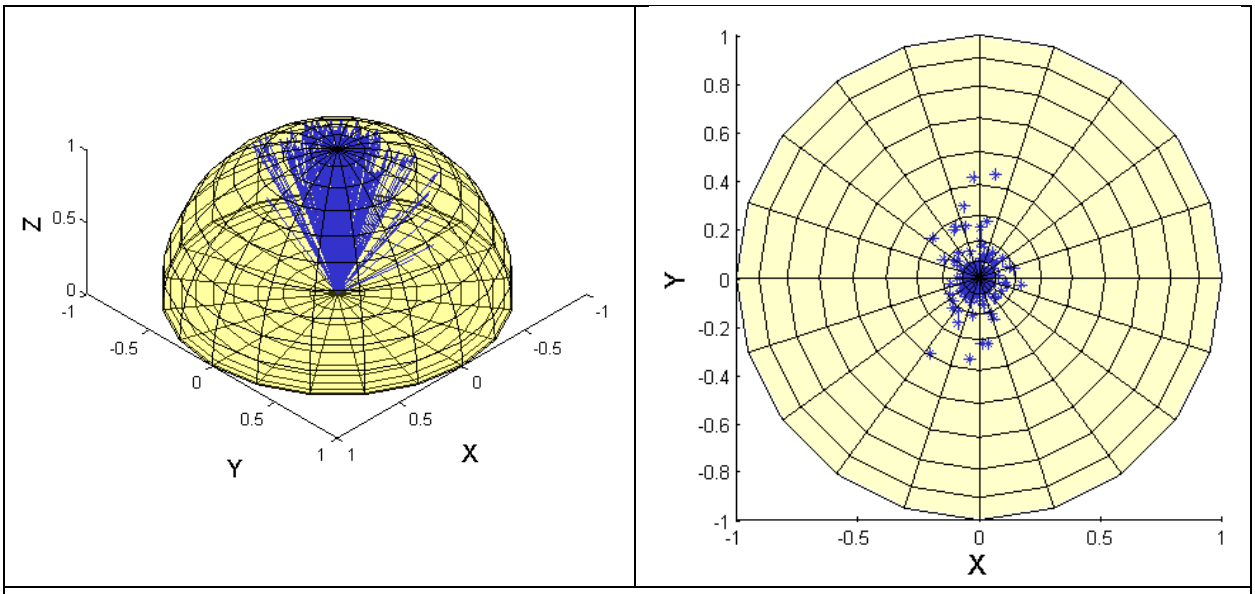

Uniform Distribution

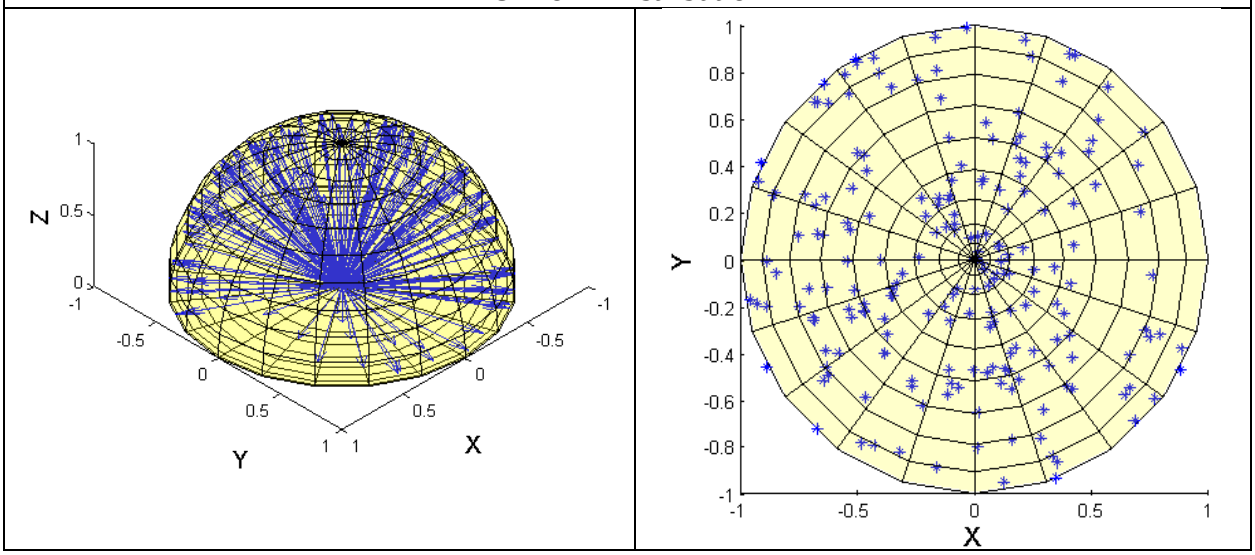

Appendix B

Table B01 shows how the orientation distributions look like when projected on a hemisphere.

Table B01 Mean Orientations

(π/2, π/2)	(π/4, π/2)
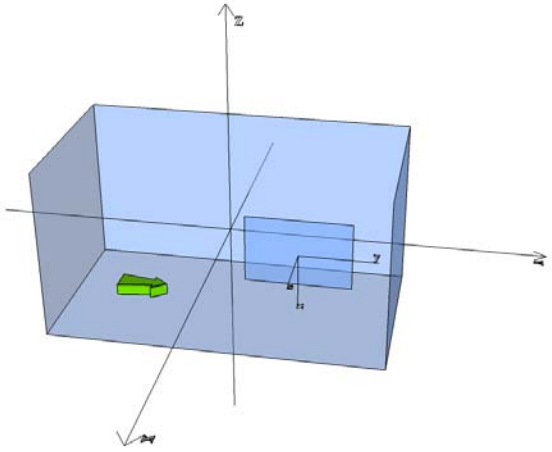	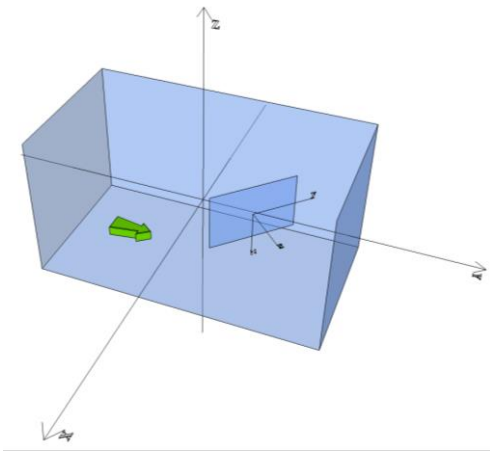
(0, π/2)	(0, π/4)
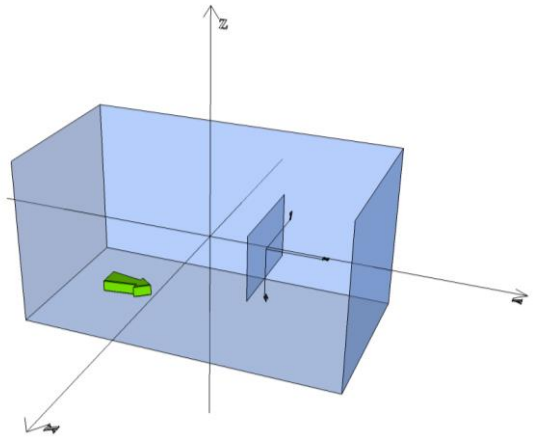	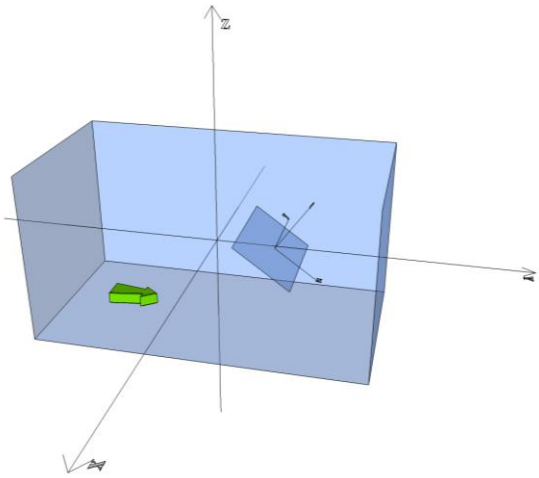
(0, 0)	(π/4, π/4)

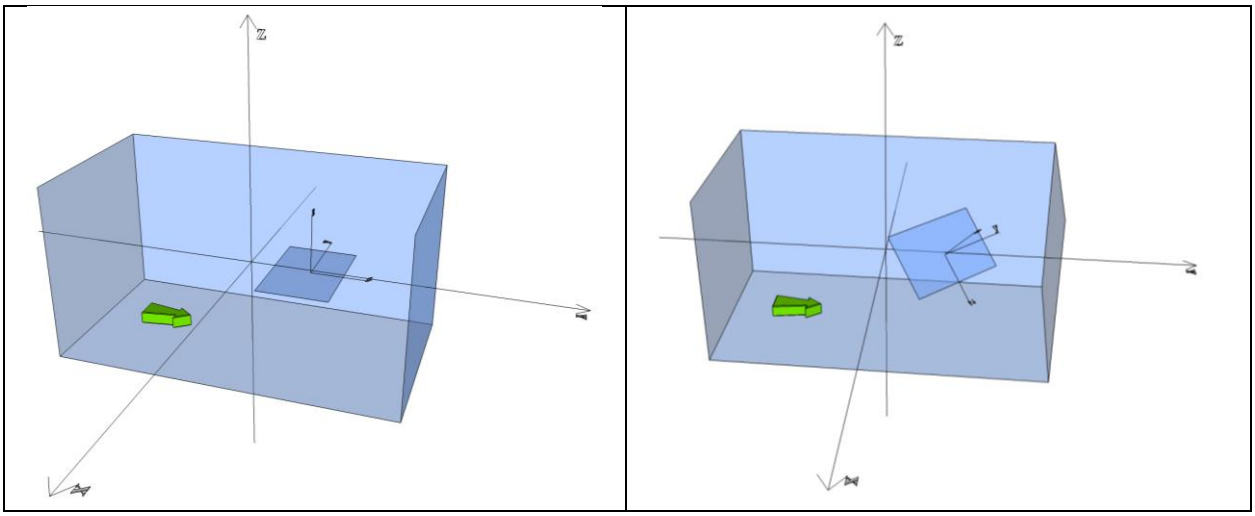
Z
Z

Appendix C

Sample Size Analysis

GEOFRAC is a stochastic model that uses several stochastic processes to model the fracture and flow in the rock. When a parametric study is conducted, a reasonable number of results should be chosen to analyze the trend of the results.

According to the law of large numbers, the average of the results obtained from a large number of trials should be close to the expected value, and will tend to become closer as more trials are performed. So, the number of results should be significant to be able to represent the entire population. However, a large sample size would be computationally costly. So, it is necessary to execute a minimal number of simulations such that the average of the simulation outputs can represent the expectation at reasonable confidence level within a confidence interval. This approach is applied to the study of all the parameters of interest in this report.

Below is an example of simulation results with sample size 200. The results are produced using GEOFRAC with the parameters listed in Table C01. The flow rate of each simulation is plotted on the graph, shown in Figure C01. The stochastic model generated 200 randomly distributed points in the range of 0 to 10.

Table C01 Parameters Used in the Example

mu (m^{-1})	EA(m^2)	m	k	rot	fvalue (m)	r	X (m)	Y (m)
3	2	4	20	1	0.005	0.001	20	40
Z (m)	ΔP (Pa)	μ (Pa·s)	kt (W/m·K)	ρ (kg/m^3)	Cp (J/kg·K)	Tr (C°)	Tw (C°)	
20	500000	0.468×10^{-3}	0.6546	983	4185	200	60	

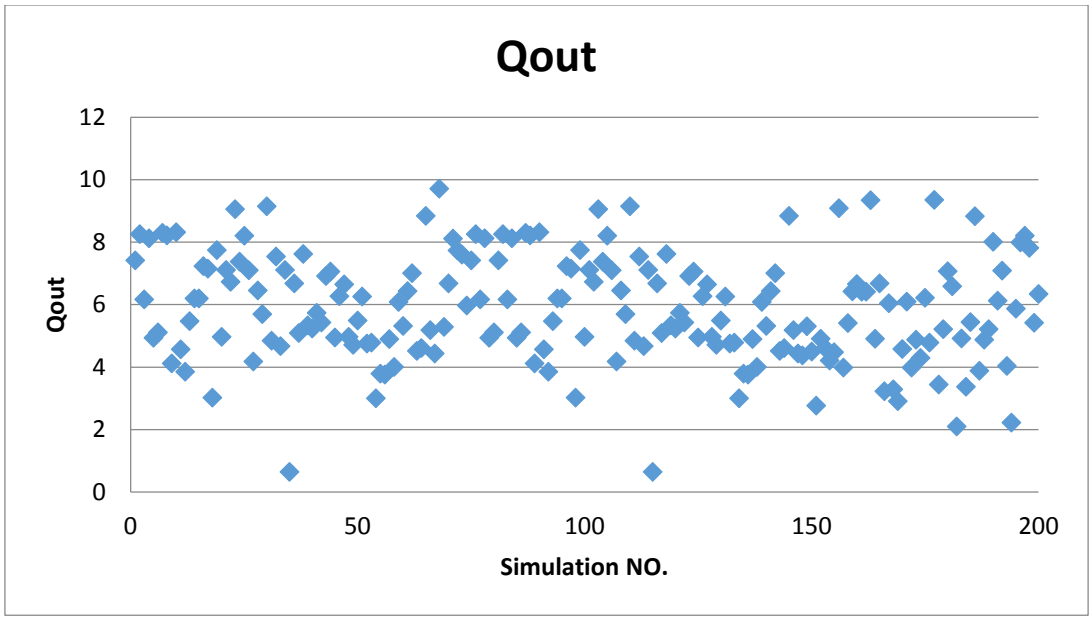

Figure C01 Qout of 200 Simulations

As predicted by *the law of large number* the average of results is close to the expected value. As shown in Figure C02, the average of Qout trends to 5.87, i.e. $\overline{Qout} = 5.87$.

Not only the average has this trend, the standard deviation of Qout also has this trend. As shown in Figure C03, the standard deviation trends to 1.70, i.e. $\sigma(Qout) = 1.70$.

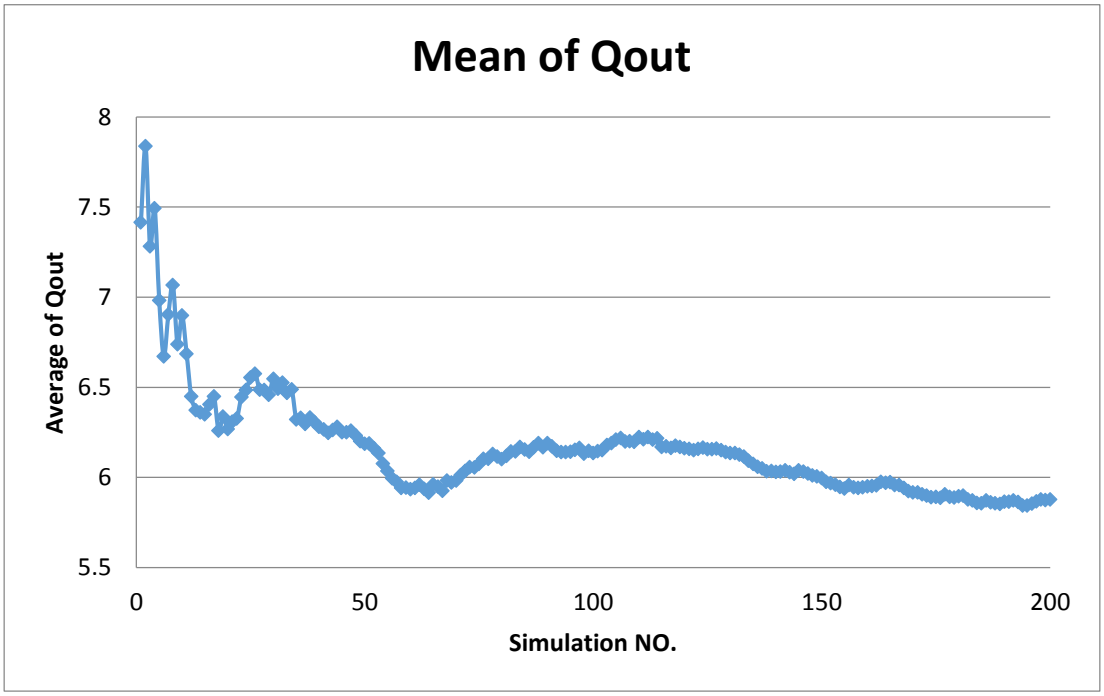

Figure C02 Average of Qout as NO. Increases

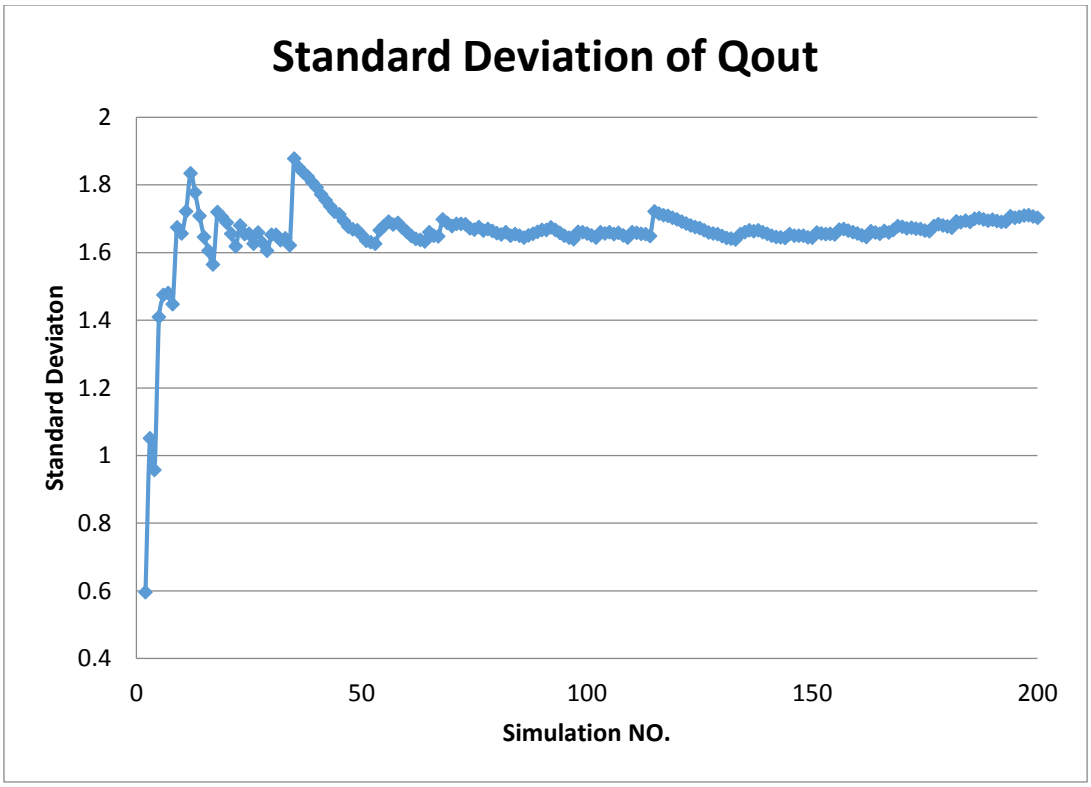

Figure C03 Standard Deviation of Qout as NO. Increases

Also, the frequency distribution is plotted to analyze the probability distribution of Qout. As shown in Figure C04, the distribution of Qout is similar to a Normal Distribution, whose expectation is located at the statistical mode.

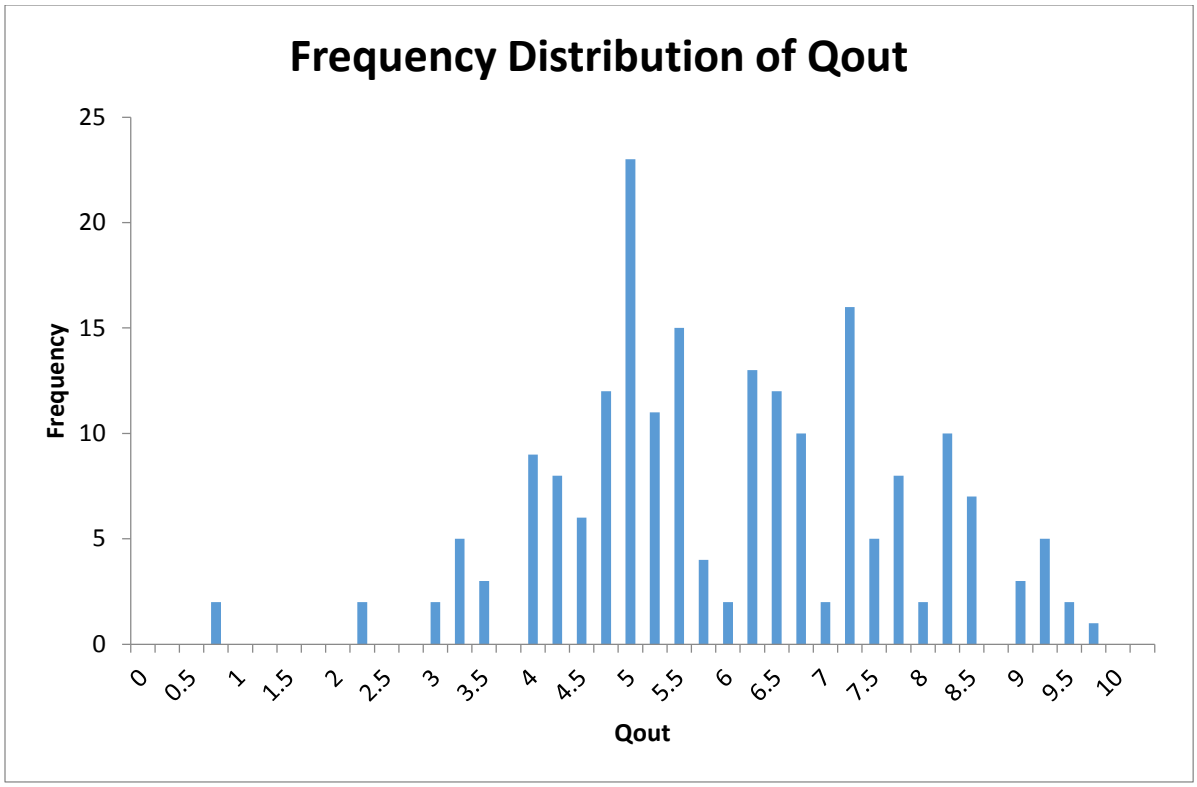

Figure C04 Frequency Distribution of Qout

According to *central limit theorem* for the sample average, for n large, $\overline{Qout}$ is approximately normally distributed with expectation of Qout E (Qout) and standard deviation$\frac{\sigma(Qout)}{\sqrt{n}}$.

Thus, the sample size with certain confidence level and confidence interval can be calculated by the following equation:

$$N = \frac{d^2 \times S^2}{t^2}$$

N: the sample size

d: x at a certain confidence level in Normal distribution

S: standard deviation of the sample

t: confidence interval, usually use percentage of sample average

In the example mentioned above, $\sigma(Qout)$ is used to estimate the standard deviation S, i.e. S=1.70. For a standard normal distribution, 90% confidence level will result in d=1.65. If we use t=10%×$\overline{Qout}$=0.587 as confidence interval, the sample size can then be calculated below:

$$N = \frac{d^2 \times S^2}{t^2} = \frac{1.65^2 \times 1.7^2}{0.587^2} = 22.83$$

With this sample size we can say that we are 90% confident that the true values of the simulation results fall within the confidence interval 10%×$\overline{Qout}$. So, in the parametric analysis of Qout with parameters listed in Table 8, we will basically use the average of 20 simulations to estimate the results.

The above description provides a good example of how the sample size is determined. In the parametric studies, all the sample sizes should be determined in this way. The approach is summarized as follows:

First, in a pilot set of 20 simulations for given parameters, we compute the observed sample mean $\bar{\boldsymbol{c}}$ and sample standard deviation ***s***.

Next, we use *s* as an approximation of the true standard deviation and use $\bar{\boldsymbol{c}}$ to calculate the confidence interval ***t*** by multiplying it by the percentage of tolerance (the example above uses 10%).

Finally, the sample size is calculated by: $N = \frac{d^2 \times S^2}{t^2}$

Table C02 summarizes the sample sizes for all the parametric studies conducted. All the sample sizes are calculated with 90% confidence level and 10%×$\bar{\boldsymbol{c}}$ confidence interval. Then we are 90% confident that the true values of the simulation results fall within the confidence interval 10%×$\bar{\boldsymbol{c}}$.

Table C02 Summary of the Sample Sizes

Parameter set (EA-P32-K-R-H)	Variable	Average	Standard Deviation	Sample Size	Note
2-3-1-0-0.005	Qout	16.73	9.08	80	
2-3-1-0-0.01	Qout	164.31	85.76	74	
2-3-1-1-0.005	Qout	5.16	2.05	43	
2-3-1-1-0.01	Qout	47.94	18.65	41	
2-3-40-0-0.01	Qout	29.22	12.70	51	With no flow path
2-3-40-1-0.01	Qout	61.30	16.94	21	
2-3-40-0-0.005	Qout	5.70	5.56	259	With no flow path
2-3-40-1-0.005	Qout	6.43	1.84	22	